DESIGN, CONSTRUCTION AND COMMISSIONING OF AN APPARATUS TO PERFORM FREQUENCY RESPONSE DIFFUSIVITY MEASUREMENTS AND HIGH TIME-RESOLUTION FTIR SPECTROSCOPY

By

Hilton Roy Heydenrych

Dissertation Presented for the Degree of

MASTER OF SCIENCE IN ENGINEERING

in the Department of Chemical Engineering

UNIVERSITY OF CAPE TOWN

November 2000

For Cathso, Ma, Pa, Lo and Gran

"It ain't about deservin'..."

Clint Eastwood in "Unforgiven" (1992)

Acknowledgements

Many thanks are due to the following people and institutions: Prof. Johannes A. Lercher for allowing me to bypass all the bureaucratic obstacles and work in his laboratory in Munich (where the apparatus described in this study was built); Prof. Cyril O'Connor for introducing me to Prof. Lercher and engineering my registration for this degree; Prof. Eric van Steen for the patient long-distance advice and encouragement; Prof. Andreas Jentys for assistance on the apparatus, understanding when I needed time to write, and insightful speed-reading corrections; Dr. Klaus Möller for nudging me in the right direction on the difficult derivations; Pam Linck for guiding me through registration; Alexander Hartung for helping me negotiate the quagmire of German bureaucracy; Dr. Ernst Bratz for his PCI card and HP Vee programming expertise (and fine home-brew); Andreas Marx for his elegant electronic solutions and help with all matters electrical; Christian Sedlmair and Cristina Paganini for introducing me to the vagaries of infrared spectroscopy and helping me settle in during the first few months; Martin Smidt for his sometimes unorthodox but always ingenious computer remedies and late night company; Shourong Zheng for useful scientific discussions and invaluable assistance with some of the experimental work; Dr. Peter Röger of Süd-Chemie for zeolite samples and mutual pining for Cape Town; Dr. Linda Callanan van Steen for proof-reading and English grammar lessons; Prof. Lovat Rees of Edinburgh for his openness with technical information and for welcoming me into his laboratory on a fact-finding mission; Lijuan Song, for putting up with my barrage of questions in Edinburgh; Dr. Dongmin Shen for valuable information on the practical implementation of the frequency response method; the Bayerischer Forschungsverbund Katalyse and the Catalysis Research Unit for financial support; and all those not specifically mentioned who helped build and commission the apparatus.

Special thanks go to the three people who kept me happy through it all: Andreas Feller for being a magnificent friend and colleague; Dr. Julia Meinershagen for frequent accompaniment to my favourite pastime, and the animated discussions thereafter; and last but certainly not least (in fact, first by a very long way), my wife and best friend, Dr. Catherine Cress, for giving it all a meaning.

Synopsis

The active catalytic sites of zeolites are usually situated within the micropores of the crystals. Since the size of zeolite micropores is of a similar order of magnitude to that of many molecules, the intracrystalline diffusion of reactants and products is often the step that determines both the reaction rate and selectivity. Thus, knowledge of the diffusion rates, and of the diffusional behaviour of molecules within zeolites, is of primary importance in the understanding of these phenomena.

While several methods are used to measure diffusivities, most of these have limitations associated with the minimum crystal size that can be used and/or the range of diffusivities that can be measured. Other problems frequently experienced are experimental complexity and the definition of experimental conditions within a range in which the theoretical models are applicable.

A powerful method for measuring diffusivities under well-defined conditions is the frequency response method, in which the pressure response to a small volume modulation in a closed system is recorded over a range of frequencies. Models have been developed to determine the diffusivity from such experiments for a variety of circumstances, including non-isothermal conditions and multiple diffusion processes.

Fourier transform infra-red (FTIR) spectroscopy can be used to monitor the uptake of sorbate molecules (and hence estimate their diffusivity) in zeolites. In addition, the behaviour of these molecules at the surface, and of the functional groups of the zeolite, can be observed. These observations reveal information about the sorption and diffusional behaviour of the molecules. For a completely reproducible process (e.g. a constant frequency volume modulation), special high time-resolution methods (i.e. rapid- and step-scan) can be used. With these techniques, very rapid molecular processes can be probed.

The objective of this study was to design, construct and commission an apparatus capable of measuring diffusivities using the frequency response method, and to integrate it with an FTIR spectrometer to allow the use of standard and high time-resolution spectroscopy.

To avoid the intrusion of impurities, even at very low sorbate pressures, the entire system was designed for ultra-high vacuum. A deflecting-membrane (i.e. not gas-dependent) pressure gauge was used to monitor sorbate pressure. Temperature-controlled frequency response and infra-red sample cells were custom-made. Square-wave volume modulation was achieved using a mild steel armature attached to flexible bellows mounted between two electromagnets, which could be alternately activated and de-activated. The same signal that drove the current in the electromagnets was used to trigger the recording of pressure and infra-red data, ensuring that these measurements were perfectly synchronised over repeated modulation cycles.

Three important limitations in the apparatus were detected during commissioning. Firstly, the quality of the square wave volume modulation was found to be acceptable only at frequencies below 1 Hz. Thus, the maximum diffusivity that could be measured was limited to 10^{-11} m^2/s (for a crystal diameter of 10 μm) or 10^{-15} m^2/s (for a crystal diameter of 0.1 μm). Secondly, in the high amplification range, the response of the pressure gauge was found to be unstable. Thus, the minimum pressure at which the dynamic range of the gauge was sufficient for frequency response experiments was 0.6 mbar. And, thirdly, for the toluene/HZSM-5 system investigated, the number of FTIR scans that had to be coadded (to achieve an acceptable signal-to-noise ratio) was such that step scan experiments would have been excessively long. Thus, only the rapid scan FTIR mode could be used, limiting the time-resolution between spectra to a minimum of 70 milliseconds.

Nonetheless, within these limitations, several significant commissioning experiments could be performed. Using the frequency response method, the diffusivity of toluene in HZSM-5 (HMFI) crystals (Si/Al=43) with a diameter of 3 μm was found (at 100°C) to be $1x10^{-14}$ m^2/s in the straight channels and $3.3x10^{-15}$ m^2/s in the sinusoidal channels. Monitoring the uptake rate of toluene in HZSM-5 crystals (Si/Al=57) with a diameter of 0.1 μm, a toluene diffusivity (at 100°C) of $2.4x10^{-17}$ m^2/s was estimated. The values obtained in both of these experiments were comparable to those reported in literature for samples of similar crystal size and acidity.

Using rapid scan FTIR spectroscopy for toluene adsorbed on HZSM-5 at 0.1 mbar and 100°C, good quality infra-red spectra were recorded with a time resolution of 0.5 seconds. Extrapolating from the parameters and conditions used, it was deduced that, within a reasonable time frame (i.e. 6 hours), high quality infra-red spectra would also be attainable at the limiting time-resolution of the rapid scan mode (i.e. 70 milliseconds).

All experiments performed on both the frequency response and infra-red sections of the apparatus were found to be reproducible within acceptable margins.

From the above findings, it was concluded that, especially if the recommended improvements were incorporated, the apparatus could be used to perform a range of experiments, including: examining the effects of adsorbed concentration on diffusivity; measuring the activation energy of intracrystalline diffusion; determining the diffusivities of sorbates in the presence of other sorbates (i.e. co- and counter-diffusion); clarifying the role of different sorbent functional groups in adsorption and desorption; and investigating the dynamics of transition states on zeolite surfaces.

Table of contents

List of figures

List of tables

Nomenclature

Where the same symbol has been used for more than one different variable, the symbol is repeated in the "Variable" column and the description should render the applicable definition clear. Subscripts are included with the variable, except in the case of subscripts in Appendix B, which are listed separately.

Roman letters

Variable	Description	SI Units
a	External area per unit particle volume ($\equiv A_c/V_c$); sorption rate method; see equation (1.11)	m^{-1}
a	Side half-length of a parallelepiped (frequency response method)	m
a	Crystal radius in frequency response derivation; see section A.2	m
a_0	Constant term in the definition of a Fourier expansion	same as G(t)
a_1; a_2; a_3	Constants in an anisotropic parallelepiped model (frequency response method); see equation (2.26)	m
a_n	Fourier coefficient; defined in equation (2.48)	same as G(t)
a_p	External surface area of a sorbent per unit mass	$m^2.kg^{-1}$
A	Parameter in frequency response method derivation; defined in equation (2.7)	-
A	Composite diffusivity term in an anisotropic parallelepiped model (frequency response method); see equation (2.26)	$m^2.s^{-1}$
A	Absorbance of a sample; defined in equation (3.2)	-
A	Summation counter in Fourier transformation algorithm; see section B.3	-
$\tilde{A}$	Interim term (in frequency response derivation); see equations (A.48) and (A.49)	s
A_B	Cross-sectional area of the bellows where it is connected to the armature; see section 4.4.3	m^2

A_c	Outer surface area of a crystal	m^2
A_ξ	Interim term in frequency response derivation; defined in equation (A.11)	-
b	Side half-length of a parallelepiped (frequency response method)	m
b	Constant in the Freundlich isotherm; see equation (5.1)	-
b_n	Fourier coefficient; defined in equation (2.49)	same as G(t)
B	Total amount of sorbate present in a planar sheet or isotropic sphere (frequency response method)	mol
B	Magnetic flux density (or magnetic field); see section 4.4.3	T
B	Summation counter in Fourier transformation algorithm; see section B.3	-
B_e	Total amount of sorbate present in a planar sheet or isotropic sphere at the initial equilibrium (frequency response method)	mol
$B(\nu)$	Spectral power density (or intensity) of light	cd
$B_B(\nu)$	Spectral power density (or intensity) of light in a background (i.e. no sample) spectrum	cd
$B_S(\nu)$	Spectral power density (or intensity) of light transmitted through an absorbing sample	cd
c	Side half -length of a parallelepiped (frequency response method)	m
c	Heat capacity of a sorbent per unit mass (frequency response method; non-isothermal model)	$J.kg^{-1}.K^{-1}$
c	Time-dependent concentration at the surface of a crystal; see equation (A.43)	$mol.m^{-3}$
c_s	Volumetric heat capacity of a particle	$J.m^{-3}.K^{-1}$
C	Concentration of a diffusing component	$mol.m^{-3}$
C^*	Concentration of labelled molecules at a constant total concentration	$mol.m^{-3}$
C_e	Equilibrium sorbate surface concentration	$mol.m^{-3}$
d	Diameter of a micropore	Å or nm

D	Constant transport diffusivity of one component in another (or a mixtures of others)	$m^2.s^{-1}$
$\check{D}$	Substitution variable; see equation (A.44)	s^{-1}
D_0	Corrected diffusivity	$m^2.s^{-1}$
D_1; D_2; D_3	Diffusivities in the three primary directions in an anisotropic parallelepiped model (frequency response method); see equation (2.26)	$m^2.s^{-1}$
$D(C)$	Concentration-dependent transport diffusivity of one component in another (or a mixtures of others)	$m^2.s^{-1}$
$D(C_e)$	Constant transport diffusivity of one component in another (or a mixtures of others)	$m^2.s^{-1}$
$\mathscr{D}$	Self-diffusivity; diffusivity due to Brownian motion in the presence of no concentration gradient	$m^2.s^{-1}$
e	Width of each arm of the magnet yoke	m
E	Equilibrium length of the bellows	m
E(r)	Particle size distribution	-
f	Modulation frequency	Hz
f_F	Friction coefficient	-
F	Force acting on an object; e.g., in the new apparatus, sum of the forces acting on the moving parts	N
F_1; F_2	Forces exerted by the two sets of bellows on the moving armature; see section E.1	N
F_B	Spring force of the bellows; see section 4.4.3	N
F(t)	Square wave input function	Depends on physical function
F_G	Gravitational force acting on the moving parts; see section 4.4.3	N
F_M	Magnetic force	N
F_P	The force exerted by the pressure differential on the armature; see section 4.4.3	N
g	Gravitational constant (= 9.8)	$m.s^{-2}$

$G(t)$	Response wave-form to input $F(t)$	Depends on physical function
h	Heat transfer coefficient between the bulk fluid phase and the external surface of a particle	$W.m^{-2}.K^{-1}$
$H(t)$	Noise component of $G(t)$	same as G(t)
ΔH	Heat of adsorption per mol of sorbate	$J.mol^{-1}$
i	Complex number $(-1)^{½}$	-
I	Intensity of light (of a certain wavelength) transmitted through an absorbing sample	cd
I_0	Intensity of light (of a certain wavelength) in a background (i.e. no sample) spectrum	cd
$\tilde{I}_1$	Integral term in frequency response derivation; see equations (A.45) and (A.46)	$mol.s.m^{-3}$
$\tilde{I}_2$	Integral term in frequency response derivation; see equations (A.54) and (A.55)	s
$I(\Delta)$	Intensity of an interferogram as a function of path difference	cd
J	Diffusive flux of a diffusing component	$mol.m^{-2}.s^{-1}$
J	Number of cycles required at each frequency for coaddition during a frequency response experiment; see section B.3	-
J^*	Diffusive flux of labelled molecules at a constant total concentration	$mol.m^{-2}.s^{-1}$
k	Spring constant of the bellows; see section 4.4.3	$N.m^{-1}$
k	Proportionality constant between surface concentration and gas-phase pressure ($k = c/P$); see equation (A.45)	$mol.m^{-3}.Pa^{-1}$
K	Frequency response parameter related to the slope of the isotherm; defined in equation (2.15)	-
K_1; K_2	K parameters for two independent diffusion processes	-
K_H	Dimensionless Henry's law constant	-
K_k	K parameter for the k^{th} kinetic species	
K_R	Constant multiplier ($K_R > 1$); see equation (5.5)	-

K_Ω	Equilibrium constant of the concentration in the storage pores (relative to the concentration in the transport pores) in the diffusion rearrangement model (frequency response method)	-
l	Infinite summation term in a parallelepiped model (frequency response method); see equations (2.23)-(2.26)	-
L	Half-thickness of a planar sheet	m
L_B	Set length of bellows; see section 4.4.4	mm
L_Z	Parameter in ZLC measurements; defined in equation (1.14)	-
m	Infinite summation term in a parallelepiped model (frequency response method); see equations (2.23)-(2.26)	-
m	Mass of a sorbent sample; see equation (2.37)	kg
m	Mass of an object in motion; e.g., in the new apparatus, the mass of the moving parts; see section 4.4.3	kg
m	Sequential number of file ($m = 1 \ldots M$) in a frequency response experiment; see section B.3	-
m_0	Adsorbed mass at time zero	kg
m_t	Adsorbed mass at time t	kg
m_∞	Adsorbed mass at equilibrium	kg
M	Total number of files in a frequency response experiment	-
n	Counter (i.e. 0, 1, 2, etc.); see section 3.1.2	-
n	Infinite summation term in a parallelepiped model (frequency response method); see equations (2.23)-(2.26)	-
n	Harmonic of a periodic function; see section 2.3.3	-
n	Constant in the Freundlich isotherm ($0 < n < 1$); see equation (5.1)	-
n	Infinite summation term; see equation (2.54)	-
n	Infinite summation term; see equation (A.43)	-
N_A	Total number of IR scan coadditions required	-
$N_{A/C}$	Number of IR scans coadded per cycle	-
$(N_A)_P$	Required number of coadditions predicted for a proposed single-step difference FTIR experiment	-

$(N_A)_R$	Required number of coadditions determined from a reference single-step difference FTIR experiment	-
N_C	Number of volume modulation cycles required	-
N_E	An even number to set the frequency of spectral collection ($=fN_E$); see section 4.7.3	-
N_I	Number of mirror positions (i.e. number of points in an interferogram) required in a step scan experiment	-
p	Relative amplitude of the pressure variation (frequency response method)	-
p_B	Relative amplitude of the pressure response in a blank (i.e. no sorbent) experiment (frequency response method)	-
p_Z	Relative amplitude of the pressure response in the presence of a zeolite (frequency response method)	-
P	Gas-phase partial pressure of a diffusing component	Pa
P_e	Equilibrium gas-phase pressure	Pa
P_x	x^{th} pressure reading taken in a frequency response experiment	Pa
$(\Delta P)_A$	Pressure differential across the armature; see section 4.4.3	Pa
q	Intracrystalline concentration	$mol.kg^{-1}$
$(\partial q/\partial P)_T$	Slope of the equilibrium isotherm	$mol.kg^{-1}.Pa^{-1}$
$(\partial q/\partial T)_p$	Slope of the equilibrium isobar	$mol.kg^{-1}.K^{-1}$
r	Radius of a crystal	m
r	Radial variable in frequency response derivation; see section A.2	m
r_M	Mean radius of the circular ring magnets	m
$\langle r^2(t)\rangle$	Mean square displacement of molecules as a function of time for three-dimensional space	m^2
R	Universal Gas Constant	$J.mol^{-1}.K^{-1}$
S_1	Length of the inner set of spacers on the magnet-bellows support; see section 4.4.4	mm
S_2	Length of the outer set of spacers on the magnet-bellows support; see section 4.4.4	mm

S_A	Surface area of a planar sheet	m^2
t	Time variable	s
t_E	Duration of a rapid- or step-scan experiment	s
t_h	Time constant for the heat exchange between a sorbent and its surroundings; defined in equation (2.29)	s
t_R	Time constant of mass exchange between the transport and storage pores in the diffusion rearrangement model (frequency response method); defined in equation (2.33)	s
T	Temperature of a sample or system	K
T_0	Isothermal temperature	K
$\bar{T}$	Transient dimensionless concentration term (in frequency response derivation) which becomes insignificant as t increases; see equation (A.10)	-
u	Substitution variable; see equation (A.41)	$mol.m^{-2}$
v	Relative amplitude of a volume variation (frequency response method)	-
v	Substitution variable; see equation (E.7)	$m.s^{-1}$
V	Volume of a system	m^3
V_c	Volume of a crystal	m^3
V_e	Equilibrium volume (frequency response method)	m^3
$(\Delta V)_P$	Volume change in a proposed single-step difference FTIR experiment	-
$(\Delta V)_R$	Volume change in a reference single-step difference FTIR experiment	-
$\hat{w}$	Interim term (in frequency response derivation); defined in equation (A.13)	m^{-1}
x	Depth coordinate within a planar sheet (frequency response method)	m
x	Linear displacement of an object; e.g., in the new apparatus, the displacement of the armature from its half-way position; see section 4.4.3	m
x	Substitution variable; see equation (A.64)	-

x	Counting variable in a summation series; see equations (B.9) and (B.10)	-
X	Half-distance between magnets; see section 4.4.3	m
X	Substitution variable; see equations (A.56) and (A.57)	-
$\langle z^2(t) \rangle$	Mean square displacement of molecules as a function of time for one-dimensional space	m^2
Z	Fixed length of the bellows in equilibrium position; see section E.1	m
ZPD	Zero path difference (see "Δ" below)	-

Greek letters

Variable	Description	SI Units
α	Summation counter in Fourier transformation algorithm; see section B.3	-
α'	Heat transfer parameter in sorption rate method; defined in equation (1.11)	-
α_{lmn}	Frequency response parameter for a parallelepiped case; defined in equations (2.25) and (2.26)	s^{-1}
α_n	Amplitude of the nth harmonic of G(t)	same as G(t)
β	Summation counter in Fourier transformation algorithm; see section B.3	-
β'	Heat transfer parameter in sorption rate method; defined in equation (1.12)	-
χ	Phase difference in the sorbate concentration variation within the zeolite pores (frequency response method)	radians
δ	Frequency response characteristic function (for a range of particle sizes)	-
δ_{1c}	Frequency response in-phase characteristic function (one-dimensional case); defined in equation (2.13)	-
δ_{1s}	Frequency response out-of-phase characteristic function (one-dimensional case); defined in equation (2.14)	-

δ_{3c}	Frequency response in-phase characteristic function (three-dimensional case); defined in equations (2.18) and (2.23) for different geometries	-
δ_{3s}	Frequency response out-of-phase characteristic function (three-dimensional case); defined in equations (2.19) and (2.24) for different geometries	-
δ_c	Overall frequency response in-phase characteristic function (different for different models)	-
$\delta_{jc}^{(k)}$	Frequency response in-phase characteristic function (j-dimensional case) for the k^{th} kinetic species	-
$\delta_{js}^{(k)}$	Frequency response out-of-phase characteristic function (j-dimensional case) for the k^{th} kinetic species	-
$\delta(r)$	Frequency response characteristic function (for a certain particle size)	-
δ_s	Overall frequency response out-of-phase characteristic function (different for different models)	-
Δ	Path difference: the difference between the distances a beam travels to (and from) a fixed and a moving mirror in FTIR spectroscopy	nm
ε	Squareness factor used to evaluate a square wave-form; e.g., in the new apparatus, the ratio between the time the armature spends in contact with the magnet face in the actual case and the time it would spend in the ideal case; see equation (4.1)	-
ϕ	Phase difference in pressure variation (frequency response method)	radians
ϕ_B	Phase lag in a blank (i.e. no sorbent) experiment	radians
ϕ_n	Phase lag of the *n*th harmonic of G(*t*)	radians
ϕ_Z	Phase lag in the presence of a zeolite	radians
$\phi_{Z\text{-}B}$	Corrected phase-lag ($\phi_Z - \phi_B$)	radians
γ	Relative amplitude of the sorbate concentration variation within the zeolite pores (frequency response method)	-

γ	Parameter in non-isothermal model (frequency response method); defined in equation (2.30)	-
η_1	Frequency response parameter for planar sheet (i.e. one-dimensional) case; defined in equation (2.9)	-
η_3	Frequency response parameter for isotropic sphere (i.e. three-dimensional) case; defined in equation (2.20)	-
φ	Interim term in frequency response derivation; defined in equation (A.12)	radians
κ	Composite term; defined in equation (2.55)	s^{-1}
λ	Wavelength of light	nm
Λ_0	Integrated IR absorbance at time zero	-
Λ_t	Integrated IR absorbance at time t	-
Λ_∞	Integrated IR absorbance at equilibrium	-
μ_0	Magnetic permeability constant ($= 4\pi x10^{-7}$)	$T.m.A^{-1}$
ν	Wavenumber of light	cm^{-1}
ρ_c	Density of a crystal	$kg.m^{-3}$
τ	The time taken for a step-change to occur (i.e. $\tau = 0$ in the ideal case)	s
ω	Angular frequency of the volume modulation (i.e. $\omega = 2\pi f$)	$radians.s^{-1}$
Ω	Sorbate concentration in the "storage" pores	$mol.kg^{-1}$
Ω_e	Sorbate concentration in the "storage" pores at the initial equilibrium.	$mol.kg^{-1}$
ξ	Dimensionless concentration; defined in equation (A.7)	-
ψ	Parameter in frequency response method derivation; defined in equation (2.8)	-
ζ	Number of pressure readings taken per cycle during a constant frequency volume modulation experiment	-

Subscripts (Appendix B only)

Subscript	Description
B	Parameter obtained during a blank (i.e. no sorbent) experiment
f	Parameter obtained at the f^{th} frequency
j	Parameter obtained in the j^{th} cycle (at a certain frequency)
m	Parameter associated with the m^{th} file in a series of experiments (with $m = 1...M$)
Z	Parameter obtained during a run in the presence of a zeolite

1. Introduction and literature review

1.1 Porous solid catalysts

Many fluid-phase chemical reactions require a solid catalyst. The activity of such catalysts depends, in part, on the extent of the surface area available for reaction. Even for extremely small non-porous materials, it is difficult to obtain surface areas of more than 1 m^2/g while, to be effective, most solid catalysts require surface areas between 5 and 1000 m^2/g (Smith, 1981). Therefore, it is necessary for most solid catalysts to be porous.

1.1.1 Kinetics and transport processes

The inherent phase boundaries between fluid and solid make it necessary to consider transport processes (i.e. mass and energy transfer) as well as intrinsic reaction rates when investigating the reaction rates of fluids over solid catalysts (Smith, 1981). The various microkinetic steps which determine the overall rate thus include: diffusion from/to the bulk fluid to/from the solid surface; diffusion into/out of the pores; adsorption/desorption onto/from the solid surface; and the intrinsic chemical steps on the surface. The slowest of these steps is the rate-determining (or rate-limiting) step. In porous catalysts, this step is often the rate of diffusion of the reactants into the pores or of the products out of the pores.

1.1.2 Classification of pores

IUPAC classification divides pores into three categories based on their size (Kärger and Ruthven, 1992):

micropores	$d < 20$ Å
mesopores	20 Å $< d <$ 500 Å
macropores	500 Å $< d$

where d is the pore diameter.

These categories are loosely based on the difference in the types of forces which control adsorption behaviour, for small gaseous sorbates, in the different pore-size

ranges. In micropores, the size of molecules is similar to the size of the pores. Surface forces dominate and, regardless of the molecule's location in the pore, it never escapes from the force-field of the surface. In mesopores, capillary forces become important while, in macropores, the surface contributes little to the sorption capacity.

Likewise, the diffusion mechanisms are different in the different regions. In micropores, diffusion is dominated by interactions between the molecules and the pore wall. In this regime, steric effects are important. Diffusion is an activated process and is known as "configurational", "intracrystalline" or "micropore" diffusion. In mesopores, the mean free path of molecules is greater than the pore size but diffusion still occurs by free flight interrupted by momentary adsorption on the wall (i.e. Knudsen diffusion). In macropores, diffusion generally occurs by a bulk mechanism. The effect of pore size on diffusivity for small gaseous sorbates, is illustrated in Figure 1.1 (Satterfield, 1991) with reference to section 1.2 for the definition of diffusivity.

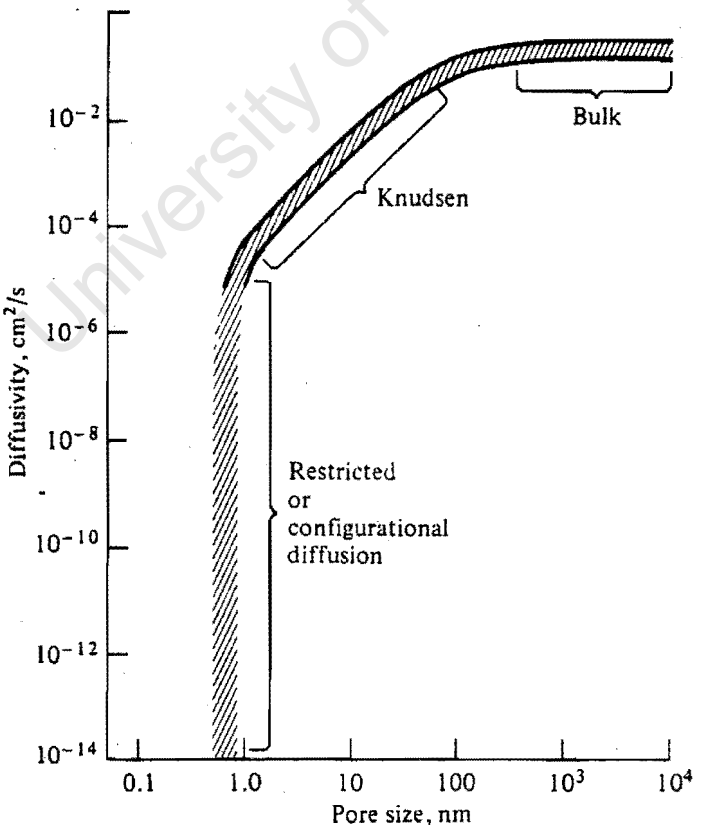

Figure 1.1 - Effect of pore size on the diffusivity of small gaseous sorbates

1.2 Diffusion phenomena

Unless otherwise noted, this overview of diffusion phenomena is based on the review of Kärger and Ruthven (1992).

The diffusivity or diffusion coefficient [$D(C)$ or D] of one component in another (or a mixtures of others) is defined by Fick's First Law of Diffusion as

$$J = -D(C) \text{ grad } C \tag{1.1}$$

where J is the diffusive flux and C the concentration of the diffusing component. By considering the conservation of mass, the following relation, known as Fick's Second Law of Diffusion, can be derived.

$$\partial C/\partial t = \text{div}[D(C) \text{ grad } C] \tag{1.2}$$

Another definition of diffusivity can be obtained by applying Fick's Second Law to a system of labelled molecules, initially located within a certain spatial element, undergoing Brownian motion (or a "random walk"). In this case, since the molecules are all of the same type (i.e. distinguished only by labelling), there is no concentration gradient and diffusivity is a constant ($\mathscr{D}$), independent of concentration. Equation (1.2) can then be simplified to

$$\partial C/\partial t = \mathscr{D}\text{div}[\text{grad } C] \tag{1.3}$$

which can then be solved to give the following equations, known as the Einstein relations:

$$\langle z^2(t)\rangle = 2\,\mathscr{D}t \tag{1.4a}$$

and

$$\langle r^2(t)\rangle = 6\mathscr{D}t \tag{1.4b}$$

where $\langle z^2(t)\rangle$ and $\langle r^2(t)\rangle$ are mean square displacements, as a function of time t, for one- and three-dimensional space respectively.

Because this diffusivity assumes a changing concentration of labelled molecules within a constant total concentration of molecules, an alternative definition can also be written

$$J^* = -\mathscr{D} \text{ grad } C^* \tag{1.5}$$

Where J^* and C^* are the diffusive flux and concentration of labelled molecules at a constant total concentration.

Thus, one can distinguish between two separate diffusion phenomena. The first is a concentration-independent Brownian molecular motion known as self-diffusion. This can be observed either by labelling a certain fraction of diffusing molecules or by determining the mean square displacements of a large number of diffusing molecules. The second diffusion phenomenon is mass transfer resulting from a concentration gradient and is known as transport diffusion.

As a first approximation, the relationship between self-diffusivity and transport-diffusivity can be ascertained by considering that the driving force for diffusion is not the concentration gradient, as is implicit in equation (1.1), but rather the gradient of chemical potential. Assuming that the resistance to the diffusional flow is in the form of a frictional force, one obtains

$$D = (RT/f_F)(\text{d ln } P/\text{d ln } C) = D_0(\text{d ln } P/\text{d ln } C) \tag{1.6}$$

where R is the Universal Gas Constant, T is the temperature, f_F is a friction coefficient and P is the partial pressure of the diffusing component. D_0 is known as the "corrected diffusivity". In a mixture of two identical species, distinguishable only by their labelling, the relation between P and C is linear. Therefore, the self-diffusivity is given by

$$\mathscr{D} = RT/f_F = D_0 \tag{1.7}$$

And equation (1.6) can be re-written

$$D = \mathscr{D}(\mathrm{d} \ln P/\mathrm{d} \ln C) \tag{1.8}$$

Implicit in this formulation is the assumption that the friction coefficient f_F is the same for both self- and transport-diffusion, which is not true in all cases, but is valid for most adsorption systems. It should also be noted that, for the diffusion of a single component within the pores of a microporous sorbent, there is no clear distinction between molecules on the surface and those in the "gas" phase. Thus, one usually considers only the "intracrystalline" concentration (q) and equations (1.6) and (1.8) are expressed as

$$D = D_0(\mathrm{d} \ln P/\mathrm{d} \ln q) = \mathscr{D}(\mathrm{d} \ln P/\mathrm{d} \ln q) \tag{1.9}$$

Equation (1.9) is known as the Darken equation.

1.3 Introduction to zeolites

Zeolites are crystalline aluminosilicates formed by the connection of tetrahedrally coordinated Si and Al atoms (known as the T-atoms) via oxygen atom bridges. Due to the different formal charges of Si (4+) and Al (3+) in the zeolite framework, the Si-tetrahedron is neutral whereas the Al-tetrahedron has a charge of (–1). The negative charge generated by the presence of an Al-tetrahedron is balanced by protons or metal cations to achieve electroneutrality. The ideal generalized chemical composition of zeolites is $M_{x/n}Al_xSi_{y-x}O_{2y}$ where M is a cation with valence n. The tetrahedral Si/Al structure, together with the charge-balancing cation is shown in Figure 1.2.

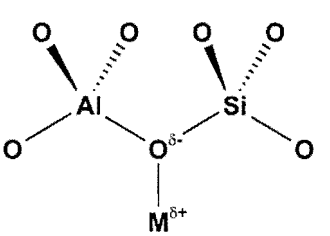

Figure 1.2 - Si/Al tetrahedral structure in zeolites

The Si- or Al-tetrahedra can combine into simple polyhedra and, from these, three-dimensional crystal structures are assembled. These crystals have one-, two- or three-dimensional channel systems with well-defined pore sizes. The diameter of the pores depends on the number of tetrahedra in a ring (Csicsery, 1984) and is typically less than 10 Å (i.e. micropores). The ZSM-5 (MFI) structure type, for example, has a system consisting of two intersecting channel-types: straight channels with pore dimensions of 5.3 x 5.6 Å and sinusoidal channels with pore dimensions of 5.1 x 5.5 Å (Meier et al, 1996). Both channel-types are made up of ten-membered rings. The MFI structure type, as well as a schematic representation of the channel system, is shown in Figure 1.3 (Eder, 1996).

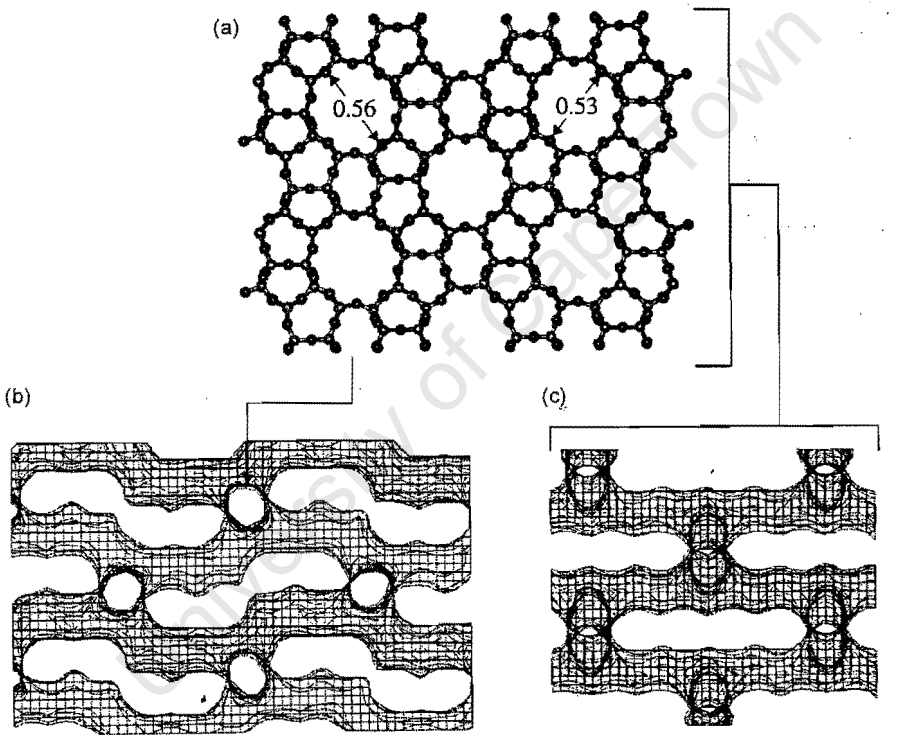

Figure 1.3 - (a) Framework of MFI viewed along the straight channels; and schematic representation of the channel system viewed (b) along and (c) perpendicular to the straight channels

1.3.1 Acid-catalysis and shape selectivity in zeolites

The cationic sites can usually be exchanged to H^+, which gives the zeolites a strong Bronsted acid character and thus makes them interesting for use as heterogeneous catalysts in acid-catalysed reactions. In addition, the fact that they have well-defined

pore-sizes, which are similar to the sizes of many molecules, makes them useful as molecular sieves or shape-selective catalysts.

The latter characteristic is a result of the fact that, in zeolites, most catalytically active sites are within the pores and, therefore, any potential reactant, product or transition state has to be able to fit into the pores. Thus, three different classes of shape-selectivity are defined for zeolites (Csicsery, 1984). Reactant selectivity occurs when only certain reactant molecules are small enough to diffuse through the zeolite pores. Product selectivity occurs when, among all the product molecules formed in the pores, only those with certain dimensions can diffuse out of the pores. Restricted transition-state selectivity occurs when certain reactions are prevented because the transition-state associated with the reaction mechanism is too large to be formed in the pores. Reactant and product selectivity can also occur to a partial extent if some types of reactant or product molecules diffuse more slowly through the pores than others.

1.3.2 Diffusion in zeolites

From section 1.3.1 it is clear that, except in the case of restricted transition-state, knowledge of the diffusion rates and of the diffusional behaviour of molecules in zeolites is of primary importance in the understanding of reactant and product shape-selectivity.

Another important issue in zeolite catalysis is that the reaction rate can be strongly reduced by diffusion limitations on the reactant. Thus, knowledge of diffusion is also important to understand and improve reaction kinetics.

1.4 Measurement of diffusion in zeolites

As mentioned in section 1.2, there are two diffusion phenomena, self- and transport-diffusion, each of which can be measured using more than one method. In sections 1.4.1 and 1.4.2 (and their subsections), a brief overview of the various methods is given. Unless otherwise noted, this overview is based on the review of Kärger and Ruthven (1992).

1.4.1 Measurement of self-diffusion

In accordance with the two definitions given in section 1.2, there are two approaches to measuring self-diffusion. The first, corresponding to equation (1.5), is to measure the Fickian diffusion of labelled molecules within a mixture in which the total concentration of the molecules remains constant. The second approach, corresponding to equation (1.4), is to measure the mean square displacement of a large number of molecules.

1.4.1.1 Tracer exchange

If one makes the reasonable approximation that the different isotopic forms of a molecule have identical thermodynamic and transport properties and if one isotope can be distinguished from the others, then the diffusion of that isotope within the mixture can be used to measure self-diffusion. This is known as the tracer exchange method and is particularly convenient when one of the isotopes is radioactive, since this provides a simple measure of the concentration of the labelled species.

There are two main methods to detect radioactivity. The Geiger-Müller counter is useful for strong β emitters but has range limitations for weak β emitters such as ^{3}H and ^{14}C which are commonly used to label adsorbents.

This difficulty can be overcome using a liquid scintillation counter (LSC) detector which requires a solution containing molecules which emit a light flash when they interact with radiation. This method is very accurate, with errors of less than 1%. However, it is applicable only to diffusion in liquids and thus not to zeolites.

In addition to using radioactive isotopes, it is also possible to use NMR to follow isotopically labelled molecules (e.g. a deuterated hydrocarbon in a mixture of the non-deuterated molecules) (Förste et al, 1990). This method provides a convenient way to evaluate the consistency of the tracer exchange approach with the mean square displacement approaches described in the sections 1.4.1.2 and 1.4.1.3.

1.4.1.2 NMR gradient methods

NMR measurements make use of an appropriate radio frequency (r.f.) magnetic pulse (known as a $\pi/2$ pulse) to shift the total magnetization of nuclear spins into the plane perpendicular to the direction of a constant magnetic field. This transverse component of total magnetization is the measured variable in NMR self-diffusion experiments.

In NMR gradient methods, inhomogeneities are created in the magnetic field by superimposing a position-dependent field on a constant field. A phase angle is accumulated by the nuclear spins as a result of their precessional motion in the combined field. This phase angle can be evaluated by measuring the spin echo after an appropriate sequence of r.f. pulses (usually a $\pi/2$ pulse followed by a π pulse). Because of the field gradient, the phase angle is position dependent. Thus, by measuring the attenuation of the spin echo, it can be ascertained whether the spins have retained their positions or whether (and how far) they have migrated. From this, the mean square displacement of the molecules and, from equation (1.4), their self-diffusivity can be determined.

A constant field gradient technique produces accurate results but the measurement range is limited because the magnitude of the constant gradient cannot be too high and the measurement time has to be shorter than the relaxation time of the transverse magnetization. Thus, only high self-diffusivities can be measured. In addition, the method is mainly applicable to diffusion in liquids where the relaxation time of the transverse magnetization is sufficiently large (and hence not to zeolites).

These limitations can be circumvented using the Pulsed Field Gradient (PFG) NMR method.

1.4.1.3 Pulsed field gradient (PFG) NMR

In this method, two identical pulsed field gradients are applied: one between the $\pi/2$ and π pulses, and one between the π pulse and the spin echo. Thus the field gradient

does not interfere with the r.f. pulses or the spin echo. Therefore, more intense field gradients can be applied, making the method useful for self-diffusion in heterogeneous systems such as zeolites. In addition, improvements have been made to the method such as: the stimulated echo method (Kärger et al, 1988), which allows longer observation times and thus permits a larger range of diffusivities to be probed; the method of alternating gradients which makes the technique sensitive to very small molecular displacements; the development of more complex pulse sequences to minimize the effect of internal field gradients (Williams et al, 1978; Karlicek and Lowe, 1980); and the combination of the PFG method with a multiple r.f. pulse sequence to overcome relaxation time limitations (Silva-Crawford et al, 1980). Self-diffusion in multi-component systems can also be probed by combining the PFG method with Fourier transform NMR.

For typical experimental conditions in sorbate-sorbent systems, it has been found that the minimum displacement that can be detected by spin echo attenuation is approximately 1 μm. Thus, the minimum self-diffusivities that can be probed by NMR are of the order 10^{-11} m^2/s.

Another factor that is very important to consider, especially in the case of zeolites, is that equation (1.4) is only valid when the observed molecular displacements are not restricted by geometric effects. Since the crystal size range of zeolites is often less than 100 μm, care has to be taken that the root mean square displacement of the diffusing molecules does not approach the crystal size, in which case the surface and the intercrystalline space play a significant role in the observed results.

1.4.1.4 NMR tracer desorption

An important extension to the PFG NMR technique is the NMR tracer desorption (or fast tracer desorption) technique (Kärger, 1982). In this method, the observation time is deliberately extended so that a sufficiently large fraction of molecules leave the crystal for intercrystalline (or long range) diffusion to become significant. By appropriate mathematical manipulation of the observed results, an intracrystalline mean lifetime can be ascertained and, from this, a desorption diffusion coefficient.

This method allows measurements of smaller diffusivities (> 10^{-15} m^2/s) in smaller crystal sizes (> 0.1 μm) than the standard PFG NMR method.

If molecular desorption is limited by intracrystalline diffusion, this coefficient coincides with the intracrystalline self-diffusivity. However, if there is any resistance to mass transfer at the crystal surface these two quantities will not be equal and thus a surface barrier can be detected by this method. A parameter known as surface permeability has been defined by which the extent of the surface barrier can be quantified.

1.4.1.5 Quasi-elastic neutron scattering (QENS)

In QENS experiments, motions occurring over a time-scale of 10^{-9} to 10^{-12} seconds broaden the elastic scattering peak of neutrons (Rees, 1994). The long-range translational motion is derived from the broadening of the elastic peak as a function of the momentum transfer and thus the diffusivity can be found using equation (1.4) (Jobic et al, 1991).

An advantage of this method is that the motion of a single nucleus with respect to the centre of mass of the sample is measured and thus data can be interpreted without considering sorbate-sorbate interactions or paramagnetic impurities (Wright and Riekel, 1978). In addition, for hydrocarbons in zeolites, only incoherent scattering has to be considered because of the large incoherent cross-section of hydrogen (Jobic et al, 1991). Coinciding results have been found in the investigation of similar systems using PFG NMR and QENS (Jobic et al, 1991). A disadvantage of the method is the need for a neutron source.

1.4.2 Measurement of transport diffusion

The measurement of transport diffusion requires a concentration gradient and a determination of the resulting molecular flux. Methods to achieve this can be divided into two groups: direct methods, in which the flux and the concentration gradient are measured simultaneously under either transient or steady state conditions; and indirect

methods. The latter can be sub-divided into two groups: uptake rate measurements, in which the internal concentration gradient is deduced from measurements of concentration at the external surface and the flux is determined by measuring the amount of sorbate passing through the surface; and chromatographic methods, in which the dynamic response of a packed column to a perturbation in flow rate or sorbate concentration is measured and used to deduce the mass transfer rate.

In general, while direct methods are more rigorous since they avoid the need for assumptions inherent in indirect methods, the latter are usually experimentally more convenient and hence more widely used. The most important methods in each of these categories are briefly described below.

1.4.2.1 Direct macroscopic methods

Optical double refraction

The first method used to measure diffusion in zeolite crystals was the double refraction method (Tiselius, 1934; Tiselius, 1935), in which polarized light was used to follow the concentration front during the adsorption of water. This method is difficult to apply to micron-sized particles and is also inappropriate for fast diffusion processes. In addition, heat effects are ignored.

Refractive index

Another method similar to double refraction is the measurement of the refractive index to follow the concentration of the sorbate within the sorbent. A light beam passing through a crystal in the direction perpendicular to the diffusive flux is deflected by an angle which depends on the gradient of the local adsorbed-phase concentration (Jost, 1952). The sensitivity of such measurements can be enhanced by using interference techniques (Tyrrell and Harris, 1984) but, as with the double refraction method, its application to zeolites is limited because there are substantial practical difficulties in the case of small crystals.

Interference microscopy

An alternative method using an interference technique is interference microscopy. In this method, an absolute difference in the optical path length, relative to a standard

beam, is determined by analysis of the interference pattern which results when these two beams are superposed on each other. The path length at different points within the crystal can then be ascertained. Because the change in optical path length is related to the refractive index which is, in turn, related to the concentration gradient, the diffusivity can thus be determined. The main drawback of this method is that, within the spatial constraints of an optical microscope of the required magnification (for zeolites), it is difficult to impose a well-defined boundary condition at the crystal surface.

X-ray absorption

Another direct method is the use of X-ray absorption (Dubinin et al, 1975). However, this can only be used if the sorbate nuclei have a cross-section (for absorption of X-rays) of a similar order of magnitude to that of the sorbent. In addition to the need for sufficiently heavy nuclei, this method also has limited spatial resolution (> 0.5 mm) and is thus also unsuitable for zeolites.

Spin mapping by NMR

Spin mapping NMR spectroscopy (Heink et al, 1978) can also be used to follow the distribution of resonant spins (of a sorbate) over the sorbent sample. This has the advantage over the X-Ray method that it does not require heavy nuclei but only a sorbate that contains protons. However, because of the low sensitivity of NMR, the signal-to-noise ratio has to be enhanced by signal accumulation (i.e. coadditions) and this gives rise to a trade-off between spatial and time resolution. As a result, a spatial resolution of less than 1 mm is generally not possible, thus making the method also unsuitable for zeolites.

Spin mapping by ESR

Another spin mapping technique is that using electron spin resonance (ESR). This is much more sensitive than NMR and thus allows a reduction in spatial resolution to about 50 μm. However, the method requires a sorbate with an unpaired electron which limits the range of sorbates that can be used.

Steady-state permeability and Wicke-Kallenbach

All the abovementioned direct methods are applied during transient adsorption. Steady state measurements are also possible using permeable, parallel-sided slabs or membranes of the sorbent with a fixed concentration of sorbate at each face. This can be done by operating either with a pressure gradient across the membrane or at a constant pressure with a concentration difference between the faces (Wicke and Kallenbach, 1941).

The former method has the disadvantage that it measures forced-flow permeability and, depending on the pore-size distribution, there is not always a clear relationship between the permeability and a well-defined diffusivity. The latter method, also known as the Wicke-Kallenbach method, eliminates some of the problems of the permeability method but difficulties are still encountered with the interpretation of data when there is a broad pore-size distribution.

Both of these types of measurement can also be conducted under transient conditions and, when performed in conjunction with the steady state experiment, can yield additional kinetic information and provide an indication of whether there are blind or blocked pores in the material.

There are two ways of measuring diffusion in zeolites using these methods. The first is to use single crystals (to measure the true transport diffusivity) but this requires large crystals, 100 μm being the lower practicable limit. Even then, the difficulties in mounting a single crystal are significant. The second possibility is to compress powder into a pellet but this introduces intercrystalline pores and may block some zeolite pores, leading to data that is unreliable.

From the above discussion it is clear that, while direct methods do not require additional steps to relate the measurement to the diffusivity, the experimental limitations in the use of these methods with zeolites, mainly related to the crystal size requirements, render the methods impracticable in most cases. Thus, it is necessary to consider experimentally more simple indirect methods.

1.4.2.2 Sorption rate methods

In sorption rate methods, the rate of uptake of sorbate, in response to a change in the pressure or concentration of the sorbate, is measured. Different techniques employ different boundary conditions and different means by which the uptake is measured. The choice of model to interpret the data depends on: the assumption of which mechanism controls mass transfer; the assumptions about the rate of heat transfer; the linearity of the equilibrium relation; and the boundary conditions at the particle surface. Naturally, if a certain model is used, the assumptions have to be verified.

Boundary conditions and resistance to mass transfer

For zeolites, as long as intercrystalline resistances (e.g. in the macropores of a pellet) are circumvented by using small particles and avoiding bed-depth effects, intracrystalline diffusion is almost always the controlling resistance to mass transfer. The most common boundary condition is a step change in surface concentration at time zero, followed either by the maintenance of a constant surface concentration or by a surface concentration which falls as the sorbate is adsorbed by the sorbent.

It should be noted that, in the case of constant surface concentration, the solution for transient sorption in the initial region of the uptake curve is the "square root law":

$$(m_t - m_0)/(m_\infty - m_0) = (2A_c/V_c)(Dt/\pi)^{1/2} \qquad (1.10)$$

where m_t, m_0, m_∞ are the adsorbed masses at time t, at time zero and at equilibrium, respectively, A_c is the outer surface area of the crystal and V_c is the volume of the crystal. Note that $2A_c/V_c = 6/r$ for a spherical crystal, where r is the crystal radius. The use of equation (1.10) to interpret sorption rate data is discussed further in section 1.5.4.

In cases where intercrystalline or macropore diffusion becomes significant, models for either macropore diffusion or diffusion in bi-porous particles can be used (Lee, 1978). These are similar to intracrystalline diffusion models except that intercrystalline porosity has to be considered.

Models which take into account a variety of geometries have also been developed for all of these cases.

Non-linearity

For simplicity, almost all models assume a constant diffusivity when solving equation (1.2). If the step change in concentration is sufficiently large, the effect of a non-linear isotherm is to invalidate this assumption. Thus, either the step-change has to be kept small enough to ensure that the isotherm is linear within the range under investigation or more complex models have to be developed which take the concentration dependence into account. The concentration dependence of the diffusivity is usually derived from equation (1.9) in combination with an equation for the isotherm.

Resistance to heat transfer

All the models mentioned above assume that the system is isothermal. While heat transfer resistance within particles or pellets is usually negligible, external film resistance is often significant (Lee and Ruthven, 1979) and cannot be ignored. For zeolites, assuming that intercrystalline resistances are avoided, the situation of greatest practical importance is thus external heat transfer resistance with intracrystalline diffusion resistance.

Two distinct effects must be considered in a non-isothermal system: the temperature dependence of the adsorbed phase concentration at equilibrium (i.e. of the isobar); and the temperature dependence of the diffusivity. The latter can be made negligible by keeping the concentration step sufficiently low but the former effect is independent of the step size (Chihara et al, 1976). Upon analysis of the relevant heat transfer, mass transfer and diffusion equations, the uptake rate is found to be dependent on two variables.

$$\alpha' = (ha/c_s)(r^2/D) \quad (1.11)$$

and

$$\beta' = (\Delta H/c_s)\rho_c(\partial q/\partial T)_p \quad (1.12)$$

where h is the heat transfer coefficient between the bulk fluid phase and the external surface of the particle, a is the external area per unit particle volume, c_s is the volumetric heat capacity of the particle, ΔH is the heat of adsorption per mol of sorbate, ρ_c is the density of the crystal and $(\partial q/\partial T)_p$ is the slope of the equilibrium isobar (assumed to be constant over the range of measurement).

The limiting case of isothermal behaviour occurs when either $\alpha' \rightarrow \infty$ (infinitely fast heat transfer) or $\beta' \rightarrow 0$ (infinite heat capacity). It can be shown that, when the ratio α'/β' is greater than 60, and as long as the uptake curves are evaluated in the region where the fractional uptake $[(m_t - m_0)/(m_\infty - m_0)]$ is less than 85%, the error in estimating diffusivity using isothermal models is less than 15% (Ruthven et al, 1980).

The limiting case of heat transfer controlling the rate occurs when $\alpha' \rightarrow 0$ and results in the solution

$$(m_t - m_0)/(m_\infty - m_0) = 1 - (\beta'/[1+\beta'])\exp[-(ha/c_s)t/(1+\beta')] \quad (1.13)$$

In cases where none of the above simplifying assumptions can be made, a more complicated model, which combines both resistances, must be used to analyse the uptake curves (Lee and Ruthven, 1979).

It should be noted that, since the relative intrusion of a sorbate into a large crystal is slower than into a small one, the effects of non-isothermality are greater when using a smaller crystal size. This can also be deduced from the above discussion of the α'/β' ratio.

In cases where intercrystalline diffusion and heat transfer are the most significant resistances, similar models are available as the ones for intracrystalline diffusion in combination with heat transfer except that, as in the isothermal case, intercrystalline porosity has to be taken into account (Ruthven and Lee, 1981).

Measurement of sorption rates

There are two main methods for measuring uptake rates. In constant pressure techniques, progress towards the new equilibrium can be measured volumetrically, gravimetrically, by NMR or by infra-red spectroscopy (i.e. using the intensity of absorbance bands in infra-red spectra) (Ballinger et al, 1989; Karge and Niessen, 1991). If the first is used, the volume is simply altered to keep the pressure constant while, in the other systems, as long as a large volume and small sample mass is used, the pressure change is, in most cases, insignificant. While gravimetric techniques are the most direct, the response of a microbalance is usually too slow to measure rapid processes. In conventional single-step experiments, NMR and IR techniques also have time- and signal-to-noise-constraints. However, these methods have the advantage of being able to distinguish between different sorbates, thus allowing the measurement of counter- or co-diffusion in multicomponent systems (Karge and Niessen, 1991). The use of infra-red spectroscopy to investigate diffusion is discussed further in section 1.5.4 and Chapter 3.

In piezometric methods, which are carried out in a fixed volume, the progress towards equilibrium is measured by monitoring the pressure. The response of a pressure transducer is significantly faster than the previously mentioned instruments, allowing more rapid diffusion processes to be probed. In practice, the time required to introduce (or remove) the sorbate (i.e. the valve effect) is usually the limiting factor. To avoid this, another method can be used, in which the sorbate is introduced and allowed to reach equilibrium. The volume is then changed, in a single step, by a very small amount, after which the pressure response is monitored (Van-Den-Begin et al, 1989). This experiment can be performed on the identical apparatus as that discussed for the frequency response method in Chapter 2.

Experimental conditions and data analysis

Diffusivity can be determined from the uptake curve simply by fitting the experimental data using the appropriate model. However, as was pointed out previously, it is important to verify that the assumptions used in developing the model are valid. As a corollary to this, if possible, the experimental conditions should be selected to minimize complications. Thus, when measuring intracrystalline diffusivity in zeolites: composite particles (or bed-depth) should be made as small as

possible to avoid intercrystalline resistances; the concentration step should be kept as small as possible to maintain linearity and eliminate significant variances in diffusivity; and large primary crystals should be used in preference to smaller ones to reduce the effects of non-isothermality. In addition, assumptions should be verified experimentally when possible (e.g. varying the size of the concentration step to check for non-linearity).

A method in which many of the above conditions can be met conveniently, and which also allows for a wide range of diffusivities to be measured, is the frequency response method, which is discussed in detail in section 1.4.3 and in Chapter 2. First, however, it is necessary to discuss the other main branch of indirect methods, column chromatography.

1.4.2.3 Finite column-length chromatography

One of the weaknesses of sorption rate methods is that, in most cases, the fluid phase is static. Hence, as has been discussed, resistance to heat transfer in the external film is often significant. In a flow system, this resistance can be reduced by using a sufficiently high fluid velocity. Methods have therefore been developed in which the diffusivity is determined by perturbing the concentration at the inlet to a column and measuring the dynamic response at the column outlet. In a typical system, a small pulse (or step change or periodic variation) of sorbate is injected into a steady flow of an inert carrier passing through a packed column. The effluent concentration is monitored continuously, usually by means of a flame ionisation detector (for hydrocarbons) or a thermal conductivity detector.

The two most important characteristics of the data are the mean retention time, which is a function of the adsorption equilibrium, and the broadening of the response peak, which is a function of both mass transfer resistances and axial dispersion. By making measurements over a range of conditions, or by performing reference experiments, it is possible to separate the effects of mass transfer resistance and axial dispersion and hence to ascertain the diffusivity.

As in sorption rate experiments, the data has to be fitted to a mathematical model. Since a primary purpose of using chromatographic methods is to eliminate heat transfer resistance, this effect is usually ignored when deriving the models. One of two models is usually employed: a linear rate model or a diffusion model.

In the former, the rate of change in adsorbed phase concentration is assumed to be directly proportional to the variation from the equilibrium concentration (Gluekauf and Coates, 1947; Gluekauf, 1955). The proportionality constant is a function of the intracrystalline diffusivity, the intercrystalline diffusivity and the external film mass transfer coefficient. Thus, once this proportionality constant has been determined by fitting the model to the data, the relevant diffusion parameter can be ascertained by making an assumption regarding the dominant mass transfer resistance (Raghavan and Ruthven, 1985).

In the diffusion model, all resistances are initially taken into consideration, leading to a complex model (Rasmuson, 1982). Assumptions regarding the dominant effects can then be used to simplify the model. Although analytical solutions are possible, it is more common, when fitting the models to data, to obtain solutions numerically (Raghavan and Ruthven, 1985).

The use of these numerical methods is time-consuming but the calculation time can be significantly reduced if good initial estimates are used. Thus, to obtain these initial parameters, the easier but less accurate method of using moments analysis to match the data in the Laplace domain (rather than the time domain as above) is used (Haynes and Sarma, 1973; Hashimoto and Smith, 1973). These values are then refined in the time domain.

Certain deviations from the ideal behaviour assumed in the models have to be taken into account. The most important are as follows: (a) Most models assume a "long" column. When resistance to mass transfer is extremely large, this assumption becomes invalid. Methods have been formulated to check when the model is no longer valid and other models can be used for this "limited penetration regime". (b) If there is a pressure drop through the column, the equilibrium relationship changes and correction factors have to be applied (Pazdernik and Schneider, 1981). (c) A non-

linear isotherm over the range of application changes the concentration profile independently of any mass transfer resistances. Non-linearity can easily be discerned by varying the pulse (or step) size and checking if the response changes. While correction of models is possible if the form of the isotherm is known, it is generally preferable to operate in the Henry's Law regime. (d) The finite pulse width (or imperfect step) of the initial perturbation is transmitted to the measured response at the column outlet. However, this can be dealt with simply by recording the response with the column bypassed and subtracting it from the experimental response. (e) The dead volume of the system, which results in a time delay and peak broadening, can also be taken account using a reference experiment in which the column is bypassed.

The most serious problem limiting the measurement of diffusion by chromatographic methods is the intrusion of axial dispersion. There are analytical methods to determine whether axial dispersion is significant (Haq and Ruthven, 1986). If it is, there are several methods which can be used to try to account for the axial dispersion experimentally. One possibility is to perform a reference experiment using a molecule with a similar molecular weight and diffusivity to the test sorbate but which is too large to enter the micropores (Kumar et al, 1982). If this is not possible, a reference column can be used, packed with non-porous particles of similar dimensions to the sorbent. This, however, ignores the possible differences in packing and the influence of micropore diffusion on axial dispersion. Another approach is to use a column with a similar internal diameter to the particle size, which avoids wall effects (Hsiang and Haynes, 1977). However, this is only practicable for large particles.

1.4.2.4 Zero length column (ZLC)

Because of the problem of axial dispersion, standard chromatographic methods cannot be used to measure rapid intracrystalline diffusion. The zero length column (ZLC) method (Eic and Ruthven, 1988) was developed to try to eliminate this restriction while maintaining the primary advantage of chromatography (i.e. negligible resistance to heat transfer).

In this method, the sorbent, usually in the form of a very thin layer between two sintered discs, is first brought to equilibrium with the sorbate (preferably in the

Henry's Law range to preserve linearity). The system is then purged with an inert gas at a high flow rate, so that the sorbate concentration at the external surface of the particles is approximately zero. The desorption rate is measured by following the composition of the effluent gas. Because the effluent concentration is extremely low, a very sensitive detector is required and the method is thus most suitable to hydrocarbon systems where a flame ionisation detector (FID) can be used.

Among the most significant challenges in this method are those involving the hardware. The small quantity of sorbent means that adsorption on any other surfaces can be significant and therefore unnecessary area and dead volume have to be avoided, lines heated and separate lines installed for saturation and purge streams. In addition, it is advisable to perform blank experiments (i.e. without sorbent) to ensure that extraneous adsorption has been eliminated.

Analysis of the diffusion and mass balance equations reveals a critical parameter,

$$L_Z = (1/3)\,(\text{Purge flow rate/Crystal volume})(r^2/K_H D) \qquad (1.14)$$

where K_H is the Henry's law constant. When $L_Z \rightarrow 0$, no kinetic data is obtained and thus this parameter should be kept as large as possible (i.e. operation at the highest flow rate possible is desirable). A large enough L_Z value also simplifies the analysis of the data, though more complicated methods can used for intermediate L_Z values (i.e. very high diffusivities).

A classic "long-time" model has been developed which has the disadvantage that data is obtained at very low concentrations and is thus more susceptible to errors in the measuring device. Thus, "short-time" models have been proposed but, because errors of non-linearity often occur in the initial part of the experiment, the "long-time" solutions are still deemed more robust (Hufton and Ruthven, 1993; Brandani, 1998; Duncan and Möller, 2000). A new "full range" method, claimed to be superior to previous methods, has recently been proposed (Han et al, 1999).

1.4.3 Frequency response method

When a periodic volume modulation is applied to an ideal gas in a closed system, the pressure of the gas varies at the same frequency as the volume and with the same function (e.g. sine wave, square wave) but 180° out of phase. When the same modulation is applied to a gas-zeolite system initially at equilibrium, the pressure response differs from that of the gas-only system because of two factors (Yasuda, 1982).

Firstly, as the pressure increases or decreases, the zeolite adsorbs or desorbs gas molecules respectively to reach a new equilibrium, thus changing the number of molecules in the gas phase and partially counteracting the initial pressure variation. This leads to a lower amplitude in the pressure response compared to the empty cell case.

Secondly, the diffusion of the sorbate molecules in or out of the zeolite micropores delays the attainment of the new equilibrium. This leads to a phase difference between the pressure responses of the gas-zeolite and gas-only cases. By considering a sinusoidal volume modulation, it can be shown (as described below) that the phase of the pressure response in the gas-zeolite case leads that of the blank case.

The following description is with reference to Figure 1.4. Starting with the initial equilibrium at time zero, as the volume is decreased sinusoidally, the pressure rises. If the system is not in the horizontal part of the isotherm, this leads to molecules adsorbing on the zeolite so that there are fewer molecules in the gas phase than at the original equilibrium. Then, as the volume starts to increase again (expansion cycle), the molecules begin to desorb from the zeolite but they are inhibited by diffusion limitations. Thus, when the original equilibrium volume is attained, there are still fewer molecules in the gas phase than at the initial equilibrium. Therefore, due to the ideal gas law, the pressure is lower than at the original equilibrium. The opposite applies to the compression cycle and hence the phase of the pressure response leads that of the gas-only case. As will be shown in Chapter 2, after an initial stabilization period, the pressure response attains a periodic steady-state with a constant amplitude and phase angle.

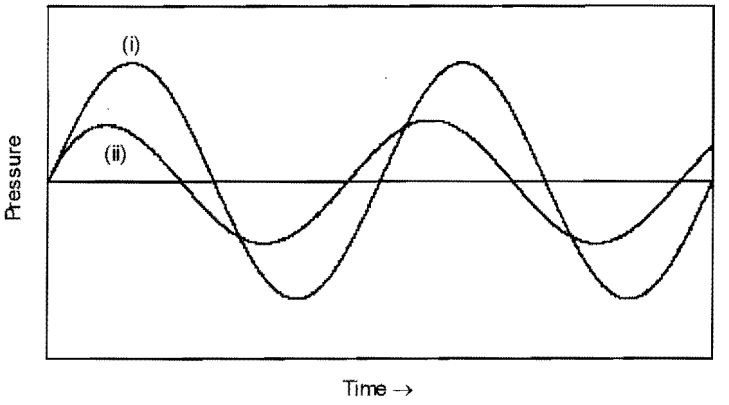

Figure 1.4 - Pressure response of a closed system to a sinusoidal volume modulation in (i) a cell containing only sorbate and (ii) a cell containing both sorbate and zeolite

It should be noted that, if diffusion is slow relative to the frequency of the volume modulation, the presence of the zeolite has a negligible effect and the pressure response curve is similar to that of the gas-only case (i.e. no phase lag and the maximum amplitude). On the other hand, if diffusion is very rapid compared to the modulation frequency, then the pressure response curve exhibits equilibrium behaviour (i.e. there is no phase lag but the amplitude of the response is at a minimum for the system). At intermediate volume modulation frequencies, the phase lag goes through a maximum and the amplitude decreases with frequency from the maximum to the minimum. It is this range that is of interest in the analysis of the frequency response.

By making certain assumptions, it is possible to formulate a quantitative expression for the pressure response to volume modulation in a closed gas-zeolite system. If this expression is analysed over a range of frequencies, the diffusion coefficient of the gas in the zeolite pores can be ascertained. This method is known as the frequency response method and the quantitative analysis is discussed in Chapter 2. Even before this, however, it is possible to enumerate the advantages of the frequency response method over other diffusion measurement methods.

Advantages of the frequency response method

In comparison to the methods of diffusion measurement discussed in sections 1.4.1 and 1.4.2, the frequency response method has the following advantages.

- The starting point of the experiment is an equilibrium system and only a small perturbation is applied to this system. Therefore, the concentration of the sorbed phase remains almost constant (i.e. the condition of isotherm linearity is met) and the measured diffusion coefficient can be assumed to be the differential diffusion coefficient at the equilibrium concentration of the sorbate on the zeolite.

- By varying the starting pressure, the diffusion coefficient can be determined as a function of equilibrium concentration (i.e. coverage).

- The compression and expansion cycles in the frequency response method give rise to both adsorption and desorption pressure responses in a single experiment. Thus, if any peculiarity causes a difference in the diffusion mechanisms for the two processes, it can be detected by this method.

- As will be shown in Chapter 2, the method is capable of separating two simultaneous diffusion processes, provided they differ by a large enough factor.

- As will be shown in Chapter 2, the pressure response that is obtained over a range of frequencies is sensitive to the shape of the zeolite crystal. Thus, analysis of the data can provide information on the crystal morphology.

1.5 Infra-red spectroscopy to investigate the behaviour of molecules in zeolites

1.5.1 Hydroxide groups

When a zeolite is exchanged to its H^+-form (see section 1.3), a bridging acidic hydroxide (Si-OH-Al) group is formed. In addition, the defects caused by the termination of the framework of tetrahedra at the outer surface of the crystal give rise to another type of hydroxyl group, known as a silanol (Si-OH) group. This group also has acidic properties but of a much lower strength than the bridging hydroxide group.

Using infra-red (IR) spectroscopy, two separate O-H stretching bands can be detected for these two groups (Jentys et al, 1989), confirming the different bond strengths. On

HZSM-5, for example, the very weakly acidic silanol (Si-OH) groups show an IR band at wavenumber 3745 cm^{-1} while the strongly acidic bridging hydroxide (Si-OH-Al) groups, usually designated as Bronsted sites, show a band at 3610 cm^{-1} (Jentys et al, 1989).

1.5.2 Lattice vibrations

To perform transmission-absorption IR spectroscopy on zeolites, samples initially in the powder form must be pressed into self supporting wafers. The thickness of the wafers cannot be controlled accurately. Thus, if quantitative data is to be extracted from experiments, the spectra have to be normalised to the wafer thickness. For many zeolites, this can be done using the intensity of the lattice vibration overtone bands. In HZSM-5, for example, these bands occur between 2100 and 1740 cm^{-1}. A typical IR spectrum of HZSM-5, showing both OH stretching vibrations bands, as well as the lattice vibration bands, can be seen in Figure 1.5a (Mirth et al, 1993).

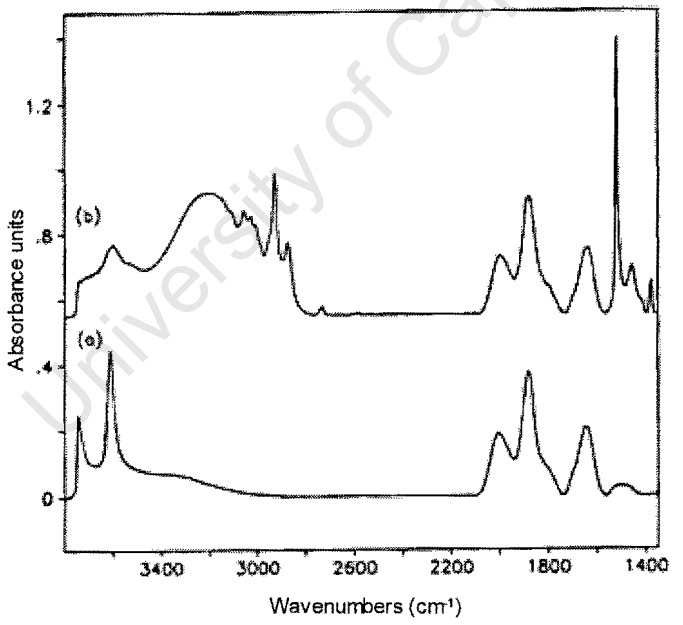

Figure 1.5 - IR spectra of (a) an activated zeolite HZSM-5 and (b) *p*-xylene adsorbed on HZSM-5

1.5.3 Adsorbed molecules and interactions with hydroxide groups

When certain probe molecules adsorb on the outer surface or in the pores of zeolites, their stretching and deformation vibrations can be detected in the middle IR range (4000-1000 cm^{-1}). Examples of these are benzene, toluene and the xylene isomers,

which exhibit bands at several wavenumbers, due to C-H stretching vibrations, C-H deformation vibrations and ring vibrations. It should be noted that the surface concentrations of adsorbed molecules is several times higher than in the gas phase concentration and, in addition, the molar extinction coefficients are enhanced by adsorption. Thus, at partial pressures of less than 1 mbar, the contribution of the gas-phase to the bands is negligible.

In addition to the bands of the adsorbing molecules themselves, an effect of these molecules on the zeolite hydroxide bands is observed. This is caused by hydrogen bonding between the hydroxide groups and the aromatic rings. The subsequent weakening of the OH bond causes a shift in the IR band to a lower wavenumber, while the statistical increase in the range of OH stretching frequencies causes a broadening of the IR band. The extent of the shift depends on the strength of the hydrogen bond formed (and hence on the acid strength of the original groups).

As an example, Figure 1.5b shows an IR spectrum for *p*-xylene adsorbed on HZSM-5, while the wavenumbers of the characteristic IR bands for xylene isomers adsorbed on ZSM-5 can be found in Table 1.1 (Mirth et al, 1993).

Table 1.1

Wavenumbers of the Characteristic IR Bands of the Adsorbed Xylene Isomers (at 373 K) at the Zeolite HZSM-5

T = 373 K p = 1 mbar HZSM-5	CH-Stretching vibrations (cm^{-1})	Ring vibrations (cm^{-1})	CH-Deformation vibrations (cm^{-1})
p-Xylene	3050, 3025, 3007 2927, 2872	1518	1379
m-Xylene	3053, 3032 2926, 2868	1610 1485	1381
o-Xylene	3072, 3031 2977, 2951, 2931 2877	1604 (weak) 1496, 1466	1390

Note. The bands used for the identification of the isomers are underlined.

As can be seen in Figure 1.5b, the interaction between *p*-xylene and the Si-OH-Al group results in a shift of 425 cm^{-1} (i.e. from 3610 to 3185 cm^{-1}), indicating a hydrogen bond of substantial strength. On the other hand, the band of the OH stretching vibration of the Si-OH groups is shifted by only 145 cm^{-1} (i.e. from 3745 to 3600 cm^{-1}), suggesting a much weaker interaction with the *p*-xylene.

1.5.4 Sorption rate measurements

When IR absorbance is linear with concentration, i.e. when the Beer-Lambert law is obeyed (Atkins, 1990), the rate of uptake of any particular molecule on a sorbent can be measured using IR spectroscopy. Thus is done by simply following the change in intensity of the appropriate IR band over time (Karge and Niessen, 1991). To take into account the statistical spread of vibrations at each band, it is preferable to use the integrated area of the peak, rather than the peak height.

If the sorption uptake is the result of a defined step-change in the sorbate partial pressure, and as long as the system reaches equilibrium, these measurements can also be used to estimate the diffusion coefficient of the sorbate in the sorbent, using a modified form of equation (1.10) (Mirth et al, 1993):

$$(A_t - A_0)/(A_\infty - A_0) = (2A_c/V_c)(Dt/\pi)^{1/2} \qquad (1.15)$$

where A_t, A_0, A_∞ are the integrated absorbances at time t, at time zero and at equilibrium, respectively. As noted in section 1.4.2.2, Equations (1.10) and (1.15) apply only in the initial or linear part of the uptake curve. Figure 1.6 shows a typical uptake curve for toluene on HZSM-5. Note also that the time delay before uptake begins is an experimental artefact and has to be subtracted before equation (1.15) can be applied.

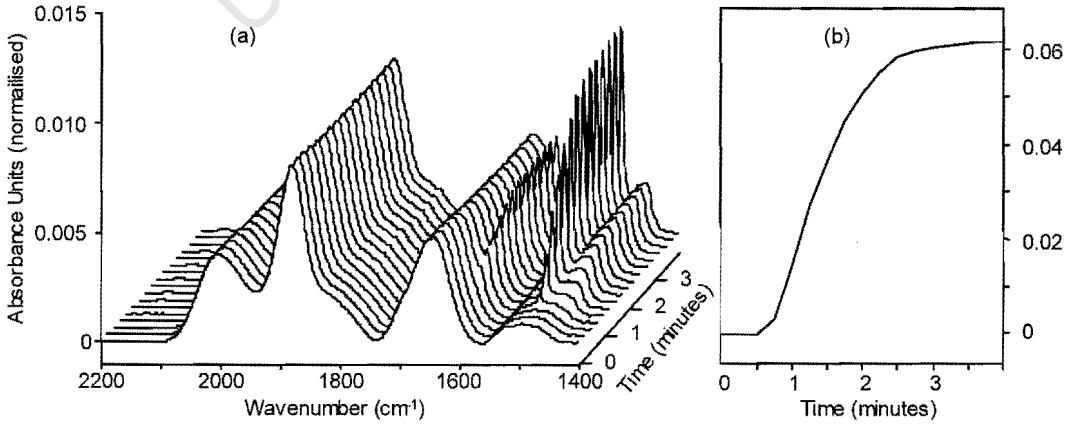

Figure 1.6 - (a) Time-resolved toluene uptake spectra on HZSM-5 and (b) time dependence of integrated toluene peak (between 1508 and 1482 cm^{-1}) after subtraction of HZSM-5 spectrum

An important feature of using IR spectroscopy to measure diffusion is that, as long as the characteristic IR bands of the components are sufficiently separated, the method can be used to measure the diffusion of one component in the presence of others (Karge and Niessen, 1991). Thus, co- and counter-diffusion can be investigated.

From the above discussion, it is clear that it would be advantageous to integrate a system used for the frequency response method with one used for IR spectroscopy since it would allow: (a) a comparison of diffusivities obtained using frequency response and sorption rate methods; (b) co- and counter-diffusivities to be measured by sorption uptake; and (c) the behaviour of molecules on the zeolite surface to be observed during a volume modulation experiment. In principal, if an appropriate model could be derived using IR band intensity rather than pressure response, it would also be possible to measure co- and counter-diffusivities using an IR-band frequency response method.

It should be noted that, when measuring diffusion, the total duration of a sorption rate experiment is usually in the order of a few minutes at most. Since a reasonable number of data points is required, standard IR equipment is not sufficient and it is necessary to use Fourier Transform Infra-Red (FTIR) spectroscopy to obtain the requisite time-resolution. A more detailed description of the theory and hardware of FTIR spectroscopy is given in Chapter 3.

For the observation of molecules during a volume modulation experiment, even standard FTIR does not have a high enough time-resolution. Thus, it is necessary to employ rapid-scan or step-scan techniques, both of which lend themselves to use in a system where a single experiment is identically repeated several times (e.g. a constant frequency volume modulation system). A detailed description of the implementation of rapid-scan and step scan techniques is given in Chapter 3. An additional application of these techniques to investigate the "surface barrier" is described in section 1.5.5.

1.5.5 High time-resolution FTIR to probe surface resistances

As discussed in section 1.4.1.3, intracrystalline self-diffusion coefficients can be measured using pulsed field gradient (PFG) NMR. In principal, self-diffusivities can also be obtained by applying the Darken equation [i.e. equation (1.9)] to the transport diffusivities measured using sorption rate methods. The values measured using the two different methods are often in agreement. However, in certain cases, the self-diffusivities measured using PFG NMR have been found to be higher (Kärger and Caro, 1977; Bülow et al, 1980).

In some of these cases, when diffusion coefficients have been measured using uptake methods over a range of crystal sizes, they have been found to be dependent on the crystal size. In these cases, at large enough crystal sizes, the measured diffusion coefficient approaches the value measured by PFG NMR (Kärger and Caro, 1977).

This implies that the coefficients measured in the uptake experiments are only apparent (i.e. not actual) diffusion coefficients and that another transport process is retarding the rate. The fact that the apparent coefficient decreases with particle size suggests that the rate-limiting step is in some way related to the external surface (since the surface area to volume ratio increases with decreasing particle size).

Conventional experimental effects related to the external surface (e.g. external film diffusion) have been eliminated and it has thus been proposed that the rate-limiting step is a "surface barrier" (Kärger and Caro, 1977).

Several theories have been proposed to explain this surface barrier. One is that it is caused by structural changes in the zeolite surface as the result of hydrothermal pre-treatment (Bülow et al, 1982; Kärger et al, 1982). This is accompanied by a decrease in the cation content in the surface layer (Kärger et al, 1987) which may give rise to "electronic" resistances. Another theory is that it is the result of the limited rate of sorption heat-release (non-equilibrium effect) (Kocirik et al, 1990). The possibility that it is caused by the blocking of a certain percentage of the pores has, however, been discounted (Kärger et al, 1986).

Starting with Kärger and Caro (1977) and Bülow et al (1980), several parameters and models have been applied to quantify the barrier. These have included structural models (Bülow, 1985), taking into account both linear and non-linear isotherms (Kocirik et al, 1986), as well as "electronic" (Kocirik et al, 1988) and non-equilibrium (Micke et al, 1994) models. Molecular dynamics simulation techniques have also been employed to describe transport processes to and through the outer surface (Ford and Glandt, 1995).

However, the observation of the behaviour of the adsorbing molecule at the surface has not yet been attempted in detail. Using FTIR and microcalorimetry at equilibrium conditions, it has been shown (Pieterse et al, 2000) that the adsorption and orientation of molecules at the zeolite outer-surface may be influenced by entropic effects. More detailed knowledge of these effects (and their possible connection to the surface barrier) could be obtained by observing the interactions of the sorbed molecules (with each other and with the hydroxide groups) under dynamic conditions.

In considering this objective, some possible problems emerge. Firstly, in a transient step that involves a large instantaneous change (e.g. the usual step-change uptake experiment), a subtle "barrier" process may not be observable. Secondly, if the surface concentration is too high, the molecular processes involved in the barrier may be masked by other processes. And, thirdly, as will be shown in Chapter 3, the time resolution (between high quality spectra) for a standard FTIR spectrometer is at least 0.5 seconds. The molecular processes involved in a surface barrier may be several orders of magnitude faster than this.

These problems can be partly resolved using rapid-scan or step-scan FTIR spectroscopy in conjunction with the same apparatus that is used for the frequency response method. A small volume change can be made rapidly to induce a repeatable but small pressure step and, in addition, the equilibrium pressure can be set to give a low surface concentration. Thus the obstacles to detecting subtle changes are significantly reduced, with the only limitation being whether the spectrometer has sufficient absorbance resolution and signal-to-noise ratio (SNR) to identify small changes in peak height. More significantly, because an experiment can be exactly repeated several times (by modulating the volume of the closed system at a constant

frequency), rapid-scan or step-scan FTIR can be used to obtain spectra with a time resolution of milli- or microseconds, with as many co-additions as are necessary to give the required SNR. Rapid-scan and step scan FTIR is discussed in detail in Chapter 3.

1.6 Objectives and overview

The two primary aims of this work were to construct and commission an apparatus to measure diffusion coefficients using the frequency response method and to integrate it with an FTIR spectrometer to allow the use of standard-mode, rapid-scan and step-scan FTIR spectroscopy.

In Chapter 2, the theoretical background of the frequency response method is discussed, including the models used to analyse data and the practicable ranges of operation. Also included in Chapter 2 are discussions on the volume modulation function and on methods to overcome general system uncertainties. In Chapter 3, the theory and implementation of rapid- and step-scan FTIR spectroscopy is discussed, preceded by an introduction to FTIR spectroscopy. In Chapter 4, a detailed description of the design and construction of the apparatus is given, including the integration of the spectrometer into the system. In Chapter 5, the commissioning of the primary functions of the apparatus is described, including the presentation and discussion of preliminary results. In Chapter 6, there is a summarizing discussion on the reproducibility and validity of the results, and on the ranges of the apparatus. Finally, in the concluding remarks in Chapter 7, recommendations are made as to how the apparatus could be improved and some future experiments on the apparatus are suggested. Calculation details, as well technical drawings of the apparatus can be found in the appendices.

Since this assignment was part of a larger project whose aim was to investigate the microkinetics of toluene disproportionation over HZSM-5 (HMFI), the diffusion of toluene in HZSM-5 was investigated in the preliminary experiments.

2. Frequency response method

It was mentioned in section 1.4.3 that the diffusivity of a sorbate in a zeolite can be ascertained from a quantitative analysis of the pressure response to volume modulation at a range of frequencies (i.e. the frequency response method). In this chapter, the theoretical models are presented and their application to determine the diffusivity is described, including the ranges of operation. Data treatment and system uncertainties are also discussed.

2.1 Theory of the frequency response method

2.1.1 Assumptions and initial equations

In the initial analysis of the frequency response method (Yasuda, 1982) the following assumptions were made.

- The ideal gas law is applicable in the closed system. At pressures below atmospheric and temperatures at or above ambient, this assumption is valid for most systems.

- The concentration of adsorbed molecules on the sorbent surface is proportional to the partial pressure of the sorbate, i.e. the isotherm is linear within the range of operation.

- The diffusion coefficient is not a function of sorbate concentration. If the variation in volume (and thus in pressure) of the system is small, the variation in sorbate surface concentration is also small and thus the assumption is valid.

- Effects due to heating and cooling during adsorption and desorption respectively are negligible. As long as changes in volume, pressure and concentration are small, thermal effects are usually negligible. However, models have been developed which take non-isothermal behaviour into account (see section 2.1.4).

- Intracrystalline diffusion is the rate controlling step, i.e. adsorption-desorption and intercrystalline diffusion are orders of magnitude faster and can be ignored. In the case of medium and small pore zeolites, diffusion is invariably more significant than adsorption-desorption. Intercrystalline diffusion is usually a function of bed-depth or pellet size and should always be taken into account when evaluating results.

In deriving equations for the frequency response method, Yasuda (1982) considered the case of a closed gas-zeolite system, initially at equilibrium, which is subjected to a sinusoidal volume modulation. Using complex notation, this can be expressed as:

$$V = V_e(1-ve^{i\omega t}) \tag{2.1}$$

where V is the volume, V_e is the equilibrium volume, v is the relative amplitude of the volume variation and ω is the angular frequency of the volume modulation (i.e. $\omega = 2\pi f$). Assuming the gas-phase pressure (P) and the sorbate concentration (C) in the zeolite pores also vary sinusoidally, these quantities can thus be expressed as follows:

$$P = P_e(1+pe^{i(\omega t+\phi)}) \tag{2.2}$$

and

$$C = C_e(1+\gamma e^{i(\omega t+\phi-\chi)}) \tag{2.3}$$

where P_e and C_e are the equilibrium gas-phase pressure and sorbate surface concentration respectively, p and γ are the relative amplitudes of the pressure and concentration variations respectively and ϕ and χ are phase differences. The last four quantities all depend on ω and, since pore diffusion is assumed to be the limiting case, γ and χ are additionally dependent on the position within the pores.

2.1.2 Diffusion in a planar sheet

If diffusion occurs through a planar sheet of thickness $2L$, Fick's second law can be expressed as

$$\partial C/\partial t = \partial/\partial x[D(C)\partial C/\partial x] \tag{2.4}$$

where x is the depth coordinate within the planar sheet.

If the volume variation is only a small percentage of the total volume, the concentration gradient will also be small and, as mentioned in the assumptions, the diffusion coefficient $D(C)$ can be assumed to be constant $D(C_e)$ or D. Thus, equation (2.4) may be written

$$\partial C/\partial t = D(\partial^2 C/\partial x^2) \tag{2.5}$$

If one sets the boundary condition that concentration is proportional to a sinusoidally varying pressure at the outer surface, equation (2.5) can be solved (see Appendix A) to give the total amount of sorbate present in the sheet (B),

$$B = B_e + pB_eAe^{i(\omega t+\phi+\psi)} \tag{2.6}$$

where B_e is the amount of sorbate present in the sheet at the initial equilibrium,

$$A = 2^{1/2}(\sin^2\eta_1+\sinh^2\eta_1)^{1/2}/[\eta_1(\cos\eta_1+\cosh\eta_1)] \tag{2.7}$$

$$\psi = \arctan[(\sin\eta_1-\sinh\eta_1)/(\sin\eta_1+\sinh\eta_1)] \tag{2.8}$$

and

$$\eta_1 = (\omega L^2/2D)^{1/2} \tag{2.9}$$

The material balance of the total system can be written

$$d/dt(PV/RT_0)+dB/dt = 0 \tag{2.10}$$

where T_0 is the isothermal temperature.

Substituting equations (2.1), (2.2) and (2.6) into equation (2.10), differentiating and separating the real and complex parts (see Appendix A) gives the following equations:

$$(\nu/p)\cos\phi - 1 = K\delta_{1c} \tag{2.11}$$

and

$$(\nu/p)\sin\phi = K\delta_{1s} \tag{2.12}$$

where

$$\delta_{1c} = (1/\eta_1)\,[(\sinh\eta_1+\sin\eta_1)/(\cosh\eta_1+\cos\eta_1)] \tag{2.13}$$

$$\delta_{1s} = (1/\eta_1)\,[(\sinh\eta_1-\sin\eta_1)/(\cosh\eta_1+\cos\eta_1)] \tag{2.14}$$

and

$$K = (RT_0/V_e)(dB_e/dP_e) \tag{2.15}$$

In frequency response terminology, δ_{1c} and δ_{1s} are known as the in-phase and out-of-phase characteristic functions, respectively. The subscript "1" denotes a one-dimensional (i.e. planar sheet) system.

2.1.3 Diffusion in an isotropic sphere

Yasuda (1982) formulated a similar set of equations for diffusion in an isotropic sphere of radius r and, when these are solved (see Appendix A), the equations derived are identical to the one-dimensional case except for the definitions of the characteristic functions.

$$(\nu/p)\cos\phi - 1 = K\delta_{3c} \tag{2.16}$$

and

$$(\nu/p)\sin\phi = K\delta_{3s} \tag{2.17}$$

where

$$\delta_{3c} = (3/\eta_3)\,[(\sinh\eta_3-\sin\eta_3)/(\cosh\eta_3-\cos\eta_3)] \tag{2.18}$$

$$\delta_{3s} = (6/\eta_3)\,[(1/2)(\sinh\eta_3+\sin\eta_3)/(\cosh\eta_3-\cos\eta_3) - (1/\eta_3)] \tag{2.19}$$

and

$$\eta_3 = (2\omega r^2/D)^{1/2} \tag{2.20}$$

where the subscript "3" denotes a three-dimensional system.

Plots of the characteristic functions for the planar sheet and isotropic sphere cases are shown in Figure 2.1.

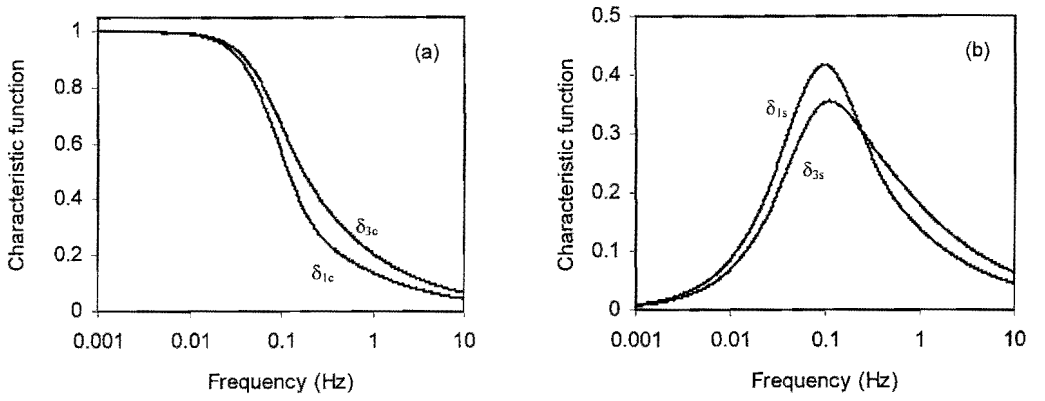

Figure 2.1 - (a) In-phase and (b) out-of-phase frequency response characteristic functions for planar sheet (δ_{1c}, δ_{1s}) and isotropic sphere (δ_{3c}, δ_{3s}) models, with a particle diameter of 1 μm and a diffusion coefficient of 1.5×10^{-14} m^2/s

2.1.4 Other diffusion models

Models for the interpretation of frequency response data have also been derived which account for: multiple diffusion processes; alternative crystal shapes; non-isothermal behaviour; and finite-rate mass exchange between "storage" and "transport" channels in zeolites. These are presented without derivation below.

Multiple diffusion processes

Multiple diffusion processes can occur in a system for several reasons, including the presence of: multiple sorbents in the solid phase; multiple sorbates in the gas mixture; and multiple states of mobility (e.g. in the straight and sinusoidal pores of MFI).

As long as the interaction between the respective diffusion processes is negligible, the treatments in sections 2.1.2 and 2.1.3 can be extended (Yasuda, 1982) to give:

$$(v/p)\cos\phi - 1 = \sum_{j,k} K_k \delta_{jc}^{(k)} \tag{2.21}$$

and

$$(v/p)\sin\phi = \sum_{j,k} K_k \delta_{js}^{(k)} \tag{2.22}$$

where subscript "j" denotes the model dimension (i.e. 1 or 3) and subscript (and superscript) "k" denotes kinetically different species.

Diffusion in a parallelepiped

Spherical and especially plane sheet models are often not representative of true crystal morphology. Thus, a model has been developed for parallelepipeds (Oprescu et al, 1992), which can be used to represent cubic, rhombic and coffin-shaped crystals. In this case, with the three side lengths $2a$, $2b$ and $2c$, equations (2.16) and (2.17) apply but with

$$\delta_{3c} = (8/\pi^2)^3 \sum_{l,m,n=1,3,5,\ldots}^{\infty} \alpha_{lmn}{}^2/[l^2m^2n^2(\alpha_{lmn}{}^2 + \omega^2)] \qquad (2.23)$$

$$\delta_{3s} = (8/\pi^2)^3 \sum_{l,m,n=1,3,5,\ldots}^{\infty} \omega\alpha_{lmn}/[l^2m^2n^2(\alpha_{lmn}{}^2 + \omega^2)] \qquad (2.24)$$

where $$\alpha_{lmn} = (\pi^2 D/4)(\, l^2/a^2 + m^2/b^2 + n^2/c^2) \qquad (2.25)$$

for an isotropic parallelepiped

and $$\alpha_{lmn} = (\pi^2 A/4)(\, l^2/a_1{}^2 + m^2/a_2{}^2 + n^2/a_3{}^2) = (\pi^2/4)(\, l^2D_1/a^2 + m^2D_2/b^2 + n^2D_3/c^2) \qquad (2.26)$$

for an anisotropic parallelepiped.

Non-isothermal behaviour

In certain cases, thermal effects can influence frequency response analysis. This is caused by temperature changes due to adsorption and desorption which, in turn, affect the equilibrium amount adsorbed. The influence of this depends on factors such as the heat of adsorption, the heat capacity of the sorbent, the heat transfer coefficient between the sorbent and the surroundings and the temperature dependence of the adsorbed amount.

Thus, a non-isothermal model has been developed (Sun and Bourdin, 1993; Sun et al, 1993), assuming that the equilibrium amount adsorbed has a linear dependence on both pressure and temperature (with the justification that, since the perturbation is small, any real dependence can be linearized in the region of operation).

$$(v/p)\cos\phi - 1 = K[\delta_{jc}(1+\omega^2 t_h^2)+\gamma(\delta_{jc}^2+\delta_{js}^2)\omega^2 t_h^2]/[(1+\gamma\delta_{js}\omega t_h)^2+(1+\gamma\delta_{jc})^2\omega^2 t_h^2] \quad (2.27)$$

$$(v/p)\sin\phi = K[\delta_{js}(1+\omega^2 t_h^2)+\gamma(\delta_{jc}^2+\delta_{js}^2)\omega t_h]/[(1+\gamma\delta_{js}\omega t_h)^2+(1+\gamma\delta_{jc})^2\omega^2 t_h^2] \quad (2.28)$$

where $t_h = c/ha_p$ (2.29)

and $\gamma = [(\partial q/\partial T)_p \,|\, \Delta H \,|\,]/c$ (2.30)

where a_p is the external surface area of the sorbent per unit mass, c is the heat capacity of the sorbent per unit mass, h is the heat transfer coefficient between the sorbent and its surroundings, ΔH is the heat of adsorption per mol of sorbate, and $(\partial q/\partial T)_p$ is the slope of the equilibrium isobar.

Diffusion-rearrangement behaviour

When diffusion takes place in one set of pores (e.g. straight channels) but sorbate molecules are immobilised in a second set (e.g. sinusoidal channels), to which the first set is interconnected, it is convenient to consider the first set as "transport" pores and the second set as "storage" pores, with a reversible mass exchange between the two pore-types.

This behaviour depends on both the rate of exchange and on the equilibrium relationship between the two pore-types. The formulation is known as the diffusion-rearrangement model (Jordi and Do, 1992; Sun and Bourdin, 1993).

$$(v/p)\cos\phi - 1 = K[\delta_{jc} + K_\Omega(\delta_{jc} - \delta_{js}\omega t_R)/(1 + \omega^2 t_R^2)] \quad (2.31)$$

$$(v/p)\sin\phi = K[\delta_{js} + K_\Omega(\delta_{js} + \delta_{jc}\omega t_R)/(1 + \omega^2 t_R^2)] \quad (2.32)$$

where K_Ω is the equilibrium constant of the concentration in the "storage" pores (relative to the concentration in the "transport" pores) and t_R is the time constant of mass exchange between the "transport" and "storage" pores, defined by

$$\partial\Omega/\partial t = (1/t_R)(\Omega_e - \Omega) \quad (2.33)$$

where Ω is the sorbate concentration in the "storage" pores and Ω_e is this concentration at the initial equilibrium.

Before presenting the technical implementation of the frequency response method, it is necessary to discuss (a) the application of the models, with special reference to: the ranges of applicability; the relevance of K; curve shape analysis; the separation of two diffusion processes; and non-isothermal and diffusion rearrangement behaviour; and (b) the acquisition and treatment of the experimental data, in particular: practicable modulation functions; equipment-related variation from ideal behaviour (and counteractive measures); and analytical techniques and related data requirements.

2.2 Application of the theoretical models

It should be noted that, in all the models, there are two equations (in-phase and out-of-phase) which, for simplicity, can be written

$$(v/p)\cos\phi - 1 = K\delta_c \tag{2.34}$$

and

$$(v/p)\sin\phi = K\delta_s \tag{2.35}$$

These equations are independent of each other and either of them could be used to obtain the diffusivity. However, of the two, equation (2.35) is more useful since, as shown for the simplest case in Figure 2.1, this equation exhibits a maximum which is easier to distinguish than the point of inflection in equation (2.34). Thus, for the remainder of this section, emphasis will be placed on the out-of-phase equation though, in practice, it is common to try to fit both equations simultaneously.

From inspection of equations (2.34) and (2.35), it can be discerned that the left-hand sides of the equations represent expressions of the experimental data, while the right-hand sides represent the theoretical curves. Thus, to ascertain the diffusion coefficient, one has to measure phase angles and amplitude ratios at a range of frequencies and plot the terms on the left hand sides as a function of frequency. Then the right hand side terms, also plotted as a function of frequency, are fitted to the data by varying the diffusion coefficient, along with K (see section 2.2.2) and other parameters in the more complex models.

Since the coefficient measured using this method is a transport diffusivity, it must be corrected using the Darken equation [i.e. equation (1.9)] to obtain a self-diffusivity or corrected diffusivity (Kärger and Ruthven, 1992).

2.2.1 Frequency, crystal size and diffusion coefficients

Figure 2.2 shows, for the case of an isotropic sphere, plots of the out-of-phase characteristic function (δ_{3s}) for (a) a single particle size and three different diffusion coefficients and (b) a single diffusion coefficient and three different particle sizes.

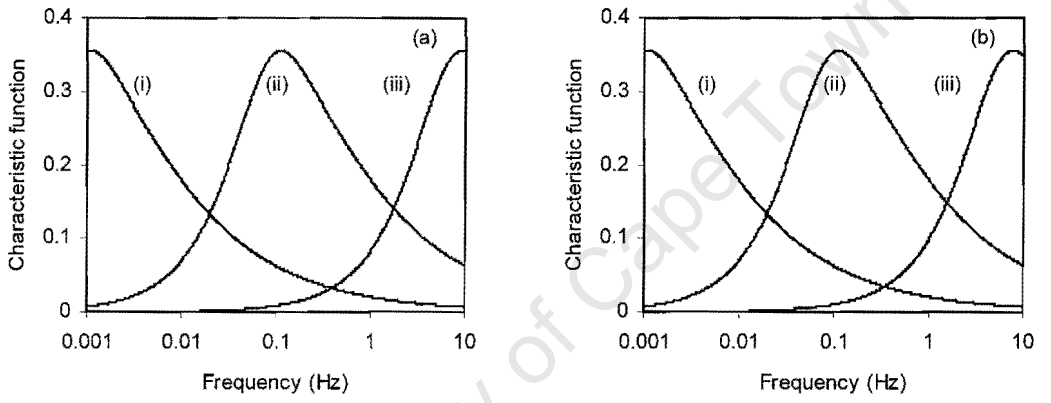

Figure 2.2 - Out-of-phase characteristic function (δ_{3s}) for: (a) particle diameter 1μm and diffusion coefficients (i) 1.5×10^{-16}, (ii) 1.5×10^{-14} and (iii) 1.25×10^{-12} m^2/s; and (b) diffusion coefficient 1.5×10^{-14} m^2/s and particle sizes (i) 10, (ii) 1 and (iii) 0.12 μm

To obtain meaningful curve fits of experimental data, the maximum of δ_{3s} must be in the frequency range used. At any particular particle size, the diffusion coefficient that gives a maximum of δ_{3s} at a particular frequency can be graphically determined. Thus a set of constant frequency curves can be constructed, showing the relationship between crystal size and diffusion coefficient. This is depicted in Figure 2.3.

Thus, for any given particle size, the diffusion coefficient determines the frequency range that is required. Alternatively, if the frequency range is fixed by the limitations of the apparatus and a certain diffusion coefficient is being measured, the maximum of δ_{3s} can be brought into the range of the apparatus by changing the particle size (e.g. for very high diffusivities, a larger particle size is required, and vice-versa).

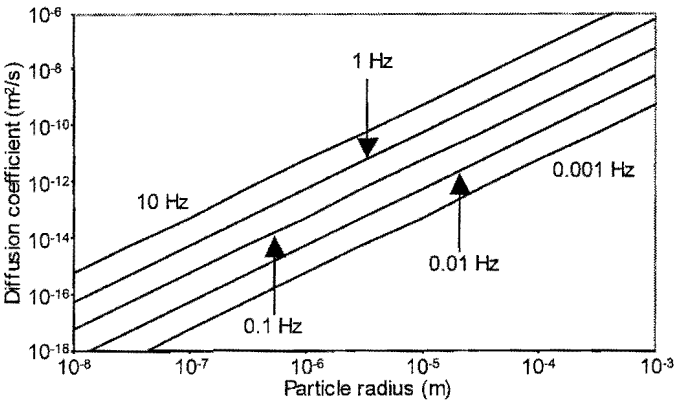

Figure 2.3 - The relationship between diffusion coefficient, particle size and ranges of applicability for the frequency response method (isotropic sphere model)

Finally, since the characteristic functions are dependent on the particle size, it is obvious that, for a sample with a wide range of particle sizes, the margin for error is greater and special care should be taken when calculating the diffusion coefficient. If the particle size distribution, E(r) is known, the characteristic functions can be corrected by integrating over the size range

$$\delta = \int \delta(r)\mathrm{E}(r)\mathrm{d}r \tag{2.36}$$

2.2.2 Sensitivity of the system to volume variation

Apart from the characteristic functions, the other term in the right hand side of equations (2.34) and (2.35) is K. From Equation (2.15), $K = (RT_0/V_e)(\mathrm{d}B_e/\mathrm{d}P_e)$

where $$\mathrm{d}B_e/\mathrm{d}P_e = m(\partial q/\partial P)_T \tag{2.37}$$

where m is the mass of the sample and $(\partial q/\partial P)_T$ is the slope of the equilibrium isotherm. Thus, K is a function of the temperature, the equilibrium volume, the sample mass and the position on the isotherm.

Since K is a constant for any particular system, the only influence it has on the right hand side term in the equations is to accentuate or flatten out the curves (see Figure 2.4). Clearly, the more drastically the curves are flattened out (i.e. the lower K is), the less sensitive the system becomes and the more difficult it is to fit the experimental data.

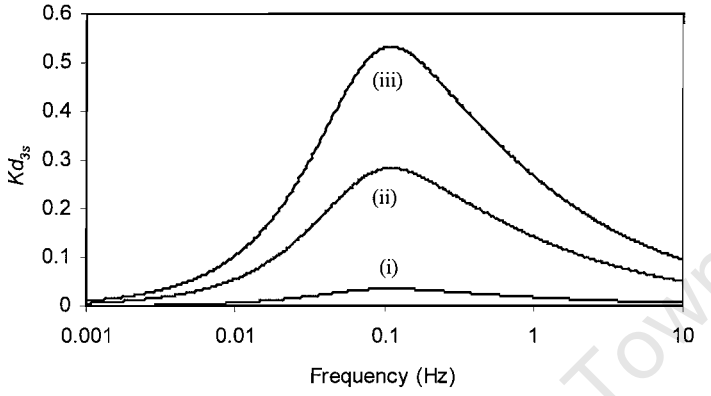

Figure 2.4 - Theoretical curves for the isotropic sphere model with particle diameter 1μm, diffusion coefficient 1.5×10^{-14} m^2/s and (i) $K = 0.1$, (ii) $K = 0.8$ and (iii) $K = 1.5$

On the other hand, if K is too large, the sorption capacity of the sorbent may be so large that it tries to adsorb more gas than is available in the system. Naturally, this is not possible but the equilibrium process that takes place in such circumstances can interfere with the frequency response data and this situation is thus not desirable.

In work done by previous researchers, K values between 0.1 and 1.5 have been found to be suitable to obtain meaningful data (Shen, 1999). This implies that: (a) the experiment should not be carried out in a region where the equilibrium isotherm is too flat; (b) the smaller the equilibrium volume of the system, the more sensitive the experiment (and the less sample mass is required); and (c) for a given system volume and set of experimental conditions, the approximate sample mass required can be calculated in advance.

Clearly, if all the variables are known, K is known. However, the following factors have to be considered. (a) The temperature of the system may not be known accurately (since often only the sample temperature is measured). (b) The volume may not be known accurately (since exact volumes of valves, bellows and other

fittings are difficult to estimate). (c) Isotherm data may not be reliable. (d) The sample mass is not known accurately (since, in the case of zeolites, the sample has to be activated *in situ* and thus loses an indeterminate mass).

Thus, as well as D, K is usually fitted as a variable and its value is compared to that calculated from the estimated variables to check that it is reasonable.

2.2.3 Influence of crystal morphology on curve shape

Figure 2.5 depicts the right hand sides of equations (2.12) and (2.17), i.e. for a planar sheet ($K\delta_{1s}$) and for an isotropic sphere ($K\delta_{3s}$), as though they were both fitted to the same set of data.

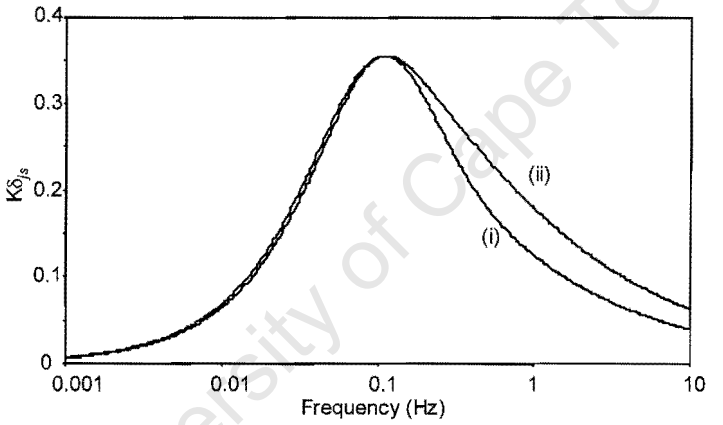

Figure 2.5 - Curve fits of the same (imaginary) data for particle diameter 1 μm and: (i) a planar sheet model with diffusion coefficient 1.7×10^{-14} m^2s^{-1} and K=0.85 ; and (ii) an isotropic sphere model with diffusion coefficient 1.5×10^{-14} m^2s^{-1} and K=1

It can be seen that the left sides of both curves are almost the same but that the right side of the curve for the planar sheet model has a steeper gradient than that for the isotropic sphere model. This suggests that the approximate morphology of the crystal can be deduced from the shape of the experimental curve.

2.2.4 Separating two independent diffusion processes

The theoretical curves for two independent diffusion processes are shown in Figure 2.6. According to equation (2.22), if these two processes are independent of each

other, the response of the system is simply the sum of the two curves, as shown in Figure 2.6.

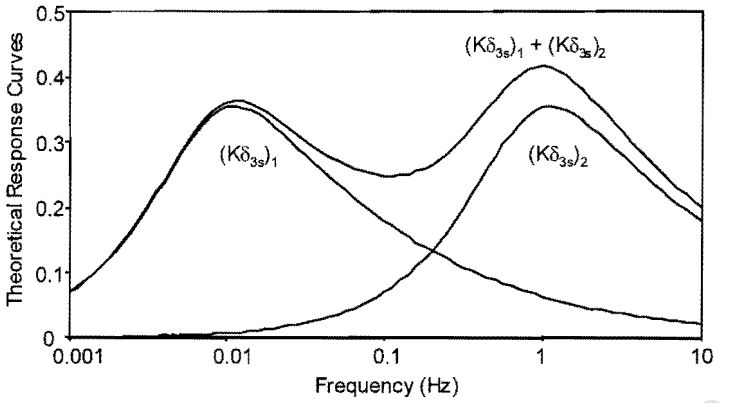

Figure 2.6 - Additive response curve for two diffusion processes with particle diameter 1μm, K=1 for both processes and diffusion coefficients of $1.5x10^{-15}$ $[(K\delta_{3s})_1]$ and $1.5x10^{-13}$ m^2s^{-1} $[(K\delta_{3s})_2]$

In this example, in which the diffusion coefficients differ by two orders of magnitude, the bimodal nature of the response curve is clear and the curve can be deconvoluted into its separate components. If the coefficients differ by a smaller factor, the second peak appears only as a shoulder on the first and the diagnosis and separation of two separate processes is more difficult. According to Rees and Shen (1993), two separate simultaneous diffusion processes can be separated as long as the coefficients differ by a factor of 3 or more.

It should be noted that the magnitude of the K-values in this case represents the distribution of the two processes, i.e. $K_1/(K_1+K_2)$ represents the fraction of molecules diffusing by the first process and $K_2/(K_1+K_2)$ by the second process. Thus the overall K (= K_1+K_2) can still be used as a check of the estimated variables (Song and Rees, 1997).

2.2.5 The effects of non-isothermal and diffusion rearrangement behaviour

The effect of finite rates of heat exchange and of mass exchange between "transport" and "storage" pores depends on the relative rates of these processes compared to diffusion. Since this information is not usually known *a priori*, it is advisable to check the applicability of the non-isothermal and diffusion re-arrangement models to

experimental data in all cases, especially when the simpler models do not provide a satisfactory fit.

Figure 2.7 shows one example of each of these models in cases where the influence is significant. Most notable is that both of the models can account for bimodal characteristic functions. It has already been shown in section 2.2.4 that two independent diffusion processes can also result in bimodality. Thus, care should be taken when interpreting bimodal experimental data (Sun and Bourdin, 1993). If a certain set of data can be fitted using more than one model, the parameters used to fit the model should be analysed in more detail to determine which model is more applicable (Song and Rees, 1997).

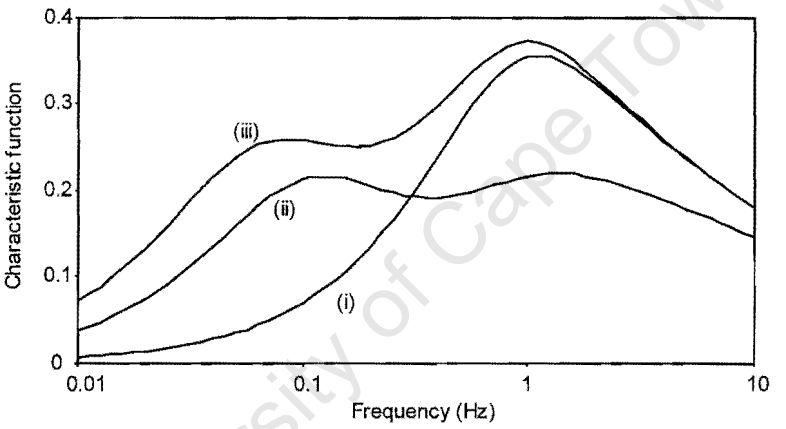

Figure 2.7 - Characteristic functions for an isotropic sphere with diameter 1 μm, diffusion coefficient 1.5×10^{-13} $m^2 s^{-1}$ and (i) diffusion as the rate-controlling mechanism; (ii) influence of non-isothermal behaviour (t_h=1s, γ=0.5); and (iii) influence of diffusion rearrangement mechanism (t_R=2.5s, K_Ω=0.4)

2.3 Acquisition and treatment of experimental data

2.3.1 Modulation function

Since the theoretical models for the frequency response method are all based on a sinusoidal volume modulation, it is clear that it would be appropriate to use this function in the experimental apparatus. However, the generation of a constant frequency sinusoidal volume modulation over a range of frequencies is not easy to implement mechanically and a more simply realizable modulation is a square wave.

The data obtained using this function can easily be manipulated for use in the frequency response equations by subjecting it to a Fourier transformation. In addition, if high quality data is obtained, the higher harmonics of the Fourier transformation can be used to probe higher frequencies than are mechanically possible. The mathematics of the Fourier transformation will be discussed in section 2.3.3.

2.3.2 Measures to counteract system delays and volume uncertainties

Regardless of which mechanical method is used to generate the square-wave volume change, certain system delays occur due to friction, compression resistance, and electrical and magnetic time-constants. The delay characteristics of the particular apparatus in this study will be discussed in section 5.3. In order to avoid these delays interfering with data, it is necessary, at each set of operating conditions, to perform a blank experiment (i.e. an experiment in which all the conditions match those of the actual experiment, except that the sample is absent). Phase lags for use in equations (2.34) and (2.35) are calculated by subtracting the blank experiment phase lags (ϕ_B) from the zeolite experiment phase lags (ϕ_Z).

$$\phi_{Z\text{-}B} = \phi_Z - \phi_B \tag{2.38}$$

where $\phi_{Z\text{-}B}$ is referred to as the corrected phase-lag.

To be able to subtract the blank cell phase lag from the phase lag in the presence of a zeolite, it is necessary to trigger the beginning of a pressure measurement exactly when the signal is sent to the square-wave modulator to change the volume. This ensures that measurements of the pressure response in the two cases have exactly the same reference point.

In many cases, the relative volume change (v) required in the governing equations is not known accurately. This can also be resolved using information from the blank experiment. Assuming the ideal gas law and comparing the conditions at the initial equilibrium to those at one extreme of the volume modulation,

$$P_e V_e = P_e(1 + p_B)V_e(1 - v) \tag{2.39}$$

where p_B is the relative amplitude of the pressure response in the blank experiment. Simplifying,

$$p_B - v - p_B v = 0 \tag{2.40}$$

and, since p_B and v are both small, $p_B v$ can be considered negligible and

$$p_B = v \tag{2.41}$$

Thus, as with ϕ_B, p_B can be ascertained from an experiment in the absence of a sorbent and, considering equations (2.38) and (2.41), equations (2.34) and (2.35) can be re-written as

$$(p_B/p_Z)\cos\phi_{Z\text{-}B} - 1 = K\delta_c \tag{2.42}$$

and

$$(p_B/p_Z)\sin\phi_{Z\text{-}B} = K\delta_s \tag{2.43}$$

where p_Z is the relative amplitude of the pressure in the presence of a zeolite.

It should be noted that, although p_B and p_Z are dimensionless relative amplitudes (i.e. not actual pressure amplitudes), since p_B/p_Z is a ratio, the actual pressure amplitudes can be used, as long as they are measured at the same base pressure in the blank and the zeolite cases.

2.3.3 Fourier transformation

A square wave input function can be represented by the following Fourier series (Goodyear, 1971):

$$F(t) = (4/\pi)\,\Sigma_{n=1,3,5...}\,(1/n)\,\sin(n\omega t) \tag{2.44}$$

The value of n is known as the harmonic of the term (i.e. the term with $n = 1$ is called the first harmonic; that with $n = 3$, the third harmonic; etc.). Assuming that, after an initial stabilisation time, the response wave-form has the same frequency, it can be expressed by the Fourier series

$$G(t) = H(t) + \Sigma_{n=1,3,5...}\,\alpha_n \sin(n\omega t + \phi_n) \tag{2.45}$$

where α_n and ϕ_n are the amplitude and phase lag of the nth harmonic and $H(t)$ is noise. This function can be trigonometrically expanded and rearranged as

$$G(t) = H(t) + \Sigma_{n=1,3,5...}\,\alpha_n \cos\phi_n \sin(n\omega t) + \Sigma_{n=1,3,5...}\,\alpha_n \sin\phi_n \cos(n\omega t) \tag{2.46}$$

The definition of the Fourier expansion of a function $G(t)$ is (Spiegel, 1974)

$$G(t) = a_0/2 + \Sigma_{n=1,3,5...}\,a_n \cos(n\omega t) + \Sigma_{n=1,3,5...}\,b_n \sin(n\omega t) \tag{2.47}$$

where the Fourier coefficients a_n and b_n are given by

$$a_n = (\omega/\pi) \int_{-\pi/\omega}^{\pi/\omega} G(t)\cos(n\omega t)\,dt \tag{2.48}$$

and

$$b_n = (\omega/\pi) \int_{-\pi/\omega}^{\pi/\omega} G(t)\sin(n\omega t)\,dt \tag{2.49}$$

Comparing equations (2.46) and (2.47), it follows that

$$a_n = \alpha_n \sin\phi_n \tag{2.50}$$

and

$$b_n = \alpha_n \cos\phi_n \tag{2.51}$$

Rearranging,

$$\alpha_n = (a_n^2 + b_n^2)^{1/2} \tag{2.52}$$

and

$$\phi_n = \arctan(a_n/b_n) \tag{2.53}$$

The values of a_n and b_n must be obtained by a numerical integration of equations (2.48) and (2.49), the details of which are shown in Appendix B.

In equation (2.46), it is implicitly assumed that oscillation occurs around a zero value. Hence, it should be noted that the equilibrium pressure (P_e) has to be subtracted from all pressure data before it undergoes the transformation.

2.3.4 Time resolution and signal-to-noise requirements

Figure 2.8 shows a pressure response curve for a gas-zeolite system subjected to a square wave volume modulation. The sharp pressure transition at each volume change and the subsequent rate of decrease in pressure provide the most important information regarding the phase lag and amplitude ratio of the system.

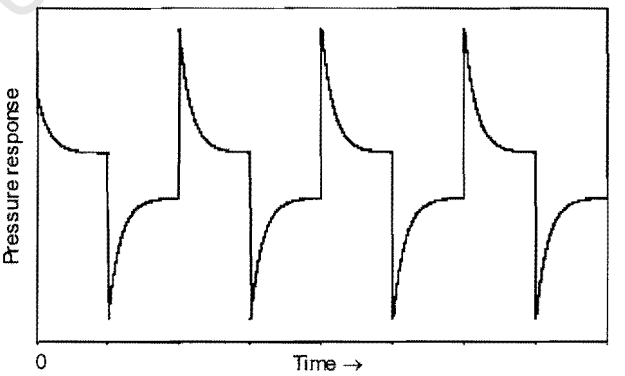

Figure 2.8 - Pressure response of a closed gas-zeolite system to a square wave volume modulation (starting at the equilibrium position at time zero)

It is clear, therefore, that a sufficient number of points (i.e. digitized pressure readings) have to be recorded in this region in order to obtain sufficiently accurate frequency response parameters. Previous studies have indicated that it is adequate to record 128 points per cycle (i.e. a sampling frequency of $128f$ where f is the frequency of the volume modulation) (Richards, 1985; Shen, 1991).

From both Figure 2.8 and equation (2.45), it is also evident that the signal-to-noise ratio (SNR) of the pressure response has to be high enough to avoid noise interfering with significant data. Methods of amplifying the pressure signal to improve SNR will be discussed in section 4.5 but, in addition, the pressure signal can be recorded over several cycles and the data for each cycle co-added and averaged to reduce noise. Previous studies have indicated that the co-addition of five cycles is sufficient to achieve acceptable SNR (Shen, 1991).

It should be noted that it is essential to have a minimum of baseline drift in the pressure reading in order to (a) obtain a successful average by co-addition of data; (b) ensure meaningful data at low frequencies; and (c) allow the subtraction of the equilibrium pressure (P_e) from all data before the Fourier transformation.

2.3.5 Stabilisation delay

Finally, it is also obvious from the initial behaviour of the curve in Figure 2.8 that the system undergoes transient behaviour before attaining a periodic steady-state pressure response. Thus, at each frequency, a stabilization period is required before data can be recorded. The length of this period depends on the particle size and diffusion coefficient and can be predicted from the original equations used to derive the frequency response equations.

In the example of the isotropic sphere (see Appendix A), the non-periodic part of equation (A.49) is given by the term:

$$\sum_{n=1}^{\infty} (1/\kappa)(1 - e^{-\kappa t}) \tag{2.54}$$

where

$$\kappa = \pi^2 D n^2 / r^2 \tag{2.55}$$

Thus, the system reaches a periodic steady state when this term, is constant, i.e. as

$$\sum_{n=1}^{\infty} (1 - e^{-\kappa t}) \rightarrow 1 \tag{2.56}$$

A plot of the "steady-state to transient ratio" [i.e., $\sum_{n=1}^{\infty} (1 - e^{-\kappa t})$] against time is shown in figure 2.9, for a single particle size and a series of diffusion coefficients. A similar set of curves can be constructed for any particle size and the time when the ratio is close enough to 1 (i.e. 0.99) can be considered to be the time required as a stabilisation delay.

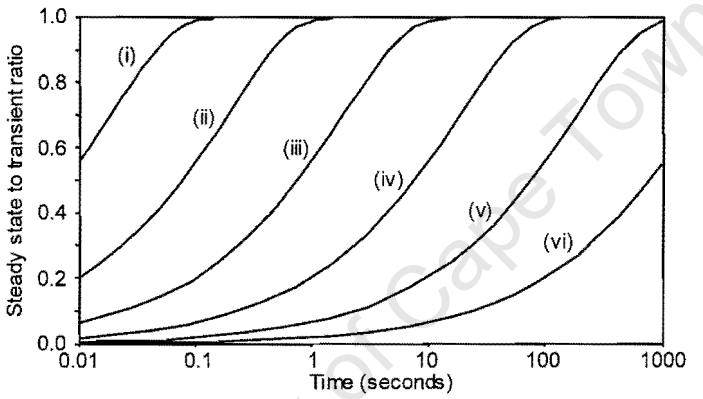

Figure 2.9 - Curves indicating the length of time required to reach a periodic steady-state pressure response to volume modulation for an isotropic sphere of diameter 1μm with diffusion coefficients (i) 10^{-12}; (ii) 10^{-13}; (iii) 10^{-14}; (iv) 10^{-15}; (v) 10^{-16}; (vi) 10^{-17} m^2s^{-1}

3. Fourier transform infra-red (FTIR) spectroscopy

In sections 1.5.4 and 1.5.5, justifications were given for the use of Fourier transform infra-red (FTIR) spectroscopy and the rapid- and step-scan modes. In sections 4.6, 4.7.3 and 4.7.4, the technical implementation of these techniques will be discussed. However, to appreciate the technical requirements, an understanding of the operation of an FTIR spectrometer is required. To facilitate this understanding and to illustrate the need for the high time-resolution modes, a brief introduction to the principles of transmission-absorption FTIR spectroscopy is presented below.

3.1 Introduction to FTIR spectroscopy

Unless otherwise stated, this introduction is based on the description in Smith (1996) and on information in the Bruker IFS66v/S User's Manual (1998).

3.1.1 The Michelson interferometer

Most FTIR spectrometers make use of a Michelson interferometer, the main elements of which are illustrated in Figure 3.1.

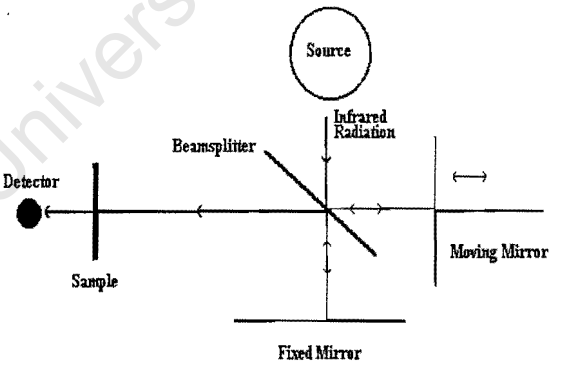

Figure 3.1 - Optical diagram of a Michelson interferometer

An IR beam passes from a radiation source to a beam splitter. For the far infra-red (FIR), middle infra-red (MIR) and near infra-red (NIR) ranges, an Hg lamp (700-4 cm^{-1}), SiC glowbar (7500-30 cm^{-1}), or tungsten lamp (30000-4000 cm^{-1}), respectively, is usually used as the radiation source. The beamsplitter is usually a Ge multilayer coating on KBr (7500-370 cm^{-1}), CaF_2 (10000-1850 cm^{-1}), Mylar (450-20 cm^{-1}) or

quartz (14000-5500 cm^{-1}). The beam splitter, which is mounted at a 45° angle, allows half the beam to pass directly through and reflects the other half of the beam an angle of 90°. The transmitted beam travels a fixed length to a stationary mirror. This reflects it back to the beam splitter where half of it is reflected towards the sample. The part of the beam that is originally reflected travels to a moving mirror which reflects it back to the beam splitter, where half of it is transmitted (and thus recombines with the reflected beam from the fixed mirror). The recombined beam passes via the sample to the detector. Common IR detector types are DLATGS (FIR and MIR), MCT (MIR), Ge diode (NIR) and InSb (NIR).

3.1.2 Path difference and interferograms

When the distance between the beam splitter and the moving mirror is exactly the same distance as that between the beam splitter and the fixed mirror, the recombined beams are exactly in phase and thus the maximum intensity reaches the detector. This mirror position is known as zero path difference (ZPD). When the moving mirror has moved from the ZPD position, the situation changes and is most easily understood by first considering a beam of monochromatic light with wavelength λ, as shown in Figure 3.2.

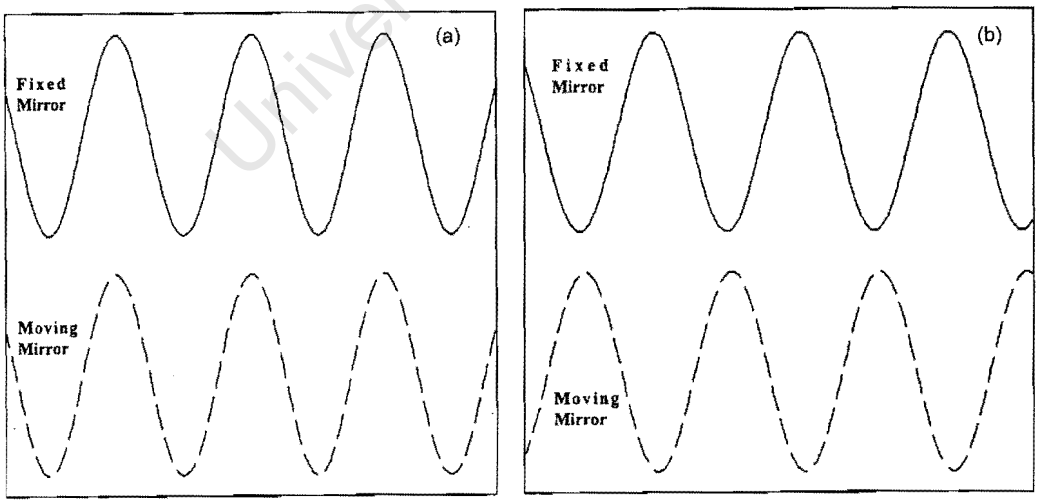

Figure 3.2 - Monochromatic light beams (wavelength λ) in a Michelson interferometer at a path difference of (a) $n\lambda$, when constructive interference occurs and (b) $(n + ½)\lambda$, when destructive interference occurs

In this case it is clear that, if the beam travels a distance (known as the path difference or Δ) $\lambda/2$ further than the beam from the fixed mirror (i.e. the mirror moves a distance $\lambda/4$), then the beams are exactly out of phase and the recombined beam has zero intensity. When the mirror moves a distance of $\lambda/2$ (i.e. $\Delta = \lambda$), the beams are once again in phase and the recombined beam intensity is the same as that at ZPD. In general, for monochromatic light, if $\Delta = n\lambda$ (for n = 0, 1, 2, etc.), the beams are exactly in phase and the resultant intensity is a maximum. Conversely, if $\Delta = (n+\frac{1}{2})\lambda$, the beams are wholly out of phase and the resultant intensity is zero. Over a continuous range, intensity is a cosine function of path difference, as shown in Figure 3.3a. This plot of intensity against path difference is known as an interferogram. For monochromatic light, the interferogram has the same wavelength as the light itself.

If a second beam of monochromatic light of wavelength 3λ were added to the first, it would exhibit similar behaviour except with intensity peaks at path difference multiples of 3λ rather than λ, as in Figure 3.3b. Since intensity is additive, a new interferogram would result, as shown in Figure 3.3c.

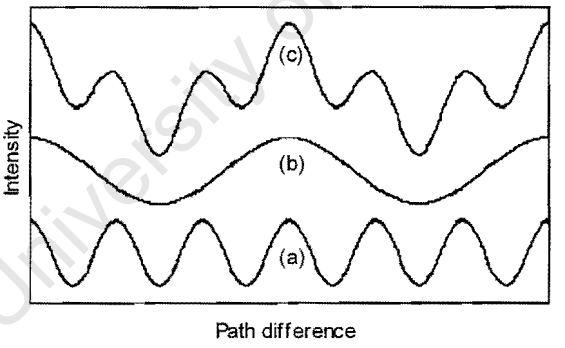

Figure 3.3 - Interferograms of monochromatic light with wavelengths (a) λ and (b) 3λ and (c) interferogram of dichromatic light with wavelengths λ and 3λ

Unlike monochromatic light, an IR beam contains light over a continuum of wavelengths and at different intensities. Thus the interferogram is more complex (see Figure 3.4). Of note is the centerburst, corresponding to ZPD, which gradually subsides to wings which have the average beam intensity.

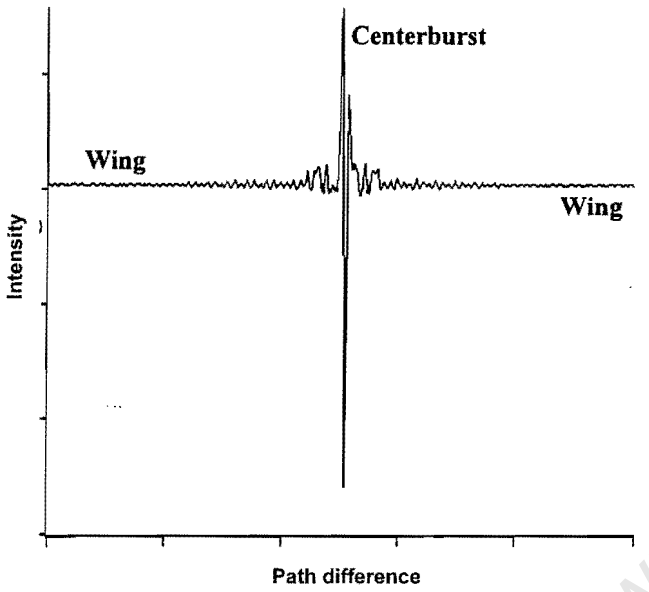

Figure 3.4 - Interferogram of a broadband infra-red source

3.1.3 Fourier transformation to obtain spectra

The interferogram in Figure 3.4 is merely an additive composite of several interferograms of monochromatic light. Since each of these is a cosine curve, the initial interferogram can readily be deconvoluted by Fourier transformation into its component cosine curves. The wavelength of each of these curves is the wavelength of the light and its amplitude is its intensity (or spectral power density). In terms of wavenumbers (ν), this power density can be written (George and McIntyre, 1987)

$$B(\nu) = \int_{-\infty}^{+\infty} I(\Delta)\cos(2\pi\nu\Delta)d\Delta \qquad (3.1)$$

where $I(\Delta)$ is the intensity of the interferogram at path difference Δ. If an experiment is performed with no sample, radiation of all wavenumbers will reach the detector and give a background spectrum [$B_B(\nu)$ vs ν]. If the beam passes through a sample, radiation of certain wavelengths is absorbed to give a single-beam spectrum [$B_S(\nu)$ vs ν]. When this is ratio'd against the background, a transmission spectrum is obtained [$B_S(\nu)/B_B(\nu)$ vs ν] and, when this is inverted and the logarithm is taken, an absorbance spectrum is obtained [A vs ν, where $A = \log_{10}\{B_B(\nu)/B_S(\nu)\}$]. Since the

power density is merely the intensity of light of a certain wavelength, the definition of absorbance is usually written

$$A = \log_{10}(I_0/I) \tag{3.2}$$

As mentioned in section 1.5.4, it can be shown (Atkins, 1990) that absorbance is usually proportional to the concentration of the absorbing species (Beer-Lambert Law).

3.1.4 Mirror position, signal-to-noise ratio, and spectral and time resolution

The detector measures intensity as a function of time while an interferogram requires intensity as a function of path difference. Therefore, in order to obtain repeatable interferograms, it is necessary to know the exact mirror velocity. This is achieved by directing a laser beam of known wavelength along the same path as the IR beam. Since the laser is monochromatic, a cosine interferogram results and it is only necessary to count the number of peaks on this interferogram to know the exact mirror position and hence velocity.

Any FTIR spectrum contains a certain level of random noise. This noise can be reduced by co-adding several interferograms before computing the spectrum. It can be shown that the signal-to-noise ratio (SNR) is proportional to the square root of the number of co-additions.

By considering two monochromatic beams of similar wavelength (λ and $\lambda + \lambda/1000$) it becomes obvious that the longer the length of the mirror scan, the easier it is to distinguish the two wavelengths. When the mirror has moved a distance of λ, the peaks of the two interferograms are $\lambda/1000$ apart, when it has travelled 2λ, they are $2\lambda/1000$ apart and so forth. It can be shown that the spectral resolution is inversely proportional to the scan length of the mirror.

In the conventional mode of FTIR spectroscopy described above, it is clear that each mirror scan results in a single interferogram which is then transformed into a single spectrum. The limiting factor to time-resolution is thus the length of time it takes for

the mirror to move from its beginning to its end position and to reset itself before the next scan. The maximum practicable scanning speed of standard FTIR equipment is approximately 20 scans per second at a spectral resolution of 4 cm^{-1}. However, a minimum of 10 coadditions is usually required to attain tolerable SNR. In addition, to avoid excessive processor memory requirements, a short processing time is needed to compute a spectrum after each set of co-additions. Thus, the highest time-resolution between high quality spectra is between 0.5 and 1 s.

The achievement of significantly higher time-resolutions using triggered rapid- or step-scan FTIR spectroscopy is described in sections 3.2.1 and 3.2.2, respectively.

3.2 High time-resolution FTIR spectroscopy

3.2.1 Rapid scan FTIR spectroscopy

As mentioned above, the time-resolution in the conventional FTIR mode is limited by the need for coadditions to achieve acceptable SNR. For an exactly repeatable process, this loss of time-resolution due to coaddition can be eliminated using the rapid scan mode. In principle, rapid scan FTIR spectroscopy is identical to conventional FTIR and differs only in the way the data is processed and in the exact timing and synchronisation of the data collection.

The means by which the higher time-resolution is achieved is best illustrated by the example of a system in which there is a square-wave volume modulation at a constant frequency. After an initial stabilisation period, each cycle is an exact repetition of the previous cycle. Thus, if the time of a scan in one cycle is exactly synchronised with the time of a scan in the next cycle (see Figure 3.5), these scans represent exactly the same point in the experiment and can thus be coadded.

Hence, the number of cycles required is determined by the number of coadditions needed for tolerable SNR, and the time-resolution is limited only by the scan-speed and mirror reset time.

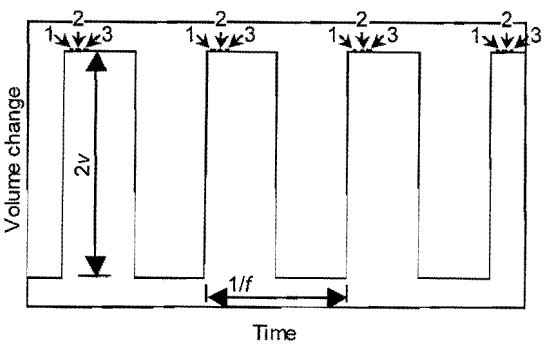

Figure 3.5 - Constant frequency ideal square-wave volume modulation with synchronized points for spectral coaddition. All spectra recorded at points labeled "1" occur at exactly the same time in the modulation cycle and can thus be co-added to increase SNR. The same applies to all points labeled "2" and "3"

A second but less significant contribution to time-resolution is in the processing of the interferograms to obtain spectra. In conventional mode, for each recorded spectrum, the required number of scans is collected, the interferograms are coadded and the final spectrum is calculated. In rapid scan mode, each scan is saved to a buffer file and the computation is only made on completion of data collection, thus eliminating processor delays during the actual experiment. This method clearly requires a large buffer memory size.

With the enhancements described above, spectra can, in principle, be recorded with a time-resolution of approximately 10 ms.

3.2.2 Step scan FTIR spectroscopy

As pointed out in section 3.2.1, even in rapid scan FTIR spectroscopy, time-resolution is limited by the fact that the scanning mirror has to travel a finite distance and therefore expend a finite period of time to collect data for a single interferogram. For an exactly repeatable process, this limitation can be eliminated using step scan FTIR spectroscopy. In this mode, the mirror does not scan an entire interferogram at once but rather moves in discrete steps, collecting a set of time-resolved intensity points at each position.

Thus, in contrast to conventional or rapid scan mode, where each data point collected during a scan represents a point in a single interferogram, the data points collected at

each mirror position in step scan mode represent single points in a time-resolved series of interferograms. In this case, the time resolution is dependent only on the speed of the analog-digital conversion (ADC) in the data acquisition processor, and on the detector. Depending on the processor/detector combination used, time resolutions of between 5 ns and 20 μs are achievable.

As the mirror moves from one fixed position to the next, the full set of interferograms is constructed with, for each mirror position, one point in each time-resolved interferogram. This is illustrated in Figure 3.6.

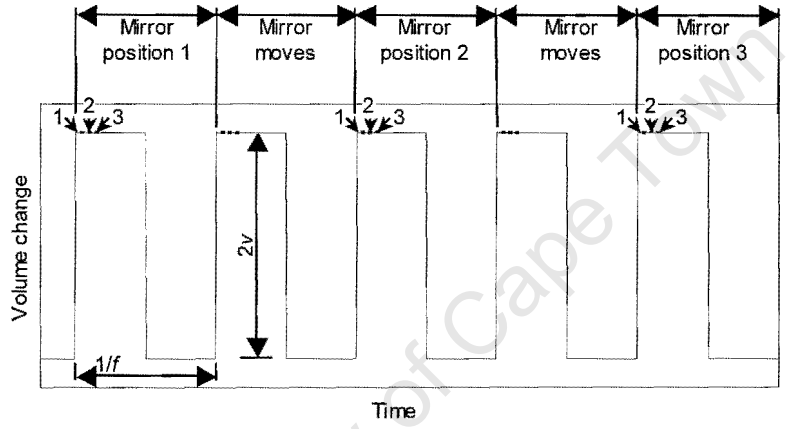

Figure 3.6 - Constant frequency ideal square-wave volume modulation with synchronized points for step scan data collection. At each mirror position, the point labelled "1" represents a point in the "time 1" interferogram. Thus "*n*" mirror positions give an interferogram with "*n*" points at "time 1" in the cycle. The same applies for "time 2" and "time 3". Thus, if "*t*" time-resolved data points are collected at each mirror position, the final result is "*t*" time-resolved spectra

It is clear that this is possible only if the commencement of data acquisition is perfectly synchronised from one cycle to the next and if the time intervals between points being recorded is also exactly the same for each cycle. The practical implementation of the synchronisation required for rapid- and step-scan FTIR will be discussed in sections 4.7.3 and 4.7.4, respectively.

The number of points (or mirror positions) required in an interferogram depends on the total distance travelled by the mirror and the distance between successive mirror positions. The former is decided by the required spectral resolution (see section 3.1.4)

while the latter should be small enough to construct a meaningful interferogram (see Figure 3.4) and, for a broadband MIR beam, is usually set automatically by the spectrometer at a half-wavelength of the laser (see section 3.1.4).

In the procedure described above, a single set of highly time-resolved spectra is obtained. However, the issue of SNR also has to be considered, i.e. several interferograms are required at each time slice. This can be achieved by taking several sets of points, synchronised over several cycles, at each mirror position. As in the other modes, these are known as coadditions.

Since interferograms collected using the step scan method are not fully constructed until the last mirror position has been reached, they cannot be coadded or reduced to final spectra until the end of the experiment. Thus, the size of processor memory required for this mode is orders of magnitude greater than for the other modes and is usually the limiting factor in the number of spectra that can be collected.

Both of these high time-resolution modes, and especially step scan, require a large number of volume modulation cycles for a complete experiment. Thus the duration of the experiment is significantly longer than in conventional mode (see section 4.7.4). This, in combination with the fact that experimental conditions have to be kept constant to obtain meaningful final spectra, gives rise to the problem that baseline drift can have a significant effect on results.

4. Design and construction of experimental apparatus

4.1 General specifications

As can be ascertained from Chapters 2 and 3, the experimental apparatus had to fulfil three primary functions.

1. Execution of volume modulation frequency response (FR) experiments.

2. The measurement of diffusion coefficients by the sorption rate method using *in situ* FTIR spectroscopy to follow the uptake.

3. *In situ* measurement (via FTIR) of the changes generated by the modulations on molecules on the surface of the sample.

These three stipulations gave rise to the following specifications. The apparatus had to be capable of:

- square-wave modulation of the volume over a frequency range of 0.001 to 10 Hz;

- recording the pressure response at a sufficiently high time-resolution and with high signal-to-noise ratio;

- triggering the pressure logging device exactly at the beginning of a cycle so that phase lags and system delays would have the same reference point for each experiment;

- recording FTIR spectra with high time-resolution and high signal-to-noise ratio (SNR); and

- triggering the measurement of each spectrum (in rapid scan mode) or interferogram point (in step scan mode) with exact reference to the beginning of a cycle.

In addition to these primary specifications, the following secondary specifications were necessary.

- Since experiments were to be performed under vacuum (10^{-3}-10 mbar), the system would have to be evacuated completely between experiments to avoid contamination. Thus, all components had to be capable of maintaining ultra high vacuum (UHV: $<10^{-4}$ mbar under static conditions and $<10^{-6}$ mbar under pumped conditions). Therefore, within the main system, only CF flanges were used with copper gaskets.

- To limit corrosion and improve the vacuum, stainless steel had to be used as the material of construction.

- Since some impurities cannot be removed within a reasonable time-span by evacuation at ambient temperatures, all vacuum components had to be bakeable up to 300°C.

- To reduce the amount of sample required (see section 2.2.2), the volume of the closed system (i.e. the section used in the modulation experiments) had to be minimized.

- Even with the system volume reduced to a minimum, the mass of a thin (<10 μm) sample wafer for FTIR experiments (<10 mg for a 10 mm diameter wafer) was considered too low to ensure a pressure response within tolerable sensitivity limits. Thus, a secondary cell had to be included to supplement the sample mass if required.

- To minimize the extent to which the secondary cell would have to be used, the sample holder in the primary cell had to be capable of accommodating the largest practicable wafer size (20 mm diameter).

- Both cells had to have sample temperature control capabilities, including temperature ramps for activation of zeolite samples.

- The dosing system had to be able to introduce the sorbate (either a gas or the vapour phase above a liquid) to the system in a controlled manner. Since a differential pressure gauge was used (see section 4.5), it also had to be possible to introduce sorbate to the reference side of the gauge.

A schematic diagram of the entire apparatus is shown in Figure 4.1.

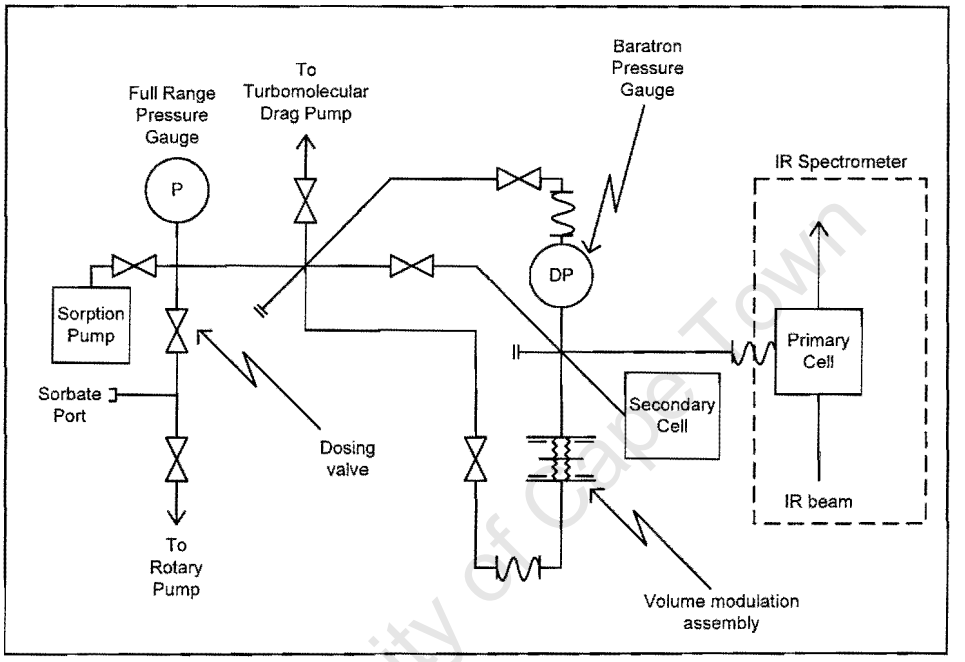

Figure 4.1 - Schematic diagram of the apparatus for frequency response and high time-resolution FTIR experiments

4.2 Primary cell

The cell to be used in the FTIR spectrometer was designated the primary cell. In the design, the following technical considerations were taken into account.

- The cell had to be equipped with IR transparent windows

- A sample holder suitable for supporting a 20 mm zeolite wafer and capable of controlling the temperature of the sample was required. It was also necessary to ensure that the wafer temperature would be as uniform as possible.

- The cell had to be capable of maintaining UHV.

- The volume of the cell had to be minimised.

A detailed description of the cell follows and, for reference, a technical drawing of the principle parts of the cell is shown in Appendix C.

Coaxial type heating wires were wound in a spiral (inner diameter approximately 21 mm) inside a stainless steel support ring (width 8 mm) and, together with a K-type thermocouple, fed through a DN40CF-flange and then sealed by soldering. The thermocouple was bent to stay in contact with the stainless steel ring.

The sample wafer was held by two rimmed, hammered-gold rings. The outer gold ring (inner diameter approximately 20 mm) fitted snugly into the ring created by the heating wire spiral. It had an 8 mm diameter opening for the infra-red beam and thus a 6 mm rim which served both to support the wafer and to ensure a uniform temperature distribution. The inner gold ring fitted snugly into the outer ring and prevented the wafer from falling out.

On the outside of the flange, the heating wires were connected via a ceramic block to an electrical cable. The thermocouple wire also fed into a cable. After a short length, both cables were connected to plugs so that the entire flange with the sample holder, heating wires and thermocouple could be disconnected and removed.

A programmable Eurotherm 2146 temperature controller was used to control the temperature in the cell. This controller made use of PID control and had manual, automatic and adaptive tuning facilities to tune the PID parameters. Its programmable functions allowed the input of multiple temperature ramps and dwell times. Since the energy requirement of the cell was small, a thyristor and 30V step-down transformer were installed to improve the control performance.

The body of the cell was constructed from a solid stainless steel block (70x70x50 mm). It was comprised of: (i) a sleeve for the sample holder of length 35 mm (rounded at the ends), width 10 mm and height 45 mm; (ii) a horizontal cylindrical

channel of diameter 10 mm leading to the vacuum system; and (iii) two horizontal cylindrical channels perpendicular to the sleeve into which circular CaF_2 windows were fitted. The total working volume of the cell was 17.4 cm^3.

Each of the window channels had a rim on the inner end and was threaded on the outer end. The inner rim supported a Teflon gasket against which the window was pressed. Another Teflon gasket was pressed against the outer side of the window and held in place by a fastener. The fastener was a hollow cylinder threaded on the outside on one end. Thus it could be inserted behind the second Teflon gasket and screwed in as tightly as necessary. A custom-made tightening tool fitted into two slots on the rim of the fastener. It should be noted that the Teflon gaskets could not withstand temperatures above 200°C; hence, the cell had to be removed if the system was baked out at 300°C.

The upper face of the body was cut to a DN40CF profile to accommodate the sample holder flange and the face at the end of the vacuum channel was cut to a DN16CF profile to accommodate the flexible pipe leading to the vacuum system.

Four threaded holes were cut into the two faces through which the IR beam passed. Using these, a thin rectangular aluminium plate was connected to each face. These plates slid into standard Bruker sample holders in the FTIR spectrometer. The sample holders could then be used to position and stabilize the cell.

4.3 Secondary cell

As mentioned in section 4.1, the secondary cell was necessary to supplement sample mass and thus improve the pressure sensitivity of the system to volume modulation. This cell consisted of a quartz glass tube (Length 80 mm, outer diameter 10 mm) connected, via a glass-metal connection to a DN16CF flange. The sample was placed in the bottom of the tube and held in position by a plug of quartz glass wool.

The cell was heated by a cylindrical oven consisting of a heating wire wound spirally around the outside of a hollow ceramic cylinder (inner diameter 22 mm, outer diameter 30 mm). This was insulated by 40 mm of quartz glass wool held in an

aluminium casing. A stainless steel sleeve was inserted into the ceramic cylinder. The sleeve was made from a solid stainless steel cylinder (diameter 21 mm, length 120 mm). An opening (diameter 12 mm, length 80 mm) was cut into one end, into which the cell was inserted. A groove was cut down the length of the opening to accommodate a thermocouple.

A programmable Eurotherm 2146 temperature controller identical to the one used for the primary cell was used to control the temperature in the cell. In this case, however, only a solid-state relay was required in place of the thyristor and step-down transformer.

4.4 Volume modulation assembly

Several options existed to drive the volume modulation. However, for the first attempt, it was decided to adopt the proven concept of Rees (1999). Thus, to produce the square-wave volume modulation, a flexible metal bellows was alternately expanded and compressed.

This was achieved by having the bellows connected to a circular disc armature which moved up and down between two closed circular ring electromagnets. The armature and the magnet yokes were constructed of mild steel. Each magnet had a copper wire ring winding that dropped into the circular slot at the centre of the magnet. A schematic drawing of the bellows-electromagnet assembly is shown in Figure 4.2. More detailed technical drawings of the separate components can be found in Appendix D. It should be noted that, while the concept of Rees (1999) was copied, considerations specific to this system led to the use of different dimensions.

The principle of the magnet operation was straightforward. First, current was supplied to the winding in the upper magnet, generating a magnetic field and bringing the armature into contact with the face of the upper magnet. Then the current was turned off in the upper magnetic and on in the lower magnet, thus bringing the armature down to the lower magnet face. This procedure was then alternated at a constant frequency.

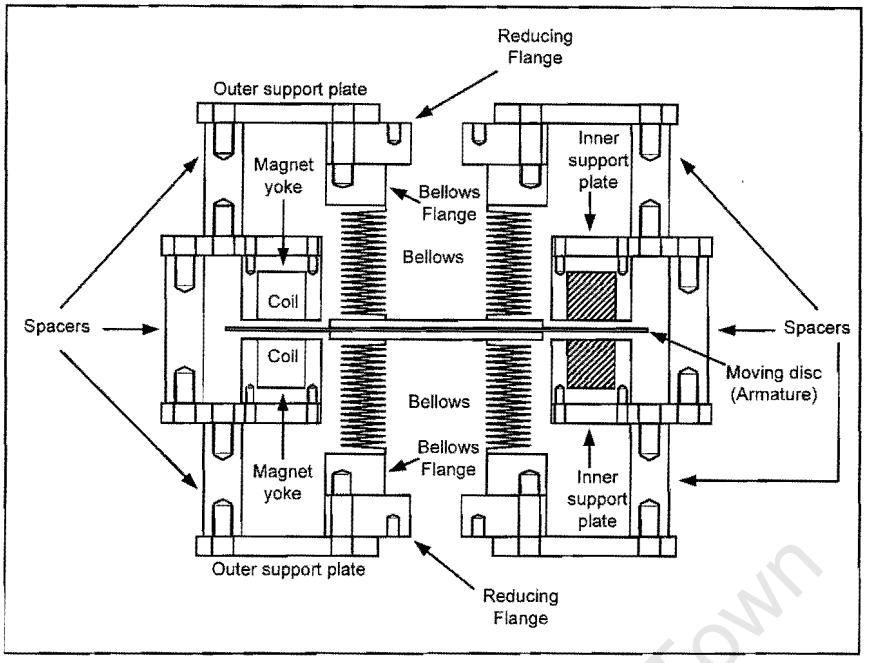

Figure 4.2 - Schematic drawing of the volume modulation assembly for the frequency response and high time-resolution FTIR apparatus. Note that this is neither drawn to scale nor is it a true cross-sectional representation

The technical considerations related to the design of the bellows-magnet assembly were as follows.

4.4.1 Bellows

As implied in sections 2.1.1 and 2.1.2, it is necessary, in frequency response experiments, to keep the volume change small to ensure approximate isotherm linearity and a constant diffusivity, and to limit thermal effects. For the FTIR measurements, however, this was not deemed essential. In addition, since this type of experiment had not previously been performed in conjunction with FTIR, the magnitude of volume change required to give an observable spectral response was not readily apparent. Therefore, in order to maintain flexibility in this regard, it was decided to use a larger volume (i.e. larger diameter) bellows than was employed by Rees (1999). This had the added advantage that, even in the standard FR mode, the armature would have to travel a shorter distance than in the Rees assembly to give a similar volume change. Thus, a bellows inner diameter in the range 30-50 mm was specified. Also to maintain design flexibility, a minimum bellows stroke of 10 mm was specified.

In each FR experiment, depending on the time allowed for stabilization before measurements (0-100 s), the bellows would have to perform between 200 and 5000 cycles. Thus, a long working life for the bellows was essential. In addition, the overall system specifications had to be taken into account, including a CF flange on the system end of the bellows. For ease of assembly, it was also desirable that this flange be rotatable and have threaded bolt-holes. On the end attached to the armature, the most important factor was to keep the mass of the flange as low as possible.

Within the above specifications, suppliers would not guarantee lifetimes of the bellows longer than 10 000 cycles. Thus, the final purchase was based on the acceptance that the bellows would last well in excess of the official guarantee.

A COMVAT Material AM 350 Compact Series bellows with the following specifications was used:

- Inner diameter 39 mm/Outer diameter 59 mm/Effective area 19.6 cm^2
- Free length 25 mm/Compressed length 5 mm/Extended length 38 mm
- Spring constant 3.9 N/mm
- Flange DN40CF Rotatable

For reasons discussed in section 4.4.3, a second bellows was attached to the opposite side of the armature. This had exactly the same specifications as the first bellows except that it had a fixed rather than rotatable flange.

4.4.2 Magnet and armature

For ease of assembly, it was desirable for the bellows to be able to pass through the hole in the centre of the ring magnets. Therefore, since the outer diameter of the bellows flange was 70 mm, the inner diameter of the ring magnet was set at 72 mm.

In most other respects, the design of Rees (1999) was followed. The width of each arm of the magnet yoke was 5 mm, the width of the slot was 15 mm and, thus, the outer diameter of the ring was 122 mm. As in the Rees design, the armature had a radius 5 mm larger than the ring magnet to ensure good contact with the yoke. Thus, the armature had a diameter of 132 mm. The mass of the armature had to be as low as

possible (see section 4.4.3) but had to remain rigid. An armature thickness of 1 mm was used.

The ring winding consisted of 1000 turns of 0.4 mm copper wire. Unlike in the Rees design, the copper windings were not permanently sealed into the magnet yoke using an epoxy resin. Instead, the copper was wound around an aluminium holder (see Appendix D) which had small indentations in its innermost surface. This holder was then fixed into position by inserting slug screws through the inner wall of the magnet yoke into the indentations. This had the advantage that, if the copper winding failed, it could more easily be discarded and replaced.

4.4.3 Analysis of the square wave modulation

For the initial part of this analysis, it is assumed that, in contrast to the depictions in Figures 4.1 and 4.2, there was a bellows only on the system side of the armature and that, on the other side, the armature was merely exposed to atmosphere.

As discussed in section 2.3.3, the Fourier transformation analysis is based on the pressure response to a square-wave volume modulation. Thus, it was essential for the wave-form to be as square as possible. Therefore, the time for the armature to move from one magnet to the other (i.e. the time for the bellows to move from the compressed position to the expanded position or vice-versa) had to be as small as possible relative to the time spent in each position. Figure 4.3 shows a typical armature trajectory, where the time for the armature to move from one magnet to the other is defined as τ.

To evaluate the wave-form quantitatively, a "squareness" factor, ε, was defined as the ratio between the time the armature spends in contact with the magnet face in the actual case and the time it would spend in the ideal case (i.e. with $\tau = 0$).

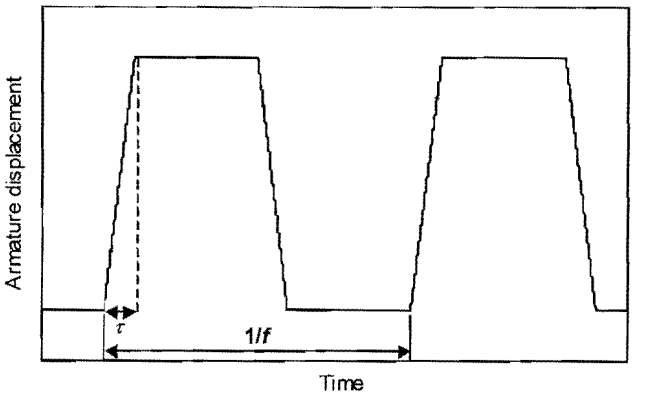

Figure 4.3 - Depiction of the realistic time-dependency of the armature displacement (or volume change) when an attempt is made to achieve square-wave modulation on the assembly described in section 4.4

Thus, considering that the magnet would move twice each cycle,

$$\varepsilon = (1/f - 2\tau)/(1/f) = 1 - 2f\tau \tag{4.1}$$

where τ can theoretically be determined by solving the differential form of Newton's second law:

$$F = m(d^2x/dt^2) \tag{4.2}$$

In equation (4.2), x is the displacement of the armature from its half-way position, m is the mass of the moving parts (the most significant contributors to this were the armature and the flange connecting the armature to the bellows) and F is the sum of the forces acting on the moving parts. In this assembly, these forces were: the magnetic force exerted on the armature; the force exerted by the pressure differential on either side of the armature; the gravitational force acting on the moving parts (since the assembly was mounted in the vertical position to avoid deformation of the bellows); and the spring force of the bellows.

The magnetic force originates from the magnetic force density, $B^2/2\mu_0$, where B is the magnetic flux density (or magnetic field) in the yoke and μ_0 (= $4\pi x10^{-7}$ Tm/A) is the permeability constant (Rees, 1999). In this case, the area over which this force would act was the face area of the magnet yoke, $A = 4\pi r_M e$ where r_M is the mean radius of

the circular ring magnets and e is the width of each arm of the magnet yoke (Rees, 1999). Thus, the magnetic force was:

$$F_M = 4\pi r_M e B^2 / 2\mu_0 \tag{4.3}$$

The force exerted by the pressure differential, the gravitational force and the bellows resistance force were, respectively:

$$F_P = (\Delta P)_A A_B \tag{4.4}$$

$$F_G = mg \tag{4.5}$$

and

$$F_B = -kx \tag{4.6}$$

where $(\Delta P)_A$ is the pressure differential across the armature, A_B is the cross-sectional area of the bellows where it is connected to the armature, g is the gravitational constant, k is a spring constant and x is the bellows displacement from their equilibrium position (assuming that, to a first approximation, the bellows can be modelled as a spring).

Using the bellows and magnet dimensions, r_M = 48.5 mm, e = 5 mm, A_B = 19.6 cm^2 and k = 3.9 N/mm. Assuming the maximum travel distance was 10 mm and that the half-way position of the armature was at the equilibrium extension of the bellows, the maximum deflection in each direction was 5 mm. The saturation flux density of mild steel, and thus in the armature, was 2 T (Rees, 1999). Since the thickness of the armature was 1 mm and $\nabla \cdot \boldsymbol{B} = 0$, the magnetic flux density in the yoke was $1/e$ times the flux density in the armature (Rees, 1999). Thus, in equation (4.3), $B \approx 0.4$ T. Since the minimum system pressure during a modulation was 10^{-3} mbar, $(\Delta P)_A \approx 1$ bar. From the dimensions of the armature and a mild steel density of 7800 kg/m^3, the mass of the armature was 107 g. Thus, assuming the bellows flange was slightly lighter, m was assumed to be 0.2 kg. Finally, $g = 9.8$ ms^{-2}.

The forces calculated using the above values were: F_M = 97 N, F_P = 196 N, F_G = 2 N and $(F_B)_{max}$ = 19.5 N. The directions of F_P and F_G relative to F_M depend on the direction in which the armature is travelling. F_B supplements F_M from when the

armature leaves the first magnet until it reaches the half-way position, then acts in the opposite direction as the armature travels from the half-way position to the other magnet.

From these values it was clear that, at typical operating conditions, the force due to the differential pressure would be dominant and the magnet would fail to move the armature. In addition, while the force due to gravity was negligible in comparison to the magnetic force, the spring force due to the bellows displacement was not.

Therefore, it was necessary to counteract the force due to the pressure differential by the method of attaching a second bellows, exactly the same as the first, on the opposite side of the armature and evacuating this bellows to approximately the same pressure as the closed system. Since the maximum operating pressure was 10 mbar, this reduced F_P by two to three orders of magnitude and rendered it negligible. The bellows were set up so that, in the half-way position of the armature, both bellows were compressed to the same degree (i.e. same displacement). Since there were two bellows, it can be shown (see Appendix E) that, $F_B = -2kx$. Therefore, equation (4.2) becomes

$$F_M - 2kx = m(d^2x/dt^2) \tag{4.7}$$

Setting the distance between the magnets to $2X$, and using the appropriate boundary conditions (see Appendix E), equation (4.7) was solved (see Appendix E) to give,

$$\tau = (m/2k)^{1/2}\{\pi/2 + \arcsin[(X - F_M/2k)/(X + F_M/2k)]\} \tag{4.8}$$

Using F_M = 97 N and m = 0.2 kg, τ and ε could be calculated as a function of the travel distance and frequency using equations (4.1) and (4.8). The results are shown in Figure 4.4.

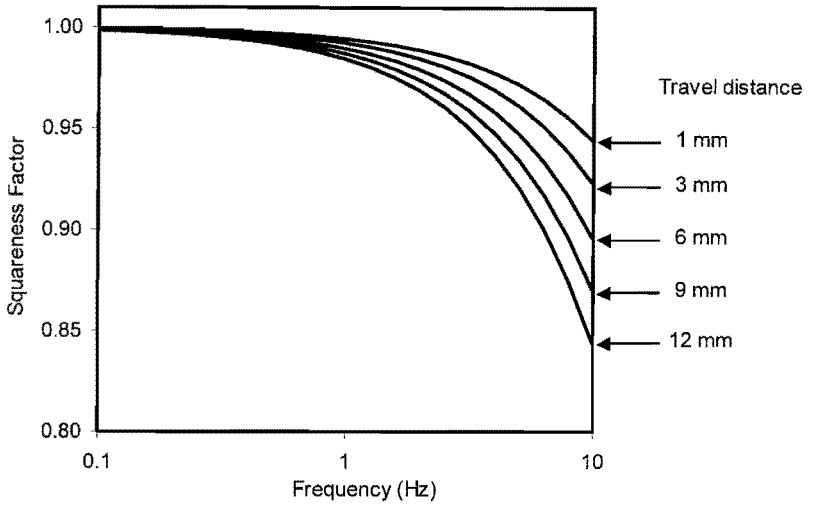

Figure 4.4 - The relationship between the squareness factor, the modulation frequency and the travel distance (armature displacement)

Rees and Shen (1993) considered the quality of their Fourier transform excellent at a frequency of 10 Hz with $\tau \approx 10$ ms. This corresponds to a squareness factor of $\varepsilon = 0.8$. Hence, for the design, it was assumed that square-wave analysis could be performed for $\varepsilon > 0.8$ which, according to the above analysis, was achievable for travel distances up to 12 mm.

It should be noted that the above analysis did not take into account the rise time of the magnetic field for the active magnet, the demagnetisation time for the non-active magnet or the eddy current damping of the magnetic system.

4.4.4 Support structure

The magnets and the bellows flanges were mounted on a support structure. The purpose of this was to be able to set the spacing between the magnets, and to determine the extension or compression of the bellows.

Each magnet was attached to a circular plate (thickness 6 mm, diameter 172 mm) with a hole of the same inner diameter (72 mm) as the magnet. This was to allow the bellows flange to be able to pass through the plate and thus facilitate the assembly of the structure. The distance between the magnets (and hence the armature travel distance) was set by inserting four spacers, 90° apart, between the two circular plates.

As was mentioned in section 4.4.1, each different experimental mode required a different volume change (or armature travel distance). Thus, it was necessary to have a range of spacer lengths.

To decouple the setting of the bellows length from the magnet spacing, each bellows flange was connected to an outer circular plate (thickness 6 mm, diameter 150 mm) separated by spacers from the inner plate. Thus, for any particular magnet spacing, the bellows length could be set by changing the length of this second set of spacers.

The bellows had a DN40CF flange while the system, to minimize volume, was in the DN16CF standard. Therefore, it was necessary to connect the bellows flange directly to a 40-16 zero-length flange reducer. It was convenient to include this reducer in the structure, between the bellows flange and the support plate. Since the reducer was then connected to a DN16CF flange (diameter 34 mm), the hole in the outer support plate had to accommodate this flange and thus had a diameter of 36 mm.

Setting the length (in mm) of the inner and outer set of spacers to S_1 and S_2 respectively, when the armature was in the half-way position, the length (in mm) of each set of bellows (L_B) was:

$$L_B = S_1/2 + S_2 - 26.2 \tag{4.9}$$

Thus, knowing from the specifications that the bellows effective area was 19.6 cm^3, the volume of the bellows in any particular configuration could be calculated.

4.4.5 The controller

The control arrangement for the volume modulation will be discussed, along with other control issues, in section 4.7.

4.5 Pressure transducer

The following technical issues were considered in the selection of the pressure transducer.

- A long-term purpose of the system was to measure diffusion coefficients for several different gas-zeolite combinations. Therefore, accurate pressure measurement was required for a range of gases. Thus, a membrane (or Baratron type) transducer, which is not gas-dependent, was specified.

- As mentioned in section 2.3.4, a sampling frequency of $128f$ was required to obtain sufficient points for phase lag evaluation. At the highest specified modulation frequency of 10 Hz, a response time of less than 0.8 ms was required. Thus, the transducer response time was specified to be <0.8 ms.

- Since experiments were to be performed in the range 10^{-3} to 10 mbar, the transducer was specified to be accurate within this range.

- During an FR experiment, the relative volume change (v) and thus relative pressure response in an empty cell (p_B) was to be approximately ±1.25 %. For a gas-zeolite system, the relative pressure change would be less than this and would depend on the K-value discussed in section 2.2.2. It was assumed that an appropriate sample mass could be selected to give p_Z a value approximately half of p_B (i.e. ±0.625 %). To obtain useful data, the actual pressure difference (i.e. $P[p_B\text{-}p_Z]$) had to be clearly distinguishable. At the lowest pressure in the operating range (10^{-3} mbar) this would translate to $6.25\text{x}10^{-6}$ mbar. Therefore, the resolution of the pressure transducer was specified to be lower than this value.

- In general, signal-to-noise ratio (SNR) can be increased by amplifying the measured signal, as long as the new signal does not exceed the range of the output instrument. Consider, for example, an output instrument with a 0-10 V range, linearly scaled to a pressure of 0-10 mbar. At an operating pressure of 0.5 mbar, the normal output signal would be 0.5 V. This could be amplified 10 times to give a signal of 5 V and would still be in the 0-10 V range. However, if the operating

pressure were 2 V, this could not be amplified 10 times, since this would give a signal of 20 V, which would saturate the output instrument (and give an "out-of-range" signal).

This problem can be circumvented by using a differential transducer. In this case, once the operating pressure has been measured with the reference side fully evacuated (i.e. as though it were an absolute transducer), gas can be admitted to the reference chamber until the differential pressure is close to zero. Then, as long as the differential pressure is not too high, the signal can be amplified by several orders of magnitude. In the example above, at an operating pressure of 2 mbar, the reference side could be pressurized until the differential pressure is 0.05 mbar. Then, with $p_B = \pm 1.25$ %, the differential pressure would vary between 0.025 and 0.075 mbar. The signal could then be amplified 100 times and the range of the output signal would be 2.5-7.5 V, still within the 0-10 V range.

Thus, the specification was made for a differential rather than absolute transducer.

- Since the transducer was to be part of the modulation system, the overall specifications regarding materials of construction, bake-out temperature and UHV fittings were taken into account.

An MKS Baratron Type 616A (differential) transducer, with a MKS Type 670B High Accuracy Signal Conditioner was used. The relevant specifications of this combination were as follows:

- Range 6.65×10^{-4}-13.3 mbar/Resolution 1.33×10^{-5} mbar
- Accuracy 0.12 % of reading
- Response time 1 ms
- Maximum signal amplification 100X

Due to limitations on available transducers, two of the original specifications could not be met. Firstly, the resolution was only half that originally specified. Thus, at operating pressures of less than 2×10^{-3} mbar, the necessary resolution was not attainable. Secondly, the response time was not 0.8 but 1 ms. Thus, the maximum modulation frequency at which the required sampling frequency could be obtained

was 7.8 Hz and only 100 rather than 128 data points could be collected at a modulation frequency of 10 Hz. Neither of these contraventions had a large impact on the originally specified pressure and frequency ranges.

The pressure transducer was in a U-shape and it was stipulated by the supplier that the ports not be mounted "in a manner that causes strain to be transmitted to the sensor head" (MKS Instruments, 1997). This was to prevent any distortion of the membrane, which would lead to inaccurate readings. In order to prevent any such strain, aluminium strips were mounted between the two end-connection flanges. This fixed the end-to-end distance and ensured that, if strain was placed on either of the flanges, it was not transmitted to the transducer. An illustration of the principle and a technical drawing of the strain isolation strips can be found in Appendix F.

The transducer sensor was temperature sensitive and its temperature thus had to be controlled within stringent limits to avoid measurement errors. This was achieved by enclosing the entire sensor head within a custom-made aluminium heating-block. A technical drawing of this block is shown in Appendix F. Heating was supplied by two 100 W cartridges which were inserted snugly into holes in the body of the block. A K-type thermocouple was also inserted into a hole in the block. The temperature was controlled by a single-setpoint Eurotherm 2132 temperature controller with PID control and facilities for manual and automatic tuning of the parameters.

4.6 FTIR spectrometer

The following were the technical considerations and specifications for the FTIR spectrometer.

- For reasons discussed in section 1.5.5 and Chapter 3, the spectrometer had to be capable of operating in both rapid- and step-scan modes, as well as in the conventional mode. This specification included any hardware or software necessary to receive trigger signals from an external source so that data collection could be synchronised with the signal driving the volume modulation.

- It was decided that, in the initial configuration, the instrument should be capable of collecting step scan spectra with a time-resolution in the microsecond range. Thus, as well as the internal AD converter, the detector (or, more accurately, the detector pre-amplifier) had to be capable of this time resolution. In addition, if possible, flexibility had to be allowed for a later extension to the nanosecond range.

- Since the IR bands of the zeolite hydroxide groups are between 3800 and 3100 cm^{-1} and most molecular vibrations of hydrocarbons occur between 3100 and 1300 cm^{-1} (see section 1.5), the minimum required frequency range for the spectrometer was 4000-1000 cm^{-1}. Thus, the beam source, beam splitter and detector had to be compatible with this specification.

- From Table 1.1, it was clear that, in order to distinguish between several species (especially isomers), a spectral resolution of less than 1 cm^{-1} would sometimes be required.

- In a typical spectrometer where a cell is mounted in the path of an IR beam, the beam usually has to travel through 20-30 cm of space from when it leaves the source to when it reaches the cell and then another 5-10 cm from when it leaves the cell to when it reaches the detector. Even if this space is purged using dry air, several air-borne impurities are observed in the spectrum. Most notable of these are CO_2 and water. In standard uptake or activation experiments, the bands of these impurities do not affect results significantly. However, in the proposed experiment where a change in peak intensity of only 1 % or less was expected, it was thought that these bands, particularly those of water, which occur over a large range of frequencies, could conceal important data. Thus, it was necessary for the entire spectrometer to be evacuated.

In accordance with the above considerations, a BRUKER IFS 66v/S spectrometer was used, with the following noteworthy specifications:

- Operating vacuum: < 3 mbar
- Frequency range 7500-370 cm^{-1}/Source: water-cooled SiC glowbar/ Beam splitter: Ge multilayer coating on KBr

- Detectors: liquid nitrogen cooled MCT; and DLATGS with KBr window; automatic mirror adjustment to accommodate either detector
- Resolution: Better than 0.25 cm^{-1}/Scanner: 20 scans/sec in normal mode; 100 scans/sec in rapid scan mode (at 12 cm^{-1} resolution)
- Electronics: 16-bit-200kHz AD converter; acquisition processor (AQP) with 4 Mb of RAM
- Rapid- and step-scan options including external trigger connections (operating on a TTL signal)
- In step scan mode, a time resolution of 20 μs

The triggering scheme to obtain the necessary synchronisation for the rapid- and step-scan modes will be discussed in sections 4.7.3 and 4.7.4 respectively.

Two important modifications were made to the as-delivered spectrometer. As stated previously, the entire spectrometer was to be evacuated during an experiment. However, while the primary cell was situated inside the spectrometer, it had three connections that had to be linked to equipment outside the spectrometer: the flexible connection leading to the vacuum system (see Figure 4.1); the power cable supplying current to the heating wires; and the thermocouple cable. Thus, all these had to penetrate the walls of the spectrometer without compromising the vacuum.

In order to achieve this, a side panel of the spectrometer was removed and replaced by a custom-made aluminium panel with seals around the three fittings. A technical drawing of this panel with its accessories can be found in Appendix G. Standard o-ring seals (which were simply screwed to the required tightness around the cables) were used for the power and thermocouple cables. However, this was not possible with the stainless steel flexible connection, since it had a DN16CF flange on either end.

In this case, a hole large enough to accommodate the flanges was cut into the panel. Two aluminium pieces on the outside of the panel then provide the seal. Each of these had a thickness of 12 mm, to cover at least two undulations of the flexible connection, and a semicircular groove with a diameter slightly greater than that of the flexible

connection. The aluminium pieces were lined with rubber on the side in contact with the panel, in the grooves and along the side where they met. These two pieces were connected to the panel and pushed together as tightly as possible around the flexible connection to obtain a seal. Finally, the boundaries and seams of this outer assembly were covered with a thin layer of silicon gel. In this manner a pressure of less than 3 mbar could be preserved in the spectrometer.

Since the primary cell was to be opened each time a new sample wafer was used, the sample compartment of the spectrometer would be regularly exposed to atmospheric conditions. If no change were made to the spectrometer configuration, this would have meant that all other components of the spectrometer were also exposed to atmosphere. For certain components such as the beamsplitter, which was sensitive to moisture and other airborne contaminants, this was undesirable. Thus, the spectrometer was modified by installing optional KBr windows with o-ring seals at either end of the sample compartment. In this way, the sample compartment could be pressurized while the other compartments remained evacuated. A potential problem with this modification was that, while the KBr windows were IR transparent, they provided additional possibilities for light scattering.

4.7 Control, triggering and synchronization arrangement

As was pointed out in sections 2.3.2, 3.2.1 and 3.2.2, it was crucial to the successful operation of both the frequency response and the high time-resolution IR experiments to be able to synchronise data collection at an exact time relative to a reference point in the volume modulation cycles.

However, before the arrangement of the synchronisation and triggering control systems can be discussed, it is necessary to describe the system that controlled the operation of the volume modulator and the pressure response data collection. An electrical circuit drawing of the entire system can be found in Appendix H.

4.7.1 Volume modulation and collection of pressure data

The current to the magnet was delivered by a Conrad 40V/3A laboratory power supply (model PS-2403-D). A TTL (0-5V) signal given by the controller to a series of relays decided whether the current was on or off and whether it was directed to one electromagnet or the other.

Because data from several cycles was to be coadded, it was essential to maintain, at each particular frequency, an exactly constant cycle period without any delays (which could be caused by the simultaneous processing of data). Therefore, a dedicated PCI card, which allowed the independent operation of the frequency controller, was used for the volume modulation and pressure data collection. The card used for this purpose was a Meilhaus ME-3000 PCI VEC-3 with 12 bit/500 kHz A/D conversion (16 single-ended or 8 differential channels), 2x16 TTL digital I/O channels, a 12 bit D/A converter (4 analog outputs) and one external trigger connection to each of the D/A and A/D sections.

The programs used to control the input and output from this card were written in HP Vee, a graphical programming language with pre-programmed modules for input and definition of variables, output data storage, mathematical operations, program loops and other necessary processes. The Meilhaus card also had pre-programmed HP Vee modules, which were merely specialized combinations of Meilhaus operations code and standard HP Vee modules.

To automate the frequency response experiment it was necessary to be able to run through a range of frequencies. In addition, at each frequency, a stabilisation delay had to be allowed between the beginning of each new modulation frequency and the onset of data collection.

The programs which were written for the operation of the volume modulator had the following sections.

- An input section, which allowed the user to input, either manually or (more usually) via a preset array, the number of frequencies over which measurements

were made, the set of frequencies, the stabilisation delay, the number of cycles that were required for coaddition, and the number of data points that would be recorded at each frequency. Also in this section, the program computed the frequency with which data was to be collected and the total measurement time at each particular modulation frequency.

- An initiator section, in which successive rows from the input array were called and sent forward to the main program.

- An actuation (or "analog out") section, in which, if the magnet pair was not yet in operation, the current from the power supply was switched on. If the magnet pair was already in operation, it was first de-activated from its existing frequency mode then activated at the next frequency. For the required square-wave generation, this was achieved by setting up a table of values (the maximum number of values was 4096, i.e. a 12 bit set), the first half of which were 5 and the second half of which were 0. Thus, this represented a single square-wave cycle. This square wave was saved in a buffer file and then executed repeatedly by a standard Meilhaus module in a "free-running" manner until a specific Meilhaus function (the "de-activation" mentioned above) was invoked to stop it. The card thus sent a TTL signal, which oscillated between 0 and 5 V at the required frequency, to a pair of relays which then delivered the current from the power supply to one or the other of the electromagnets.

- A data collection (or "analog in") section, during which, starting at a designated time, the number of pressure data points specified in the input array was logged at the frequency calculated in the input array. Simultaneously with logging the pressure data, the AI section also recorded the TTL signal sent to the magnets.

Once the required number of data points had been collected at any particular frequency, the program transferred the data to a sequentially numbered file, then looped back to the initiator section. There it chose the next row from the array of input data and proceeded again through the actuator and data collection sections.

The Meilhaus card had one limitation with respect to the procedure in the analog-out section. The timer module had a start frequency of 3 MHz and determined the frequency using two dividing factors. These had maxima of 2^{16}–1 (i.e. 16 bit) and 2^{12} (i.e. 12 bit) respectively. Therefore, the low frequency limit was $3x10^6/(2^{16}–1)(2^{12})$ or 0.011 Hz. Thus, for frequencies lower than this, a different program which did not utilize the independent operation mode had to be used. At such low frequencies the processing delays were not significant.

4.7.2 Triggering of pressure logging measurements

As mentioned in the description of the "data collection" section, the signal driving the magnets was recorded at the same time as pressure data. Therefore, the phase lags could be ascertained by comparing these two sets of data. However, data analysis could be made even more straightforward if the onset of pressure measurements occurred exactly when the TTL signal changed from 0 to 5 V or vice-versa. This was achieved by connecting this signal directly to the A/D section external trigger on the card. The A/D data collection module could then be set to activate its logging procedure on either a positive-edge (0 to 5V) or negative-edge (5 to 0 V) trigger.

It is noted that the use of the magnet-driver signal as a reference to measure phase lags assumed a constant time between the signal being sent and the armature leaving the magnet.

4.7.3 Synchronization of rapid scan measurements

In the rapid scan mode of the IR spectrometer, an internal program (on OPUS software provided by the spectrometer supplier) allowed the onset of a scan (or a series of scans) to be actuated by a positive- or negative-edge TTL signal on up to 4 different channels. The program also allowed a scan (or set of scans) to be saved into a user-designated buffer file. The methodology for collecting data was thus as follows, with reference to Figure 4.5 [Note: in the description that follows, the term "positive-edge" can be replaced by "negative-edge" and the word "scan" can be replaced by the phrase "set of scans"].

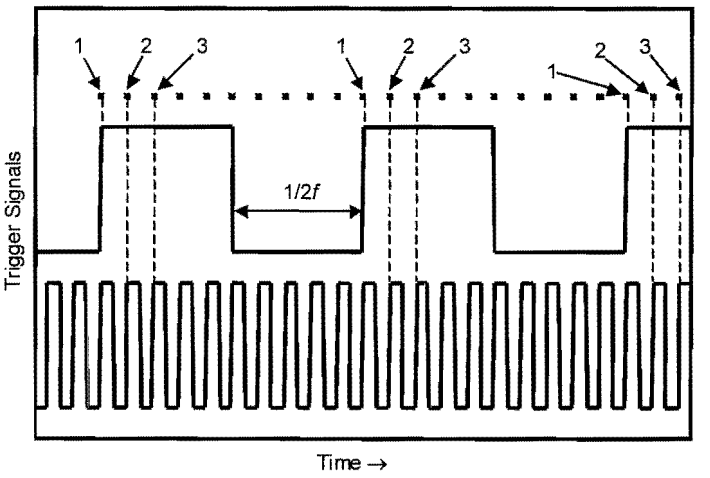

Figure 4.5 - Magnet-driving signal at frequency *f* and second signal at frequency 10*f* used to trigger rapid scan measurements. Measurements labeled "1" are triggered by the lower frequency signal and saved into buffer file 1 to be coadded at the end of the experiment. Subsequent scans are triggered by the higher frequency signal and saved into buffer files 2, 3 and beyond

Along with the magnet-driver signal (at frequency f), the card output a second TTL signal at frequency fN_E (where N_E is an even number). This second signal was in phase with first at the beginning of each cycle. By entering the appropriate commands in the OPUS software, the first scan in a rapid scan measurement was activated by a positive-edge trigger on the channel carrying the magnet-driver signal. This first scan was then saved into buffer file "1". The second scan was activated by a positive-edge trigger on the channel carrying the second TTL signal. This second scan was saved into buffer file "2". Several additional scans were activated by positive-edge triggers on the channel carrying the high frequency signal and saved into successively numbered buffer files. A loop could be created in the OPUS program so that the procedure was repeated on each successive volume modulation, using the same set of buffer files as previously. Thus, each repetition of the loop coadded another scan to the appropriate buffer file.

The only limitation was that buffer memory not be exceeded. In addition, to avoid any confusion regarding the timing and synchronisation, it was advisable to make sure that, when a set of scans was taken at each positive edge of the high frequency signal, the scans were completed before the next positive edge signal (e.g. if fN_E = 20 Hz,

each set of scans had to be completed in less than 0.05 seconds. Thus, if the scanning frequency was 100 scans/second, a set had to contain less than 5 scans).

Depending on the time resolution required is was sometimes possible to obtain several coadditions within a single cycle (e.g. if the scanner speed was 20 scans/second and the required time-resolution was only 0.5 seconds, then 10 coadditions could be made within one cycle). Thus, from the number of coadditions per cycle ($N_{A/C}$) and the total number of coadditions required (N_A), the number of cycles required (N_C) could be determined

$$N_C = N_A/N_{A/C} \tag{4.10}$$

The duration of the experiment (t_E) could then be determined from the number of cycles and the modulation frequency

$$t_E = N_C/f \tag{4.11}$$

4.7.4 Synchronization of step scan measurements

Before describing the triggering algorithm for the step-scan mode it is worth noting and defining the parameters which could be set in the OPUS software.

- Stabilization delay: the time allowed for the mirror to settle down after it had stabilized in a certain position. The mirror took approximately 20 ms to move from one position to the next and stabilize itself. Thus, even when the stabilization delay was set to zero, the spectrometer waited 20 ms before taking measurements. Thus, stabilization delay was only necessary in special cases and, if used otherwise, it only increased measurement time unnecessarily.

- Delay before experiments: an additional time between the end of the stabilization delay and the collection of data. This was usually set to zero for the type of experiment conducted in this study.

- Number of time slices: the number of time-resolved points collected during each cycle. From section 3.2.2, it is clear that this was also the required number of time-resolved spectra.

- Time resolution: the time between acquisition of successive data (i.e. the time-resolution between successive spectra).

- Coaddition repeat count: the number of spectral coadditions required to make up each final spectrum.

- Experiment trigger source: allowed the use of an internal or external (positive- or negative-edge) TTL trigger. For the experiments conducted in this study, this was set to "external positive (or negative) edge".

The following are noted about the internal mechanism of the spectrometer in step-scan mode

- Any external trigger signal sent during the time that the mirror was moving and stabilizing or during the user-specified "stabilization delay" or "delay before experiments" times was ignored by the spectrometer.

- On completion of the delay times, data was not recorded until the appropriate external trigger was received.

- When the trigger was received, the spectrometer collected the user-specified number of data points at the user-specified time-resolution. Any external trigger sent during this time was ignored.

- Once the required number of data points had been collected, the spectrometer reset itself for the next coaddition of data and awaited the next trigger signal.

- If no further co-additions were required at the mirror's current position, it moved to the next position and repeated the above procedure.

As with the pressure data logging and the rapid scan measurements, the magnet-driver signal was used to actuate and synchronise the step-scan measurement. Depending on whether data was collected during a full volume-modulation cycle (which was unnecessary if only the initial molecular responses to the pressure pulse were required) or only during an initial portion of the volume modulation, two scenarios arose. These are now described with reference to Figure 4.6.

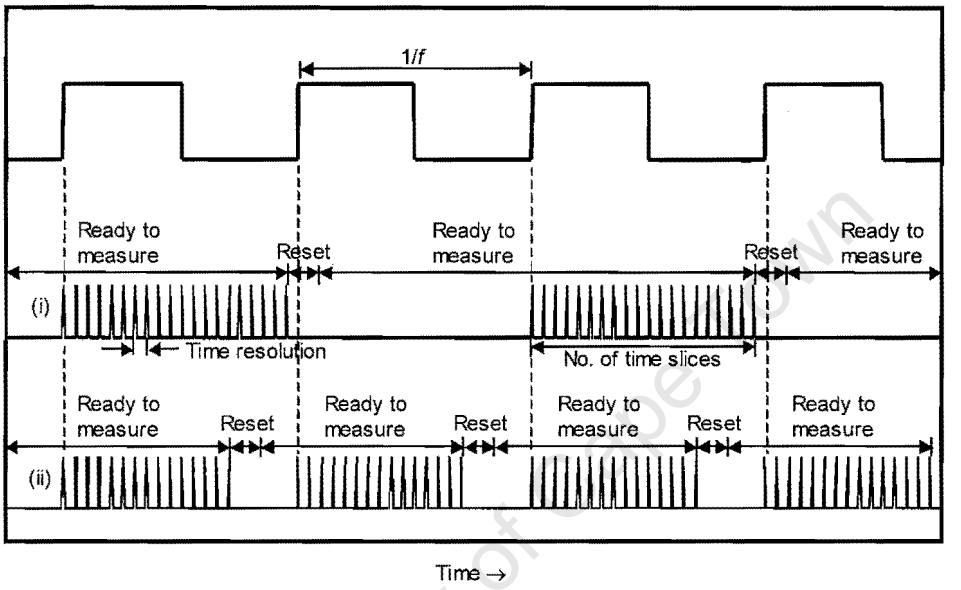

Figure 4.6 - Triggering scheme for step scan measurements. The magnet driver signal activates the measurement pulses only when the spectrometer is not in "reset" (for another coaddition) mode. Thus in (i) scenario 1, when data is taken over the full cycle, measurements can only be taken every second cycle while in (ii) scenario 2, when data is only taken for part of the cycle, measurements can be made on every cycle

In both scenarios, the mirror moved and was stabilized then, when the positive-edge TTL signal was received (i.e. when the volume underwent a step-change), measurements began. In scenario 1, in which data was required over a full cycle, the "number of time slices" and "time-resolution" were specified such that the final data point was taken as the cycle ended (e.g. at a 1 Hz modulation, 1000 data points could be taken with a time-resolution of 1 ms). Then, since the reset time for the next co-addition was not infinitesimally small, the next positive-edge trigger passed while the spectrometer was still resetting. Thus, a whole cycle passed (and was thus "wasted") before the next set of measurements began.

In scenario 2, this problem was avoided since the reset occurred before the cycle ended and thus received the positive-edge trigger at the beginning of the next cycle.

Since the mirror movement and stabilization took 20 ms, the same situation as for the coadditions existed each time the mirror changed position to record the next interferogram point.

Thus, from the number of mirror positions (i.e. number of points in the interferogram) (N_I), and the number of coadditions required (N_A), the number of cycles required (N_C) was,

for scenario 1, $N_C = 2N_I N_A$ (4.12)

and, for scenario 2, $N_C = N_I N_A$ (4.13)

In addition to these two scenarios, there was the possibility of using a second TTL signal from the card at a higher frequency (as described in section 4.7.3). In this way, in combination with appropriate "delay before experiment" inputs, points from some other time in the cycle could be measured.

In sections 4.4.1 and 3.2.2 respectively, it was noted that the number of cycles required (N_C) had implications on the lifespan of the bellows and that the baseline had to be kept stable for the duration of the experiment (t_E). From equations (4.11), (4.12) and (4.13), it is clear that these parameters depend on number of mirror positions (N_I), the number of coadditions (N_A) and the modulation frequency. For the full spectrometer range (7500-370 cm^{-1}) at a spectral resolution of 12 cm^{-1}, N_I = 2591. Thus, with N_A = 10, even for scenario 2 above N_C = 25910 and, at a modulation frequency of 1 Hz, the experiment would take approximately 7 hours. In section 5.7.3, it will be discussed how these excessively high values could be reduced.

4.8 Vacuum system

The various components of the vacuum system are discussed with reference to the overall schematic diagram in Figure 4.1.

4.8.1 Ultra high vacuum pump

The specification for the UHV pump was that it be capable of evacuating the system to less than 10^{-6} mbar. Since the volume of the system was relatively small (see Appendix I), the smallest pump available was used for this purpose. This was a Balzers turbomolecular drag pumping station (model TSU 071 E) which consisted of a mini-turbomolecular-drag pump (model TMU 071 P) with a diaphragm pre-pump (model MVP 015 T) and a display control unit (model DCU 100). The overall unit was rated for 60 l/s of N_2 at 10^{-9} mbar.

These three components were originally mounted on a single baseplate. However, in this format the vibration of the membrane pump caused significant disturbance to the system (e.g. the Baratron pressure gauge was sensitive to excessive vibration). Therefore, the membrane pump was decoupled from the structure and connected to the turbomolecular pump only by flexible tubing.

The turbomolecular-drag pump was fitted with an optional 32 W casing heating unit to accelerate the attainment of final vacuum during start-up and to improve efficiency during operation. This heating unit could only be used in tandem with a water cooling unit which was supplied with water at a temperature of 15°C by an MGW Lauda thermostat. Distilled water was used to prevent deposits on the coolers.

The pump operation as well as the heating unit was controlled by the DCU 100 which was also capable of displaying a pressure gauge output and was thus used to display the sorbate system pressure reading (see section 4.9).

4.8.2 Cryogenic sorption pump

The turbomolecular-drag pump was allowed a maximum fore-vacuum pressure of 10 mbar. During start-up the pressure was initially brought below this level by the diaphragm pump before the turbomolecular pump was started. However, during conventional operation, when the system was opened to replace or remove a sample, rather than switching off the turbomolecular pump, the shut-off valve was merely

closed. Before this valve could be re-opened, the system pressure had to be reduced below 10 mbar.

This was achieved using an MDC cryogenic sorption pump (model SP-150), which consisted of a pump body containing adsorbent material suspended inside a liquid nitrogen dewar. This was capable of evacuating a 20 litre chamber from atmosphere to 1 mbar in less than a minute. When the adsorbent material was saturated, it could be reactivated using a wrap-around bake-out heater.

4.8.3 Vacuum system pressure gauge

The pressure in the vacuum system was monitored at all times using a Balzers Compact Full Range gauge (model PKR 261). This consisted of two separate measurement systems (Pirani and cold cathode), the signals of which were combined to give a uniform output in the range $5x10^{-9}$ to 1000 mbar. The output was displayed on a Balzers SingleGauge vacuum measurement unit (model TPG 251 A).

4.8.4 Tubing, fittings and volume of closed system

CF-flanged nominal bore NW16 or NW35 tubing was used for the system and use was made of flexible couplings where necessary. All-metal angle or straight-line valves were used for isolation.

In the section of the system which was sealed for the closed system experiments, the volume was minimized (see section 2.2.2) by using NW16 nominal bore tubing wherever possible. The volumes of the various components of the closed system are listed in Appendix I, together with the overall closed-system volume as a function of the armature travel distance between the magnets.

To assist with the evacuation of the system, 525 W Isopad heating tapes were used to maintain the tubing and valve temperatures at higher than ambient (50-80°C). The temperature was controlled by a single-setpoint Eurotherm 2132 temperature controller identical to that used for the Baratron heater.

4.9 Sorbate dosing system

The sorbate dosing system is discussed with reference to Figure 4.1. This system was only exposed to the rest of the system when introducing a sorbate. Therefore, it was not necessary for it to be designed for UHV. Thus, apart from the CF flange connecting the dosing valve to the main system, the rest of the components had Cajon, Swagelock or ISO-KF connections. The main components were:

- a two-stage rotary pump (Balzers model DUO 2.5 A) capable of evacuating the system to less than $5x10^{-3}$ mbar;
- a catalyzer trap (Balzers model URB 025), consisting of a heated chamber filled with catalyst pellets, to protect the pump from hydrocarbons;
- a compact Pirani pressure gauge (Balzers model TPR 265) with a range of 10^{-4} to 1000 mbar, the output of which was displayed on the DCU 100 unit (see section 4.8.1); and
- a precision dosing valve (Balzers model UDV 040) with a minimum adjustable gas flow of less than 10^{-9} mbar.l/s.

The procedure for dosing was as follows. The liquid-vapour bulb (or gas bottle) was connected to a ¼" or 1/8" Swagelock port between the dosing valve and the pump isolation valve. The isolation valve was opened to evacuate the whole sorbate system. The isolation valve was then closed and the liquid-vapour bulb valve opened to introduce the sorbate. If necessary, the liquid-vapour bulb valve was closed and the pump isolation valve opened again to flush the system of impurities from previous experiments. If this was not necessary, the system was ready for the dosing valve to be opened to introduce the vapour to the main system.

5. Commissioning and preliminary results

5.1 Objectives and overview of commissioning

The basic aim of commissioning was to put the apparatus into operation and to compare its performance with the original specifications presented in Chapter 4.

5.1.1 Preliminary procedures

Before actual commissioning could commence it was necessary first to perform some preliminary steps. These included verifying the vacuum tightness of the system, eliminating extraneous vibrations, tuning the temperature controllers and aligning the infra-red beam. Since these tasks were trivial and were completed successfully, no further description is necessary.

5.1.2 Main commissioning procedures

As mentioned in Chapter 4, the new apparatus was intended to have three primary functions. These were: (a) the measurement of diffusion coefficients using the frequency response method; (b) the measurement of diffusion coefficients by the sorption rate method using *in situ* FTIR spectroscopy to follow the uptake rate; and (c) the *in situ* measurement, using high time-resolution (rapid-scan and step-scan) FTIR techniques, of the behaviour of molecules on the sample surface during volume modulation.

The first major objective of the commissioning exercise was thus to confirm that the apparatus could perform these three functions successfully. The initial step in the realization of this objective was to ensure that the raw data collected by the apparatus was acceptable.

Frequency response method

Thus, for the frequency response method, the first task was to perform a set of blank experiments (i.e. experiments in which the pressure response to volume modulation was measured in a system containing no sorbent) over the full modulation frequency

range. From this, the quality of the square wave could be evaluated (see section 4.4.3). In addition, the system delays (i.e. the blank experiment phase lags, ϕ_B) and the relative amplitudes of the pressure change in the blank cell (p_B) could be ascertained at each frequency. As explained in section 2.3.2, it was necessary to know these values in order to process the experimental data in the presence of a sorbent. Another purpose of the blank runs was to ensure that the pressure differential was within the range in which isotherm linearity could be assumed.

Thereafter, pressure response data was collected in the presence of a sorbent and, as long as the system was sufficiently sensitive to the modulations at the chosen operating conditions (see section 2.2.2), the frequency response parameters could be determined. This data was then fitted to an appropriate model (see section 2.2) and the diffusion coefficient ascertained.

FTIR spectroscopy

For the FTIR spectroscopy, the first task was to obtain spectra of sorbent samples and to compare these to spectra obtained with the same samples on another spectrometer. Once satisfactory initial spectra had been obtained, sorption rate experiments could be carried out at various pressures, and diffusivities determined using equation (1.15).

Rapid-scan FTIR spectroscopy experiments were used to obtain spectra with high time-resolution and signal-to-noise-ratio. Based on the results of these experiments and for reasons discussed in section 5.7.3, no meaningful step-scan experiments could be performed.

Reproducibility and validity

All the above experiments were carried out several times under similar conditions to assess reproducibility (i.e. whether the results could be reproducibly obtained within acceptable limits of experimental error). In addition, to determine the validity of these measurements, it was necessary to compare the results to those obtained with other instruments in the laboratory and to those that have been reported in literature for similar systems. These two aspects are examined in depth in this chapter and the findings are summarized in section 6.1.

Comparison with specifications

Once it had been ascertained that the apparatus could successfully perform its three primary functions, the second major objective of commissioning was to evaluate its limiting measurement conditions (i.e. the ranges and resolutions at which the various instruments could still record meaningful data) and to compare these to the original specifications presented in Chapter 4. The fulfilment of this objective is referred to, where appropriate, in this chapter, while the findings regarding the more important specifications are summarized in section 6.2.

5.2 Sample characterization

Two H-ZSM5 (HMFI) samples, both supplied by Süd-Chemie AG were used in the experiments described in this chapter. According to the specifications supplied by Süd-Chemie, both of these samples had Si/Al ratios of 45 ($SiO_2/Al_2O_3 = 90$), with the only difference being the crystal size. Nominally, one sample had a particle size less than 0.1 μm and was designated HMFI90-0.1 while the other had a particle size of 0.5-3 μm and was designated HMFI90-3.

NH_3 adsorption experiments in a Setaram TG/DSC-111 microbalance were used to determine acid site concentrations on the two samples. The results obtained were 0.286 mmol/g for HMFI90-0.1 and 0.377 mmol/g for HMFI90-3. Assuming the ideal unit cell formula of $H_xAl_xSi_{96-x}O_{192}$ for H-ZSM5, these corresponded to Si/Al ratios of 57 and 43 respectively, indicating that HMFI90-0.1 had undergone some framework dealumination.

5.2.1 Scanning electron microscopy (SEM)

From sections 2.1.2-2.1.4, it is clear that, to measure the diffusion coefficient, it was necessary to know the size of the particles more accurately than was given in the original specifications. In addition, it was useful to have information on the morphology of the crystals. Thus, scanning electron microscopy (SEM) was performed on the samples. The results are shown in Figure 5.1. From these results it appeared that HMFI90-0.1 actually had a particle size of approximately 0.5 μm while

most of the HMFI90-3 crystals were 3 μm, with a few smaller crystals. In both cases, the crystals appeared to be roughly spherical (i.e. spheroid).

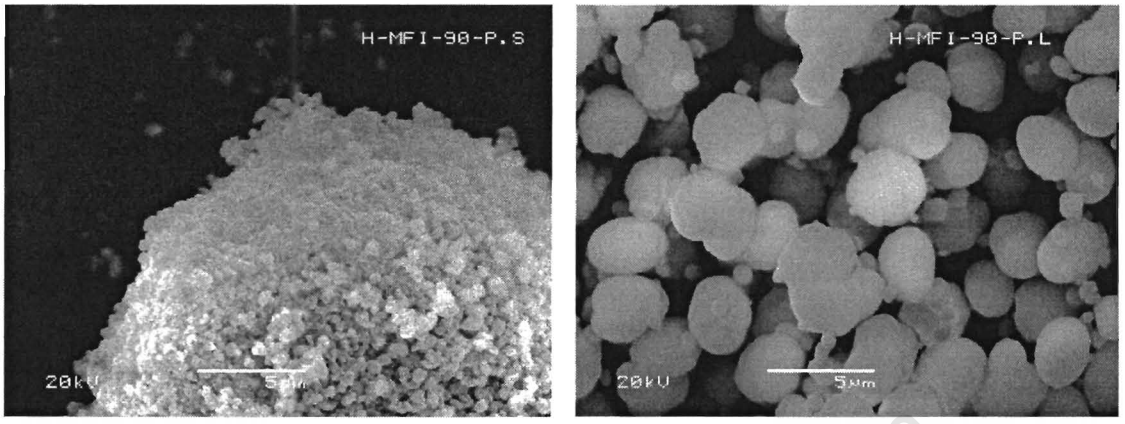

(a) (b)

Figure 5.1 - Scanning electron micrographs of (a) HMFI90-0.1 and (b) HMFI90-3

5.2.2 Equilibrium isotherms

As discussed in section 2.2.2, it was necessary to know the characteristics of the sorbate-sorbent equilibrium isotherm before performing frequency response experiments. This was to: (a) ensure that the experimental conditions were in a range with sufficient sensitivity to volume modulation; and (b) estimate the sample mass required. The same arguments regarding sensitivity applied to the experiments using FTIR spectrocopy.

Another reason for needing the isotherms was for use in the Darken equation, i.e. equation (1.9). As explained in section 1.2, the use of the Darken equation was necessary to correct transport diffusivities for concentration dependence.

Since toluene was used as the sorbate for all experiments and experiments were performed at either 100°C or 130°C, toluene isotherms were measured (on a modified Setaram TG-DSC 111 thermoanalyzer) for the two samples at both of these temperatures. The results are shown in Figure 5.2. Since experiments were performed only at pressures lower than 1.4 mbar, only this region of the isotherms is shown.

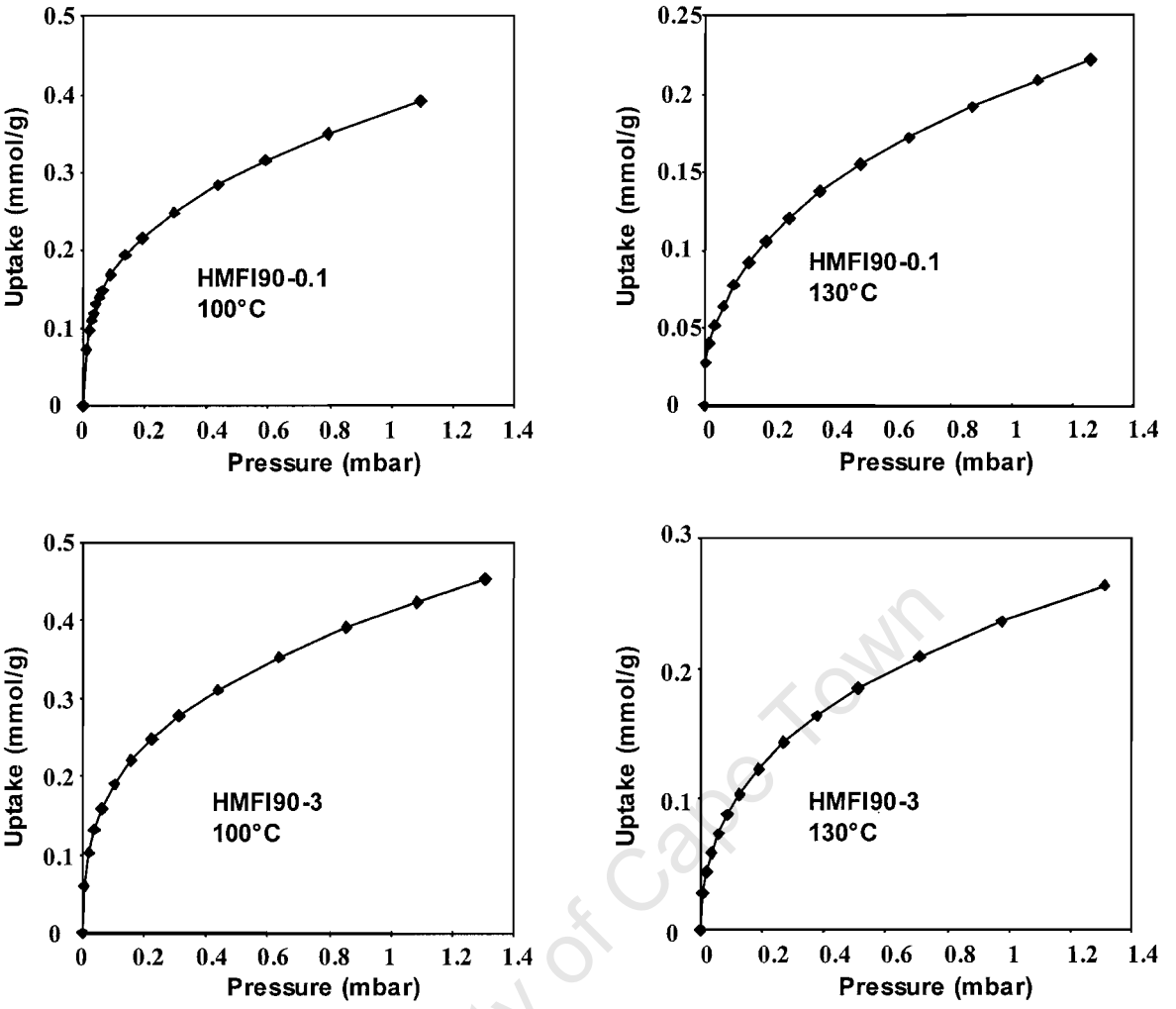

Figure 5.2 – Equilibrium isotherms for toluene on H-ZSM5 (HMFI) samples. The temperatures and materials are shown on the isotherms.

In the pressure range of interest, all four isotherms could be fitted very well using a Freundlich isotherm (Kapteijn et al, 1999)

$$q = bP^n \tag{5.1}$$

where b and n are constants ($n < 1$). The constants for each of the isotherms are given in Table 5.1.

The slopes of these isotherms could then be determined at any operating pressure. Thus, with the assumption that K should be between 0.1 and 1.5 (see section 2.2.2), the mass requirements for experiments at 0.1 and 1 mbar could be estimated from

equations (2.15) and (2.37) and are shown in Table 5.2. These values were calculated assuming a system equilibrium volume of 237 cm^3 (see Appendix I).

Table 5.1 – Constants for use in the Freundlich isotherm, equation (5.1)

		Freundlich constants	
Sorbate	**Temperature (°C)**	*b*	*n*
HMFI90-0.1	100	0.3804	0.3435
	130	0.1992	0.3930
HMFI90-3	100	0.4190	0.3594
	130	0.2433	0.4204

Table 5.2 – Estimated mass ranges for frequency response experiments at different temperatures and pressures

		Pressure (mbar)	
		0.1	1.0
Sorbate	**Temperature (°C)**	**Mass range (mg)**	
HMFI90-0.1	100	1 – 20	6 – 84
	130	2 – 35	9 – 129
HMFI90-3	100	1 – 17	5 – 79
	130	2 – 25	8 – 125

Taking the natural logarithm of equation (5.1) and combining it with equation (1.9), the following relation between transport and corrected diffusivity could be obtained

$$D_0 = nD \tag{5.2}$$

It is interesting to note that, because the isotherms could be represented by the Freundlich equation, the Darken coefficient was not pressure dependent (within the range of interest).

5.3 Blank experiments on the FR apparatus

The first set of blank experiments was performed at a pressure of approximately 1 mbar and a temperature of 100°C. The system was evacuated to less than 10^{-6} mbar then toluene was introduced to a pressure of 1 mbar. Finally, the system isolation valve was closed and the volume modulation set in motion. The magnet spacing was

set at approximately 3 mm to effect a volume change of about 2.5% (i.e. ±1.25%) of the total volume. The experiments were performed with the amplification function of the signal conditioner set at each of its three settings: X1, X0.1 and X0.01 (corresponding to no amplification, 10 times amplification and 100 times amplification respectively). The results of the blank run at a frequency of 0.1 Hz are shown in Figure 5.3.

Although the signal appeared stable at the X1 setting, the noise was clearly in discrete jumps of approximately 0.003 mbar. Since the pressure change between the upward and downward stroke was approximately 0.02 mbar, these discrete jumps represented about 15% of the total pressure change. This indicated that the dynamic range of the signal was too low and a higher amplification was required. At the X0.1 setting, the signal was reasonably stable, although there was some noise at the transition edges. In contrast, at the X0.01 setting, the instability at the transition edge was unacceptable. Many attempts were made to analyse and solve this problem, both within the laboratory and by the manufacturer. These included attaching an oscilloscope directly to the output of the signal conditioner (to exclude the possibility that the A/D converter was causing the problem) and replacing the signal conditioner itself. However, until now, the difficulty has proved insurmountable. Thus, the X0.01 range could not be used under the conditions of rapid pressure transition, seriously limiting the range of operation.

In the initial experiments, the apparatus was set to perform volume modulations over the specified frequency range (0.001-10 Hz). However, it was found that the armature did not respond at frequencies above 4.5 Hz. In addition, as can be seen in Figure 5.4, the quality of the pressure response data at high frequencies was unsatisfactory.

At a modulation frequency of 4.4 Hz (Figure 5.4a), not only was the response not a square-wave but, in addition, the upward and downward strokes were clearly asymmetric. This asymmetry was still strongly evident at a frequency of 2 Hz (Figure 5.4b) but less significant at 1 Hz (Figure 5.4c). The noise accompanying the upward and downward strokes continued to affect the appearance of the square wave significantly, even at lower frequencies (e.g. at 0.5 Hz - see Figure 5.4d). However, it was found that, when experiments were repeated and the frequency response

parameters (ϕ_B and p_B) were determined (using 5 cycles to obtain an average as described in section 2.3.4), these parameters were reproducible at frequencies below 1.3 Hz.

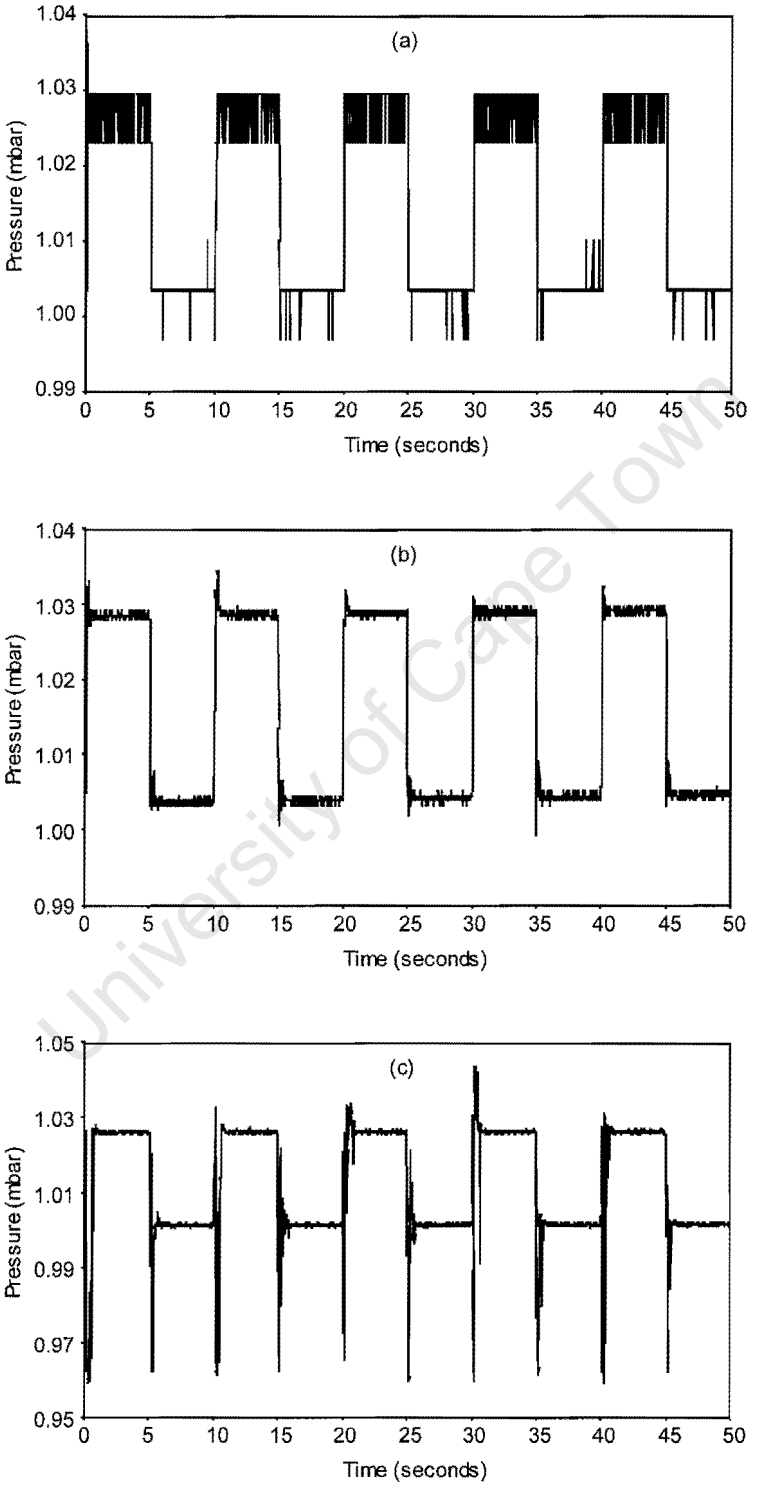

Figure 5.3 - Response of the Baratron pressure transducer (in the absence of a sorbent) to a system volume modulation at a frequency of 0.1 Hz with the range of the amplifier on the signal conditioner set to: (a) X1 (no amplification); (b) X0.1 (10 times amplification); and (c) X0.01 (100 times amplification)

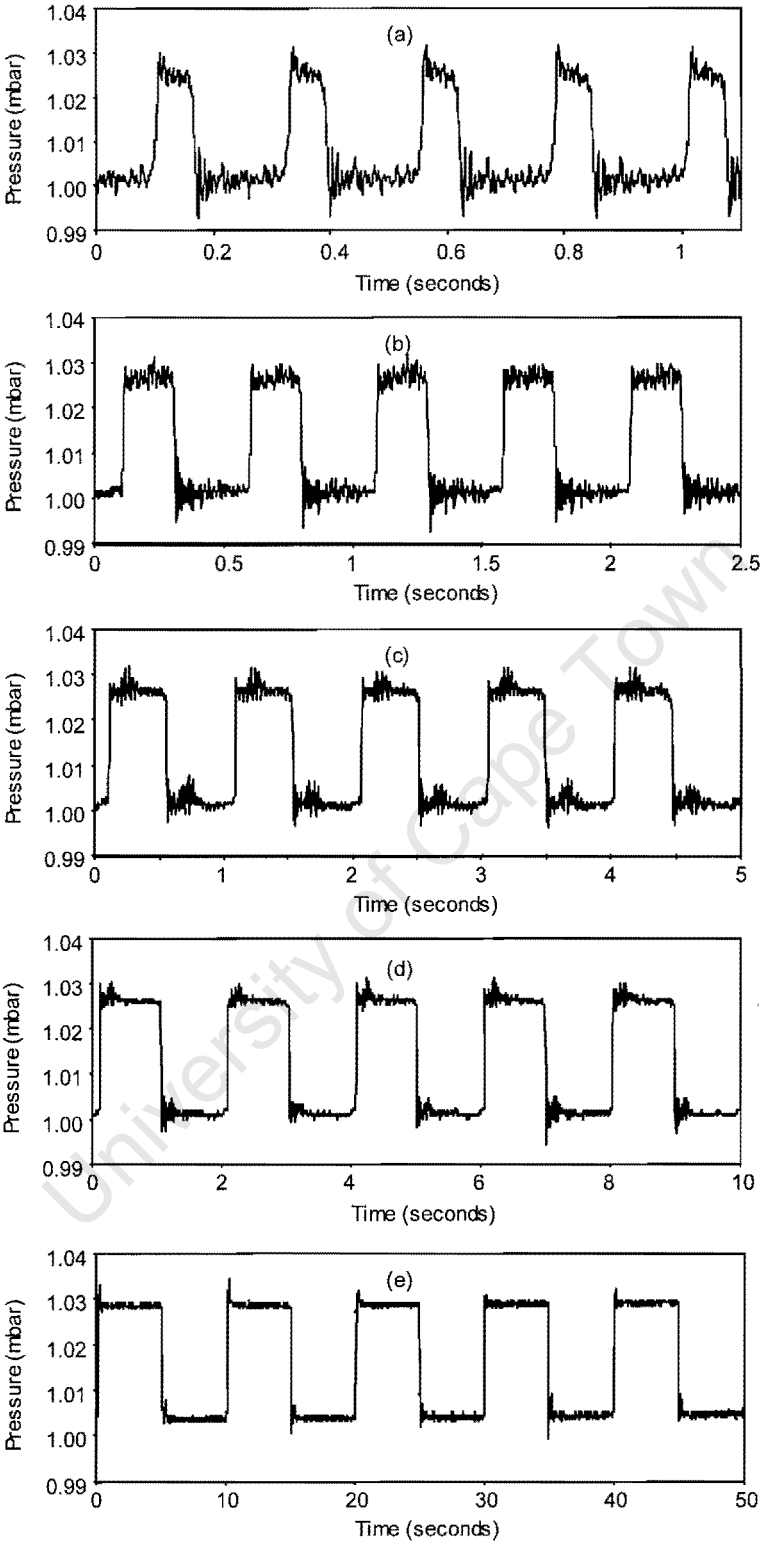

Figure 5.4 - Response of the Baratron pressure transducer (in the absence of a sorbent) to a system volume modulation at frequencies of: (a) 4.4 Hz; (b) 2 Hz; (c) 1 Hz; (d) 0.5 Hz; and (e) 0.1 Hz

Another aspect to be considered was the "squareness" factor (ε) discussed in section 4.4.3. At a modulation frequency of 1 Hz, this factor was found to be 0.97. As discussed in section 4.4.3, values of ε greater than 0.8 were considered acceptable.

Thus, for the reasons discussed above, it was decided to operate the apparatus at modulation frequencies of 1 Hz and below during the remainder of the commissioning exercise.

From Figure 5.4e, it was estimated that the difference in the system pressure when the armature was in its up and in its down positions was 0.025 mbar and the mean operating pressure was 1.016 mbar. Therefore the relative pressure change was 2.4% (or ± 1.2%). According to Rees and Shen (1993), this was a sufficiently small pressure change to be able to assume isotherm linearity and a constant diffusivity. From the equilibrium isotherms in Figure 5.2, it can be confirmed that this was true for the toluene/ H-MFI system at 100 and 130°C.

Another problem was observed in the low frequency (i.e. long time) ranges. From Figure 5.5, it can be seen that, at a modulation frequency of 0.02 Hz, there was a gradual drift in the baseline pressure over time. This was further accentuated at lower frequencies. The following explanation was proposed. Since current flowed through

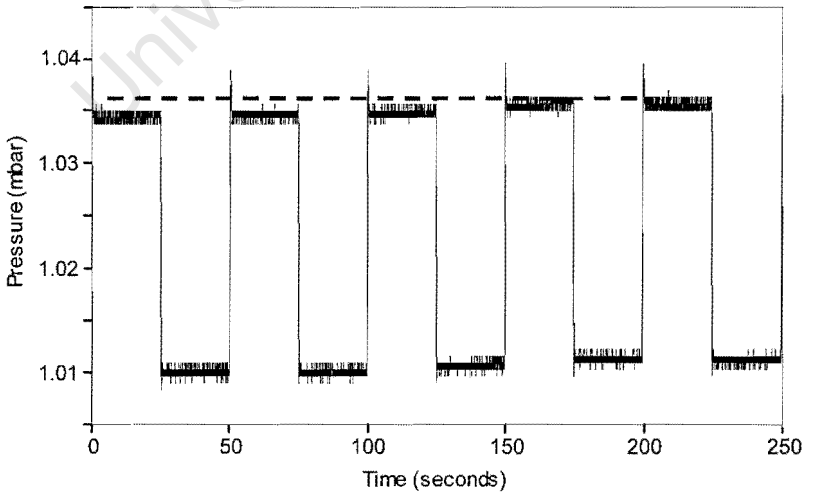

Figure 5.5 - Response of the Baratron pressure transducer (in the absence of a sorbent) to a system volume modulation at a frequency of 0.02 Hz. The dotted line is included to show the extent of the drift in the baseline pressure

the copper wires in the magnet, heat was generated. Thus, when the magnets were in operation for a significant length of time, the temperature of the magnets rose. This, in turn, heated up the bellows and the gas in the bellows and, over a period of time, this led to an increase in the system pressure. This was problematic since, as was pointed out in section 2.3.4, it was essential for the success of the experiment to limit baseline drift. To eliminate this problem, two block water coolers were installed, one in contact with each magnet. These were cooled with water on the same circuit as the turbomolecular-drag pump cooler (see section 4.8.1). After this modification was introduced, the baseline pressure drift was reduced significantly.

A final purpose of the blank experiments was to obtain the phase lags (ϕ_B) and the relative amplitudes of the pressure change (p_B) since these parameters were required for use in equations (2.42) and (2.43). The results of two blank experiments at different temperatures (100°C and 130°C) are shown in Figure 5.6.

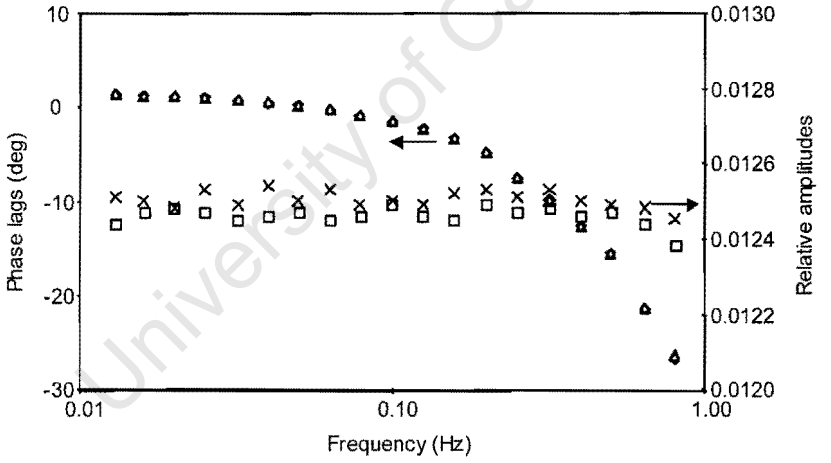

Figure 5.6 – Experimentally determined pressure response parameters (in the absence of a sorbent) for a system volume modulation over a range of frequencies: phase lags at 100°C (◇) and 130°C (△); and relative pressure amplitudes at 100°C (□) and 130°C (×).

As was expected, the phase lags became more negative with increasing frequency (since the system delays became more significant). Theoretically, the phase lags should never be greater than zero. However, the Fourier transform was affected by the noise that accompanied the upward and downward strokes (see Figure 5.4) and thus calculated slightly positive values at low frequencies. However, it is clear from Figure 5.6 that this was at least reproducible, even at different temperatures. Since

these phase lags were to be subtracted from those obtained in experiments in the presence of a sorbent which would experience the same noise effect, these values were considered to be acceptable.

The relative pressure amplitudes were, as expected, approximately constant. However, at the higher temperature, the values were consistently higher. This indicated that, when experiments were performed at different temperatures, new blank experiments would have to be performed at each new temperature.

5.4 Frequency response experiments

The next commissioning step was to perform frequency response experiments in the presence of a sorbent. An appropriate amount of sample (see Table 5.2) in the powdered form was introduced into the secondary cell and held in place by a quartz wool plug. The system was evacuated to less than 10^{-6} mbar and then the sample was activated by heating it to 550°C at the rate of 10°C/min and keeping it at that temperature for 1 hour before returning it to the temperature of the experiment (100°C or 130°C). Thereafter, toluene was introduced to a pressure of approximately 1 mbar, the system valve was closed and volume modulation commenced. Figure 5.7 shows the pressure response to volume modulation at selected frequencies during a successful experiment.

It can be seen that, at the high frequency (1 Hz), the response was similar to that during the experiment in the absence of a sorbent, i.e. the amplitude ratio (p_B/p_Z) (defined in section 2.3.2) was approximately equal to unity and the phase lag (ϕ_Z) was similar to the blank experiment phase lag (ϕ_B), indicating that the diffusion process was significantly slower than the modulation process. At an intermediate frequency (0.013 Hz), the pressure amplitude was reduced, i.e. p_B/p_Z became greater than 1 and a positive phase lag appeared, indicating that diffusion and modulation processes were of a similar order of magnitude (i.e. the time for the system to reach a new equilibrium was similar to the cycle time). At a low frequency (0.0023 Hz), a constant pressure amplitude was established (i.e. p_B/p_Z reached a maximum at some value greater than 1) and the phase lag (ϕ_Z) once again tended to that of the blank

experiment (ϕ_B). This indicated that the diffusion process was significantly faster than the modulation frequency (i.e. the time for the system to reach a new equilibrium became insignificant in comparison to the cycle time).

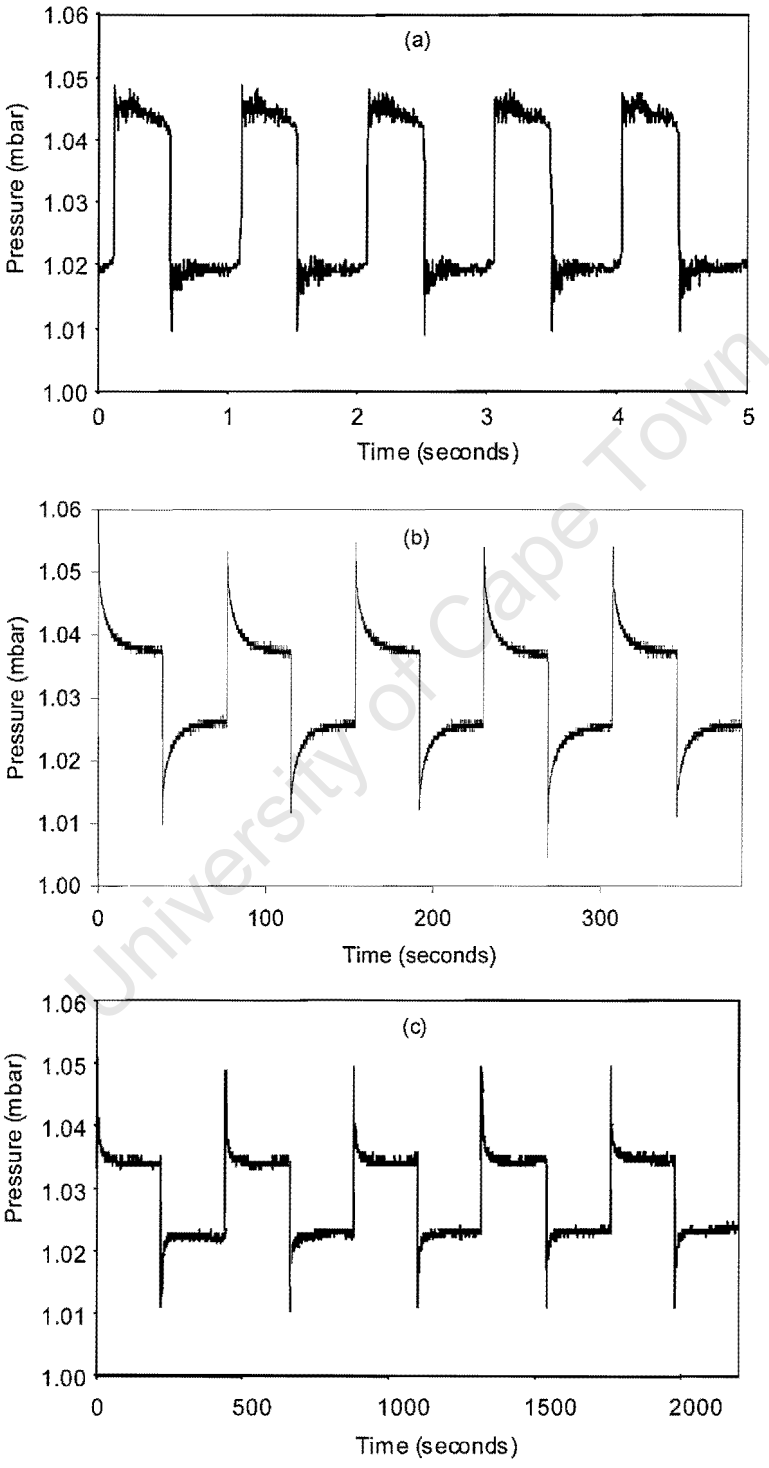

Figure 5.7 - Pressure response (at a base pressure of 1.03 mbar of toluene) to a system volume modulation in the presence of HMFI90-3. Modulation frequencies are: (a) 1 Hz; (b) 0.013 Hz; and (c) 0.0023 Hz. Clearly to be seen are the reduction in amplitude from high to low frequency and the larger phase lag in at intermediate frequency than at high or low frequency

In the initial experiments, however, the trends seen in Figure 5.7 were not observed. As can be seen in Figure 5.8, both the pressure amplitude ratio (p_B/p_Z) and the corrected phase lag ($\phi_{Z\text{-}B}$) (defined in section 2.3.2) showed a continuous upward trend with decreasing frequency.

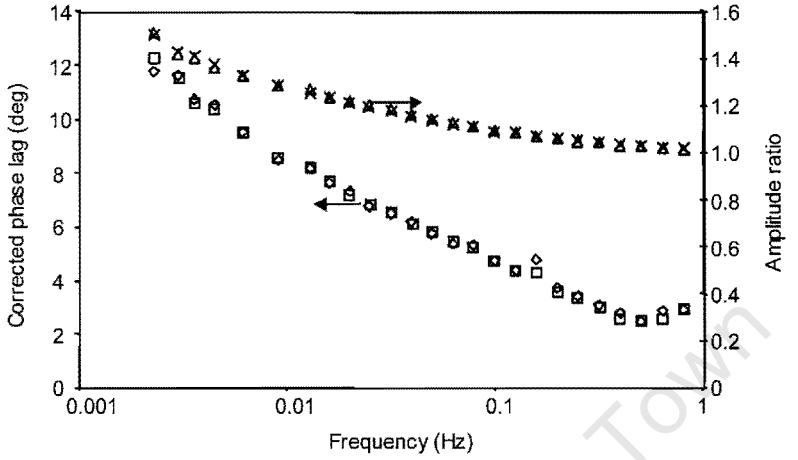

Figure 5.8 – Experimentally determined frequency response parameters for a system in the presence of HMFI90-3 at a base pressure of 0.8 mbar of toluene and a temperature of 100°C: corrected phase lags for experiments 1 (◇) and 2 (□); and pressure amplitude ratios for experiments 1 (△) and 2 (×). No maximum in the phase-lag curve or flattening of the amplitude ratio curve is seen because of bed-depth effects

A recent study (Song and Rees, 2000) has reported an intracrystalline toluene diffusivity in an MFI-material (Silicalite-1) at 100°C of 1.5 x 10^{-12} m^2/s. Even for a diffusivity two orders of magnitude lower than this (i.e. 1.5 x10^{-14} m^2/s), in a 3 μm crystal, the phase lag should show a maximum at approximately 0.01 Hz (see Figure 2.3). Thus, it was recognized that another process was masking intracrystalline diffusion.

These experiments were performed in the secondary cell and, as described in section 4.3, the sample was initially introduced simply by placing it in the bottom of the tube and holding it in position using a plug of quartz glass wool. The bed-depth was approximately 0.5-1 cm. Based on the assertion of Harkness (1999) that particles should be well-dispersed in the quartz wool, it was thus proposed that bed-depth effects (i.e. intercrystalline diffusion) were masking the intracrystalline process. Thus, in the experiments that followed, efforts were made to disperse the sample within the quartz wool plug. The results of a set of such experiments are shown in Figure 5.9.

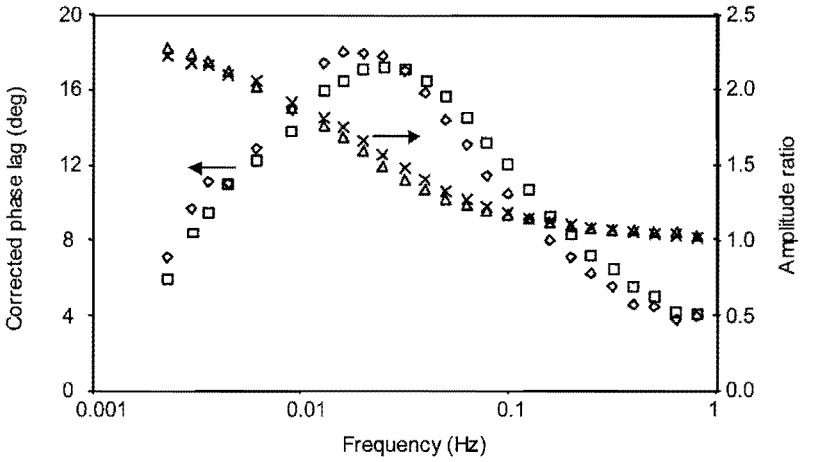

Figure 5.9 - Experimentally determined frequency response parameters for a system in the presence of HMFI90-3 at a base pressure of 1 mbar of toluene and a temperature of 100°C: corrected phase lags for experiments 1 (◇) and 2 (□); and pressure amplitude ratios for experiments 1 (△) and 2 (×). In this case, in contrast to the experiments shown in Figure 5.8, the particles were well-distributed within a quartz wool plug

In this case there was clearly a maximum in the corrected phase lag curve and a flattening in the amplitude ratio curve at low frequencies. Thus, with the particles well-dispersed within the quartz wool, the system was considered satisfactory for use in determining diffusivities. However, before doing this, it was instructive first to compare the experimental data representing the left hand sides of equations (2.42) and (2.43) for the HMFI90-3/toluene system at 100°C and 130°C. This data is shown in Figure 5.10.

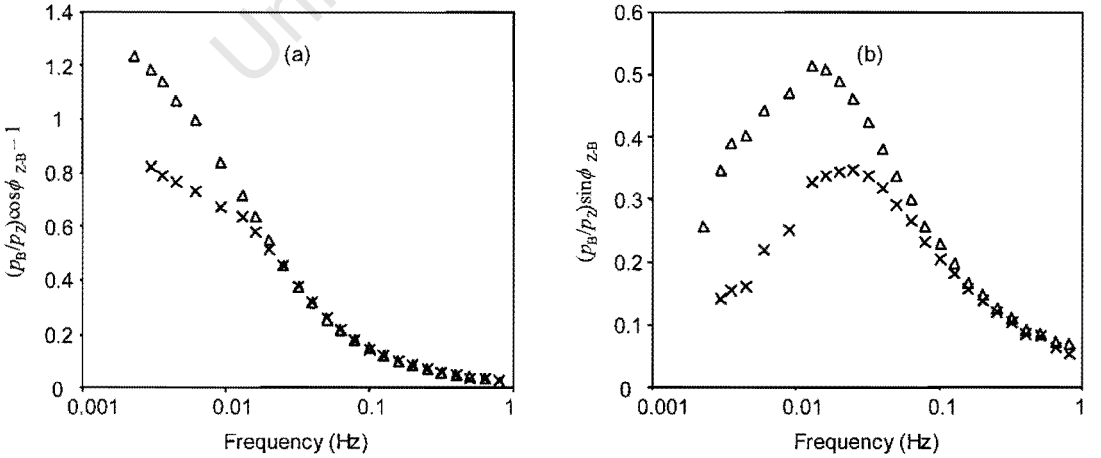

Figure 5.10 - Experimental data representing the left hand sides of (a) equation (2.42); and (b) equation (2.43) for a system in the presence of HMFI90-3 at a base pressure of 1 mbar of toluene and at temperatures of 100°C (△) and 130°C (×)

Firstly, as would intuitively be expected, the data points at 130°C were lower than those at 100°C at the lower frequencies. This was because, at the higher temperature, less toluene was adsorbed on the sorbate (see Figure 5.2). Thus, the gas-phase pressure amplitude was not as much reduced as at 100°C (i.e. p_Z remained closer to p_B). Consequently, p_B/p_Z was higher. Secondly, the peak maximum in Figure 5.10b occurred at a higher frequency at 130°C indicating, as expected, that diffusion was faster at the higher temperature. Finally, from Figure 5.10b, while the curves were smooth at higher frequencies, they both exhibited a kink at lower frequencies, indicating the possible existence of another peak. Thus, the data was fitted not only using a simple single diffusion model but also with more complex models, i.e., models taking into account two-diffusion processes, non-isothermal behaviour, diffusion re-arrangement behaviour and bimodal size distribution (see sections 2.1.4 and 2.2.1). In addition, in all of these cases, the data was fitted using both the isotropic sphere model and the planar sheet model. The results of the curve-fitting can be seen in Figure 5.11 while the parameters determined from the models are shown in Table 5.3.

As can be seen from Table 5.3, the lowest corrected diffusivity obtained from any of the models was 1.45×10^{-15} m^2/s and the highest was 1.0×10^{-14} m^2/s. Thus, regardless of which model was used, the diffusivity determined varied by less than one order of magnitude.

From Figure 5.11, it can be seen that, of the ten models used, the following could be discarded on the basis of a poor curve fit: the simple single diffusion process models in both the isotropic sphere and planar sheet cases; the two diffusion process (isotropic sphere) model; the non-isothermal (planar sheet) model; the diffusion re-arrangement (planar sheet) model and the bimodal size distribution (isotropic sphere) model. However, the remaining four models all had sufficiently good curve-fits to be considered as possibly applicable models. Thus, a closer inspection of the parameters was made to try to distinguish between these models.

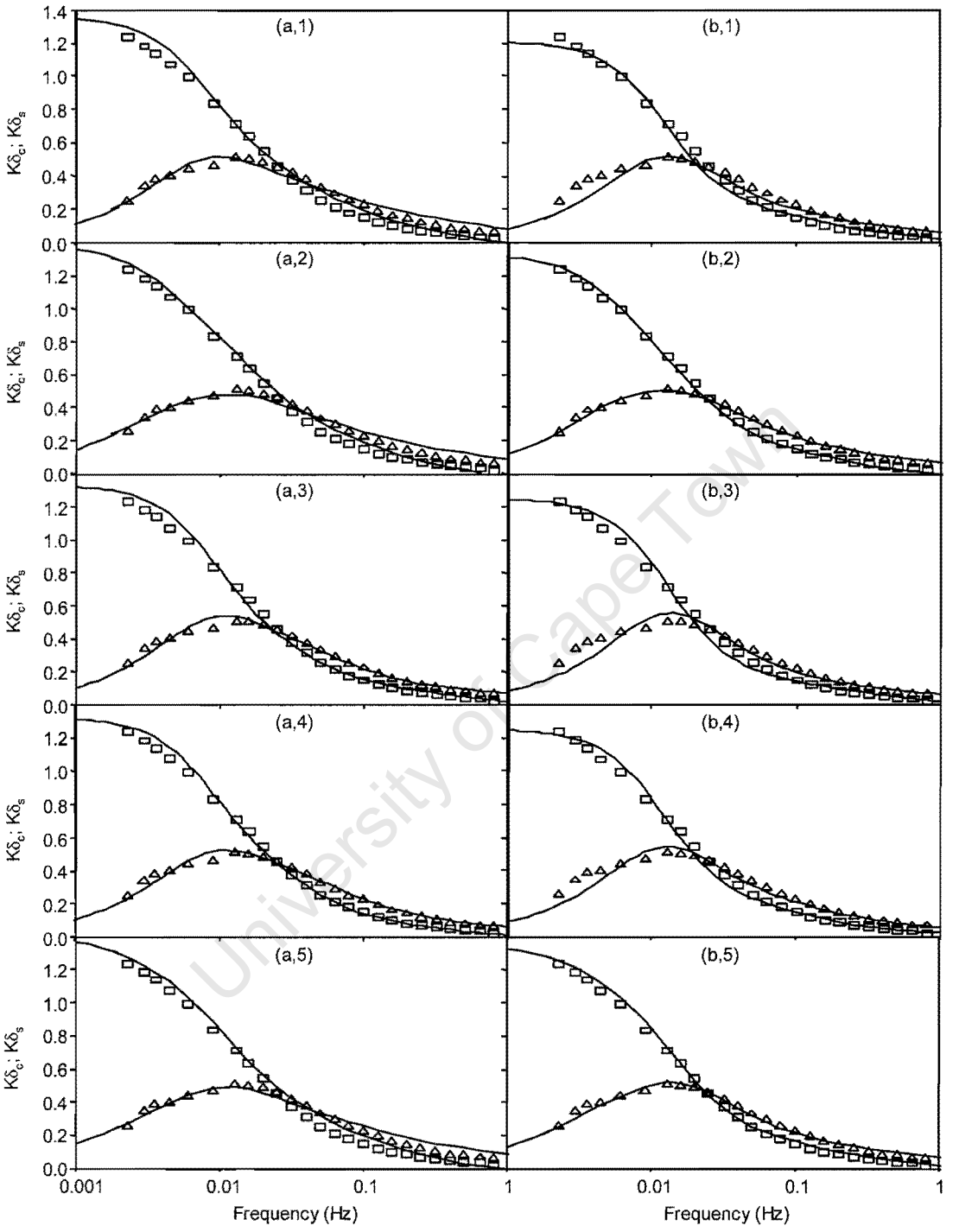

Figure 5.11 - Curve fits of the experimental frequency response data for the HMFI90-3/toluene system at 1 mbar and 100°C using both (a) isotropic sphere and (b) planar sheet models in combination with models for (1) a single diffusion process; (2) two diffusion processes; (3) non-isothermal behaviour; (4) diffusion rearrangment behaviour; and (5) bimodal size distribution. In each case both (□) the in-phase (δ_c) and (△) out-of-phase (δ_s) characteristic functions were fitted. The parameters used in each of these models are shown in Table 5.3.

Table 5.3 – Parameters used to fit models to the frequency response data of toluene on HMFI90-3 at 1 mbar and 100°C

Model		Diffusivity[#] 10^{-15} m^2/s	K	Other Parameters*
Isotropic sphere	Single diffusion process	4.30	1.45	
	Two diffusion processes	7.20	1.50	K_1 = 0.8
		2.15		K_2 = 0.7
	Non-isothermal behaviour	5.40	1.40	t_h = 1 s
				γ = 2
	Diffusion rearrangement	4.65	0.98	t_R = 2.5 s
				K_Ω = 0.40
	Bimodal size distribution	1.45	1.50	$r_{c,1}$ = 1.50 μm (25%)
				$r_{c,2}$ = 0.75 μm (75%)
Planar sheet	Single diffusion process	6.45	1.25	
	Two diffusion processes	10.10	1.40	K_1 = 0.7
		3.25		K_2 = 0.7
	Non-isothermal behaviour	7.90	1.30	t_h = 1.5 s
				γ = 1
	Diffusion rearrangement	6.45	1.05	t_R = 1.0 s
				K_Ω = 0.22
	Bimodal size distribution	2.00	1.40	$r_{c,1}$ = 1.50 μm (25%)
				$r_{c,2}$ = 0.75 μm (75%)

[#] Diffusivities shown are corrected using equation (5.2) and the parameters from Table 5.1.

* Except in the case of the bimodal size distribution model, a crystal diameter of 3μm (i.e., r_c = 1.5 μm) was assumed in all cases.

First, it was necessary to consider equations (2.15) and (2.37). It should be noted that the sample mass initially introduced for this experiment was 83 mg. From previous work, this sample was known to lose approximately 5% of its mass during activation. Thus m in equation (2.37) was approximately 79 mg. From Figure 5.2, $(\partial q/\partial P)_T$ was estimated to be 1.46 x10^{-9} mol.mg^{-1}.Pa^{-1} and, from appendix I, the volume V_e was estimated to be 2.37x10^{-4} m^3. Thus, with T_0 = 373 K and R = 8.314 J.mol^{-1}.K^{-1}, the K-value estimated from the isotherm (i.e. K_{iso}) was 1.51. Of the four models still under consideration, three were fitted using K-values of 1.40 which was reasonably close to

K_{iso}. However, the diffusion re-arrangement (isotropic sphere) model required a K-value of 0.98. Thus this model was also disregarded.

In order to fit the bimodal size distribution (planar sheet) model, a size distribution had to be assumed in which only 25% of the particles had a diameter of 3μm while the remaining 75% had a diameter of 1.5μm. From the SEM micrograph (see Figure 5.1b), it is clear that, while there were some smaller crystals, the majority had a diameter of approximately 3μm. Thus, this model could not be valid.

For the non-isothermal behaviour (isotropic sphere) model, it was necessary to interpret the two parameters (t_h and γ) in terms of their constituent physical properties [see equations (2.29) and (2.30)]. From the data presented in Song and Rees (1997), the specific heat capacity, c, was estimated to be 795 $J.kg^{-1}.K^{-1}$ and, assuming a spherical crystal, the external surface area per unit mass, a_p, 1135 $m^2.kg^{-1}$. Thus for t_h = 1 s, the heat transfer coefficient, h, was estimated to be 0.7 $W.m^{-2}.K^{-1}$. The values found by Song and Rees (1997) were all greater than 15 $W.m^{-2}.K^{-1}$. Thus, the value found in this experiment did not seem reasonable. From Figure 5.2, $(\partial q/\partial T)_p$ was estimated to be 5.83 x 10^{-3} $mol.kg^{-1}.K^{-1}$. Thus, for $\gamma = 2$, ΔH was estimated to be 273 $kJ.mol^{-1}$. Previous calorimetric experiments have found this value to be of the order 100-120 $kJ.mol^{-1}$ (Zheng, 2000). Thus, this value also seemed unreasonable. Therefore, because the parameters required to fit the model were not physically realistic, this model was also discredited.

Finally, the two-diffusion processes (planar sheet) model was investigated. The phenomenon of two separate diffusion processes occurring during toluene diffusion in MFI materials has been reported previously at a similar temperature and pressure and has been attributed to either (i) differences between the diffusion process in the straight channels and that in the sinusoidal channels or (ii) differences in the energy barriers for toluene diffusing with the methyl group in front and with the methyl group behind (Song and Rees, 2000).

As can be seen from Table 5.3, the model used to fit the data had equal K-values, indicating that the distribution of the two diffusion processes was roughly equal. In

the aforementioned study, the two *K*-values of Song and Rees (2000) were also similar.

The SEM micrograph (see Figure 5.1b) showed the particles to be spheroid which mitigated against a planar sheet model. However, since zeolite crystals are well-ordered in each of the three lattice planes, it is quite likely that diffusion can only occur in a linear (i.e. not radial) direction at each face and thus that a planar sheet (rather than an isotropic sphere) model is more appropriate.

For the abovementioned reasons, the two-diffusion processes (planar sheet) model was considered best to represent the HMFI90-3/toluene system. Thus this model was also used to fit the data obtained at 130°C. The results are shown in Figure 5.12.

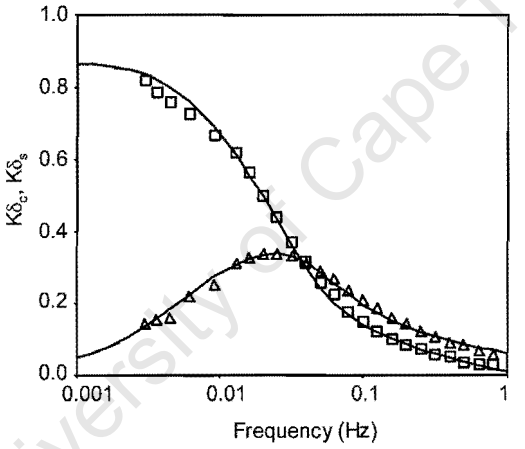

Figure 5.12 - Curve fit of the experimental frequency response data for the HMFI90-3/ toluene system at 1 mbar and 130°C using the two diffusion process (planar sheet) model. Both (□) the in-phase (δ_c) and (△) out-of-phase (δ_s) characteristic functions were fitted. The corrected diffusivities used to fit the data were $D_1 = 1.7 \times 10^{-14}$ m^2/s, $D_2 = 5.0 \times 10^{-15}$ m^2/s, $K_1 = 0.62$ and $K_2 = 0.30$.

The two corrected diffusivities obtained from the curve fit were 1.7 x 10^{-14} m^2/s and 5.0 x 10^{-15} m^2/s and the respective *K*-values were 0.62 and 0.30, giving an overall *K*-value of 0.92. The sample was the same as the one used for the experiment at 100°C (i.e. m = 79 mg). From Figure 5.2, $(\partial q/\partial P)_T$ was estimated to be 8.48 x10^{-10} mol.mg^{-1}.Pa^{-1}. Thus, with $V_e = 2.37 \times 10^{-4}$ m^3, T_0 = 403 K and R = 8.314 J.mol^{-1}.K^{-1}, the *K*-value estimated from the isotherm (i.e. K_{iso}) was 0.95. Thus, the experimental *K*-value was within a reasonable margin of K_{iso}.

It should be noted that the two diffusivity values were closer together than those at 100°C ($[D_1/D_2]_{100°C}$ = 7, $[D_1/D_2]_{130°C}$ = 3.4) and that the first diffusion process was more dominant at 130°C than at 100°C ($[K_1/K_2]_{100°C}$ = 1, $[K_1/K_2]_{130°C}$ = 2.1). These findings were in line with those of Song and Rees (2000) who found that, at a sufficiently high temperature (415K), the data could be fitted using a single diffusion process model (i.e. $K_2 = 0$ in the two diffusion processes model). This was attributed to the fact that, at high temperatures, the differences between the energy barriers in the two channel-types (or between the two toluene orientations) became smaller and thus the two diffusivities more similar.

In the study of Song and Rees (2000), the diffusivities of toluene in Silicalite-1 (assumed to be corrected though not stated as such) was found to be 1.5 x 10^{-12} m^2/s and 1.3 x 10^{-13} m^2/s at 100°C and (by interpolation) approximately 1.7 x 10^{-12} m^2/s at 130°C. Thus, the values found on HMFI90-3 in this study were significantly smaller than these. This could have been caused by one or both of the following factors.

Firstly, the crystal size used by Song and Rees was larger (a cuboid crystal was used with an equivalent diameter of 4.5 μm). As mentioned in section 1.5.5, a dependence of apparent diffusivity on crystal size has been reported previously with lower apparent diffusivities in smaller crystal sizes. This has been attributed to a surface barrier. The idea of a surface barrier was further supported by the fact that there was an intersection in the data for the in- and out-of-phase characteristic functions. According to Yasuda (1991), this would indicate the presence of a "skin" effect.

Secondly, it has been reported that, at least at temperatures below 500K (Choudary and Srinivasan, 1986; Masuda et al, 1998), diffusion of aromatics is impeded by an increase in acidity in MFI-materials. Thus, from Silicalite-1, which has virtually no acidity, to HMFI90-3, with an acid site concentration of 0.377 mmol/g, there could be a marked reduction in diffusivity.

5.5 IR spectra of activated materials

The first important task in the commissioning of the new FTIR spectrometer was the acquisition of a spectrum for activated H-ZSM5 (HMFI) and comparison of this with spectra obtained on another spectrometer. From previous experiments on a Bruker IFS 88 spectrometer, it was known that HMFI90-3 was not transparent in the high frequency range (wavenumbers > 3000 cm^{-1}). Thus HMFI90-0.1 was used for the FTIR commissioning experiments.

Wafers of the material were pressed and introduced into the sample holder of the primary cell. The system was evacuated to less than 10^{-6} mbar and then the sample was activated by heating it to 550°C at the rate of 10°C/min and keeping it at that temperature for 1 hour before returning it to 100°C. An IR spectrum of the wafer was then measured using 30 scans (or coadditions) at a spectral resolution of 4 cm^{-1}.

The data collected on the FTIR spectrometer was reduced and analysed using GRAMS software. First, an absorbance spectrum was obtained (as described in section 3.1.3) using a background spectrum obtained at ultra-high vacuum prior to the introduction of the sample wafer. As proposed in section 1.5.2, the spectrum was then normalised by integrating the lattice vibration overtone bands of HMFI90-0.1 (between 2100 and 1740 cm^{-1}) and dividing by the result. The normalised spectrum is shown in Figure 5.13b. Figure 5.13a shows a similarly normalised spectrum for the same material activated under the same conditions and using the same settings on a different spectrometer (Bruker IFS 88) and in a different vacuum cell. Figure 5.13c shows the difference between these two spectra.

As can be seen, the two spectra had similar bands for the bridging hydroxyl group (3610 cm^{-1}) but the silanol band (3745 cm^{-1}) was about 20% smaller and a new broad band appeared at 3530 cm^{-1}, possibly attributable to nested hydroxyl groups within the pores. The only major difference in the paths of the two IR beams was that, in the new apparatus, there was a set of KBr windows to maintain vacuum in the working compartments of the spectrometer (see section 4.6). Thus to ensure that this was not the cause of a scattering effect, these windows were removed but this had no significant effect.

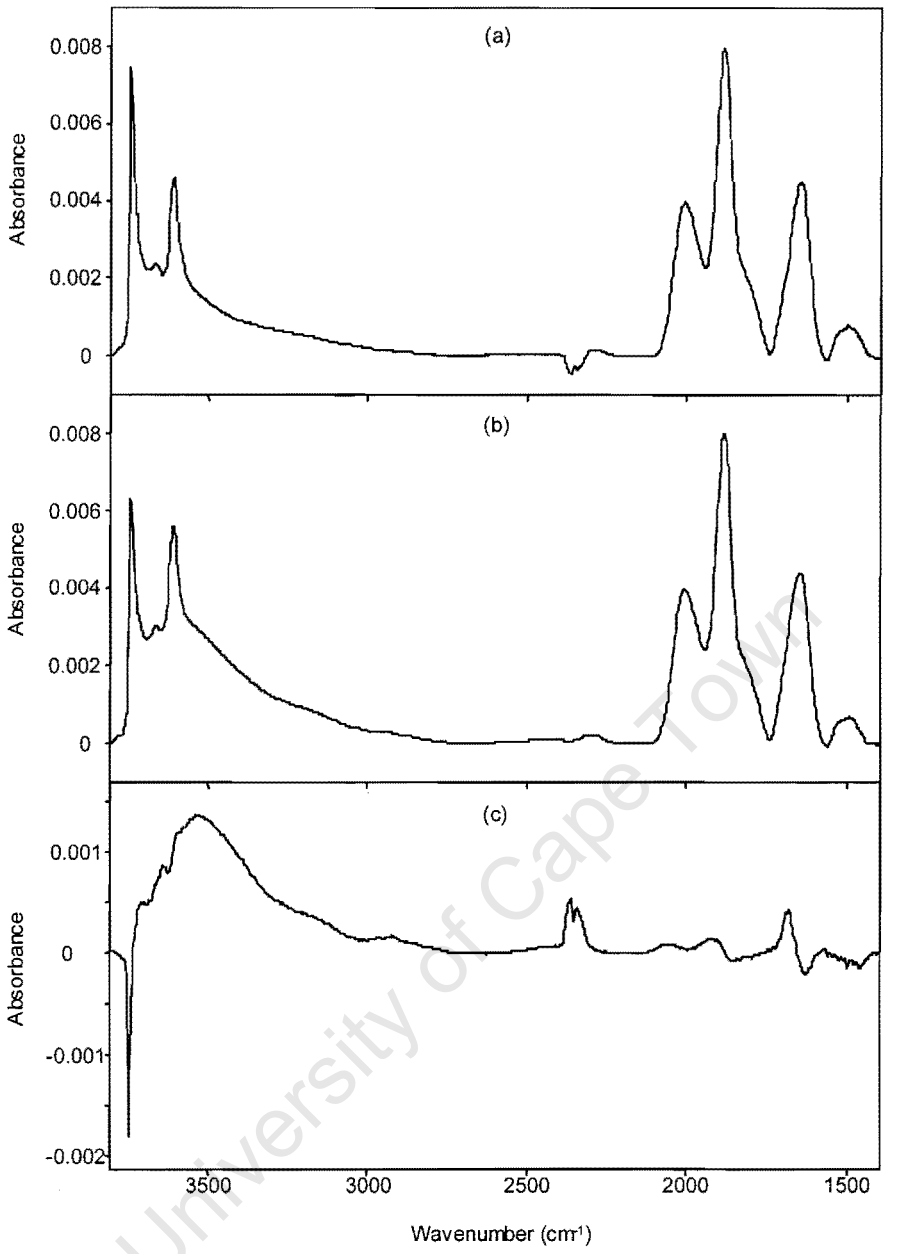

Figure 5.13 – Normalised infra-red spectra (resolution 4 cm^{-1}) recorded for HMFI90-0.1 at ultra high vacuum and 100°C using (a) an existing vacuum cell in a Bruker IFS 88 spectrometer; and (b) the new primary cell in the new Bruker IFS 66 v/S spectrometer with the large (20 mm diameter) sample holder. The difference spectrum between these two, i.e. (a) subtracted from (b), is shown in (c)

A second theory was that the discrepancy was the result of a temperature difference between the two cells, which could cause a difference either in the activation conditions (which could then result in some structural changes in the zeolite) or in the measurement conditions (which could result in a difference in the molar extinction coefficient of the OH stretching bands). A support to this theory was that, when the lattice peaks of HMFI90-0.1 were monitored during activation in the two cells, there were differences in the peak positions at the same apparent temperature. It was

thought that the temperature discrepancy could be due to the large sample holder in the new cell. Thus a new (8 mm diameter) sample holder was constructed.

When the lattice peak positions of HMFI90-0.1 were monitored during activation in the small-diameter sample holder and compared to the peak positions in the existing vacuum cell, the differences, at the same apparent temperatures, were smaller than in the case of the large-diameter sample holder. However, the new sample holder

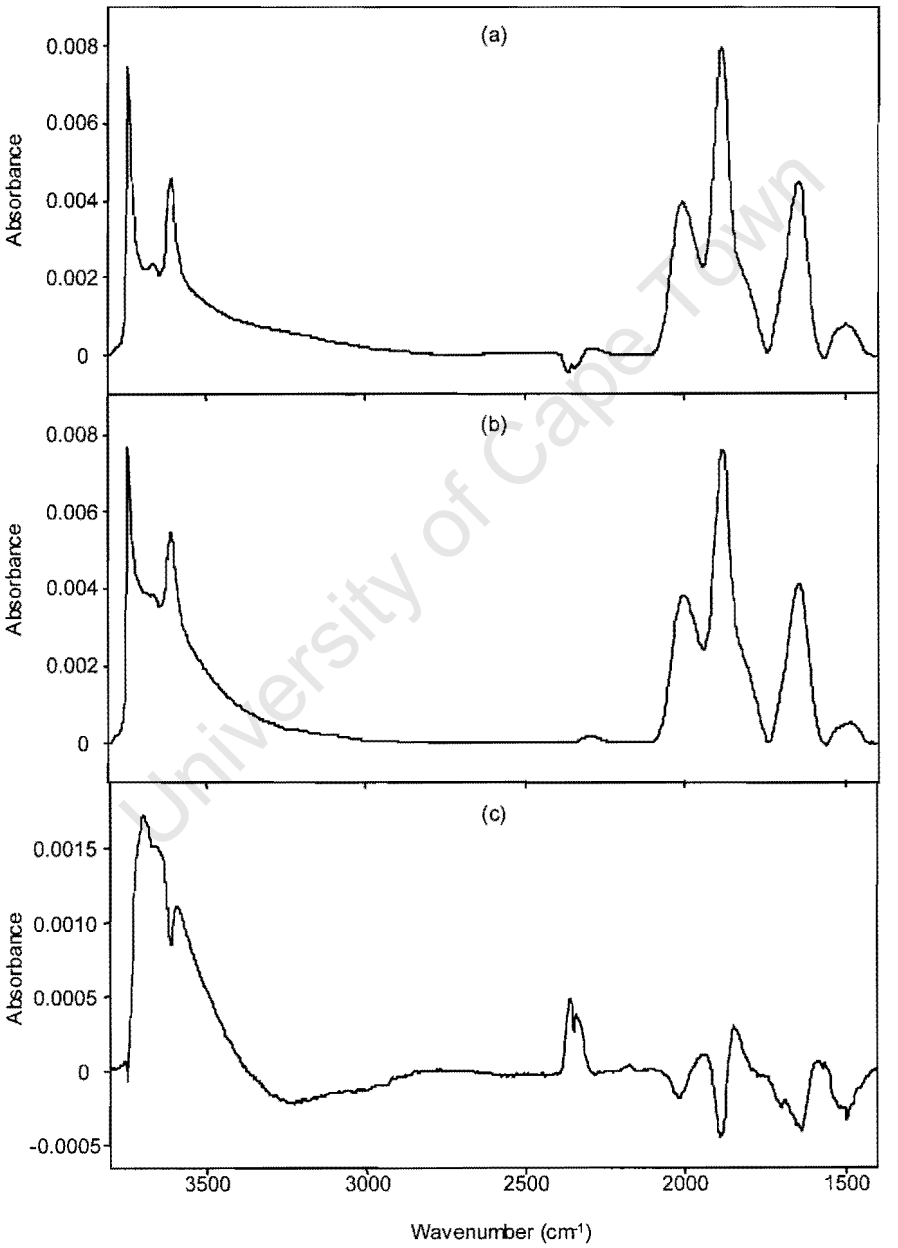

Figure 5.14 – Normalised infra-red spectra (resolution 4 cm^{-1}) recorded for HMFI90-0.1 at ultra high vacuum and 100°C using (a) an existing vacuum cell in a Bruker IFS 88 spectrometer; and (b) the new primary cell in the new Bruker IFS 66 v/S spectrometer with the small (8 mm diameter) sample holder. The difference spectrum between these two, i.e. (a) subtracted from (b), is shown in (c)

seemed to give rise to new spectral discrepancies. An activated HMFI90-0.1 spectrum is shown in Figure 5.14b. For comparison, Figure 5.14a again shows the spectrum recorded on the Bruker IFS 88 spectrometer and Figure 5.14c shows the difference spectrum.

In this case, the silanol bands (3745 cm^{-1}) were similar but the bridging hydroxyl band (3610 cm^{-1}) in the new cell was about 10% smaller than that in the existing vacuum cell. In addition, in the new cell, the broad band at 3530 cm^{-1} had been replaced by a new asymmetric broad band at 3700 cm^{-1}. Until now, no explanation has been found for this and it was decided that, since the bridging hydroxyl sites were of more interest than the silanol groups, the large-diameter sample holder was preferable for the following experiments.

5.6 Toluene sorption rates (using FTIR spectroscopy)

The experimental procedure for measuring the uptake rate of toluene on HMFI90-0.1 was as follows. After the sample was introduced, activated and brought to a temperature of 100°C as described in section 5.5, the valve to the turbomolecular pump was closed and toluene was admitted as rapidly as possible to the required pressure via the dosing valve. Simultaneously with the commencement of toluene admission, the recording of spectra on the FTIR spectrometer was begun. The spectral resolution was set at 4 cm^{-1} and the frequency with which spectra were recorded was based on experience of previous experiments (and refined as experience was gained on the new apparatus). The pressure was maintained at a constant value by manually adjusting the dosing valve and the experiment lasted until it was clear, from the time-resolved transmission IR spectra, that the system had reached equilibrium at the new pressure. Two experiments, with each experiment repeated three times, were performed: one with a zero to 0.1 mbar pressure step and the second with a zero to 1 mbar pressure step.

The data collected on the FTIR spectrometer was reduced and analysed using GRAMS software. Absorbance spectra were obtained and normalised as described in section 5.5. Thereafter, difference spectra were obtained by subtracting the normalised spectrum of the activated sample from the normalised uptake spectra. The

toluene uptake curve ($A_t - A_0$ vs. t; see section 1.5.4) was acquired by integrating the toluene ring vibration band (between 1508 and 1482 cm^{-1}) of the time-resolved difference spectra. This curve was normalised by dividing by the equilibrium uptake amount ($A_\infty - A_0$). Finally, the diffusion coefficient was ascertained, using equation (1.15), by plotting the normalised uptake against $t^{1/2}$ and obtaining the slope of the initial part of the curve. It should be noted that, following the example of Mirth and Lercher (1991), the portion of the curve between normalized uptakes of 0.3 and 0.8 was used. Note also that, in accordance with the discussion in section 1.5.4, the time delay before the commencement of uptake was subtracted before equation (1.15) was plotted.

The key steps in the above procedure are illustrated in Figure 5.15 for one of the experiments with a zero to 0.1 mbar pressure step. The results of the experiments are shown in Table 5.4.

Table 5.4 – Toluene diffusivities in HMFI90-0.1 at 100°C determined from toluene sorption rate experiments using time-resolved FTIR spectroscopy to follow the uptake

Pressure step	**mbar**	0 to 0.1				0 to 1.0			
Diffusivity*	**10^{-17} m^2/s**	2.77	2.44	2.57	5.81	9.01	9.85	10.10	11.90

* Diffusivities uncorrected (since they are compared to uncorrected diffusivities in the text)

For each pressure step, the diffusivities determined were the same within a reasonable error margin (i.e. less than half an order of magnitude). When similar experiments were performed on the HMFI90-0.1/toluene system using the Bruker IFS 88 spectrometer and a carrier gas in a flow cell rather than a vacuum system, the diffusivity (uncorrected) obtained using a 0 to 1 mbar pressure step at a temperature of 100°C was 5.2 x 10^{-17} m^2/s (Zheng, 2000). Thus, the value obtained using a different instrument and cell was the same within half an order of magnitude, with the discrepancy probably attributable to a small temperature difference.

When Karge and Nießen (1991) investigated an H-ZSM5/benzene system at 122°C using the sorption rate of benzene monitored by FTIR, they found (with a 0 to 1.15 mbar pressure step) an uncorrected diffusivity of 5.7 x 10^{-14} m^2/s, i.e. almost three orders of magnitude higher than in this study.

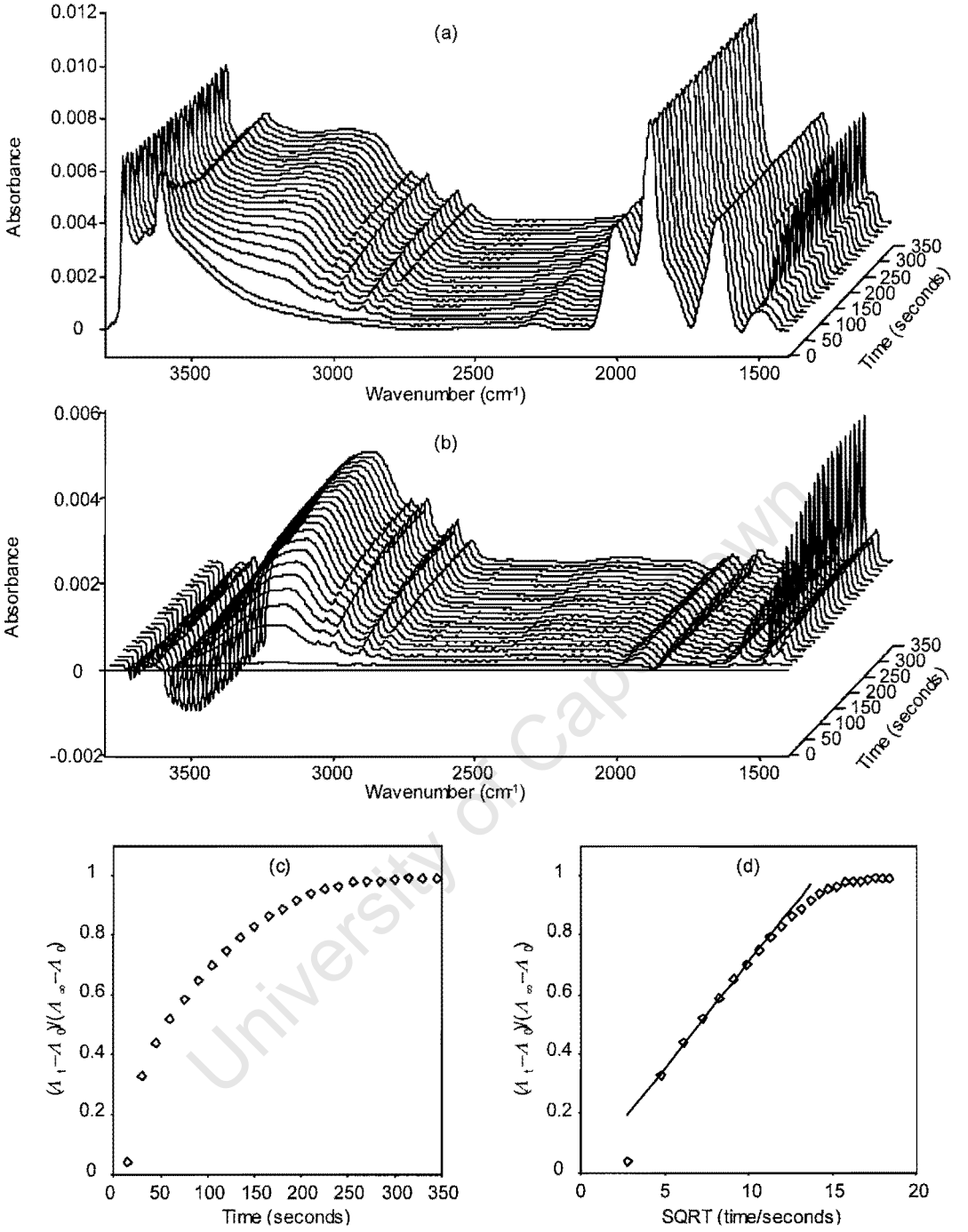

Figure 5.15 - The key steps in determining the diffusion coefficient from the sorption rate of toluene on HMFI90-0.1 for a 0 to 0.1mbar pressure step at 100°C. (a) Normalized time-resolved infra-red spectra (resolution 4 cm^{-1}) of toluene uptake on HMFI90-0.1. (b) Time-resolved difference spectra of toluene uptake on HMFI90-0.1, i.e. the spectrum of the activated zeolite subtracted from the spectra in (a). (c) Normalized toluene uptake rate obtained by plotting the integrated toluene band (1508-1482 cm^{-1}) , divided by the equilibrium uptake, against time. (d) Plot of normalized toluene uptake against $t^{1/2}$, i.e. equation (1.15) or the "square root law". The solid line shows the slope of the initial part of the curve, from which the diffusion coefficient is ascertained

While the higher temperature may have played some role, the primary reason for this major discrepancy was probably the crystal size (the crystals used in the study of Karge and Nießen had an equivalent diameter of approximately 6 μm compared to the 0.5 μm in this study). On a different system (methane in chabazites), Kärger and Caro (1977) found up to a four orders-of-magnitude difference between apparent diffusivities measured in small and large crystals, an observation they attributed to a surface barrier. Similarly, the low diffusivity of toluene in HMFI90-0.1 was thus attributed to a surface barrier.

From Table 5.4, it can be seen that the diffusivities determined using the 0 to 0.1 mbar pressure step were approximately half an order of magnitude lower than those ascertained using the 0 to 1 mbar pressure step. This highlighted two potential drawbacks of this type of experiment. Firstly, it was possible that the two diffusivities should have been the same and were not because the pressure step was so large that the non-linearity of the isotherm had an impact on the analysis of the results, i.e. equation (1.15) was not applicable. Secondly, it was possible that diffusivity actually did increase with adsorbed concentration. However, this would also render the results incorrect since, in such a pressure step experiment, the adsorbed concentration changes over time from the initial to the final value. Thus, if the diffusivity is concentration-dependent, only an average diffusivity is ascertained. Thus, the pressure step should be as small as possible, e.g. to determine the diffusivity of toluene at 1 mbar (and the equivalent adsorbed concentration), a pressure step from 0.9 mbar to 1 mbar would be preferable. As mentioned previously, this is one advantage of the frequency response method over the classic sorption rate methods: it measures diffusivity over a negligibly small concentration range.

5.7 High time-resolution FTIR spectroscopy

The final of the three primary functions to be commissioned was high time-resolution FTIR spectroscopy. Before rapid scan experiments could be performed, however, it was necessary to ascertain the number of coadditions (or scans) that would be required per spectrum to attain acceptable signal-to-noise-ratio (SNR) at each pressure. This parameter was determined under static conditions.

In the frequency response method, a small (< 2.5%) volumetric change was necessary to eliminate non-linearity and limit thermal effects. These issues were not of primary concern in the commissioning of the FTIR spectrometer and thus, for convenience, the spacing between the magnets for the volume modulation was increased to 10.5 mm. Since the secondary cell and an accompanying elbow were removed for these experiments, the volume change was approximately 8% of the total volume.

It should be noted that the required number of coadditions for acceptable SNR was a function of the change in the adsorbed concentration. This, in turn, depended (a) on the percentage volume (and hence pressure) change and (b) on the position on the equilibrium isotherm, i.e. on the pressure, the temperature and the particular sorbate-sorbent system under investigation. Thus, the parameters found in this study should not be used universally and new parameters should be ascertained for each new system and for each new magnet spacing.

5.7.1 Single-step difference spectra

The introduction and activation of the wafer of HMFI90-0.1, and the introduction of toluene to the desired pressure were performed as described in section 5.5 and 5.6. All experiments were performed at 100°C. Spectra were collected with a spectral resolution of 8 cm^{-1}. At each pressure (0.01, 0.1 and 1 mbar) the following procedure was performed. With the magnet system activated so that the volume was at its minimum, the system was allowed to reach equilibrium. Several spectra were then recorded, using a different number of coadditions (1, 10, 30, 100, 300, 1000) for each spectrum. The magnet polarity was then reversed to effect a stepwise change to the maximum volume. Once the system had been allowed to re-equilibrate, spectra were again recorded using a different number of coadditions for each spectrum.

The spectra were processed as described in section 5.5 and then, for each pair recorded using a certain number of coadditions, the spectrum recorded at the minimum volume was subtracted from the spectrum recorded at the maximum volume. The results, at selected coaddition counts, are shown in Figures 5.16, 5.17 and 5.18 for 0.01, 0.1 and 1 mbar respectively.

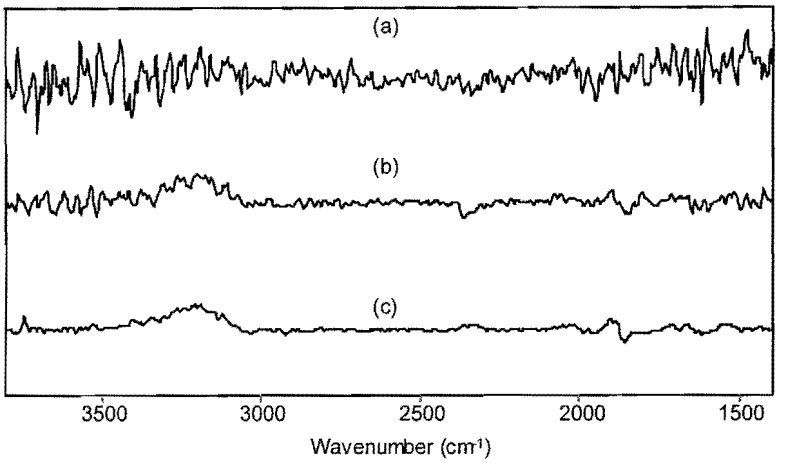

Figure 5.16 - Normalized difference infra-red spectra (resolution 8 cm^{-1}) of toluene adsorbed on HMFI90-0.1 at 100°C and 0.01 mbar using (a) 10, (b) 100 and (c) 1000 spectral coadditions. The difference spectra were obtained by recording a spectrum at equilibrium, effecting a stepwise increase in volume, allowing the system to re-equilibrate, recording a second spectrum and then subtracting the first spectrum from the second. The volume change was approximately 8% of the total volume

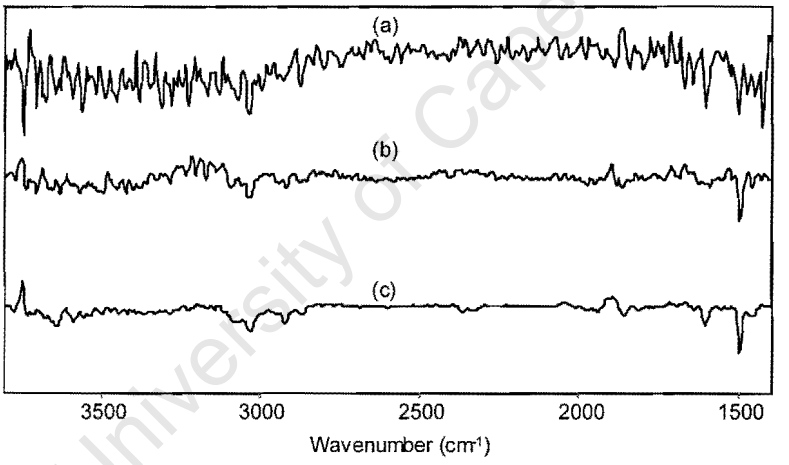

Figure 5.17 - Normalized difference infra-red spectra (resolution 8 cm^{-1}) of toluene adsorbed on HMFI90-0.1 at 100°C and 0. 1 mbar using (a) 10, (b) 100 and (c) 1000 spectral coadditions. The difference spectra were obtained as described in the caption to Figure 5.16

From Figure 5.16, it is clear that, at 0.01 mbar, the SNR was too low at coaddition counts of both 10 and 100. Only with 1000 coadditions did the SNR appear acceptable. At this number of coadditions, the positive silanol band at 3745 cm^{-1} (indicating a desorption from silanol groups) could be clearly observed. However, a negative toluene ring vibration band at 1495 cm^{-1} (indicating the expected desorption of toluene) was hardly visible, indicating that the SNR may still have been too low. An unexplained broad band appeared in the 3200 cm^{-1} region.

From Figure 5.17, it can be seen that, at 0.1 mbar, the SNR was clearly too low at 10 coaddition counts. At 100 coaddition counts, there was still significant noise, particularly in the high frequency range (thus obscuring the silanol band at 3745 cm^{-1}) but certain features of the spectrum were still clearly recognizable, e.g. the negative toluene ring vibration band at 1495 cm^{-1} and the negative C-H stretching bands in the 3000 cm^{-1} region. At 1000 coaddition counts, most spectral features were clearly discernable, though the negative bridging hydroxyl band at 3610 cm^{-1} was still partially obscured by noise.

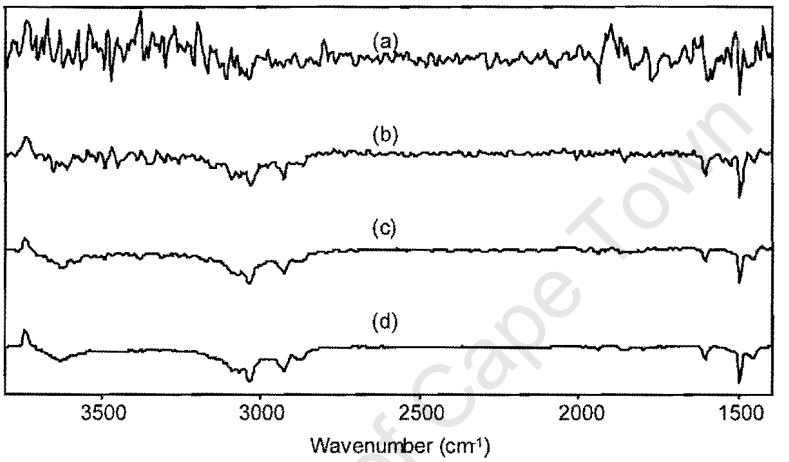

Figure 5.18 - Normalized difference infra-red spectra (resolution 8 cm^{-1}) of toluene adsorbed on HMFI90-0.1 at 100°C and 1 mbar using (a) 1, (b) 10, (c) 100 and (d) 1000 spectral coadditions. The difference spectra were obtained as described in the caption to Figure 5.16.

From Figure 5.18, it is clear that, at 1 mbar, a single scan was not sufficient to achieve acceptable SNR. However, at 10 coaddition counts, the principal spectral features were visible. Using 100 coadditions, the principal features were clearly resolved with the exception again of the negative bridging hydroxyl band. When 1000 coadditions were used, this band was clearly discernable, though not a sharp as might have been expected.

Thus, depending on the purpose of a future study, the following number of coadditions would be required at each pressure: 10-100 at 1 mbar, 100-1000 at 0.1 mbar and 1000 or more at 0.01 mbar. The reason for the increasing number of counts required at lower pressure was that, while the isotherm was steeper at lower pressures, the pressure change induced by the volume change was reduced by a larger factor and

thus the overall sensitivity of the adsorbed concentration to the volume change was smaller. This could also be deduced by differentiating equation (5.1) to give

$$\Delta q/\Delta P \approx \mathrm{d}q/\mathrm{d}P = nbP^{n-1} \tag{5.3}$$

and

$$\Delta q \approx nbP^{n-1}(\Delta P) \tag{5.4}$$

Considering two experiments, with the second at a higher pressure than the first, i.e.,

$$K_R P_1 = P_2 \text{ where } K_R > 1 \tag{5.5}$$

then

$$K_R(\Delta P)_1 \approx (\Delta P)_2 \tag{5.6}$$

Thus,

$$(\Delta q)_1 \approx nbP_1^{n-1}(\Delta P)_1 \tag{5.7}$$

and

$$(\Delta q)_2 \approx nbP_2^{n-1}(\Delta P)_2 = nbP_1^{n-1}(\Delta P)_1(K_R)^n \tag{5.8}$$

Therefore,

$$(\Delta q)_2/(\Delta q)_1 \approx (K_R)^n \tag{5.9}$$

Thus, since $K_R > 1$ and $n > 0$, $(\Delta q)_2 > (\Delta q)_1$. Note that, while this treatment was applied to a Freundlich isotherm, the same would apply for all except extremely rectangular isotherms.

It was pointed out above that the number of coadditions required would have to be ascertained for each new magnet spacing. However, by noting that SNR is proportional to ΔV (assuming an approximately linear isotherm within the range of variation) and to the square root of the number of coadditions (see section 3.1.4), one could predict the number of scans required for each new magnet spacing by

$$(N_A)_P = (N_A)_R [(\Delta V)_R/(\Delta V)_P]^2 \tag{5.10}$$

where $(\Delta V)_R$ and $(\Delta V)_P$ are the volume changes in the reference experiment and in the proposed experiment, respectively, and $(N_A)_R$ and $(N_A)_P$ are the required number of coadditions determined in the reference experiment and predicted for the proposed experiment, respectively.

5.7.2 Rapid scan experiments

Before describing the rapid scan experiments, it is necessary to point out a speed limitation. While the specification of the scanner speed (see section 4.6) was 100 scans/second, this could not be achieved for this experiment for two main reasons. Firstly, a spectral resolution of 8 cm^{-1} was used (rather than the 12 cm^{-1} on which the specification was based). Secondly, the specification was for a standard DLATGS detector. Because an MCT detector was used, a linearity correction had to be made. This, in turn, required the phase resolution to be adjusted so that the number of phase interferogram points was greater than 500 (Bruker, 1995). The net result of these two factors was that the maximum scanner speed that could be attained was 20 scans/second.

Based on the analysis of the single-step difference spectra, rapid scan experiments were performed (at 100°C) at pressures of 0.1 mbar and 1 mbar, using 1000 and 100 coadditions per spectrum respectively. A volume modulation frequency of 0.025 Hz (i.e. 40 seconds/cycle) was used and spectra were collected at a time-resolution of 0.5 seconds (i.e. 2 spectra per second).

Thus, for the 0.1 mbar experiment, the procedure was as follows. The introduction and activation of the wafer of HMFI90-0.1, and the introduction of toluene to the desired pressure were performed as described in section 5.5 and 5.6. Thereafter, the system isolation valve was closed and volume modulation was started. After an appropriate stabilization delay, the collection of spectra commenced. Since the time-resolution was 0.5 seconds and the scanner speed was 20 scans/second, only 10 scans could be collected within each time-frame per cycle. Since 1000 scans per spectrum were required, it was thus necessary to coadd scans from 100 successive cycles as described in 4.7.3. The same applied to the experiment at 1 mbar except that only 10 cycles were necessary (since only 100 scans per spectrum were required).

The results of these experiments are shown in Figure 5.19. These spectra were obtained in the same way as those of the single-step spectra, with the first spectrum used as the reference (i.e., each spectrum had the first one subtracted from it) to obtain the set of difference spectra.

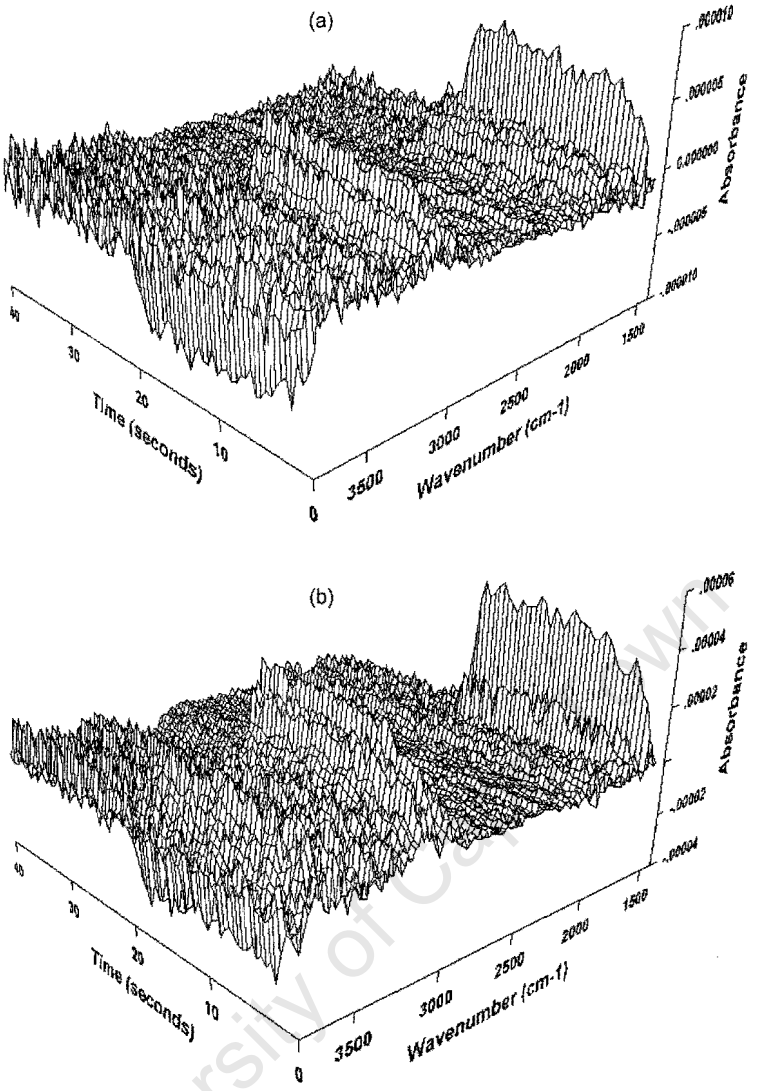

Figure 5.19 – Normalized difference infra-red spectra (resolution 8 cm^{-1}) showing the response of toluene adsorbed on HMFI90-0.1 at 100°C and (a) 0.1 and (b) 1 mbar to a volume modulation at 0.025 Hz. The volume modulation is approximately 8% of the total volume. The difference spectra were obtained by subtracting the spectrum at time zero from the time-resolved spectra, which were collected in the rapid scan FTIR mode.

The spectra contained more noise than their counterparts in the single step experiments. This was to be expected, partly because of real fluctuations in the dynamic case and partly because of baseline drift during the experiment. However, in both cases, the principal features of the spectra (i.e. O-H stretching of the silanol groups at 3745 cm^{-1}, C-H stretching of toluene in the 3000 cm^{-1} region, and toluene ring vibration at 1495 cm^{-1}) were clearly visible with, as expected, the bands larger in the 1 mbar case. As seen in the single-step experiments, the volume modulation did not have a strong effect on the bridging hydroxyl (or Bronsted) groups (3610 cm^{-1}).

To further investigate this observation, the integrated toluene, silanol and Bronsted bands were plotted against time as can be seen in Figure 5.20.

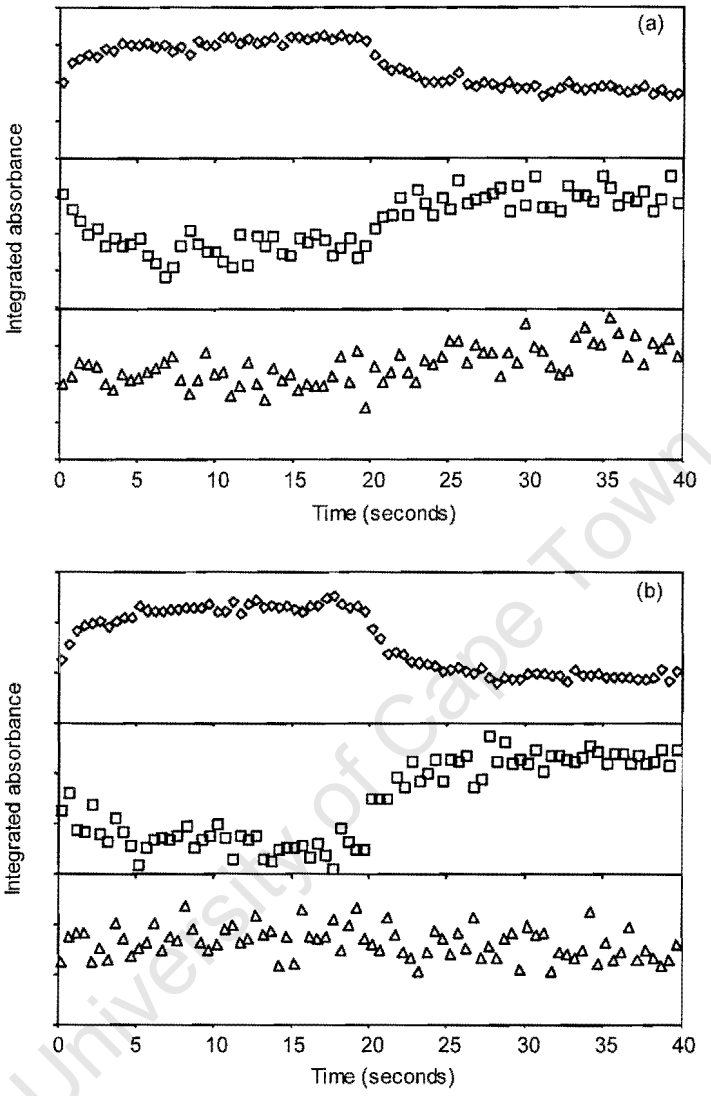

Figure 5.20 – Integrated toluene (◇), silanol (□) and Bronsted (△) infra-red bands for the response of toluene adsorbed on HMFI90-0.1 at 100°C and (a) 0.1 and (b) 1 mbar to a volume modulation at 0.025 Hz. The ranges of integration were 1508-1482 cm^{-1} (toluene), 3765-3700 cm^{-1} (silanol), 3640-3570 cm^{-1} (Bronsted).

It should be noted that no quantitative information could be obtained from the data in Figure 5.20 since that would require knowledge of the molar extinction coefficient of the three bands, which is beyond the scope of this study. More noteworthy was the observation that, while both the toluene and the silanol bands showed clear trends during the up and down volume steps, the Bronsted band exhibited only random variation, indicating that the occupation of Bronsted sites did not change during the adsorption and desorption steps.

5.7.3 Step scan experiments

As noted in section 5.7.1, even at a pressure of 1 mbar, the number of scans required per spectrum (N_A) to achieve acceptable signal-to-noise-ratio was 100. It was also noted in section 4.7.4 that, using the full spectrometer range (7500-370 cm^{-1}) at a spectral resolution setting of 12 cm^{-1} (which would be the lowest tolerable resolution for practical measurements), the number of interferogram points (N_I), i.e. mirror positions, required would be 2591. Thus, from equation (4.13), the number of cycles required (N_C) would be 259100. At a modulation frequency of 1 Hz, which was found in section 5.3 to be the highest frequency at which reproducible modulation could be attained, an experiment would therefore take 72 hours. To maintain a stable baseline (which is essential for step scan measurements) for that period of time would be impossible.

One possible solution to this problem would be to narrow the frequency range of the infra-red beam by installing an optical filter. With the narrower bandwidth, the distance between interferogram points could be increased, thus reducing the total number of points. For example, filters can be purchased for the following wavenumber ranges: 1200-1680, 1600-2090, 2020-2500, 2500-3280 and 3200-4150 cm^{-1}. At a spectral resolution of 12 cm^{-1}, the number of interferogram points required for these bandwidths would be 102, 94, 114, 150 and 190, respectively. Using the 1200-1680 cm^{-1} filter, therefore, the duration of an experiment (under the conditions mentioned above) could be reduced to less than 3 hours, which is a reasonable time-span to maintain a stable baseline. However, at lower pressures at which, for example, more than 300 scans were required, the duration would still be intolerable. The use of optical filters would also mean that several experiments would be required to observe the full frequency range. In addition, care would have to be taken to ensure that the linearity correction for the MCT detector was still valid.

Taking these factors into account, in combination with the fact that the time-resolution offered by the rapid scan mode was considered sufficient for the systems under investigation, it was decided not to purchase the optical filters and thus no meaningful step scan experiments could be performed.

6. Discussion

The details of the commissioning tests and the preliminary results have already been discussed in depth in Chapter 5. Thus, with a few exceptions, this chapter serves mainly as a summary of the findings.

6.1 Experimental results

In this section, the reproducibility and validity of the experimental results are briefly discussed.

6.1.1 Reproducibility

Frequency response method

For blank experiments (see Figure 5.6) the dependence of the phase lag on the frequency could be excellently reproduced. The relative amplitude could also be reproduced if the temperature and pressure were kept constant but, at different temperatures or pressures, there were slight (usually less than 0.5%) offsets. Thus, while not essential, the acquisition of a new set of blank-run parameters when operating at new conditions was recommended.

In experiments with a sorbent (see Figure 5.9), the relative amplitudes were reproducible to within an accuracy of 10% and the phase lags to within an accuracy of 15%. However, these differences in the frequency response parameters resulted only in corresponding differences in K-values, which were used only to validate the K-value predicted from the isotherm. More importantly, the frequency at which the maximum in phase lag occurred was reproducible to within a factor of 2, meaning that the diffusivities measured were reproducible to within half an order of magnitude which, for diffusivity measurements, is negligible.

It should be noted that a prerequisite to obtaining reproducible results was that bed-depth (i.e. intercrystalline) effects had to be eliminated by ensuring that the particles were well-dispersed in the quartz wool plug.

Sorption rate using FTIR spectroscopy

As shown in Table 5.4, the variation in diffusivities obtained from the sorption rate method, using FTIR spectroscopy to follow the uptake, was less than half an order of magnitude. Noting, in addition, that some of these experiments were performed on different sample wafers, it was concluded that the apparatus could obtain reproducible results using this method.

Single step FTIR spectroscopy

The difference spectra recorded for a single step-wise change in the volume (see section 5.7.1) were reproducible within 5% (based on the main spectral features) at 100°C and pressures of 0.01, 0.1 and 1 mbar.

Rapid scan FTIR spectroscopy

Rapid scan experiments were repeated at 100°C and 0.1 mbar. With respect to the response of the silanol (3745 cm^{-1}) and toluene (1495 cm^{-1}) bands, the results were reproducible to within 10%.

6.1.2 Validity

Frequency response method

As described section 5.4, the diffusivities obtained from the frequency response method using this apparatus were two orders of magnitude lower than those previously reported using the same method (Song and Rees, 2000). However, this could be explained by the difference in crystal sizes and in the acid site concentration of the experimental samples. This assertion was supported by the results shown in Table 6.1 for the MFI/toluene system at 100°C.

From Table 6.1, the decrease in diffusivity with decreasing crystal size and increasing acid site concentration (i.e. decreasing Si/Al ratio) was clear. To evaluate which effect had more influence would require further work. However, the results obtained on the new apparatus using the frequency response method could be considered valid.

Table 6.1 – Reported diffusivities (at 100°C) of toluene in MFI materials with various crystal sizes and Si/Al ratios

Reference	Crystal diameter* μm	Si/Al ratio	Diffusivity# 10^{-17} m^2/s
Song and Rees (2000)	4.5	∞	150000
This study	3	45	1000
Müller et al (1994)	2	35	23[&]
Masuda et al (1998)	1.1	20	7[§]

* For non-spherical crystals an equivalent diameter of a sphere was calculated.

It was not clear from all studies whether the diffusivities had been corrected. However, from equation (5.2), the difference would probably be less than half an order of magnitude.

& The actual experiment was performed at 47°C. Therefore this value was estimated using the activation energy of 51 kJ/mol estimated in Masuda et al (1998). An activation energy 10 kJ/mol higher or lower would only change the value by a factor of less than 2.

§ The actual experiments were done at higher temperatures and this value was estimated by extrapolating the Arrhenius plot.

Sorption rate method using FTIR spectroscopy

As discussed in section 5.6, the diffusivities determined by the sorption rate method, using FTIR to follow the uptake, were the same (within a reasonable error) as those measured on a similar apparatus using the same sorbent (Zheng, 2000). They were lower, by almost three orders of magnitude, than those reported for a similar system, i.e. with benzene rather than toluene as the sorbate (Karge and Nießen, 1991), but, as in the case of the frequency response measurements mentioned above, the difference could be attributed to the crystal size (and hence a possible surface barrier).

Taking an average of the diffusivities in Table 5.4 and correcting them using equation (5.2) and the parameters in Table 5.1, the diffusivity obtained for the system was 2.4 x 10^{-17} m^2/s. Considering that the particle diameter of HMFI90-0.1 was 0.5 μm, this value followed the trend (based on crystal size) predicted from Table 6.1. The Si/Al ratio was 57 (see section 5.2) so the trend based on acid site concentration was not followed but it could be argued that, in this case, the dependence of apparent diffusivity on crystal size outweighed the dependence on acid site concentration.

Based on these arguments, it was concluded that the measurements of diffusivity using the sorption uptake method on this apparatus were valid.

FTIR spectroscopy

While the principal spectral features for toluene adsorption on HMFI could be observed in the results of single-step and rapid scan FTIR spectroscopy experiments (see section 5.7.1 and 5.7.2), the details of these could not be analysed for validity since there was no comparable data available.

6.2 Ranges of the apparatus compared to the original specifications

In this section, the ranges of the apparatus are examined and compared to the original specifications.

6.2.1 Pressure

As pointed out in section 5.3, the Baratron pressure transducer could not record acceptable data when using the X0.01 (100 times amplification) range. This meant that, since the less sensitive X0.1 (10 times amplification) setting had to be used, the transducer was not sensitive enough to measure small variations at low pressures. This is illustrated in Figure 6.1 for a blank experiment using a 0.1 Hz volume modulation at a pressure of 0.1 mbar.

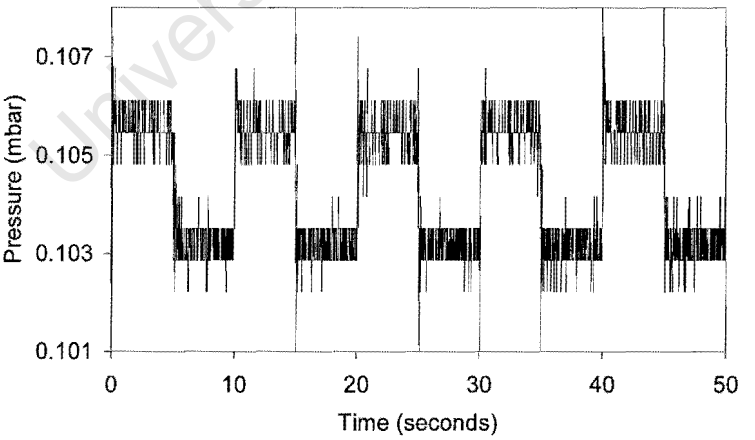

Figure 6.1 - Response of the Baratron pressure transducer (in the absence of a sorbent) to a system volume modulation at a frequency of 0.1 Hz with the range of the amplifier on the signal conditioner set to X0.1 (10 times amplification)

As can be seen in Figure 6.1, the noise occurred in discrete jumps of approximately 0.0003 mbar. Since the pressure change between the upward and downward stroke was approximately 0.002 mbar, these discrete jumps represented about 15% of the total pressure change, indicating that the dynamic range of the signal was too low.

Estimating that 40 discrete points within the total pressure change would be sufficient to obtain acceptable results, 0.6 mbar would thus be the low pressure limit for frequency response experiments. The original specification for the pressure transducer was that it should be possible to perform this type of experiment at 10^{-3} mbar. Thus, the actual performance was almost three orders of magnitude worse than specified.

6.2.2 Modulation frequency

As pointed out in section 5.3, the armature did not respond when the modulator was set to run at frequencies above 4.5 Hz and, in addition, the quality of the data at frequencies above 1 Hz was not good enough to obtain reproducible results. Thus the usable frequency range for the apparatus was 0.001-1 Hz, compared to the 0.001-10 Hz originally specified. With reference to Figure 2.3, this reduced the range of diffusion coefficients that could be probed.

6.2.3 Time-resolution of FTIR spectroscopy

As pointed out in section 5.7.3, it was not possible to perform step-scan experiments due to the long time duration and the expected baseline drift in the signal. Thus the upper limit of time-resolution was provided by the rapid scan mode. As mentioned in section 5.7.2, because of limitations imposed by considerations of detector linearity, the maximum scanner speed was 20 scans/second at a spectral resolution of 8 cm^{-1} and thus 30 scans/second at a resolution of 12 cm^{-1} (compared to the 100 scans/second originally specified). In addition, in rapid scan mode, interferograms could only be collected in pairs. Thus, the effective maximum time-resolution was 0.067 s (15 scans/second).

Another possible limitation would be the duration of the experiment. For example, if 6 hours were assumed to be the longest time the IR baseline could be kept constant (since the MCT detector would have to be re-filled with liquid nitrogen every 6 hours, which would often change the baseline), at a volume modulation frequency of 1 Hz (i.e. the maximum), the number of cycles would be 21600 and the number of coadditions thus 43200. Therefore, such a limitation would only be significant in a system extremely insensitive to pressure variation.

6.2.4 Miscellaneous

It was pointed out in section 2.3.5 that a stabilization delay was required in the frequency response method before the attainment of a periodic steady-state. The same applied to rapid (and step) scan experiments, in which the response to modulation had to be identical for each cycle. Thus, it was important to note that these experiments were only useful for processes which were reversible within the experimental time-span and not, for example, for processes in which a rapid irreversible initial step was under investigation.

7. Concluding remarks

In this chapter, a brief overview of the future of the new apparatus is presented. Firstly, based on the shortcomings of the apparatus discussed in Chapters 5 and 6, recommendations are made as to what improvements could be made. Secondly, suggestions are made regarding the type of experiments that could be performed on the apparatus.

7.1 Recommendations for improvements to the apparatus

Pressure transducer

As discussed in section 6.2.1, frequency response experiments could only be performed at pressures of 0.6 mbar and higher. This means that, for most gas-zeolite systems, diffusivities at very low coverages could not be measured. Thus attempts should be made to improve the pressure sensitivity of the system, while avoiding any accompanying noise at the transition edges.

One possibility would be to try (in conjunction with the supplier) to improve the Baratron transducer. Another option is to investigate other types of pressure gauge which do not rely on a deflecting membrane system (which may be the cause of the noise at the transition edge). If the transition-edge noise can be eliminated, then the option of including larger-range amplifiers (i.e. 1000 or 10000 times amplification) should also be investigated (Note: to attain the original specification, which was that frequency response experiments be performed at 10^{-3} mbar, a 600 times improvement in dynamic range is required, i.e. 6000 times amplification).

The second strategy would be to install a series of lower range Baratron gauges to be used with the X0.1 range amplification setting, thus allowing measurements at lower pressures. In this regard, it should be noted that the lowest pressure range available in the bakeable model from MKS Instruments (the supplier of the current Baratron transducer) is 6.65 x 10^{-5}-1.33 mbar. A transducer with a range of 1.33×10^{-6}-0.133 mbar is available in a non-bakeable model. To achieve the original specification (see above), the low end of the range would have to be no more than 1.1×10^{-6} mbar.

Modulation frequency

As pointed out in section 6.2.2, the frequency of the volume modulation had an upper limit of 1 Hz which, in turn, imposed an upper limit on the range of diffusivities that could be measured (see Figure 2.3). Thus, action should be taken to increase the modulation frequency at which high quality data can be recorded.

Some possibilities suggested by Rees (1999) were to: (a) ensure that the sense of the drive currents in both sets of windings are such that the direction of magnetization in the armature is always either radially outwards or inwards; (b) quarter the magnet cores; (c) employ a different armature design which would allow the use of straight magnets made of stacked laminations, each with its own winding; (d) use better magnetic materials than mild steel (e.g. a cobalt alloy) for the armature and magnet yokes; and (e) program the drive-current to generate a short high-current pulse, accompanied by a demagnetising pulse in the opposite set of coils, to produce the transition, followed by a weak holding current.

The first three suggestions would all prevent or reduce current being induced in the armature and/or magnet cores which opposes the magnetization caused by the current in the coils (i.e. eddy current damping). The last two suggestions would accelerate the rise time of the magnetization.

System volume

As pointed out in section 5.3, the quality of the pressure response wave-form was not entirely satisfactory and enhancements would lead to smaller errors in the determination of frequency response parameters. The measures mentioned in the discussion on modulation frequency would contribute greatly to the wave-form quality. However, another improvement would be a reduction in the volume of the system since this would allow the travel distance of the armature to be reduced to attain the same percentage volume change, which would thus lead to faster transitions and possibly less noise at the transition edge.

Since frequency response experiments were (and will probably continue to be) exclusively carried out using the secondary cell, the volume of the primary cell and of the flexible connection (i.e. currently almost 25% of the total volume) could be

eliminated during these experiments. While this could be done by removing the entire primary cell assembly (including the vacuum feedthrough cover for the spectrometer), this would compromise the flexibility of the apparatus. Thus, the insertion of a valve between the flexible connection and the main system would be preferable. For obvious reasons, the piping of the valve itself should occupy as little volume as possible.

Primary (infra-red) cell sample holder

As discussed in section 5.5, there were discrepancies between the spectra of activated samples recorded on the new apparatus and those recorded on other spectrometers. To increase the level of confidence in FTIR measurements, it is necessary to resolve this issue. Thus, it is necessary to further investigate the causes of these discrepancies and to implement solutions.

As mentioned in section 5.5, it is possible that the discrepancies were caused by extreme temperature effects, which led either to structural changes in the material (in the case of the temperature being too high) or to incomplete activation (in the case of the temperature being too low). Thus, a first step would be to examine the temperature variations of the sample wafer in detail, and to try to relate this to a temperature gradient in both the wafer itself and the sample holder.

One way to achieve this would be to find a sample whose IR spectral bands have well-defined shifts with temperature. Thus, at a series of temperatures (as indicated by the thermocouple at the edge of the sample holder), the actual temperature of the wafer could be determined under both steady-state and dynamic (i.e. during a temperature ramp) conditions. Another possibility would be to remove the sample holder from the cell and measure the temperature of the wafer directly using another thermocouple. This would have the additional advantage that the behaviour, at high temperatures, of the sample holder itself could be observed directly. While this method would be more exact, it should be noted that the temperature gradient may be different under atmospheric conditions to that at the ultra-high vacuum conditions normally existing in the cell during activation.

Once the problem has been analysed in this way, it will hopefully become clearer what steps could be taken to solve it. At the very least, a calibration can be made between the thermocouple reading and the actual temperature, though the drawback of this solution would be that the temperature gradient may depend on the thermal properties of the material and hence the calibration would not be valid for other sorbents.

On the other hand, if it were found that the temperature gradient was negligible, then other causes for the spectral discrepancy would have to be found, e.g. the detector or some as yet unidentified interference to the IR beam.

7.2 Suggestions for future experiments

There is a vast array of experiments that could be performed on this apparatus. Therefore, in this section, an attempt is made to describe only the type of experiments that could be performed. Even with this limitation, only a small selection is included which is not intended to be exhaustive. It should also be noted that the suggested experiments for the frequency response apparatus are in addition to its basic function, which is simply to measure the diffusivities of sorbates in zeolites (or other microporous materials) at any particular set of conditions, i.e. temperature and pressure (or concentration).

Separation of half-waves in the frequency response method

Until now, in the frequency response experiments on the apparatus, the pressure response has been considered only over a full cycle (i.e. the adsorption and desorption curves have been assumed to be symmetric). In future experiments it would be useful to try to separate the two half-waves and compare them, to ascertain whether there is a difference between the adsorption and desorption behaviour, even at the incremental volume change (in which non-linearity should not be significant). Observed differences may give an insight into thermal and finite-rate adsorption effects.

Single step frequency response experiments

Rees and Shen (1993) have described a single-step experiment, which they called the single-step frequency-response (SSFR) method, to measure diffusivity on a frequency

response apparatus. This method is can be modelled as a sorption rate method with the boundary condition of a changing surface concentration (Kärger and Ruthven, 1992). The advantage of this method over most step-change methods is that, as with the full frequency response method, the variation is small and thus the condition of isotherm linearity is valid. Thus, this provides another method of measuring diffusivity on this apparatus. In this experiment too, the diffusivity during adsorption and desorption can be evaluated separately, with differences giving an insight into thermal and finite-rate adsorption effects.

Comparison of methods

Given the fact that three methods for measuring diffusivity (frequency response, SSFR, and sorption rate using FTIR) are now available on this single apparatus, an obvious suggestion is to perform a comparison of the values determined by each of the three methods. If the values are similar, a higher level of confidence will be attained; if the discrepancies are large, a clear indication will be given of experimental shortcomings. Naturally, the sorption rate FTIR method is only viable for sorbents that are IR transparent and sorbates with a distinct IR band.

Studies of coverage (or pore-filling) effects on diffusivity

As pointed out in section 1.4.3, the fact that frequency response measurements are performed at an almost constant concentration means that the diffusivities determined can be assumed to be at the equilibrium concentration. Thus, by varying the initial pressure for different experiments, the dependence of the diffusivity on concentration (or coverage or pore-filling) can be determined.

One example of where this might be useful is in the case of sorbate-sorbent systems where the sorption isotherm can be represented by a double-Langmuir model. In these cases, it has been hypothesized (Kapteijn, 2000) that there are two regimes: the first in which there is a rapid uptake of the sorbate in one pore-type; and the second in which there is a slower uptake of sorbate in the another pore-type. This would imply two separate diffusion regimes with a sharp transition at the concentration where the filling of the second pore-type commences. The transition could be probed using this method.

Activation energies of diffusion

Since micropore diffusion is an activated process (see section 1.1.2), it can be represented by an Arrhenius equation and, for any sorbate-sorbent system, an activation energy of diffusion can be determined by measuring diffusivities over a range of temperatures. For these experiments, a different pressure has to be used at each temperature in order to achieve a constant intracrystalline concentration (to decouple the concentration dependence). Thus the frequency response and SSFR methods lend themselves to these measurements since the starting pressure can be accurately adjusted.

Co- and counter- diffusion

As mentioned in section 1.5.4, as long as the characteristic IR bands of two sorbates are clearly separable, the co- and counter-diffusion of the two molecules within a zeolite can be measured (Karge and Nießen, 1991). However, as pointed out by both Kärger and Ruthven (1992) and Rees (1994), the usual models for single component diffusion are no longer valid because the driving force for each component (i.e. the gradient of chemical potential) is modified by the presence of the other components in the system (in accordance with the multicomponent adsorption isotherm). Thus, the correct treatment of these systems requires a solution of Fick's diffusion law for mixtures.

Role of different sorbent groups in adsorption/desorption

In sections 5.7.1 and 5.7.2, it was shown that, under certain conditions, some functional groups in the sorbent may play a stronger role than others during adsorption and desorption steps. Both single step and rapid scan FTIR spectroscopy can be used to ascertain more about these roles and at which conditions each functional group plays an important role. Furthermore, rapid scan FTIR can be used to ascertain whether there is a time dependency related to these roles. For example, it could be hypothesized that, under certain conditions, the bridging hydroxyl group of a zeolite plays an initial role in adsorption before relaxing to an equilibrium state. If the initial interaction were within the time frame of the rapid scan time resolution, this method could be used to test the hypothesis. This could also give an insight into the ordering of the molecules (in the pores or on the external surface of the sorbent) during the dynamic process of adsorption/desorption close to equilibrium.

Dynamics of transition states and their relation to surface resistances

Pieterse et al (2000) have shown that, for di-branched alkanes, there is a sharp transition from one state of ordering to another at a certain coverage. If this process is reversible, the dynamics of the transition could be investigated using rapid scan techniques, i.e. by having the two extremes of the volume modulation set so that the associated coverages straddle the transition coverage. These processes may not be exclusive to systems with di-branched alkanes but could also occur in other sorbate-sorbent systems and may be an explanation for the existence of the surface barrier observed in some systems and mentioned in sections 1.5.5, 5.4 and 5.6. Thus, this experiment could give an insight into surface resistances.

Even if the process is not reversible, some information could be obtained using a single-step technique, though the dynamics could then not be probed unless they were very slow.

Combining the analysis of pressure and IR spectral responses

As is clear from the preceding chapters, the new apparatus can record both the pressure response and the response of IR spectral bands to a volume modulation or a single-step volume change. In the case of a volume modulation at a constant frequency, these responses can both be recorded with a high time-resolution. Thus, an obvious strategy would be to combine the analysis of these two responses to ascertain the relationship between the gas-phase pressure, the adsorbed concentration and arrangement of the sorbate, and the state and behaviour of the functional groups of the sorbent. Ultimately, with appropriate models, the frequency response behaviour of not only the pressure but also of the spectral bands could be analysed. In general the combination of the methods could give a clearer picture on the processes that govern sorption and diffusion of molecules in zeolites and other microporous materials.

References

Atkins P.W. "Physical Chemistry", 4th Edition, Oxford University Press, Oxford, **1990**.

Ballinger T.H.; Basu P.; Yates J.T. "IR Spectroscopic Studies of Adsorbate Diffusion in Porous Catalysts" *J. Phys. Chem.* **1989**, *93*, 6758.

Brandani S. "Effects of Nonlinear Equilibrium on Zero Length Column Experiments" *Chem. Eng. Sci.*, **1998**, *53*, 2791.

Bruker Analytische Messtechnik GmbH; "OPUS /IR Version 2, Reference Manual" **1995**.

Bruker Optik GmbH; "IFS 66v/S User's Manual" **1998**.

Bülow M. "Transportwiderstände in Grenzflächenschichten von Zeolithkristallen und ihre Bedeutung für die Sorptionskinetik" *Z. Chem.*, **1985**, *25*, 81.

Bülow M.; Struve P.; Finger G.; Redszus C.; Ehrhardt K.; Schirmer W.; Kärger J. "Sorption Kinetics of n-Hexane on MgA Zeolites of Different Crystal Sizes – Study of the Rate-Limiting Transport Mechanism" *J. Chem. Soc. Faraday Trans. I*, **1980**, *76*, 597.

Bülow M.; Struve P.; Pikus S. "Influence of Hydrothermal Pretreatment on Zeolitic Diffusivity Detected by Comparative Sorption Kinetics and Small Angle X-Ray Scattering Investigations" *Zeolites*, **1982**, *2*, 267.

Carslaw H.S.; Jaeger J.C. "Conduction of Heat in Solids", 2nd edition, Oxford University Press, London, **1959**.

Chihara K.; Suzuki M.; Kawazoe K. "Effect of Heat Generation on Measurement of Adsorption Rate by Gravimetric Method" *Chem. Eng. Sci.*, **1976**, *31*, 505.

Choudhary V.R.; Srinivasan K.R. "Sorption and Diffusion of Benzene in H-ZSM-5: Effect of Si/Al Ratio, Degree of Cation Exchange and Pretreatment Conditions" *J. Catal.* **1986**, *102*, 328.

Crank J. "The Mathematics of Diffusion" 2nd edition, Clarendon Press, Oxford, **1975**.

Csicsery S.M. "Shape Selective Catalysis in Zeolites" *Zeolites*, **1984**, *4*, 202.

Dubinin M.M.; Erashko I.T.; Kadlec O.; Ulin V.I.; Voloshchuk A.M.; Zolotarev P.P. "Kinetics of Physical Adsorption by Carbonaceous Adsorbents of Biporous Structure" *Carbon*, **1975**, *13*, 193.

Duncan W.L.; Möller K.P "On the Diffusion of Cyclohexane in ZSM-5 Measured by Zero-Length-Column Chromatography" *Ind. Eng. Chem. Res.*, **2000**, *39*, 2105.

Eder F. "Thermodynamics and Siting of Alkane Sorption in Molecular Sieves" PhD Thesis, University of Twente, **1996**.

Eic M.; Ruthven D.M. "A New Experimental Technique for Measurement of Intracrystalline Diffusivity" *Zeolites*, **1988**, *8*, 40.

Evnochides S.K.; Henley E.J. "Simultaneous Measurement of Vapor Diffusion and Solubility Coefficients in Polymers by Frequency Response Techniques" *J. Polym. Sci., Part A-2*, **1970**, *8*, 1987.

Ford D.M.; Glandt E.D. "Molecular Simulation Study of the Surface Barrier Effect. Dilute Gas Limit" *J. Phys. Chem.* **1995**, *99*, 11543.

Förste C.; Kärger J.; Pfeifer H.; Riekert L.; Bülow M.; Zikanova A. "Comparison of Nuclear Magnetic Resonance Tracer Exchange and Molecular Uptake of Benzene on Pentasils" *J. Chem. Soc. Faraday Trans.*, **1990**, *86*, 881.

George W.O.; McIntyre P.S. "Infrared Spectroscopy" in "Analytical Chemistry by Open Learning" series, John Wiley and Sons, Chichester, **1987**.

Glueckauf E. "Theory of Chromatography. Part 10. Formulae for Diffusion into Spheres and their Application to Chromatography" *Trans. Faraday Soc.* **1955**, *51*, 1540.

Glueckauf E.; Coates J.I. "Theory of Chromatography. Part IV. The Influence of Incomplete Equilibrium on the Front Boundary of Chromatograms and on the Effectiveness of Separation" *J. Chem. Soc.*, **1947**, 1315.

Goodyear C.C. "Signals and Information", Butterworth, London, **1971**.

Han M.; Yin X.; Jin Y.; Chen S. "Diffusion of Aromatic Hydrocarbon in ZSM-5 Studied by the Improved Zero Length Column Method" *Ind. Eng. Chem. Res.*, **1999**, *38*, 3172.

Haq N.; Ruthven D.M. "A Chromatographic Study of Sorption and Diffusion in 5A Zeolite" *J. Colloid Interface Sci.*, **1986**, *112*, 164.

Harkness I., Personal Communication, Edinburgh, **1999**.

Hashimoto N.; Smith J.M. "Macropore Diffusion in Molecular Sieve Pellets by Chromatography" *Ind. Eng. Chem. Fund.*, **1973**, *12*, 353.

Haynes H.W.; Sarma P.N. "A Model for the Application of Gas Chromatography to Measurements of Diffusion in Bidisperse Structured Catalysts" *AIChE J.*, **1973**, *19*, 1043.

Heink W.; Kärger J.; Pfeifer H. "Applications of Zeugmatography to Study Kinetics of Physical Adsorption" *Chem. Eng. Sci.*, **1978**, *33*, 1019.

Hsiang T. C.-S.; Haynes H.W. "Axial Dispersion in Small Diameter Beds of Large, Spherical Particles" *Chem. Eng. Sci.*, **1977**, *32*, 678.

Hufton J.R.; Ruthven D.M. "Diffusion of Light Alkanes in Silicalite Studied by the Zero Length Column Method" *Ind. Eng. Chem. Res.*, **1993**, *32*, 2379.

Jentys A.; Warecka G.; Lercher J.A. "Surface Chemistry of H-ZSM5 Studied by Time-Resolved IR Spectroscopy" *J. Molec. Catal.*, **1989**, *51*, 309.

Jobic H.; Bee M.; Caro J.; Bülow M.; Kärger J.; Pfeifer H. "Microdynamics of Guest Molecules in Zeolites Studied by Quasi-Elastic Neutron Scattering and NMR Pulsed Field Gradient Technique" in "Catalysis and Adsorption by Zeolites" Öhlmann G.; Pfeifer H.; Fricke R.; Eds., Elsevier Science, Amsterdam, *Stud. Surf. Sci. Catal.*, **1991**, *65*, 445.

Jordi R.G.; Do D.D. "Frequency Response Analysis of Sorption in Zeolite Crystals with Finite Intracrystal Reversible Mass Exchange" *J. Chem. Soc. Faraday Trans.* **1992**, *88*, 2411.

Jost W. "Diffusion in Solids, Liquids, Gases" Academic Press, New York, **1952**.

Kärger J. "A Study of Fast Tracer Desorption in Molecular Sieve Crystals" *AIChE J.*, **1982**, *28*, 417.

Kärger J.; Caro J. "Interpretation and Correlation of Zeolitic Diffusivities Obtained from Nuclear Magnetic Resonance and Sorption Experiments" *J. Chem. Soc. Faraday Trans. I*, **1977**, *73*, 1363.

Kärger J.; Ruthven D. "Diffusion in Zeolites and Other Microporous Solids", John Wiley & Sons, New York, **1992**.

Kärger J.; Heink W.; Pfeifer H.; Rauscher M.; Hoffmann J. "NMR Evidence of the Existence of Surface Barriers on Zeolite Crystallites" *Zeolites*, **1982**, *2*, 275.

Kärger J.; Bülow M.; Millward G.R.; Thomas J.M. "A Phenomenological Study of Surface Barriers in Zeolites" *Zeolites*, **1986**, *6*, 146.

Kärger J.; Pfeifer H.; Seidel R.; Staudte B.; Gross T. "Investigation of Surface Barriers on CaNaA Type Zeolites by Combined Application of the NMR Tracer Desorption Method and X-Ray Photoelectron Spectroscopy" *Zeolites*, **1987**, *7*, 282.

Kärger J.; Pfeifer H.; Heink W. "Principles and Applications of Self-Diffusion Measurements by Nuclear Magnetic Resonance" *Adv. Magn. Res.*, **1988**, *12*, 1.

Kapteijn F., Personal Communication, Munich, **2000**.

Kapteijn F.; Moulijn J.A.; van Santen R.A.; Wever R. "Chemical Kinetics of Catalyzed Reactions" in "Catalysis: An Integrated Approach" 2nd Edition, van Santen R.A ; van Leeuwen P.W.N.M.; Moulijn J.A.; Averill B.A.; Eds., Elsevier, Amsterdam, **1999**.

Karge H.G.; Nießen W. "A New Method for the Study of Diffusion and Counter-Diffusion in Zeolites" *Catalysis Today*, **1991**, *8*, 451.

Karlicek R.F.; Lowe I.J. "A Modified Pulsed Gradient Technique for Measuring Diffusion in the Presence of Large Background Gradients" *J. Magn. Res.*, **1980**, *37*, 75.

Kocirik M.; Struve P.; Bülow M. "Surface Resistance Limited Sorption Kinetics in Zeolite Crystals with a Non-Linear Sorption Isotherm" *Z. Phys. Chem. (Leipzig)*, **1986**, *267*, 446.

Kocirik M.; Struve P.; Fiedler K.; Bülow M. "A Model for the Mass-Transfer Resistance at the Surface of Zeolite Crystals" *J. Chem. Soc. Faraday Trans. I*, **1988**, *84*, 3001.

Kocirik M.; Zikanova A.; Struve P.; Bülow M. "Peculiarities of the Mass Transport Across Zeolite Crystal Surfaces" *Z. Phys. Chem. (Leipzig)*, **1990**, *271*, 43.

Kumar R.; Duncan R.C.; Ruthven D.M. "A Chromatographic Study of Diffusion of Single Components and Binary Mixtures of Gases in 4A and 5A Zeolites" *Can. J. Chem. Eng.*, **1982**, *60*, 493.

Lee L.K. "The Kinetics of Sorption in a Biporous Adsorbent Particle" *AIChE J.*, **1978**, *24*, 531.

Lee L.K.; Ruthven D.M. "Analysis of Thermal Effects in Adsorption Rate Measurements" *J. Chem. Soc. Faraday Trans. I*, **1979**, *75*, 2406.

Masuda T.; Fujikata Y.; Nishida T.; Hashimoto K. "The Influence of Acid Sites on Intracrystalline Diffusivities Within MFI-Type Zeolites" *Microporous and Mesoporous Materials*, **1998**, *23*, 157.

Meier W.M.; Olson D.H.; Baerlocher Ch. "Atlas of Zeolite Structure Types", 4th edition, Elsevier, London, **1996**.

Micke A.; Bülow M.; Kocirik M. "A Nonequilibrium Surface Barrier for Sorption Kinetics of *p*-Ethyltoluene on ZSM-5 Molecular Sieves" *J. Phys. Chem.* **1994**, *98*, 924.

Mirth G.; Lercher J.A. "Coadsorption of Toluene and Methanol on HZSM-5 Zeolites" *J. Phys. Chem.*, **1991**, *95*, 3736.

Mirth G.; Cejka J.; Lercher J.A. "Transport and Isomerization of Xylenes over HZSM-5 Zeolites" *J. Catal.* **1993**, *139*, 24.

MKS Instruments, Inc; "MKS Baratron Type 615A/616A/617A High Accuracy Sensor Heads" **1997**.

Müller G.; Narbeshuber T.; Mirth G.; Lercher J.A. "Infrared Microscopic Study of Sorption and Diffusion of Toluene in ZSM-5" *J. Phys. Chem.* **1994**, *98*, 7436.

Oprescu, D.; Rees L.V.C.; Shen D. "Diffusion of Sorbates in Zeolites by the Frequency Response Method: Particle Shape and Anisotropic Effects" *J. Chem. Soc. Faraday Trans.* **1992**, *88*, 2955.

Pazdernik O.; Schneider P. "Peak Moments for Gas Chromatographic Columns with a Pressure Drop" *J. Chromatogr.* **1981**, *207*, 181.

Pieterse J.A.Z; Veefkind-Reyes S.; Seshan K.; Lercher J.A. "Sorption and Ordering of Dibranched Alkanes on Medium Pore Zeolites Ferrierite and TON" *J. Phys. Chem.*, **2000**, in press.

Raghavan N.S.; Ruthven D.M. "Simulation of Chromatographic Response in Columns Packed with Bidisperse Structured Particles" *Chem. Eng. Sci.*, **1985**, *40*, 699.

Rasmuson A. "Time Domain Solution of a Model for transport Processes in Bidisperse Structured Catalysts" *Chem. Eng. Sci.*, **1982**, *37*, 787.

Rees L.V.C. "Exciting New Advances in Diffusion of Sorbates in Zeolites and Microporous Materials" in "Zeolites and Related Microporous Materials: State of the Art 1994" Weitkamp J.; Karge H.G.; Pfeifer H.; Holderich W.; Eds., Elsevier Science, Amsterdam, *Stud. Surf. Sci. Catal.*, **1994**, *84*, 1133.

Rees L.V.C., Personal Communication, Edinburgh, **1999**.

Rees L.V.C.; Shen D. "Characterization of Microporous Sorbents by Frequency Response Methods" *Gas. Sep. Pur.*, **1993**, *7*, 83.

Richards R.E. "Study of the Diffusion and Adsorption of Gases in Zeolites", PhD Thesis, University of London, **1985**.

Ruthven D.M.; Lee L.K. "Kinetics of Non-Isothermal Sorption: Systems with Bed Diffusion Control" *AIChE J.*, **1981**, *27*, 654.

Ruthven D.M.; Lee L.K.; Yucel H. "Kinetics of Non-Isothermal Sorption in Molecular Sieve Crystals" *AIChE J.*, **1980**, *26*, 16.

Satterfield C.N., "Heterogeneous Catalysis in Industrial Practice" 2nd edition, McGraw-Hill, New York, **1991**.

Shen D. "Sorption and Frequency-Response Diffusion in Zeolites" PhD Thesis, University of London, **1991**.

Shen D., Personal communication, e-mail, **1999**.

Silva-Crawford M.; Gerstein B.C.; Kuo A.-L.; Wade C.G. "Diffusion in Rigid Bilayer Membranes. Use of Combined Multiple Pulse and Multiple Pulse Gradient Techniques in Nuclear Magnetic Resonance" *J. Am. Chem. Soc.*, **1980**, *102*, 3728.

Smith B.C. "Fundamentals of Fourier Transform Infrared Spectroscopy", CRC Press, Boca Raton, **1996**.

Smith J.M. "Chemical Engineering Kinetics" 3rd edition, McGraw-Hill, New York, **1981**.

Song L.; Rees L.V.C. "Adsorption and Transport of n-Hexane in Silicalite-1 by the Frequency Response Technique" *J. Chem. Soc., Faraday Trans.*, **1997**, *93*, 649.

Song L.; Rees L.V.C. "Adsorption and Diffusion of Cyclic Hydrocarbon in MFI-Type Zeolites Studied by Gravimetric and Frequency-Response Techniques" *Microporous and Mesoporous Materials*, **2000**, *35-36*, 301.

Spiegel M.R. "Theory and Problems of Fourier Analysis", McGraw-Hill, New York, **1974**.

Sun L.M.; Bourdin V. "Measurement of Intracrystalline Diffusion by the Frequency Response Method: Analysis and Interpretation of Bimodal Response Curves" *Chem. Eng. Sci.* **1993**, *48*, 3783.

Sun L.M.; Meunier F.; Kärger J. "On the Heat Effect in Measurements of Sorption Kinetics by the Frequency Response Method" *Chem. Eng. Sci.* **1993**, *48*, 715.

Tiselius A. "Die Diffusion von Wasser in einem Zeolithkristall. Ein Beitrag zur Frage der Beweglichkeit Adsorbierter Moleküle" *Z. Phys. Chem. A*, **1934**, *169*, 425.

Tiselius A. "Sorption und Diffusion von Ammoniak in Analcim" *Z. Phys. Chem. A*, **1935**, *174*, 401.

Tyrrell H.J.V.; Harris K.R. "Diffusion in Liquids: A Theoretical and Experimental Study", Butterworths, London, **1984**.

Van-Den-Begin N.; Rees L.V.C.; Caro J.; Bülow M. "Fast Adsorption-Desorption Kinetics of Hydrocarbons in Silicalite-1 by the Single-Step Frequency Response Method" *Zeolites*, **1989**, *9*, 287.

Wicke E.; Kallenbach R. "Die Oberflächendiffusion von Kohlendioxyd in Aktiven Kohlen" *Kolloid. Z.*, **1941**, *97*, 135.

Williams W.D.; Seymour E.F.W.; Cotts R.M "A Pulsed-Gradient Multiple-Spin-Echo NMR Technique for Measuring Diffusion in the Presence of Background Magnetic Filed Gradients" *J. Magn. Res.*, **1978**, *31*, 271.

Wright C.J.; Riekel C. "The Uniaxial Rotation of Ethylene Adsorbed by Sodium 13X Zeolite" *Molec. Phys.*, **1978**, *36*, 695.

Yasuda, Y. "Determination of Vapor Diffusion Coefficients in Zeolite by the Frequency Response Method" *J. Phys. Chem.* **1982**, *86*, 1913.

Yasuda, Y. "Detection of Surface Resistance in a Gas/Porous-Adsorbent System by Frequency Response Method" *Bull. Chem. Soc. Jpn.* **1991**, *64*, 954.

Zheng S., Personal Communication, Munich, **2000**.

Appendices

A. Frequency Response Models

A periodic volume modulation can be represented, in complex terms, as

$$V = V_e(1 - ve^{i\omega t}) \tag{A.1}$$

where V_e is the equilibrium volume, v is the relative amplitude of the volume variation and ω is the angular frequency of the volume modulation (i.e. $\omega = 2\pi f$). Assuming the gas phase pressure and the sorbate concentration in the zeolite pores also vary sinusoidally, these quantities can thus be expressed as follows:

$$P = P_e(1 + pe^{i(\omega t + \phi)}) \tag{A.2}$$

and

$$C = C_e(1 + \gamma e^{i(\omega t + \phi - \chi)}) \tag{A.3}$$

where P_e and C_e are the equilibrium gas-phase pressure and sorbate surface concentration respectively, p and γ are the relative amplitudes of the pressure and concentration variations respectively, and ϕ and χ are phase differences.

A.1 Diffusion in a planar sheet

If diffusion occurs through a planar sheet, Fick's second law can be expressed as

$$\partial C/\partial t = \partial/\partial x(D(C)\partial C/\partial x) \tag{A.4}$$

With the assumption that $D(C) = D(C_e) = D$, equation (A.4) becomes

$$\partial C/\partial t = D(\partial^2 C/\partial x^2) \tag{A.5}$$

If one sets the boundary conditions that: (i) before the modulation begins ($t < 0$), the concentration in the sheet is the equilibrium concentration ($C = C_e$); and (ii) at the outer surface, concentration is proportional to a sinusoidally varying pressure, i.e.

$$C = C_e[1 + pe^{i(\omega t+\phi)}] \qquad \text{at } x = \pm L \tag{A.6}$$

then, letting $$\xi = (C - C_e)/(pC_e) \tag{A.7}$$

$$\xi = 0 \qquad \text{at } t < 0 \text{ and } -L \le x \le L \tag{A.8}$$

and $$\xi = e^{i(\omega t+\phi)} \qquad \text{at } t \ge 0 \text{ and } x = \pm L \tag{A.9}$$

The solution of equation (A.5) is thus (Carslaw and Jaeger, 1959; Evnochides and Henley, 1970)

$$\xi = A_\xi e^{i(\omega t+\phi+\varphi)} + \mathcal{T} \tag{A.10}$$

where $$A_\xi = \{[\cosh(2\hat{w}x)+\cos(2\hat{w}x)]/[\cosh(2\hat{w}L)+\cos(2\hat{w}L)]\}^{1/2} \tag{A.11}$$

and $$\varphi = \arg\{\cosh[\hat{w}x(1+i)]/[\cosh[\hat{w}L(1+i)]\} \tag{A.12}$$

with $$\hat{w} = (\omega/2D)^{1/2} \tag{A.13}$$

and $\mathcal{T}$ is a transient term which becomes insignificant as t increases, i.e. the term disappears at a periodic steady state.

The total amount of sorbate in the sheet can be obtained by integrating the concentration over the whole sheet (noting that the sheet is symmetrical on either side of $x = 0$)

$$B = 2S_A \int_0^L C\,dx \tag{A.14}$$

Where S_A is the surface area of the sheet. Substituting back from equation (A.7)

$$B = 2S_A C_e \int_0^L (1 + p\xi)\,dx \tag{A.15}$$

or $$(B - B_e)/pB_e = (1/L) \int_0^L \xi\,dx \tag{A.16}$$

where B_e ($= 2S_A C_e L$) is the equilibrium amount in the sheet (in moles).

The solution of equation (A.16) is (Evnochides and Henley, 1970)

$$B = B_e(1 + pAe^{i(\omega t+\phi+\psi)}) \quad (A.17)$$

where $$A = 2^{½}(\sin^2\eta_1+\sinh^2\eta_1)^{½}/[\eta_1(\cos\eta_1+\cosh\eta_1)] \quad (A.18)$$

$$\psi = \arctan[(\sin\eta_1-\sinh\eta_1)/(\sin\eta_1+\sinh\eta_1)] \quad (A.19)$$

and $$\eta_1 = (\omega L^2/2D)^{½} \quad (A.20)$$

The material balance of the total system can be written

$$d/dt(PV/RT_0)+dB/dt = 0 \quad (A.21)$$

Substituting equations (A.1), (A.2) and (A.17) into equation (A.21), differentiating and cancelling terms, one obtains:

$$(P_eV_e/RT_0)(pe^{i(\omega t+\phi)}-ve^{i\omega t}-2pve^{i(2\omega t+\phi)}) = -pB_eAe^{i(\omega t+\phi+\psi)} \quad (A.22)$$

Since this is a steady state periodic function, any time can be used to evaluate the terms. In this case, it is convenient to set $t = 0$. Rearranging terms and multiplying by $(1/p)e^{-i\phi}$

$$(v/p)e^{-i\phi}-1+2v = (RT_0B_e/P_eV_e)Ae^{i\psi} \quad (A.23)$$

Since v is small relative to unity, the term $2v$ can be considered negligible. Both the real and the imaginary sides of equation (A.23) must be equal. Therefore, expanding $e^{-i\phi}$ and $e^{i\psi}$, and separating the real and imaginary parts gives the equations

$$(v/p)\cos\phi - 1 = (RT_0B_e/P_eV_e)A\cos\psi \quad (A.24)$$

and $$(v/p)\sin\phi = (-RT_0B_e/P_eV_e)A\sin\psi \quad (A.25)$$

Now, letting $$\delta_{1c} = A\cos\psi \quad (A.26)$$

and $$\delta_{1s} = -A\sin\psi \quad (A.27)$$

$$\delta_{1c}^2 = A^2\cos^2\psi = A^2/\mathrm{cosec}^2\psi = A^2/(1+\tan^2\psi) \quad (A.28)$$

From (A.19) $\tan\psi = (\sin\eta_1 - \sinh\eta_1)/(\sin\eta_1 + \sinh\eta_1)$ (A.29)

and, therefore $1+\tan^2\psi = 2(\sin^2\eta_1 + \sinh^2\eta_1)/(\sin\eta_1 + \sinh\eta_1)^2$ (A.30)

From (A.18), (A.28) and (A.30),

$$\delta_{1c} = (1/\eta_1)\,[(\sinh\eta_1 + \sin\eta_1)/(\cosh\eta_1 + \cos\eta_1)] \quad (A.31)$$

and, from (A.26), (A.27) and (A.31),

$$\delta_{1s} = (1/\eta_1)\,[(\sinh\eta_1 - \sin\eta_1)/(\cosh\eta_1 + \cos\eta_1)] \quad (A.32)$$

From (A.2) and (A.17),

$$dP/dt = i\omega P_e p e^{i(\omega t+\phi)} \quad (A.33)$$

$$dB/dt = i\omega B_e p A e^{i(\omega t+\phi+\psi)} \quad (A.34)$$

Therefore, $dB/dP = (dB/dt)/(dP/dt) = B_e A e^{i\psi}/P_e$ (A.35)

As $\omega \to 0$, it can be shown that $A \to 1$ and $e^{i\psi} \to 1$ (since $\psi \to 0$). Thus,

$$dB_e/dP_e = dB/dP\,\big|_{\omega\to 0} = B_e/P_e \quad (A.36)$$

From equations (A.24)–(A.27) and (A.36)

$$(v/p)\cos\phi - 1 = K\delta_{1c} \quad (A.37)$$

and $(v/p)\sin\phi = K\delta_{1s}$ (A.38)

where $K = (RT_0/V_e)(dB_e/dP_e)$ (A.39)

A.2 Diffusion in an isotropic sphere

Fick's second law for radial diffusion in an isotropic sphere is:

$$\partial C/\partial t = (1/r^2)[\partial/\partial r\{D(C)r^2\partial C/\partial r)\}] \quad (A.40)$$

Using the substitution

$$u = Cr \tag{A.41}$$

and the assumption that $D(C) = D(C_e) = D$, equation (A.40) becomes

$$\partial u/\partial t = D(\partial^2 u/\partial r^2) \tag{A.42}$$

[Note: for the purposes of this derivation **only**, r is used as a variable and a as the crystal radius. However, in the main text (e.g. in Chapter 2), r denotes the crystal radius]. With the boundary conditions that the initial concentration in the sphere is zero and that the time dependent concentration at the surface of the crystal (i.e. at radius a) is c, then the solution of equation (A.42) is (Crank, 1975)

$$C = (-2\check{D}a/\pi^2 r)\sum_{n=1}^{\infty}(-1)^n \exp(-\check{D}n^2 t)n\pi\sin(n\pi r/a)\int_0^t \exp(\check{D}n^2 t)c\,dt \tag{A.43}$$

where $$\check{D} = \pi^2 D/a^2 \tag{A.44}$$

From equations (A.2) and (A.43) and the assumption that $k = c/P$ is a constant,

$$C = (-2\check{D}a/\pi^2 r)\sum_{n=1}^{\infty}(-1)^n \exp(-\check{D}n^2 t)n\pi\sin(n\pi r/a)\tilde{I}_1 \tag{A.45}$$

where $$\tilde{I}_1 = kP_e \int_0^t \exp(\check{D}n^2 t)\,[1+p\exp(i\omega t + i\phi)]\,dt \tag{A.46}$$

Integrating,

$$\tilde{I}_1 = kP_e\{[1/(\check{D}n^2)][\exp(\check{D}n^2 t)-1] + [p/(\check{D}n^2+i\omega)][\exp(\check{D}n^2 t + i\omega t + i\phi)-\exp(i\phi)]\} \tag{A.47}$$

Substituting back into equation (A.45),

$$C = (-2\check{D}kP_e a/\pi^2 r)\sum_{n=1}^{\infty}(-1)^n n\pi\sin(n\pi r/a)\tilde{A} \tag{A.48}$$

where

$$\tilde{A} = [1/(\check{D}n^2)][1-\exp(-\check{D}n^2 t)] + [p/(\check{D}n^2+i\omega)][\exp(i\omega t + i\phi)-\exp(-\check{D}n^2 t+i\phi)] \tag{A.49}$$

For a periodic steady state, $t \rightarrow \infty$ and $\exp(-\check{D}n^2t) \rightarrow 0$. Thus, equation (A.49) simplifies to

$$\tilde{A} = [1/(\check{D}n^2)] + [p/(\check{D}n^2+i\omega)]e^{i(\omega t+\phi)} \tag{A.50}$$

The total amount of sorbate in the sphere can then be obtained by integrating the concentration over the whole sphere

$$B = \int_0^a 4\pi r^2 C dr \tag{A.51}$$

Substituting (A.48) into (A.51),

$$B = (-8\check{D}kP_e a/\pi)\int_0^a \sum_{n=1}^{\infty}(-1)^n n\pi r\sin(n\pi r/a)\tilde{A}\, dr \tag{A.52}$$

The first part of the sum in equation (A.50) represents the non time-dependent part of the equation. When equation (A.50) is substituted into equation (A.52), this term hence becomes the equilibrium sorption amount in the sphere,

$$B_e = (-8\check{D}kP_e a/\pi)\int_0^a \sum_{n=1}^{\infty}(-1)^n n\pi r\sin(n\pi r/a)\,[1/(\check{D}n^2)]dr \tag{A.53}$$

Equation (A.52) then becomes

$$B = B_e - (8\check{D}kP_e a^3/\pi)pe^{i(\omega t+\phi)}\tilde{I}_2 \tag{A.54}$$

where $$\tilde{I}_2 = \int_0^a \sum_{n=1}^{\infty}(-1)^n(1/a)(n\pi r/a)\sin(n\pi r/a)[1/(\check{D}n^2+i\omega)]dr \tag{A.55}$$

Alternatively, $$\tilde{I}_2 = \sum_{n=1}^{\infty}[(-1)^n/(\check{D}n^2+i\omega)]\int_0^a (1/a)(n\pi r/a)\sin(n\pi r/a)dr \tag{A.56}$$

and, making the substitution $X = n\pi r/a$,

$$\tilde{I}_2 = \sum_{n=1}^{\infty}[(-1)^n/(\check{D}n^2+i\omega)]\int_0^{n\pi}[1/(n\pi)]X\sin X dX \tag{A.57}$$

Integrating,

$$\tilde{I}_2 = \sum_{n=1}^{\infty}[(-1)^n/(\check{D}n^2+i\omega)]\,[1/(n\pi)][-X\cos X - \sin X]_0^{n\pi} \tag{A.58}$$

or $$\tilde{I}_2 = -\sum_{n=1}^{\infty}(-1)^n\cos(n\pi)/(\check{D}n^2+i\omega) \tag{A.59}$$

Thus, equation (A.54) becomes

$$B = B_e + (8\check{D}kP_e a^3/\pi)pe^{i(\omega t+\phi)}\sum_{n=1}^{\infty}(-1)^n\cos(n\pi)/(\check{D}n^2+i\omega) \quad (A.60)$$

Noting that $(-1)^n\cos(n\pi) = 1$ and $1/(\check{D}n^2+i\omega) = (\check{D}n^2-i\omega)/(\check{D}^2n^4+\omega^2)$, equation (A.60) can re-written

$$B = B_e + (8\check{D}kP_e a^3/\pi)pe^{i(\omega t+\phi)}\sum_{n=1}^{\infty}(\check{D}n^2-i\omega)/(\check{D}^2n^4+\omega^2) \quad (A.61)$$

This series can be calculated analytically by making use of the following infinite series formulae (Yasuda, 1982):

$$\sum_{n=1}^{\infty} n^2/(n^4+x^4) = \pi/(2\sqrt{2}x)\{[\sinh(\sqrt{2}\pi x)-\sin(\sqrt{2}\pi x)]/[\cosh(\sqrt{2}\pi x)-\cos(\sqrt{2}\pi x)]\} \quad (A.62)$$

and

$$\sum_{n=1}^{\infty} 1/(n^4+x^4) = \sqrt{2}\pi/(4x^3)\{[\sinh(\sqrt{2}\pi x)+\sin(\sqrt{2}\pi x)]/[\cosh(\sqrt{2}\pi x)-\cos(\sqrt{2}\pi x)]\} - 1/(2x^4) \quad (A.63)$$

Setting $x = (\omega/\check{D})^{1/2}$ (A.64)

and $\eta_3 = (2\omega a^2/D)^{1/2}$ (A.65)

and re-substituting equation (A.44), one obtains

$$B = B_e + (4\pi a^3/3)kP_e p(\delta_{3c} - i\delta_{3s})e^{i(\omega t+\phi)} \quad (A.66)$$

where $\delta_{3c} = (3/\eta_3)\,[(\sinh\eta_3-\sin\eta_3)/(\cosh\eta_3-\cos\eta_3)]$ (A.67)

and $\delta_{3s} = (6/\eta_3)\,[(1/2)(\sinh\eta_3+\sin\eta_3)/(\cosh\eta_3-\cos\eta_3) - (1/\eta_3)]$ (A.68)

Now, substituting equations (A.1), (A.2) and (A.66) into the material balance equation (A.21), then differentiating and cancelling terms, one obtains

$$(V_e/RT_0)(pe^{i(\omega t+\phi)}-ve^{i\omega t}-2pve^{i(2\omega t+\phi)}) = -(4\pi a^3/3)kp(\delta_{3c}-i\delta_{3s})e^{i(\omega t+\phi)} \quad (A.69)$$

Since this is a steady state periodic function, any time can be used to evaluate the terms. In this case, it is convenient to set $t = 0$. Rearranging terms and multiplying by $(1/p)e^{-i\phi}$,

$$(v/p)e^{-i\phi} - 1 + 2v = (4\pi a^3/3)(RT_0/V_e)k(\delta_{3c} - i\delta_{3s}) \tag{A.70}$$

Since v is small relative to unity, the term $2v$ can be considered negligible. Both the real and the imaginary sides of equation (A.70) must be equal. Therefore, expanding $e^{-i\phi}$ and separating the real and imaginary parts gives the equations

$$(v/p)\cos\phi - 1 = K\delta_{3c} \tag{A.71}$$

and

$$(v/p)\sin\phi = K\delta_{3s} \tag{A.72}$$

where

$$K = (4\pi a^3/3)(RT_0/V_e)k \tag{A.73}$$

As in the planar sphere case, it can be shown that this quantity is related to the equilibrium isotherm by differentiating equations (A.2) and (A.66).

$$dP/dt = i\omega P_e p e^{i(\omega t + \phi)} \tag{A.74}$$

$$dB/dt = i\omega(4\pi a^3/3)kP_e p(\delta_{3c} - i\delta_{3s})e^{i(\omega t + \phi)} \tag{A.75}$$

$$dB/dP = (dB/dt)/(dP/dt) = (4\pi a^3/3)k(\delta_{3c} - i\delta_{3s}) \tag{A.76}$$

$$dB_e/dP_e = dB/dP\,\big|_{\omega \to 0} \tag{A.77}$$

As $\omega \to 0$, it can be shown that $\delta_{3c} \to 1$ and $\delta_{3s} \to 0$. Therefore,

$$dB_e/dP_e = (4\pi a^3/3)k \tag{A.78}$$

and

$$K = (RT_0/V_e)(dB_e/dP_e) \tag{A.79}$$

B. Calculation of frequency response parameters from experimental data

B.1 Theory

The Fourier transformation of the pressure response to a square-wave volume modulation has been discussed in section 2.3.3. In this discussion, the n^{th} harmonic phase lag (ϕ_n) and amplitude ratio (α_n) are shown to be

$$\alpha_n = (a_n^2 + b_n^2)^{1/2} \tag{B.1}$$

and

$$\phi_n = \arctan(a_n/b_n) \tag{B.2}$$

where a_n and b_n are Fourier coefficients given by

$$a_n = (\omega/\pi) \int_{-\pi/\omega}^{\pi/\omega} G(t)\cos(n\omega t)dt \tag{B.3}$$

and

$$b_n = (\omega/\pi) \int_{-\pi/\omega}^{\pi/\omega} G(t)\sin(n\omega t)dt \tag{B.4}$$

The function $G(t)$ is, in this case, the experimental pressure response, P. At periodic steady-state, P, $\cos(n\omega t)$ and $\sin(n\omega t)$ are periodic functions with frequency $\omega/2\pi$. Therefore, equations (B.3) and (B.4) can be written

$$a_n = (\omega/\pi) \int_{0}^{2\pi/\omega} P\cos(n\omega t)dt \tag{B.5}$$

and

$$b_n = (\omega/\pi) \int_{0}^{2\pi/\omega} P\sin(n\omega t)dt \tag{B.6}$$

Making the substitution $x = (\omega/2\pi)t$, equations (B.5) and (B.6) become

$$a_n = 2 \int_{0}^{1} P\cos(2\pi nx)dx \tag{B.7}$$

and

$$b_n = 2 \int_{0}^{1} P\sin(2\pi nx)dx \tag{B.8}$$

In terms of a numerical integration, where the ζ is the number of sampled points in a single cycle, equations (B.7) and (B.8) can be written (for small enough intervals)

$$a_n = (2/\zeta)\sum_{x=1}^{\zeta} P_x \cos(2\pi nx/\zeta) \tag{B.9}$$

and

$$b_n = (2/\zeta)\sum_{x=1}^{\zeta} P_x \sin(2\pi nx/\zeta) \tag{B.10}$$

B.2 Procedure

For simplicity, this procedure will discuss the use only of the first harmonic (n = 1). However, this can easily be extended to higher harmonics.

For each pressure, P_e, and for each sorbate, a blank experiment (i.e. no sorbent) is performed over a range of frequencies. If, for the fth frequency, the number of cycles required for co-addition is J, then, for the jth cycle,

$$a_{j,f} = (2/\zeta) \sum_{x=\zeta(j-1)+1}^{\zeta(j)} P_x \cos(2\pi x/\zeta) \tag{B.11}$$

and

$$b_{j,f} = (2/\zeta) \sum_{x=\zeta(j-1)+1}^{\zeta(j)} P_x \sin(2\pi x/\zeta) \tag{B.12}$$

and, for the fth frequency,

$$a_{B,f} = \left(\sum_{j=1}^{J} a_j \right) / J \tag{B.13}$$

and

$$b_{B,f} = \left(\sum_{j=1}^{J} b_j \right) / J \tag{B.14}$$

where subscript B refers to a blank experiment. Thus, at the fth frequency, in accordance with equations (B.1) and (B.2),

$$\alpha_{B,f} = (a_{B,f}^2 + b_{B,f}^2)^{1/2} \tag{B.15}$$

and

$$\phi_{B,f} = \arctan(a_{B,f}/b_{B,f}) \tag{B.16}$$

The same procedure is then performed in the presence of a sorbent, giving rise to the equations

$$\alpha_{Z,f} = (a_{Z,f}^2 + b_{Z,f}^2)^{½} \quad \text{(B.17)}$$

and

$$\phi_{Z,f} = \arctan(a_{Z,f}/b_{Z,f}) \quad \text{(B.18)}$$

where subscript Z refers to an experiment in the presence of a sorbent (e.g. zeolite).

The frequency response parameters which are used in equations (2.42) and (2.43) are then, for the f^{th} frequency,

$$(p_Z/p_B)_f = \alpha_{B,f}/\alpha_{Z,f} \quad \text{(B.19)}$$

and

$$(\phi_{Z\text{-}B})_f = \phi_{Z,f} - \phi_{B,f} \quad \text{(B.20)}$$

B.3 Algorithm

When pressure has been recorded over a series of frequencies, M data files exist with, in each file, the following information

- m = sequential number of file ($m = 1 \ldots M$)
- f_m = frequency associated with file m
- J_m = number of cycles over which pressure was recorded at frequency f_m
- ζ_m = number of pressure sample points within each cycle
- $J_m\zeta_m$ pressure measurements

The computer algorithm to process this data appears on the following page.

For $m = 1$ to M

Let $A = 0$

Let $B = 0$

For $j = 1$ to J_m

Let $\alpha = 0$

Let $\beta = 0$

For $x = [\zeta_m(j-1) + 1]$ to $[\zeta_m j]$

$\alpha = \alpha + P_x \cos(2\pi x/\zeta_m)$

$\beta = \beta + P_x \sin(2\pi x/\zeta_m)$

Next x

$a = 2\alpha/\zeta_m$

$b = 2\beta/\zeta_m$

Let $A = A + a$

Let $B = B + b$

Next j

$a_m = A/J_m$

$b_m = B/J_m$

$\alpha_m = (a_m^2 + b_m^2)^{1/2}$

$\phi_m = \arctan(a_m/b_m)$

Save m, f_m, α_m and ϕ_m to a file

Next m

C. Technical drawings of the primary cell

C.1 Chamber

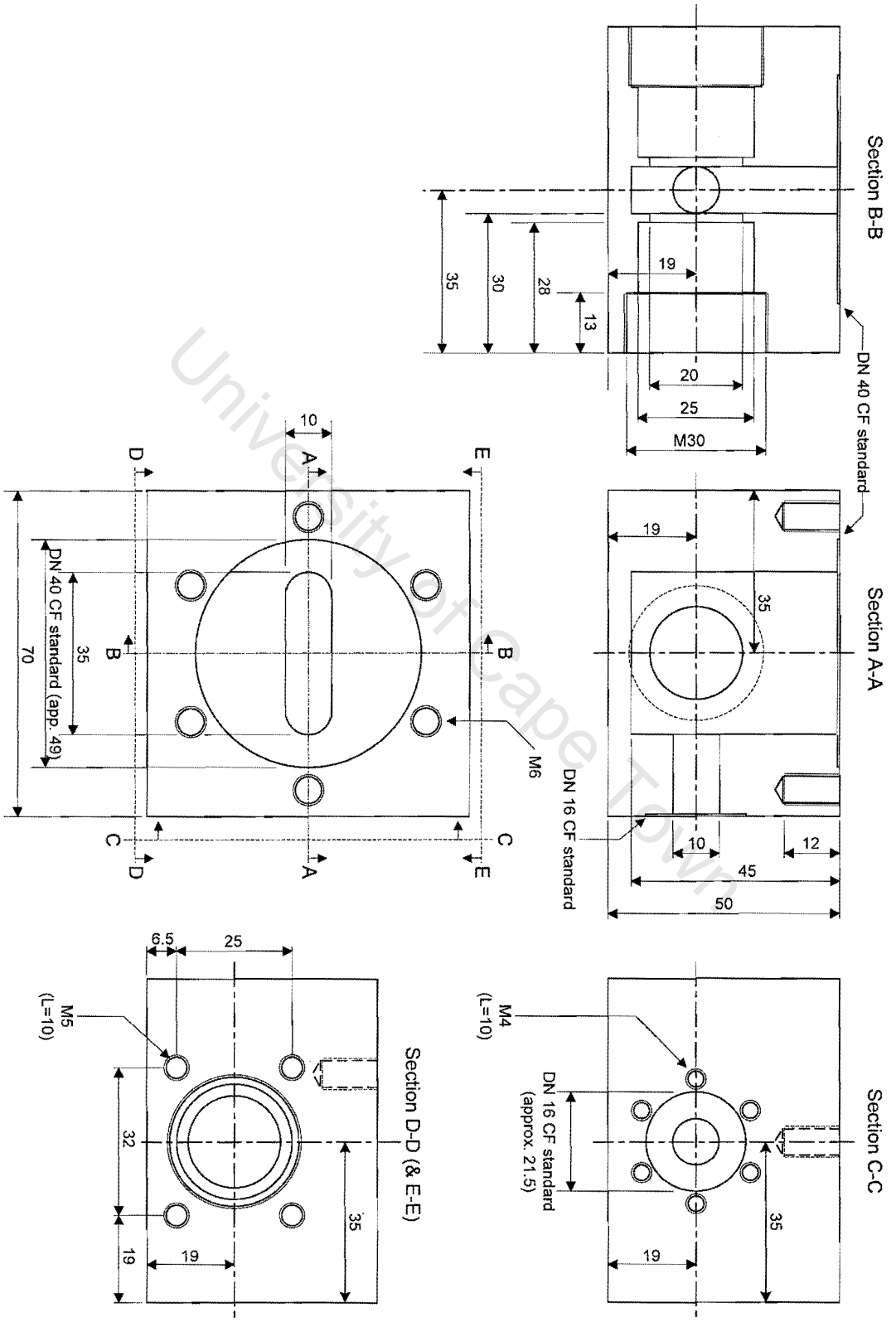

C.2 Sample holder

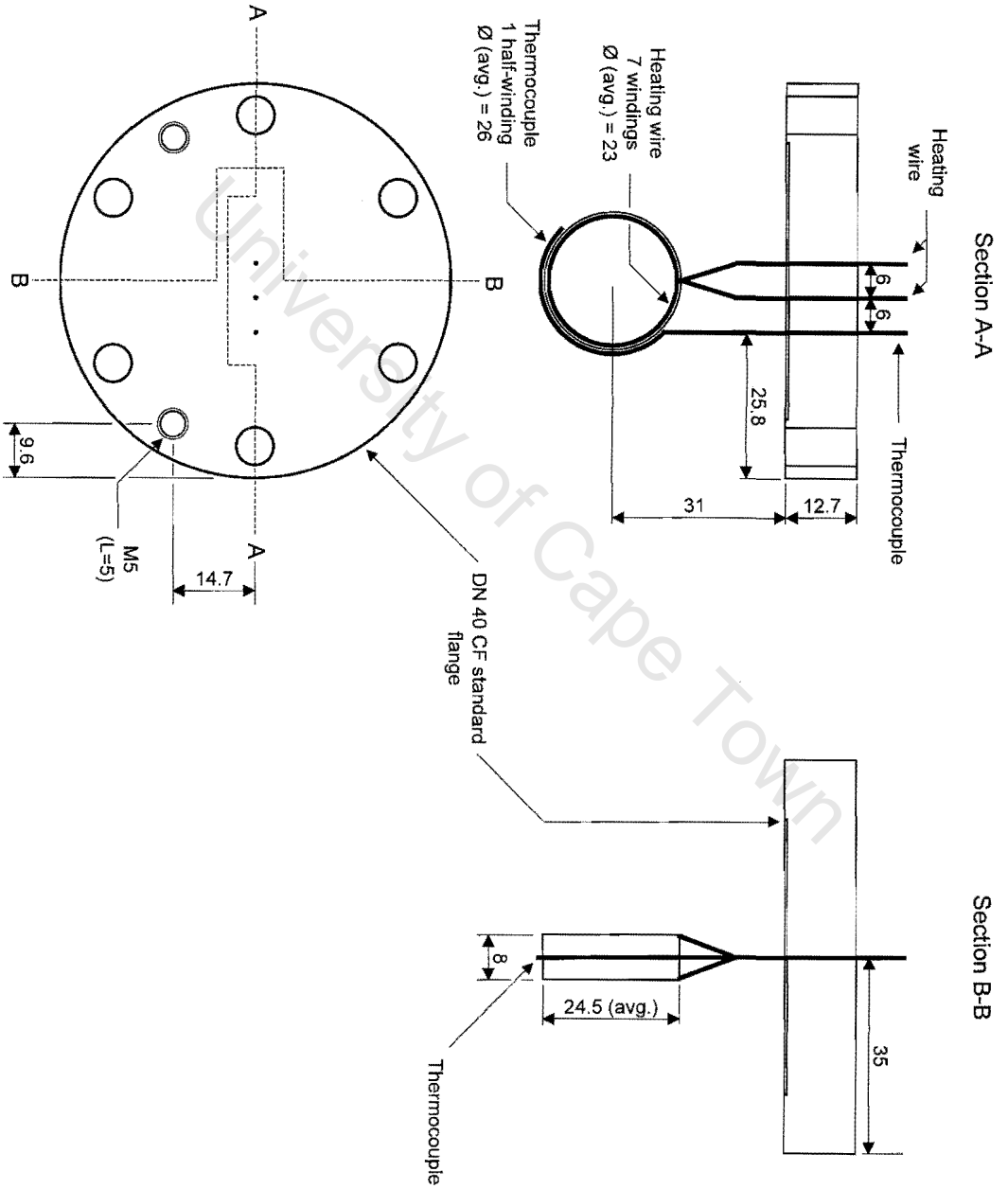

C.3 Accessories

Window fasteners (X2)

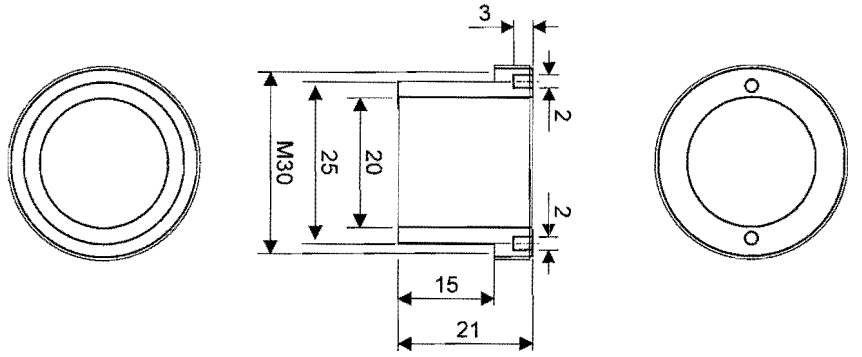

Gold ring sample supports

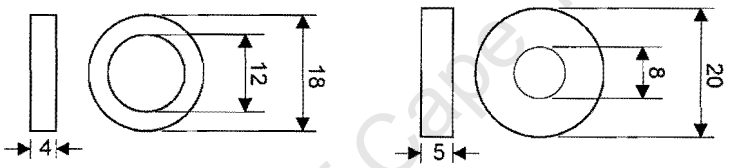

Aluminium positioning plate (X2)

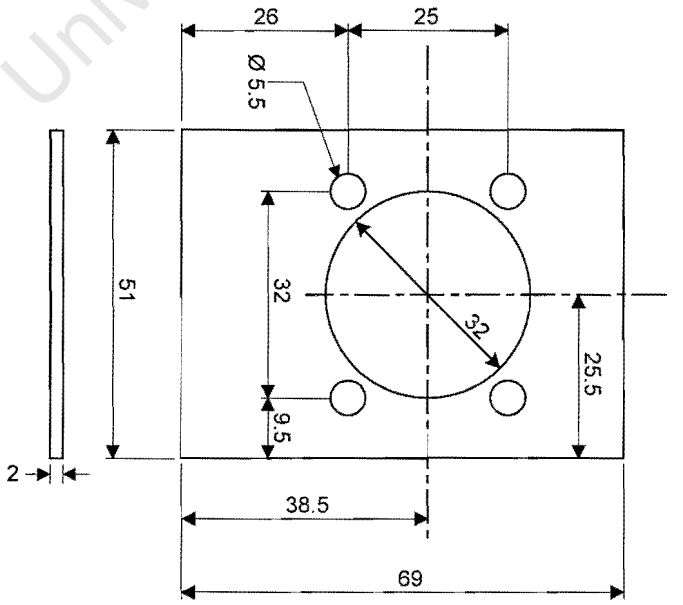

D. Technical drawings of the magnet-bellows assembly

D.1 Inner support plate

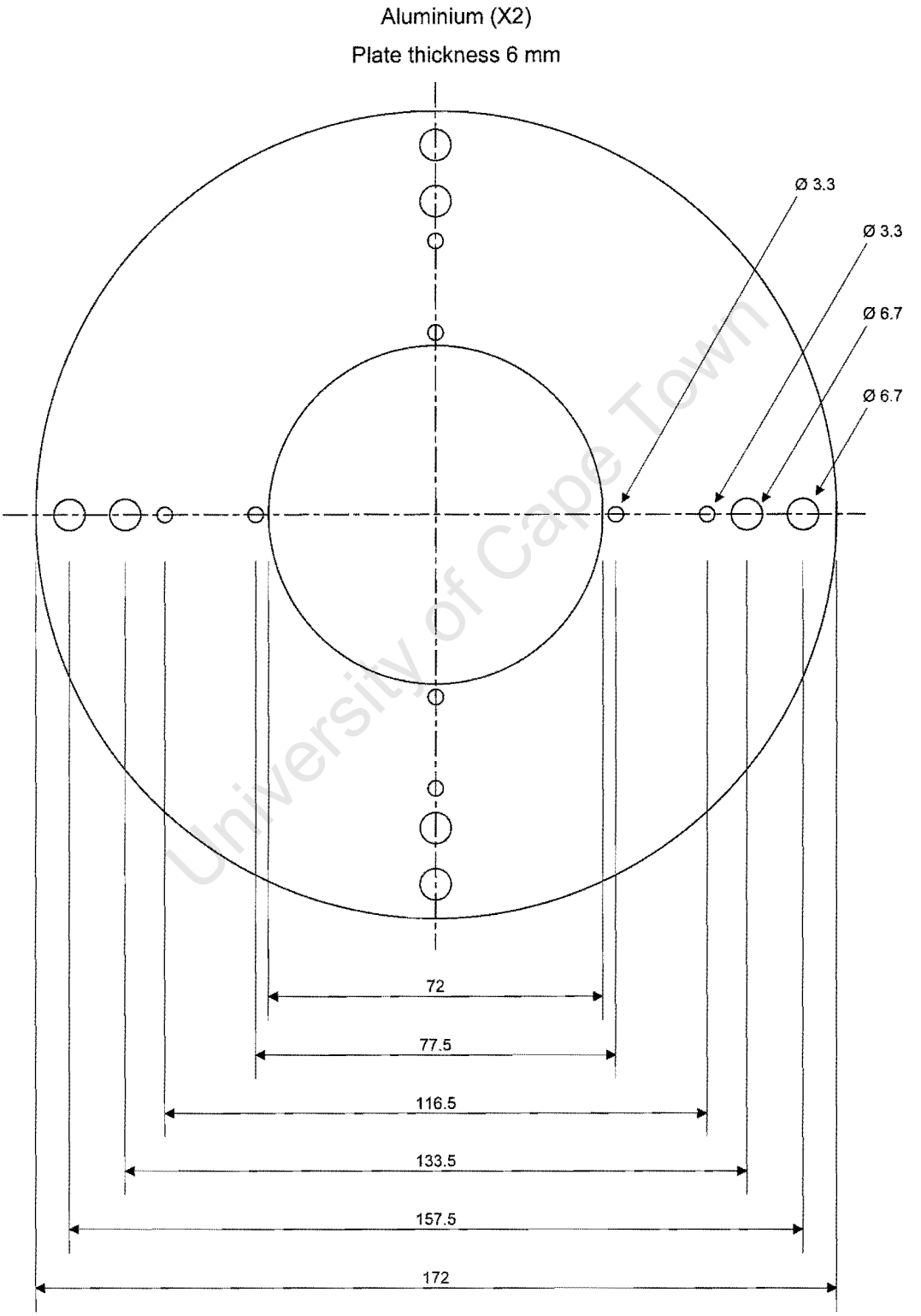

D.2 Outer support plate.

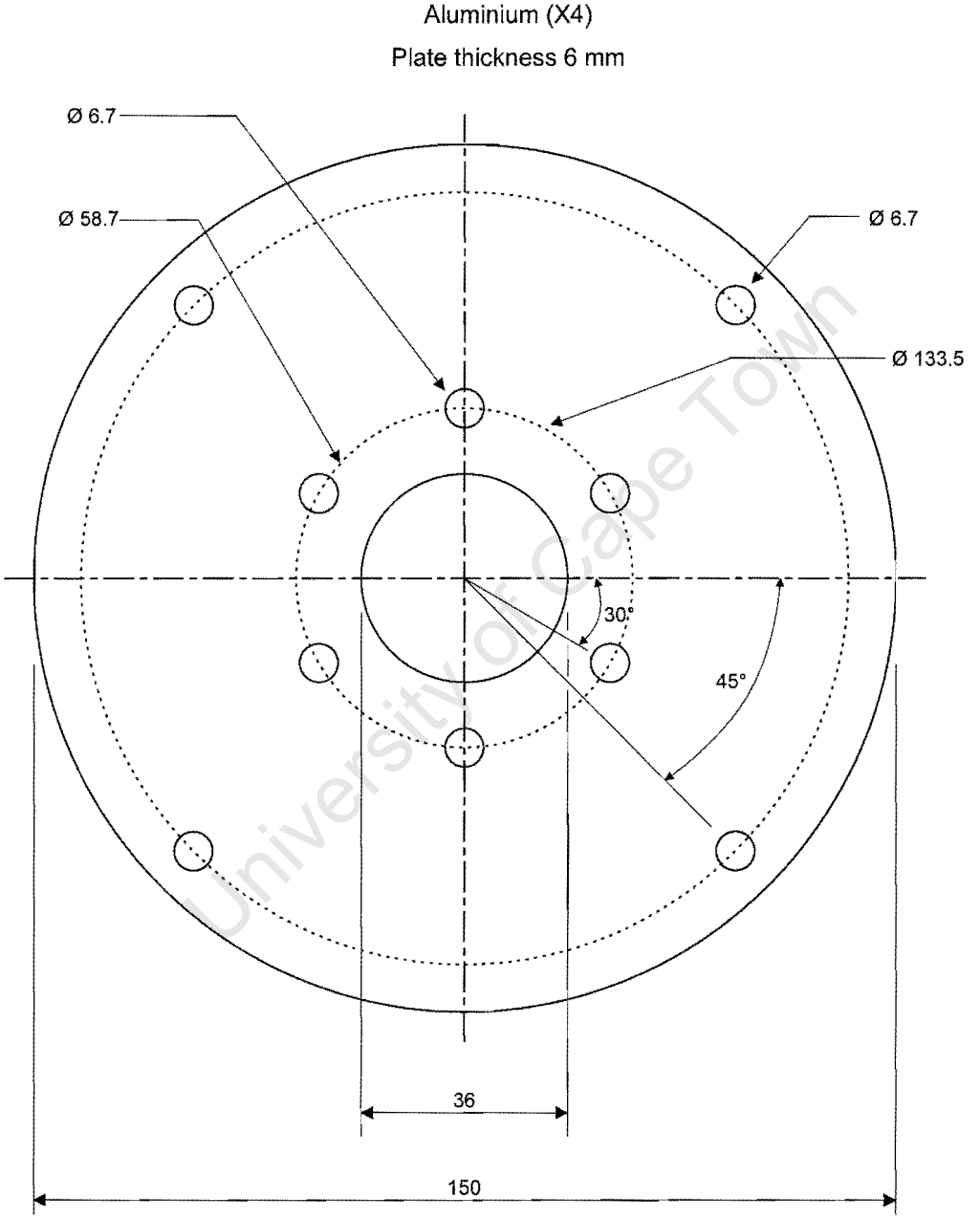

D.3 Armature plate

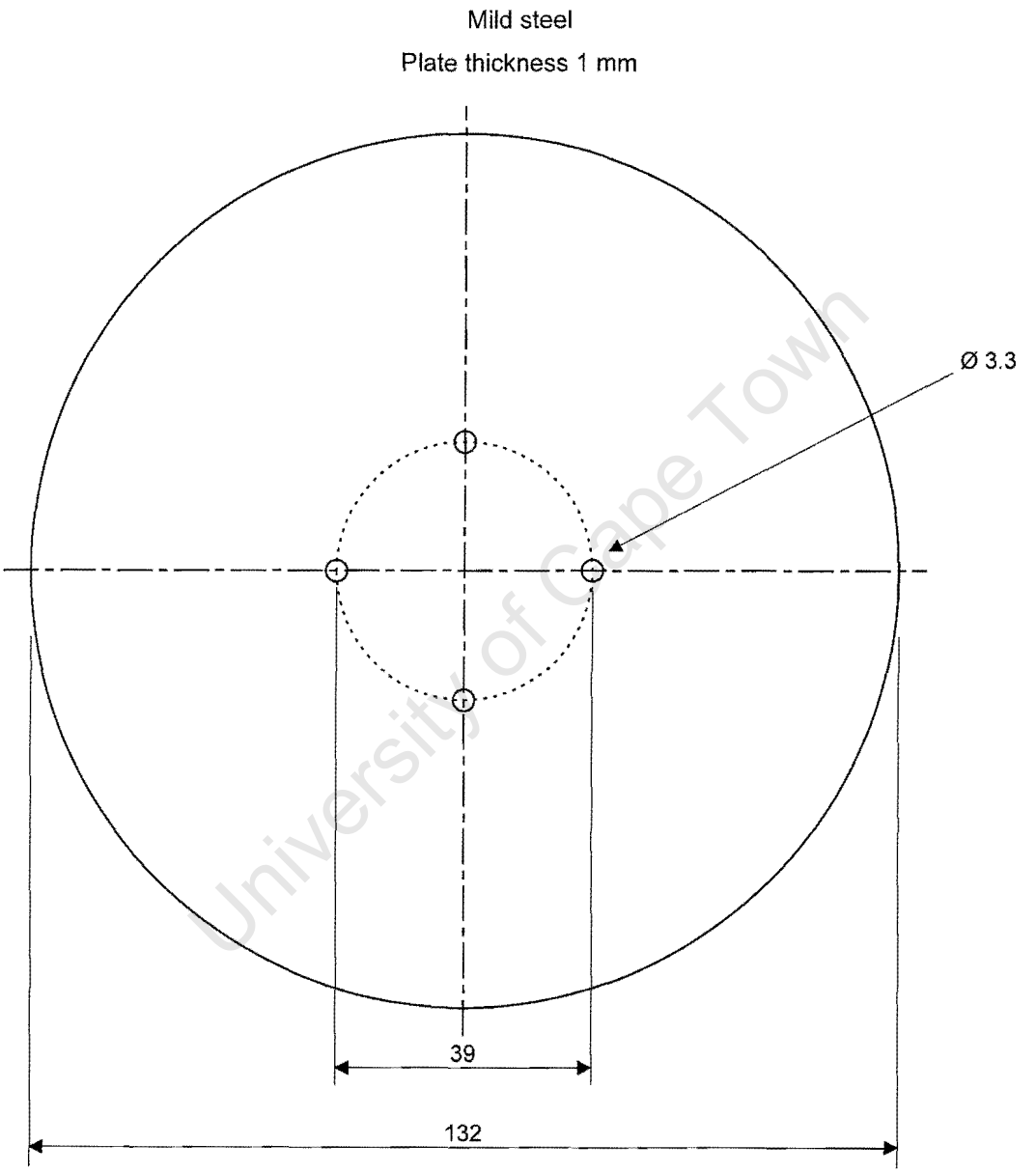

D.4 Spacers (example)

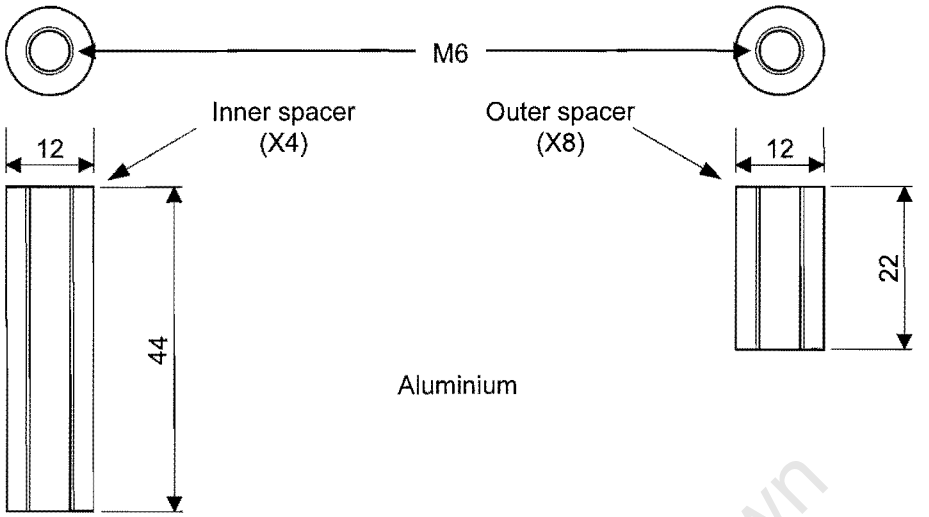

D.5 Magnet yoke

Mild Steel (X2)

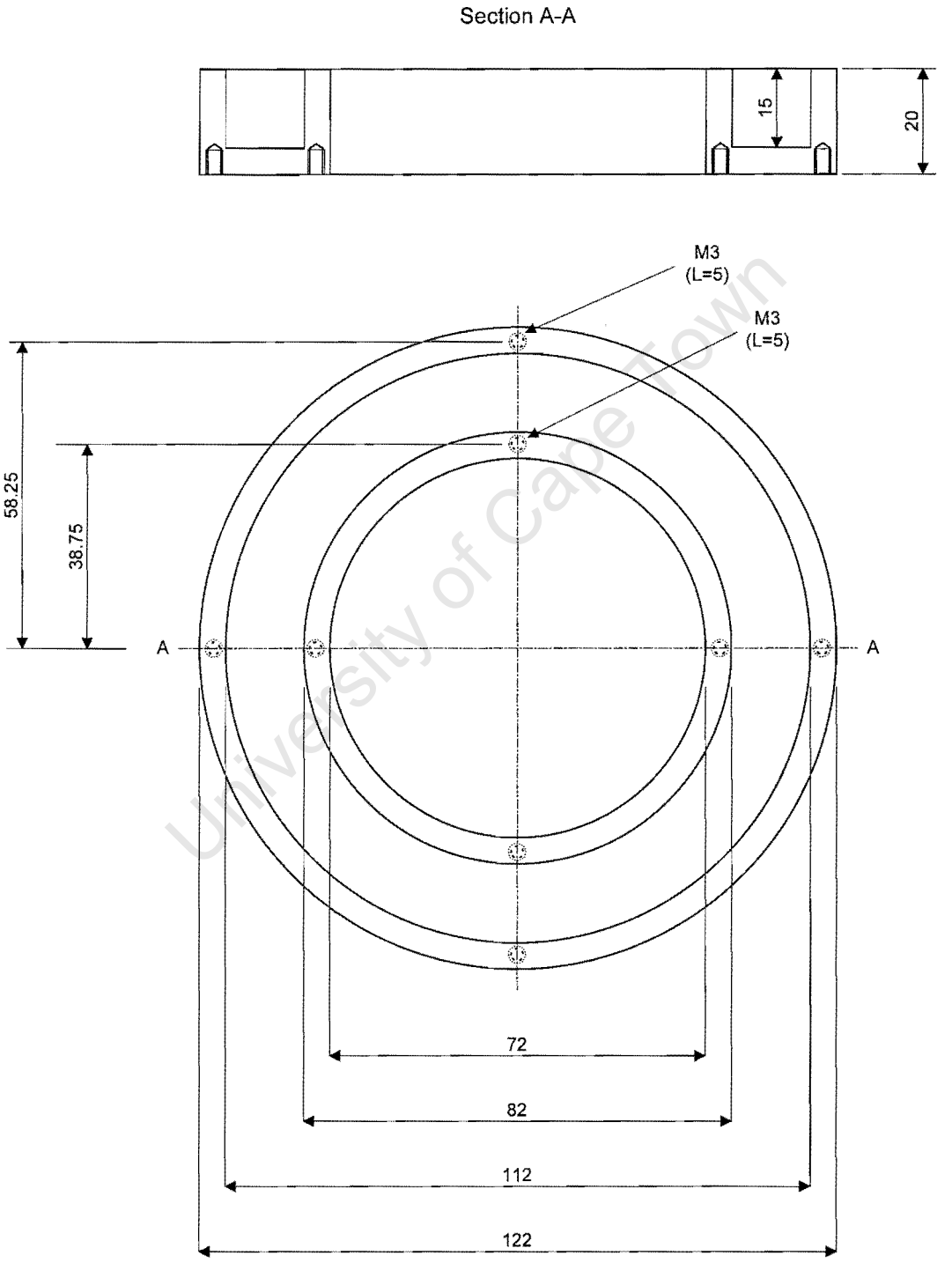

D.6 Frame for copper windings

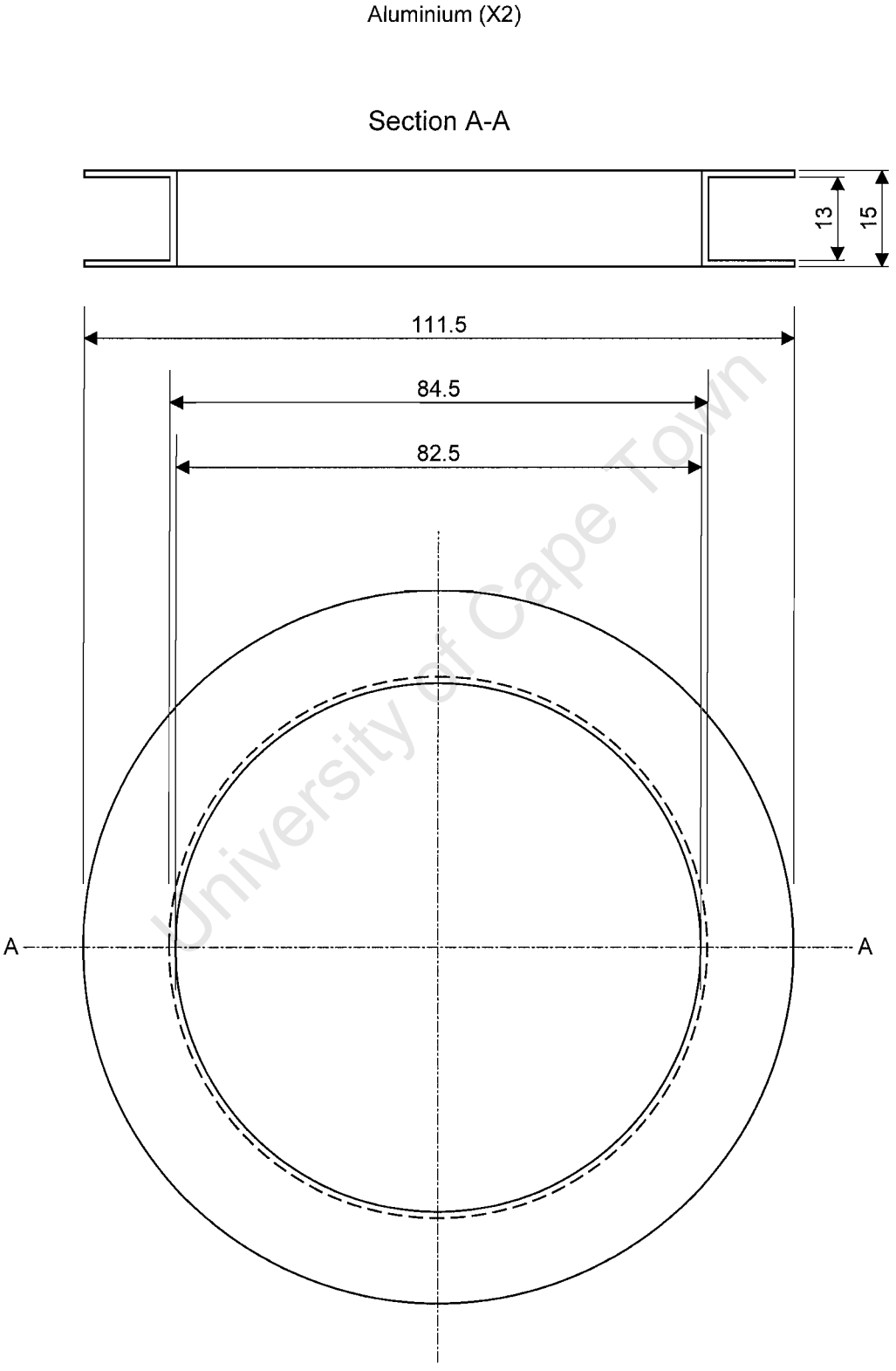

E. Solution of the force equations on the armature

E.1 The "spring" force of the bellows

For displacements that are small relative to their overall length, bellows can be modelled as springs with a spring constant k, such that $F = -kx$ where x is the displacement from the equilibrium position and F is the force in the direction of the displacement. The negative sign implies that F is always in the opposite direction to the displacement. Figure E.1 shows the movement of an armature mounted between two bellows.

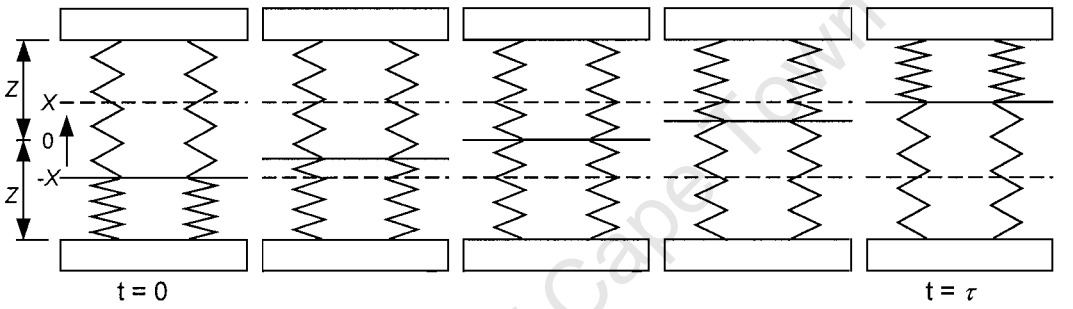

Figure E.1 – An armature mounted between two similar bellows moves from position (–*X*) to position *X* over time τ

It can be assumed that: (a) at the zero position of the armature, both bellows have the same length, Z; (b) both bellows have the same equilibrium length E; and (c) both bellows have the same spring constant k.

Consider an armature displaced from its centre position by x. Four possibilities exist:

(i) $Z < E - x$

(ii) $E - x < Z < E$

(iii) $E < Z < E + x$

(iv) $E + x < Z$

If F_1 is the force exerted by one bellows and F_2 the force exerted by the other, then the forces exerted by the bellows pair on the armature is as follows for each case:

(i) $F_1 = -k\{-[E-(Z+x)]\} = -k(-E+Z+x)$

$F_2 = -\langle -k\{-[E-(Z-x)]\}\rangle = k(-E+Z-x)$

$F_B = F_1 + F_2 = -2kx$

(ii) $F_1 = -k[(Z+x)-E] = -k(Z+x-E)$

$F_2 = -\langle -k\{-[E-(Z-x)]\}\rangle = k(-E+Z-x)$

$F_B = F_1 + F_2 = -2kx$

(iii) $F_1 = -k[(Z+x)-E] = -k(Z+x-E)$

$F_2 = -\langle -k\{-[E-(Z-x)]\}\rangle = k(-E+Z-x)$

$F_B = F_1 + F_2 = -2kx$

(iv) $F_1 = -k[(Z+x)-E] = -k(Z+x-E)$

$F_2 = -k\{-[(Z-x)-E]\} = -k(-Z+x+E)$

$F_B = F_1 + F_2 = -2kx$

Hence, regardless of the case, the force exerted by the two bellows on the armature is always

$$F_B = -2kx \qquad \text{(E.1)}$$

E.2 The overall force equation

According to Newton's second law:

$$F = m(d^2x/dt^2) \qquad \text{(E.2)}$$

where x is the displacement of the armature from its half-way position, m is the mass of the moving parts and F is the sum of the forces acting on the moving parts. From the argument in section 4.4.3, only the magnetic force and the spring force of the bellows need be considered, i.e.

$$F_M - 2kx = m(d^2x/dt^2) \qquad \text{(E.3)}$$

If the distance between the magnets is $2X$ (see Figure E.1), then the boundary conditions are:

$$dx/dt = 0 \qquad \text{at } x = -X \qquad \text{(E.4)}$$

$$x = -X \qquad \text{at } t = 0 \qquad \text{(E.5)}$$

$$t = \tau \qquad \text{at } x = X \qquad \text{(E.6)}$$

Rearranging equation (E.3) and making the substitution $v = dx/dt$,

$$d^2x/dt^2 = dv/dt = v(dv/dx) = (-2k/m)x + F_M/m \qquad \text{(E.7)}$$

Integrating,
$$(\tfrac{1}{2})v^2 = (\tfrac{1}{2})(dx/dt)^2 = (-k/m)x^2 + (F_M/m)x + C_1 \qquad \text{(E.8)}$$

From boundary condition (E.4), $C_1 = (k/m)X^2 + (F_M/m)X$ (E.9)

Thus, substituting equation (E.9) in equation (E.8) and completing the square

$$dx/dt = (2k/m)^{1/2}[(X + F_M/2k)^2 - (x - F_M/2k)^2]^{1/2} \qquad \text{(E.10)}$$

Integrating, $t = (m/2k)^{1/2}\{\arcsin[(x - F_M/2k)/(X + F_M/2k)] + C_2\}$ (E.11)

From boundary condition (E.5), $C_2 = \pi/2$. Therefore, substituting this and boundary condition (E.6) into equation (E.11)

$$\tau = (m/2k)^{1/2}\{\pi/2 + \arcsin[(X - F_M/2k)/(X + F_M/2k)]\} \qquad \text{(E.12)}$$

F. Technical drawings of the pressure gauge accessories

F.1 Heater – main body

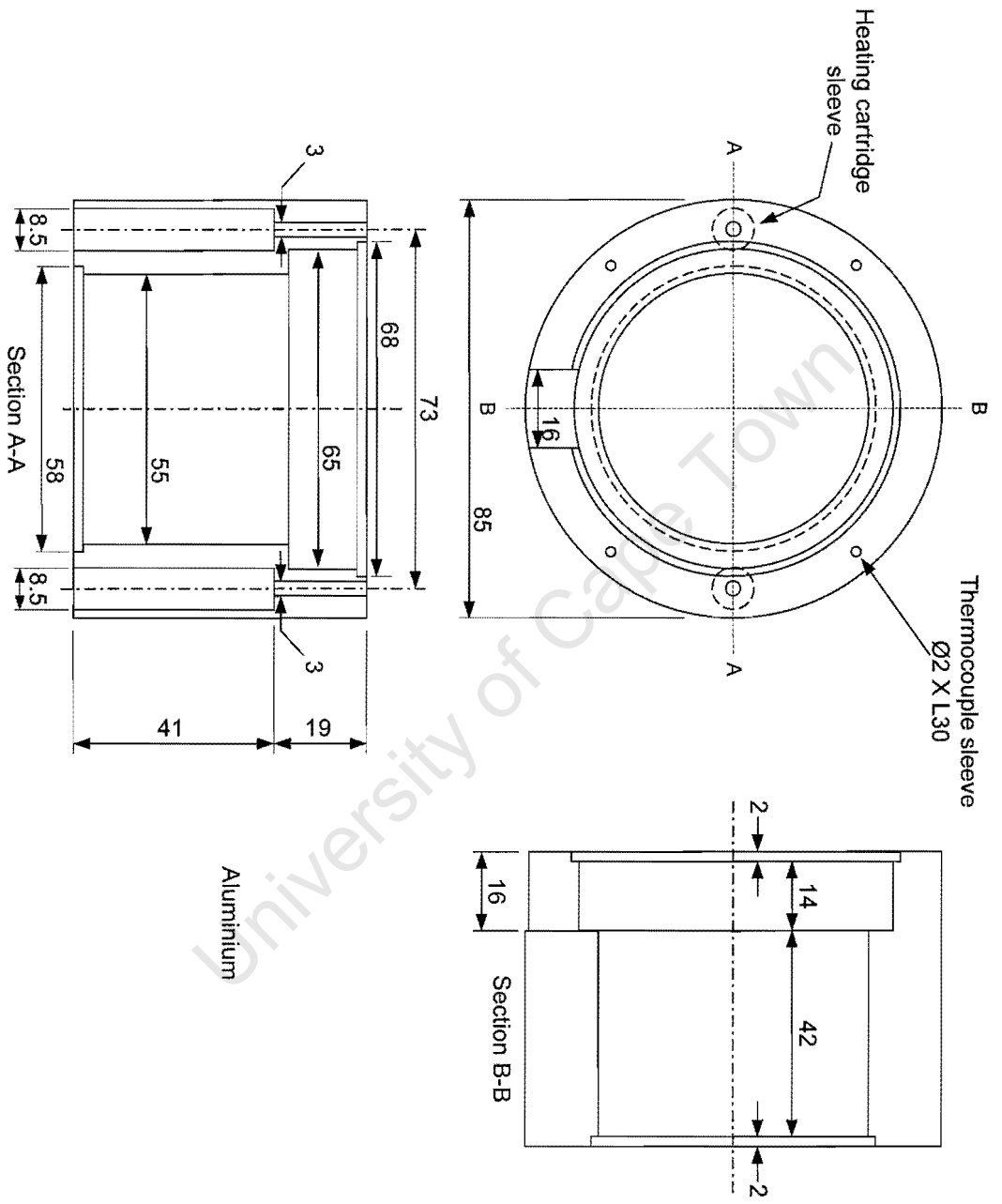

It should be noted that, for ease of assembly, the heater was cut in half (along section B-B) after construction. Thus, once it was mounted around the pressure gauge, it was held together by a set of clamps.

F.2 Heater – end covers

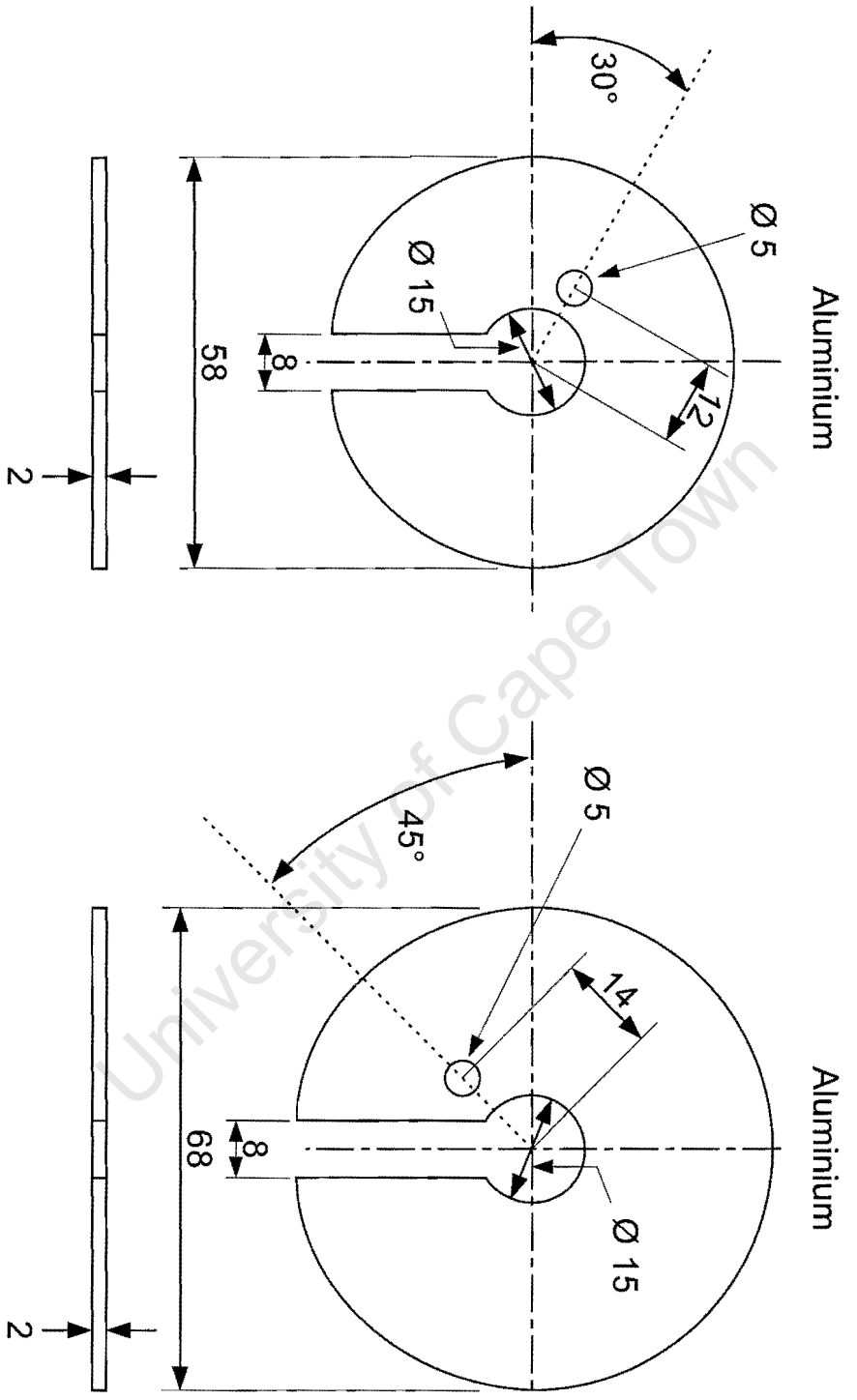

F.3 Strain prevention strips

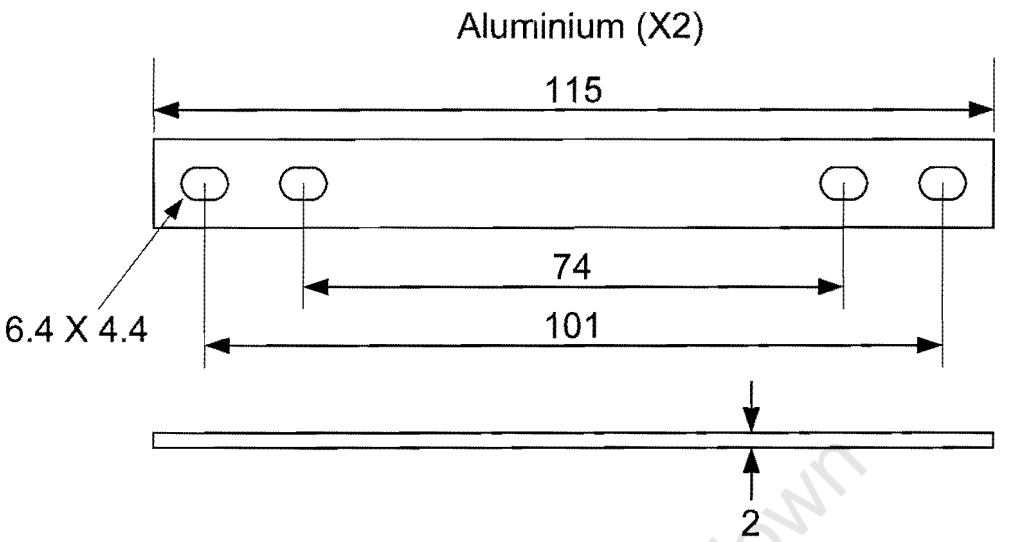

The principal of the strain prevention strips is shown below. When the flanges at the end of the U-shaped transducer tubing were connected to the system, the strips were bolted into place and thus maintained a fixed distance between the flanges. The oval-shaped holes allowed flexibility when the strips were first inserted so that the strips themselves did not distort the tubing.

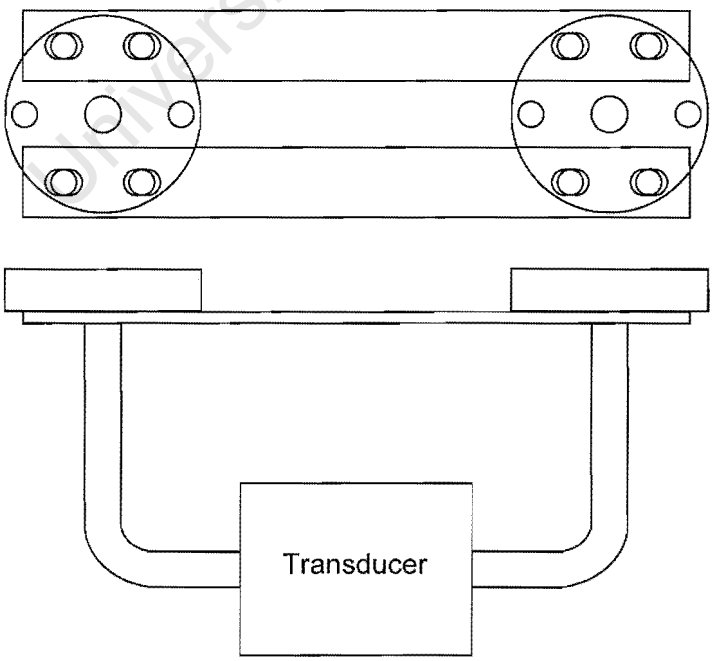

G. Technical drawings of the vacuum feedthrough panel for the IR spectrometer

G.1 Main plate

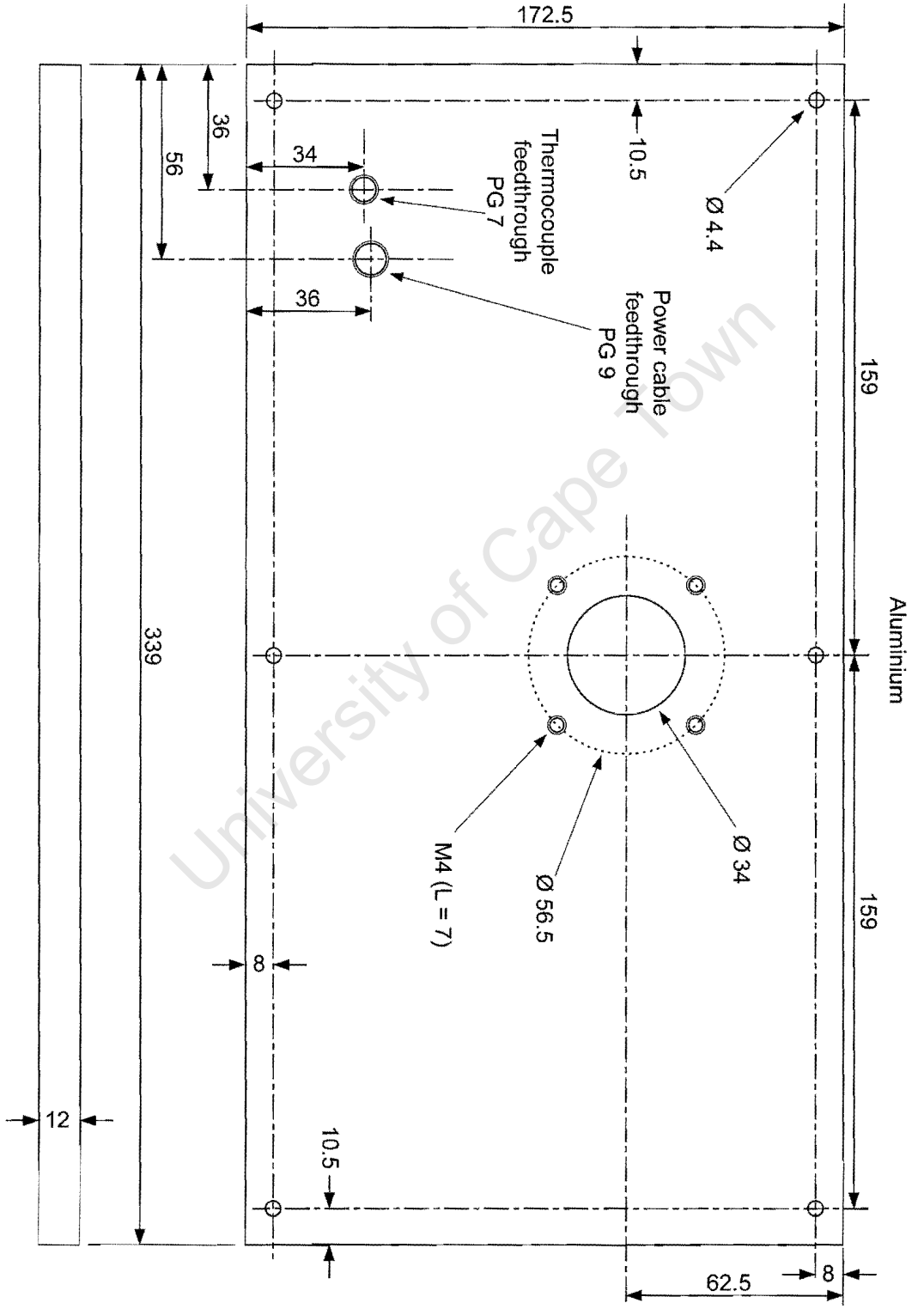

G.2 Secondary seals

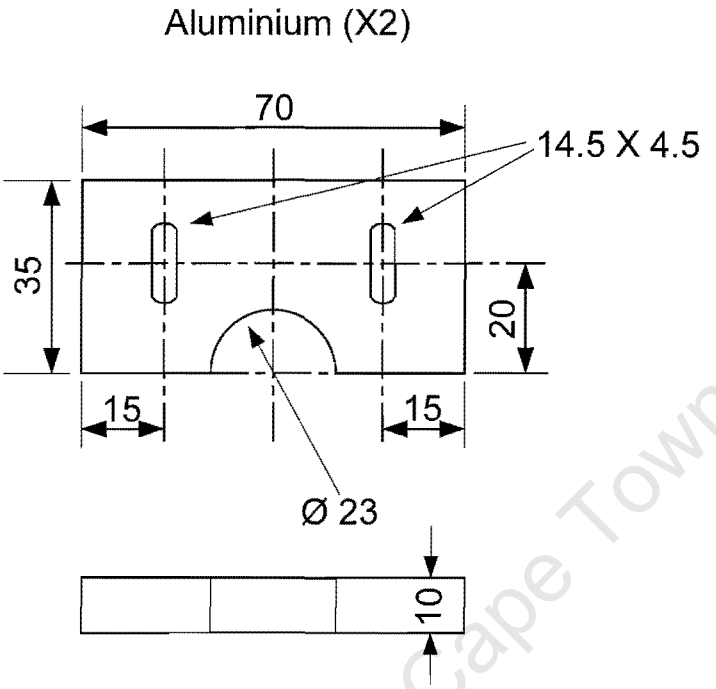

H. Electrical circuit drawings

H.1 Control circuit diagram (overall)

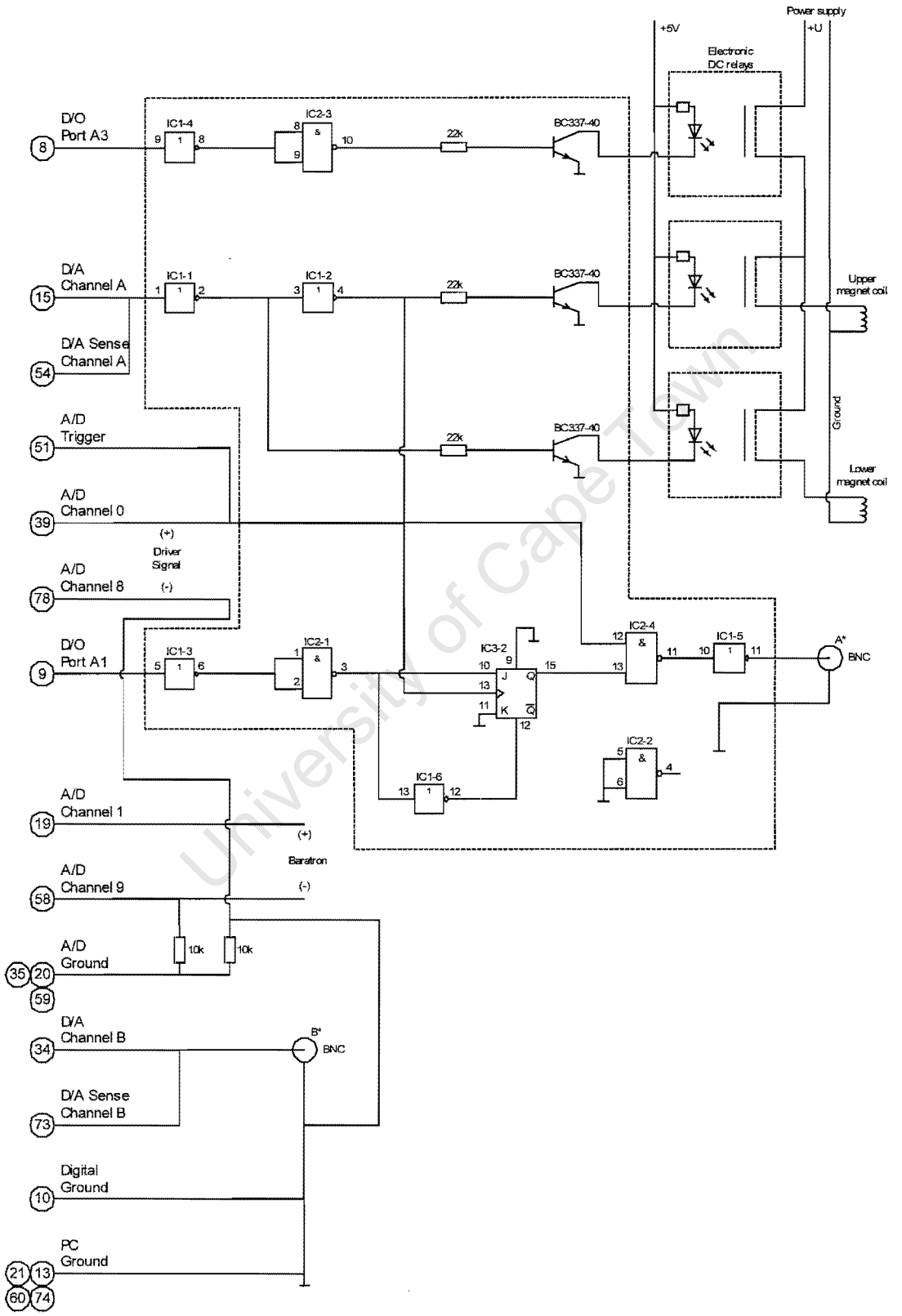

H.2 Control circuit diagram (terminal block)

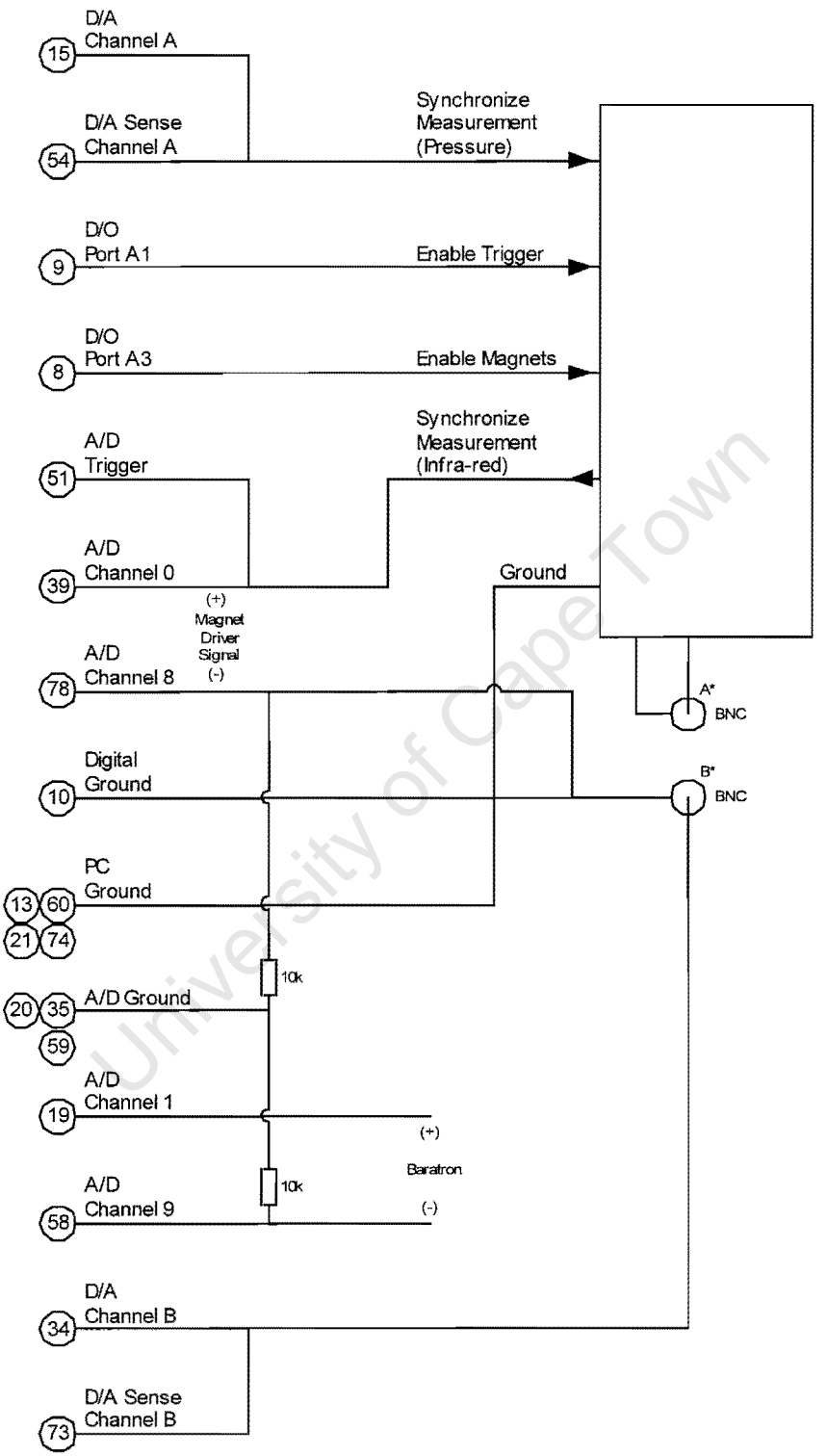

H.3 Terminal block

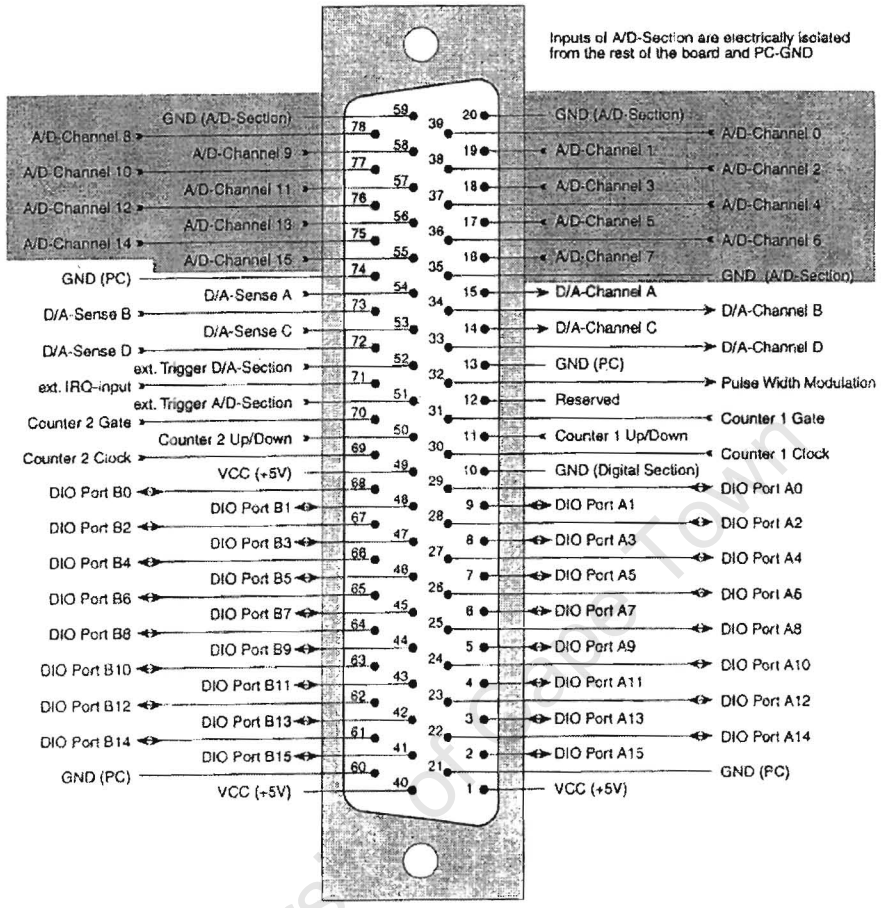

H.4 Logic modules (integrated circuits)

IC1 CD4584

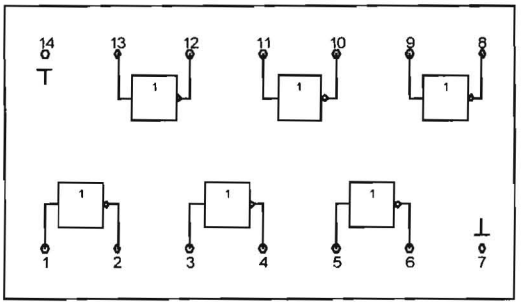

IC2 CD4011

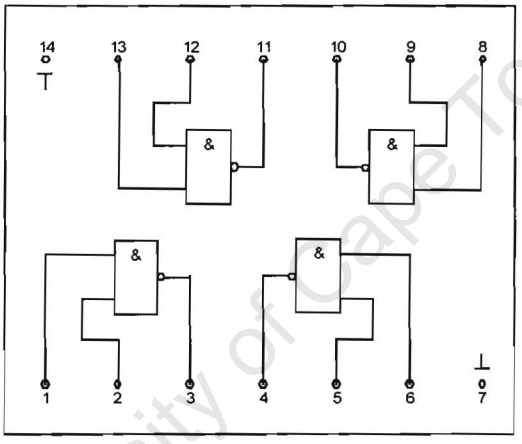

IC3 HCF4027

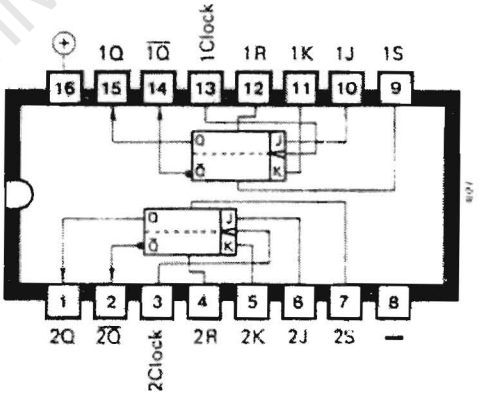

I. Estimate of the system volume

I.1 Fixed-volume components

The following table shows the calculated volumes of all the fixed-volume components in the closed frequency response system. It should be noted that exact dimensions of some fittings were not known and thus some of the values were only estimates. In sections 2.2.2 and 2.3.2, it was shown that, for the FR method, it is not essential to know the exact absolute and relative volumes.

Part	Sub-part	Number	Diameter/Height	Width	Length	Volume		
			cm	cm	cm	Sub-part cm3	Part cm3	Cumulative cm3
Primary Cell	Main compartment (parallelopiped)	1	2.50	1.00	4.50	11.25		
	Main compartment (half-cylinder)	2	1.00		4.50	3.53		
	Windows vacancies	2	2.00		0.20	1.26		
	Vacuum line	1	1.00		1.75	1.37	17.42	17.42
Flexible connection		1	1.66		18.00	38.96	38.96	56.37
Six-way cross	Continuous straight tube	1	1.72		7.60	17.66		
	Interrupted straight tube	2	1.72		5.88	27.32	44.98	101.36
Elbow		2	1.72		5.98	27.81	27.81	129.17
Pressure gauge		1	0.64		15.00	4.75	4.75	133.92
Secondary Cell	Flange	1	1.60		0.73	1.47		
	Glass/metal and transition glass	1	0.85		8.80	4.99		
	Quartz glass	1	0.80		8.00	4.02	10.48	144.40
In-line valve		1	2.54		2.00	10.13	10.13	154.53
Zero length adaptors		2	1.72		1.27	5.90	5.90	160.44
Right-angled valve		1	1.72		3.81	8.85	8.85	169.29
Straight run		1	1.72		3.50	8.13	8.13	177.42
Bellows Fittings	Plate fitting	1	5.10		0.30	6.13		
	Flange (incl. fitting)	1	3.80		1.60	18.15	24.27	201.69

I.2 Variable-volume components

As mentioned in section 4.4.4, a range of spacer lengths was necessary to allow for a range of armature travel distances. The following tables show, for two different outer (secondary) spacer lengths, the most important absolute and relative volumes calculated for a range of inner (primary) spacer lengths.

Spacing		Travel			Bellows length			Bellows Volume			System volume		
Primary	Secondary	Distance	Volume	Fraction	(equilibrium)	(compressed)	(extended)	(equilibrium)	(compressed)	(extended)	(equilibrium)	(compressed)	(extended)
mm	mm	mm	cm3	%	mm	mm	mm	cm3	cm3	cm3	cm3	cm3	cm3
43.0	22	2.0	3.92	1.66	17.30	16.30	18.30	33.91	31.95	35.87	235.60	233.64	237.56
43.5	22	2.5	4.9	2.08	17.55	16.30	18.80	34.40	31.95	36.85	236.09	233.64	238.54
44.0	22	3.0	5.88	2.49	17.80	16.30	19.30	34.89	31.95	37.83	236.58	233.64	239.52
44.5	22	3.5	6.86	2.89	18.05	16.30	19.80	35.38	31.95	38.81	237.07	233.64	240.50
45.0	22	4.0	7.84	3.30	18.30	16.30	20.30	35.87	31.95	39.79	237.56	233.64	241.48
45.5	22	4.5	8.82	3.71	18.55	16.30	20.80	36.36	31.95	40.77	238.05	233.64	242.46
46.0	22	5.0	9.8	4.11	18.80	16.30	21.30	36.85	31.95	41.75	238.54	233.64	243.44
46.5	22	5.5	10.78	4.51	19.05	16.30	21.80	37.34	31.95	42.73	239.03	233.64	244.42
47.0	22	6.0	11.76	4.91	19.30	16.30	22.30	37.83	31.95	43.71	239.52	233.64	245.40
47.5	22	6.5	12.74	5.31	19.55	16.30	22.80	38.32	31.95	44.69	240.01	233.64	246.38
48.0	22	7.0	13.72	5.70	19.80	16.30	23.30	38.81	31.95	45.67	240.50	233.64	247.36
48.5	22	7.5	14.7	6.10	20.05	16.30	23.80	39.30	31.95	46.65	240.99	233.64	248.34
49.0	22	8.0	15.68	6.49	20.30	16.30	24.30	39.79	31.95	47.63	241.48	233.64	249.32
49.5	22	8.5	16.66	6.89	20.55	16.30	24.80	40.28	31.95	48.61	241.97	233.64	250.30
50.0	22	9.0	17.64	7.28	20.80	16.30	25.30	40.77	31.95	49.59	242.46	233.64	251.28
50.5	22	9.5	18.62	7.66	21.05	16.30	25.80	41.26	31.95	50.57	242.95	233.64	252.26
51.0	22	10.0	19.6	8.05	21.30	16.30	26.30	41.75	31.95	51.55	243.44	233.64	253.24
51.5	22	10.5	20.58	8.44	21.55	16.30	26.80	42.24	31.95	52.53	243.93	233.64	254.22
52.0	22	11.0	21.56	8.82	21.80	16.30	27.30	42.73	31.95	53.51	244.42	233.64	255.20
52.5	22	11.5	22.54	9.20	22.05	16.30	27.80	43.22	31.95	54.49	244.91	233.64	256.18
53.0	22	12.0	23.52	9.58	22.30	16.30	28.30	43.71	31.95	55.47	245.40	233.64	257.16
53.5	22	12.5	24.5	9.96	22.55	16.30	28.80	44.20	31.95	56.45	245.89	233.64	258.14
54.0	22	13.0	25.48	10.34	22.80	16.30	29.30	44.69	31.95	57.43	246.38	233.64	259.12
54.5	22	13.5	26.46	10.72	23.05	16.30	29.80	45.18	31.95	58.41	246.87	233.64	260.10
55.0	22	14.0	27.44	11.09	23.30	16.30	30.30	45.67	31.95	59.39	247.36	233.64	261.08

Spacing		Travel			Bellows length			Bellows Volume			System volume		
Primary	Secondary	Distance	Volume	Fraction	(equilibrium)	(compressed)	(extended)	(equilibrium)	(compressed)	(extended)	(equilibrium)	(compressed)	(extended)
mm	mm	mm	cm3	%	mm	mm	mm	cm3	cm3	cm3	cm3	cm3	cm3
43.0	26	2.0	3.92	1.61	21.30	20.30	22.30	41.75	39.79	43.71	243.44	241.48	245.40
43.5	26	2.5	4.9	2.01	21.55	20.30	22.80	42.24	39.79	44.69	243.93	241.48	246.38
44.0	26	3.0	5.88	2.41	21.80	20.30	23.30	42.73	39.79	45.67	244.42	241.48	247.36
44.5	26	3.5	6.86	2.80	22.05	20.30	23.80	43.22	39.79	46.65	244.91	241.48	248.34
45.0	26	4.0	7.84	3.19	22.30	20.30	24.30	43.71	39.79	47.63	245.40	241.48	249.32
45.5	26	4.5	8.82	3.59	22.55	20.30	24.80	44.20	39.79	48.61	245.89	241.48	250.30
46.0	26	5.0	9.8	3.98	22.80	20.30	25.30	44.69	39.79	49.59	246.38	241.48	251.28
46.5	26	5.5	10.78	4.37	23.05	20.30	25.80	45.18	39.79	50.57	246.87	241.48	252.26
47.0	26	6.0	11.76	4.75	23.30	20.30	26.30	45.67	39.79	51.55	247.36	241.48	253.24
47.5	26	6.5	12.74	5.14	23.55	20.30	26.80	46.16	39.79	52.53	247.85	241.48	254.22
48.0	26	7.0	13.72	5.52	23.80	20.30	27.30	46.65	39.79	53.51	248.34	241.48	255.20
48.5	26	7.5	14.7	5.91	24.05	20.30	27.80	47.14	39.79	54.49	248.83	241.48	256.18
49.0	26	8.0	15.68	6.29	24.30	20.30	28.30	47.63	39.79	55.47	249.32	241.48	257.16
49.5	26	8.5	16.66	6.67	24.55	20.30	28.80	48.12	39.79	56.45	249.81	241.48	258.14
50.0	26	9.0	17.64	7.05	24.80	20.30	29.30	48.61	39.79	57.43	250.30	241.48	259.12
50.5	26	9.5	18.62	7.42	25.05	20.30	29.80	49.10	39.79	58.41	250.79	241.48	260.10
51.0	26	10.0	19.6	7.80	25.30	20.30	30.30	49.59	39.79	59.39	251.28	241.48	261.08
51.5	26	10.5	20.58	8.17	25.55	20.30	30.80	50.08	39.79	60.37	251.77	241.48	262.06
52.0	26	11.0	21.56	8.55	25.80	20.30	31.30	50.57	39.79	61.35	252.26	241.48	263.04
52.5	26	11.5	22.54	8.92	26.05	20.30	31.80	51.06	39.79	62.33	252.75	241.48	264.02
53.0	26	12.0	23.52	9.29	26.30	20.30	32.30	51.55	39.79	63.31	253.24	241.48	265.00
53.5	26	12.5	24.5	9.66	26.55	20.30	32.80	52.04	39.79	64.29	253.73	241.48	265.98
54.0	26	13.0	25.48	10.02	26.80	20.30	33.30	52.53	39.79	65.27	254.22	241.48	266.96
54.5	26	13.5	26.46	10.39	27.05	20.30	33.80	53.02	39.79	66.25	254.71	241.48	267.94
55.0	26	14.0	27.44	10.75	27.30	20.30	34.30	53.51	39.79	67.23	255.20	241.48	268.92